# Tailoring optical resonances
# in photonic crystals with an optical nanofiber

February 2018

TETSUMOTO, Tomohiro

A Thesis for the Degree of  Ph.D. in Engineering

# Tailoring optical resonances in photonic crystals with an optical nanofiber

February 2018

Graduate School of Science and Technology
Keio University

TETSUMOTO, Tomohiro

# Abstract

The progress made on nano-fabrication technologies has made it possible to devise sophisticated optical nano- and micro-cavities that can confine light in a tiny space. These devices are widely used in the fields of nonlinear optics and quantum optics because they allow us to obtain a high photon density inside an optical microcavity. Among them, photonic crystal nanocavities are suitable for applications that use nonlinear optical effects and the quantum properties of light, because they enable obtaining high $Q$ resonant modes and the dense integration of the devices on a chip owing to their small size. On the other hand, there are challenges in cavity quantum electrodynamics applications for the quantum information technology with conventional photonic crystal nanocavities; The coupling efficiency of light from a cavity to an optical fiber is low, the deterministic control of resonant wavelengths and $Q$s, and the implementation of the polarization diversity are difficult.

In this study, it is shown that these problems can be solved simultaneously by employing optical nanofibers. The proposal has been made for two types of photonic crystal nanocavities of a nanofiber-coupled photonic crystal cavity and a silica nanobeam cavity. The former cavity enables a high coupling efficiency with an optical fiber besides the tuning of the wavelength and the $Q$ of the resonant mode, and on top of them, the latter cavity enables the polarization diversity.

Chapter 1 reviews the background of the study and describes the motivation.

Chapter 2 summarizes the theories needed for this study and describes principles of forming photonic bandgap and a photonic crystal nanocavity, and numerical methods used in this study.

Chapter 3 presents the principle behind the formation of a nanofiber-coupled photonic crystal nanocavity. By measuring the optical properties, I show that a coupling efficiency of 99.6% can be achieved at most and, furthermore, that the wavelength and the $Q$ of the resonant mode can be tuned by controlling nanofiber's diameter and contact length between a photonic crystal.

Chapter 4 shows a demonstration of the formation of coupled resonances by using a fiber coupled photonic crystal nanocavity. Avoided crossing was observed in the spectrum domain by taking advantage of the wavelength controllability of the resonant modes.

Chapter 5 reports the design, fabrication and characterization of a silica nanobeam cavity. I show that the quality factors for both the TE and TM modes exhibit values higher than $10^4$, and confirm the orthogonality of these two modes. In addition, by changing the nanofiber's diameter and the distance between the silica nanobeam cavity and the optical nanofiber used for inputting and outputting light, I achieve a coupling efficiency of more than 95% and, furthermore, show that the wavelength and the $Q$ of the resonant mode can be tuned.

Chapter 6 describes the design of a silica nanobeam cavity with two spectrally overlapped

orthogonal modes. By demonstrating numerically the localization of circularly polarized light, I show the possibility of the polarization diversity of this device.

Chapter 7 summarizes the results I report in each chapter and concludes the thesis.

# Abbreviation

Summary of abbreviations is presented in Tab. 1 for easy search, although they are defined in the article at the first appearance.

Table. 1: Summary of abbreviations (alphabetical order)

| Abbreviation | Original expression |
|---|---|
| 1D | One dimentional |
| 2D | Two dimentional |
| 3D | Three dimentional |
| CE | Coupling effiency |
| CMT | Coupled mode theory |
| CVD | Chemical vapor deposition |
| DUT | Device under test |
| EB | Electron beam |
| FDTD | Finite differential time domain (method) |
| FEM | Finite element method |
| FP | Fabri Perot |
| FSR | Free spectral range |
| FWHM | Full width at half maximum |
| ICP | Inductively coupled plasma |
| IR | Infrared |
| LER | Line edge roughness |
| PBG | Photonic bandgap |
| PC | Polarization controller |
| PhC | Photonic crystal |
| PM | Power meter |
| PML | Perfect matching layer |
| PWE | Plane wave expansion method |
| QED | Quantum electrodynamics |
| SEM | Scanning electron microscope |
| SOI | Silicon on insulator |
| TE | Transverse electric |
| TEOS | Tetraethyl orthosilicate |
| TLD | Tunable laser diode |

Table. 1: Summary of abbreviations (alphabetical order)

| Abbreviation | Original expression |
|---|---|
| TM | Transverse magnetic |
| TO | Thermo optic |
| UV | Ultraviolet |
| VOA | Variable optical attenuator |
| WGM | Whispering gallery mode |

End of the table.

# Contents

CONTENTS

# Chapter 1

# Introduction

The physical implementation of photonic quantum networks has widely been studied for the implementation of quantum information technologies such as quantum simulators and quantum communication systems [1]. These technologies, consisting of channels and nodes, exploit the nonclassical nature of light and demonstrate profoundly different properties from classical systems. Optical fibers are considered suitable channels as they carry photons over long distance with negligible loss and decoherence. On the other hand, for quantum nodes on-demand and deterministic control of quantum states and photon emission of quantum light sources are required. For the development of ideal quantum nodes cavity quantum electrodynamics (QED) has widely been studied. Optical cavities are used to enhance the light–matter interaction in quantum sources, which enables the dynamic control of photon emission. Photonic crystal (PhC) nanocavities are promising platforms owing to their high $Q$ value and extremely small mode volume, as well as the compatibility with the semiconductor processes. However, the optical properties of nanocavities are usually not optimized for applications during the fabrication, thus a post-tuning method is required.

This thesis presents and discusses a method of optimizing the optical properties of PhC nanocavities for cavity QED applications, from a device engineering viewpoint. Nanofibers are employed not only for efficient coupling of light but also for controlling losses ($Q$s), mode profiles, and resonant wavelengths of nanocavities. The scheme simultaneously enables both the tailoring of optical resonances and the efficient connection between the on-chip nanocavities and the fiber-optic communication technology.

In this chapter, the background of the research is introduced. First, the overview of quantum information technology is reviewed. Then, the general characteristics of the key devices of optical nano- and microcavities are presented. Next, the applications of optical nano- and microcavities are described including cavity QED technology. Then, the challenges of PhC nanocavities for cavity QED applications are described. Finally, the motivation of the study is discussed.

# 1.1 Quantum information technology

## 1.1.1 Overview

A quantum is the smallest scale of physical quantities including a photon, a phonon, and an electron. Particularly, it exhibits completely different nature from those observed in the classical systems, despite the fact that these systems are built up of quanta. Quantum information technology is the discipline enabling the realization of quantum computers and quantum communication, where important quantum phenomena are employed including superposition, entanglement, and Heisenberg uncertainty.

A quantum computer is a machine, which has the potential to solve certain types of problems much faster than conventional classical computers. The basic algorithms for computing were proposed and developed in the 1980s and 1990s [2–5]. They employ quanta as binary digits known as quantum bits or qubits. Examples of qubits are superconducting qubits, spin qubits, and photonic qubits [6–8]. Unlike classical binary digits, which hold one binary value ("0" or "1"), qubits can hold a combination of two binary values ("0" and "1") at the same time, owing to the quantum nature of superposition (Fig. 1.1). The number of states in the superposition increases exponentially in accordance with the increase of the number of qubits, coherently interacting with each other. This nature enables the simulation of the enormous number of options in a short time. It should be noted that quantum computers do not work as the classical computers, in the sense that they have areas of specialty, which depends on their architectures. There are two types of quantum computers: gate-type and ising-type. Gate-type quantum computers are good in solving problems with a large number of options, such as prime factor decomposition and molecular simulation. Recently, IBM Corporation calculated the ground-state energy of $BeH_2$ using a gate-type quantum computer using six qubits [9]. Ising-type quantum computers are used for solving optimization problems. The pioneering quantum computer venture company, D-Wave Systems Incorporated adapted this type for its machines to solve optimization problems using a quantum annealing algorithm [10, 11].

In this way, the development of quantum computers provides powerful methods to explore complex problems. On the other hand, it exhibits a security threat to conventional cryptographic communication technology, which based on the difficulty of solving prime decomposition problems consisting enormous prime numbers. However, another quantum phenomenon, the Heisenberg uncertainty provides an alternative technology for secure communication, known as quantum communication [12]. Superpositioned and entangled quanta can be used as keys and shared between the sender and the receiver in the communication. The keys are used to decrypt encrypted messages. The security of the communication is guaranteed by the fact that the states of the quantum keys cannot be established without measuring them, thus it is possible to detection the presence of eavesdroppers. The photon is considered as an ideal information carrier for communication owing to the long propagation and the coherent length and to the existence of sophisticated fiber-optic infrastructure.

Both quantum computing and communication require the physical implementation of the quantum network (Fig. 1.2). It consists of quantum nodes, which are coupled to each other coherently by quantum channels. The technology allows the increase of the number of qubits for computing and the extension of the communication distance. The fundamental role of the channels is only to deliver the quanta coherently over a long distance. For such a channel,
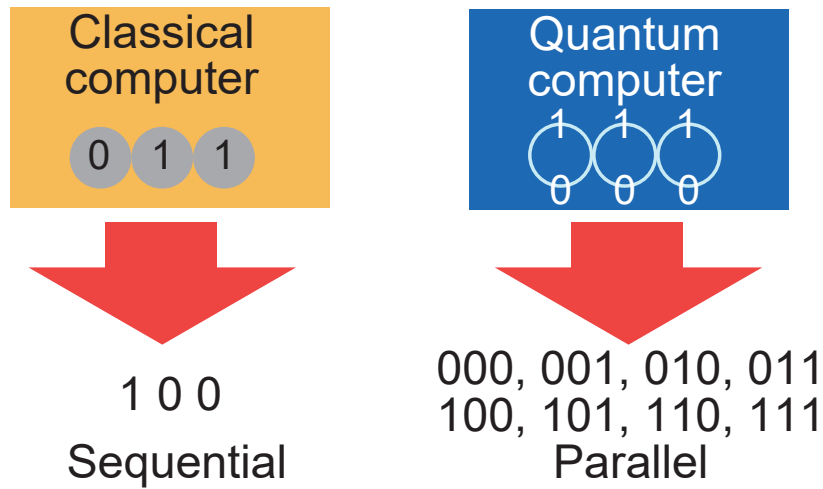
Fig. 1.1. Schematic illustration of the difference between a classical computer and a quantum computer. As classical bits hold either "0" or "1", they present a single solution. On the other hand, qubits hold "0" and "1" at the same time and express many states in parallel.

the optical fiber is considered as the most promising candidate. On the other hand, for the quantum nodes multiple functions are required, such as generation of single and entangled photons, quantum states transfer (teleportation), and storage (delay) of quantum states [13–15]. In addition, to use the fiber-optic network as channels, efficient coupling to the optical fibers is required. In this regard, photonic quantum nodes are favorable, as no conversion technology is required, whereas transducers are required to bridge the other types of quantum nodes and the conventional optical communication technology [16, 17].
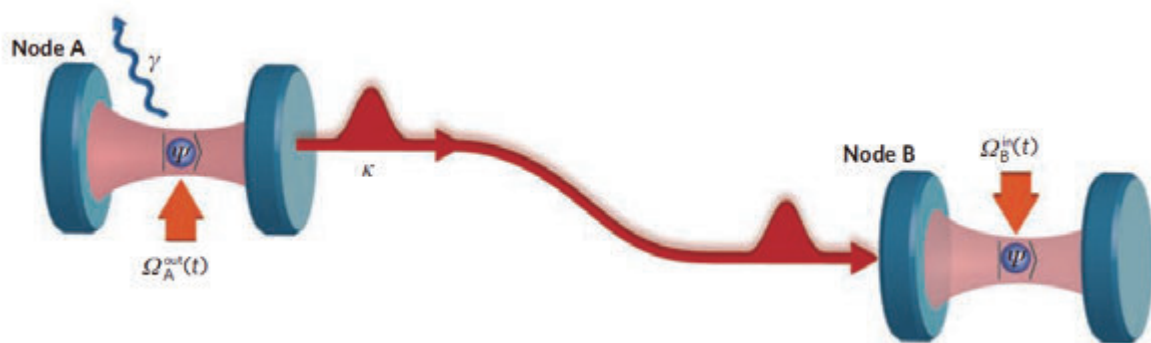


Fig. 1.2. Schematic illustration of an example of a quantum network. Quantum state transfer and entanglement distribution from node A to node B are drawn in the setting of cavity QED. At node A, a pulse of the control field $\Omega_A^{out}(t)$ causes the transformation of atomic state $\Psi$ into the state of a flying photon. At node B, the pulse $\Omega_B^{in}(t)$ is applied to map the state of the flying photon into an atom in the cavity, thereby realizing the transfer of the state $\Phi$ from node A to node B. $\kappa$ and $\gamma$ are the decay rate of the cavity modes and the atomic decay rate to modes other than the cavity mode, respectively. [Reprinted with permission from H. J. Kimble, Nature **453**, 1023-30 (2008)]

### 1.1.2 Single photon sources

Single photon sources are critical and fundamental for quantum information technologies because single photons are promising carriers of information. The simplest way to generate single photons is attenuating laser light. This method reduces the average number of photons in each optical pulse to less than 1. Such pulses are called weak coherent pulses and exhibit the quantum nature. However, the population of the number of photons obeys the Poisson distribution; therefore, there are pulses with more than one photon or zero photons. The presence of an excessive number of photons increases the risk of the wiretap of the information and the empty pulses degrade the information volume and the transmission distance of the communication system.

As an alternative, atoms or atom-like emitters are employed. An atom holds a clean quantum system with discrete electronic levels in which only a single electron can occupy a certain quantum state (e.g., electronic shells, orbits, and spins) owing to the Pauli exclusion principle for fermions. Thus, a single photon will be emitted when an electron is excited selectively and undergoes the transition between two levels in such a system. The discrete systems are observed in artificial atoms of quantum dots and color centers in materials as well as atoms and ions. Although deterministic and on-demand emissions of indistinguishable photons at an arbitrary rate are required for the ideal sources, these are difficult to implement in free space since the emission process is nondeterministic and irreversible. To address this issue, control of the emission is explored by employing optical cavities, whose details are described in Chapter 1.3.1.

## 1.2 Optical nano- and microcavities

### 1.2.1 Overview

The development of semiconductor processes enabled the fabrication of wavelength-size cages of light on a chip. These optical components are known as optical nano- and microcavities. Various kinds of optical nano- and microcavities have been developed and used for various applications in nonlinear optics and quantum optics. The performance of optical cavities are mainly characterized by two parameters: quality factor ($Q$) and mode volume ($V$). The quality factor determines the capability of light confinement of optical cavities, by multiplying the photon lifetime in the cavities by their optical period as:

$$Q = \omega\tau, \tag{1.1}$$

where $\tau$ is the photon lifetime, which indicates the time until the intensity of light in the cavity, $I$ decays to $1/e$ of the initial value of $I_0$, as given by the following equation (see Fig. 1.3(a)).

$$I = I_0\exp(\frac{t}{\tau}). \tag{1.2}$$

As time is associated with the spectrum by the Fourier transform, the quality factor can also be determined by the spectral width of the resonant peak of a cavity as (see Fig. 1.3(b)):

$$Q = \frac{f}{\Delta f}, \tag{1.3}$$

$$Q = \frac{\lambda}{\Delta\lambda},$$

(1.4)

where $f$ and $\lambda$ are the resonant frequency and the resonant wavelength of the peak, respectively, and $\Delta f$ and $\Delta\lambda$ are the corresponding full width at half maximum (FWHM) values.
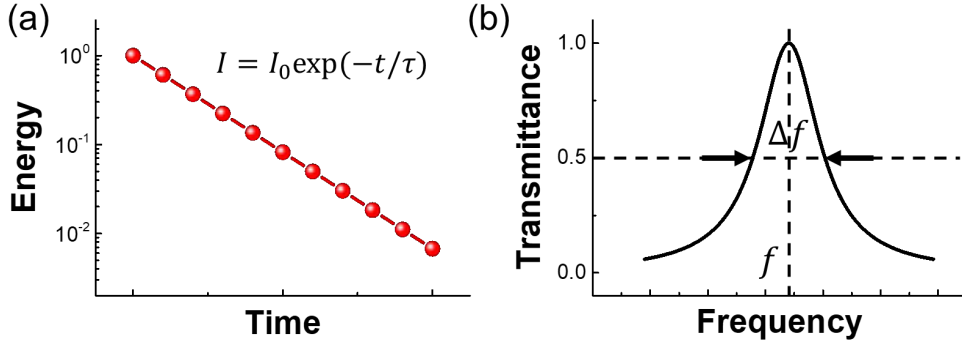


Fig. 1.3. Decay of the energy in an optical cavity (a) and definition of the FWHM of the resonant peak (b).

On the other hand, the mode volume indicates the size of the space where light is localized. It is defined by the following equation:

$$V = \frac{\iiint \epsilon |E(x, y, z)|^2 dxdydz}{\max[\epsilon|E(x, y, z)|^2]},$$

(1.5)

where $E(x, y, z)$ is the amplitude of the electric field in the cavity and $\epsilon$ is the dielectric constant of the medium. Generally speaking, a higher $Q$ and a smaller $V$ are favorable for nonlinear applications, where strong light–matter interaction is required, thus cavities with high $Q/V$ values have widely been studied.

Figure 1.4 shows the map of the quality factor and the mode volume of various optical nano- and microcavities. These can be roughly categorized into three groups, PhC nanocavities, whispering gallery mode (WGM) cavities, and semiconductor ring resonators, depending on their features and fabrication methods.

PhC nanocavities exhibit an extremely small mode volume, based on photonic bandgap (PBG) confinement. The $Q$ factors have been improving according to the development of fabrication techniques and their highest value is in the order of $10^7$ [18].

WGM microcavities can access the regime of ultra-high $Q$ factors of over $10^8$, and they confine light by total reflection. Specifically, ultra-high $Q$ factors of over $10^8$ had already achieved in the 1990s [19]. Although their mode volume is relatively large compared to other nano- and microcavities, they have several advantages in nonlinear applications, as higher-order nonlinearities are proportional to the power of $Q$.

The semiconductor ring resonators are circular optical waveguides fabricated on chips. Their $Q$s have also been improved owing to the progress of semiconductor fabrication technology. These devices are compatible with the complementary metal oxide semiconductor (CMOS) process, although usually electron beam (EB) lithography is used to control the gap

distance between the resonator and the optical waveguide. Light confinement becomes similar to that in WGM, if their diameter is small.

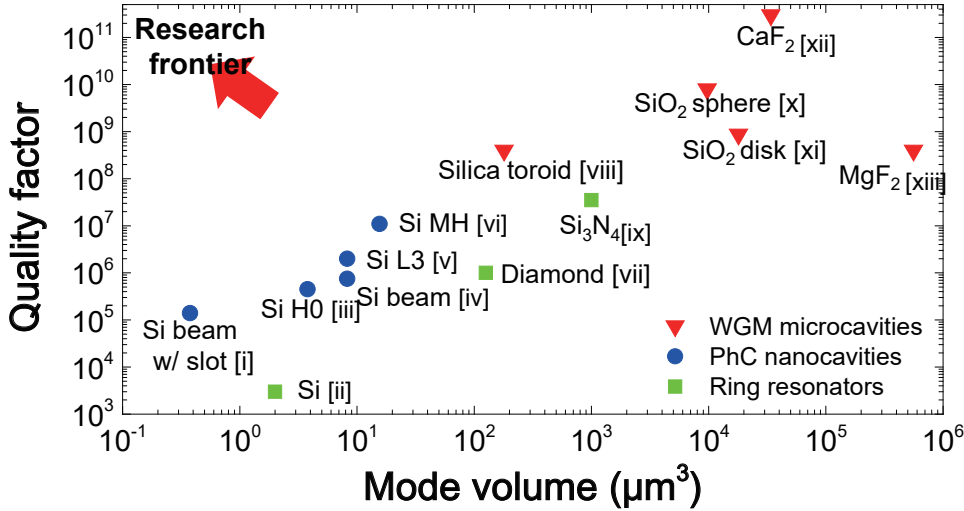The details of each type of cavity are described in the following sections.



Fig. 1.4. Mapping of quality factor and mode volume of nano- and microcavities. The values are obtained from the following references: [i] Ref. [20]; [ii] Ref. [21]; [iii] Ref. [22]; [iv] Ref. [23]; [v] Ref. [24]; [vi] Ref. [18]; [vii] Ref. [25]; [viii] Ref. [26]; [ix] Ref. [27]; [x] Ref. [19]; [xi] Ref. [28]; [xii] Ref. [29]; [xiii] Ref. [30].

### 1.2.2   Photonic crystal nanocavities

Pioneering works for the calculation of the photonic band structures of a three-dimensional (3D) PhC were demonstrated by K. Ohtaka *et al.* after 1979 [31,32]. These studies presented several important features of the PhC, such as the increase of the density of states [32]; however, PBG, where the density of state vanishes [33], was not investigated. The concept of PBG gained much attention following the two independent studies presented by E. Yablonovitch and S. John in 1987 [34,35]. The idea of PBG is analogical to that of the electronic band gap, and it prohibits the existence of light with certain wavelength in the structure. It enables the achievement of the ultimate confinement of light; If a defect is introduced in a PhC with PBG, light can exist in the defect, but cannot move out of it, thus it is confined in the defect. It is worth noting that the volume of the defect can be reduced to approximately the same as or less than the cubic wavelength in the material.

Studies of artificial PhC begun with the development of (3D) structures, which formed the PBG in all directions and polarizations [36], however, their fabrication was difficult. There have been many attempts to fabricate a 3D PhC structure for the near infrared (IR) range [37] by self-assembly methods [38,39], a combination of photoelectrochemical etching and focused-ion-beam drilling [40], one-step two-directional deep etching [41,42], direct laser writing [43], layer-by-layer methods including wafer fusion [44,45], micro manipulation [46,47], and hybrid approaches [48,49]. The highest $Q$ value for 3D PhC nanocavities was achieved using micro manipulation techniques [47]. 3D PhC nanocavities are mainly used for controlling light

emission from quantum light sources, which has been the main motivation for the studies of the devices since their first proposal [34, 36]. There are also different unique directions of research, such as fabricating waveguides in the 3D structure [50] and implementing chirality by controlling the periodicity of the lattices [51].
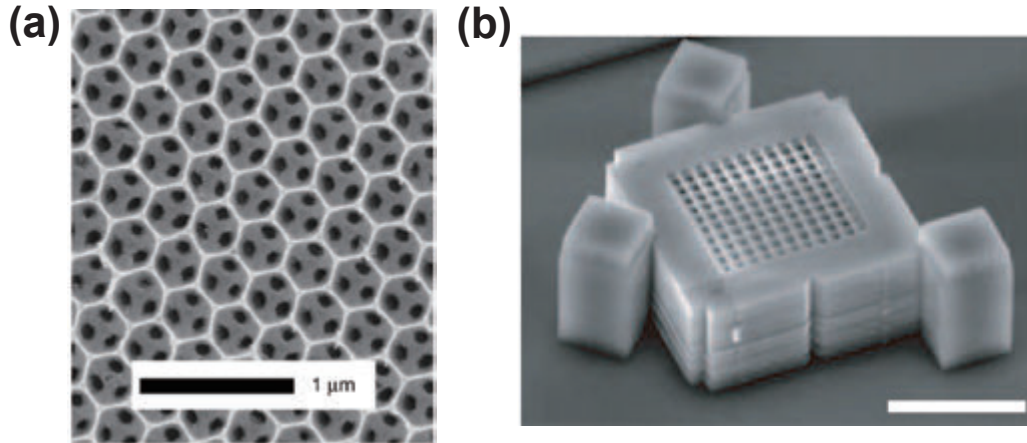


Fig. 1.5. Scanning electron microscope (SEM) image of a titania inverse opal 3D PhC (a) and (b). [Reprinted with permission from P. Lodahl, *et al.*, Nature **430**, 654-657 (2004)]. (b) SEM image of a 3D PhC nanocavity fabricated with micromanipulation technique [Reprinted with permission from K. Aoki, *et al.*, Nature Photonics **2**, 688-92 (2008)].

The facilitation of the fabrication led to the development of two-dimensional (2D) PhC nanocavities, where periodic structures were formed in two dimensions in a thin slab. The pioneering works by Caltech and KAIST research groups focused on cavities for low threshold lasers [52–55]. The first breakthrough in achieving a high $Q$ in 2D PhC nanocavities was the introduction of the concept of the light cone, which describes out-of-plane radiation loss components of cavity modes in the reciprocal space [56]; this demonstrated a clear strategy for improving $Q$ (i.e., reducing the components within light cone). Then, the shift L3 cavity was developed [57], which was formed by introducing three air holes in the PhC and shifting two holes at each side of the defect slightly to achieve a Gaussian mode profile of cavity. This small modification reduced the out-of-plane radiation loss significantly (such a hole shift design was also explored in [58]). By further optimizing the amount of the shift of the air holes, a $Q$ higher than $10^5$ was achieved [59]. The next breakthrough for high $Q$ PhC nanocavities was the design of mode-gap cavities, which are formed by modulating the guided mode of the line-defect PhC waveguide (hence, the expression "mode-gap"). This type of cavity exhibits high $Q$ as it is based on the guided mode, which originally contains small radiation loss components. There are mainly two modulation methods: lattice constant modulation (i.e., hetero type cavities) [60] and width modulation [61]. A $Q$ higher than $10^6$ was obtained in the spectral domain with double hetero cavity [62] and in time-domain with width modulated cavity [63]. Furthermore, the use of a multi-hetero design tripled the value of the highest $Q$ [64, 65]. It should be noted that the introduction of mode-gap cavities also enabled the achievement of ultra-high $Q$ higher than $10^6$, even with cladded structures [66–68], which is important in ensuring the mechanical stability of the PhC structures. Recently, chemical reduction of material absorption was studied

for the improvement of $Q$ and a $Q$ value of $9 \times 10^6$ was reported in 2014 [69]. This approach further improved $Q$ and the highest $Q$ value currently exceeds $1.0 \times 10^7$ [18]. Although the theoretical limit of $Q$ is higher than $10^9$ [70], the highest obtained value is approaching the material $Q$ of silicon. Thus, the study of other proper materials may be necessary to achieve an ultimately high $Q$ for PhC nanocavities.

Although the recent highest values were achieved with mode-gap type cavities, the highest $Q$ values for bandgap type cavities (i.e., point defect cavities, such as H0, H1, L3) are also have to be considered, as they usually possess a smaller mode volume than that of mode-gap cavities. An L3 cavity with a $Q$ of over 1 million [24] and an H1 cavity with a $Q$ of over 100 thousand [22] was presented by a systematic design optimization.

Owing to the availability of silicon photonics foundry services for research use, PhC nanocavities can be fabricated with a CMOS-compatible process. A high $Q$ exceeding $10^5$ was achieved for the structure with silica clad using 248 nm KrF lithography [71] and a value of $10^6$ was demonstrated for the structure with air clad using 143 nm ArF immersion photography [72]. This trend is important for the mass production of the PhC devices, as the conventional EB lithography method takes significant time for the fabrication.
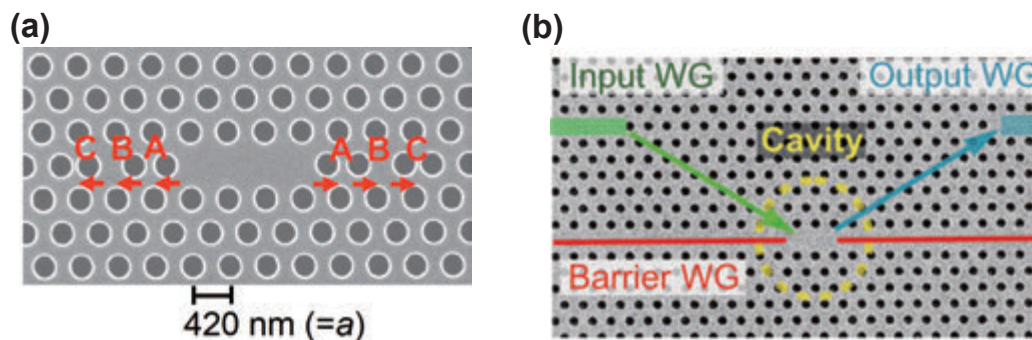


Fig. 1.6. (a) SEM image of an L3 PhC nanocavity. [Reprinted with permission from Y. Akahane, *et al*., Optics Express **13**, 1202-14 (2005)] (b) SEM image of a width-modulated PhC nanocavity. [Reprinted with permission from E. Kuramochi, *et al*., Applied Physics Letters **88**, 041112 (2006)].

One-dimensional (1D) PhC nanocavities are generally referred to as nanobeam cavities (Note that dielectric multi-layers are not reviewed here, although they are also 1D PhC). They are formed in a rectangular waveguide by forming a 1D Bragg mirror. Although the pioneering proposal and demonstration of this cavity were in 1995–1997 [73–75] (see Fig. 1.7(a)), it took significant time before the expansion of the application of these devices started in end of the 2000s. Before the mid-2000s, some theoretical studies investigated their high $Q$ cavity design by using a tapering hole strategy [76, 77]. This led to a series of experimental demonstrations of nanobeam cavities on silicon on insulator (SOI) substrates with high $Q$ values of up to $1.5 \times 10^5$, in the late 2000s [78–80] (see Fig. 1.7(b)). For nanobeam cavity, the current highest $Q$s were demonstrated shortly after these studies, by the Harvard research group in air-bridge configuration [23] and by the NTT research group in SOI configuration [81].

One of the most important advantages of the nanobeam type cavities is the number of available materials for the core layer. A high $Q$ factor is achievable even with low-index materials with a reasonably small mode volume, because a sufficiently wide PBG can be
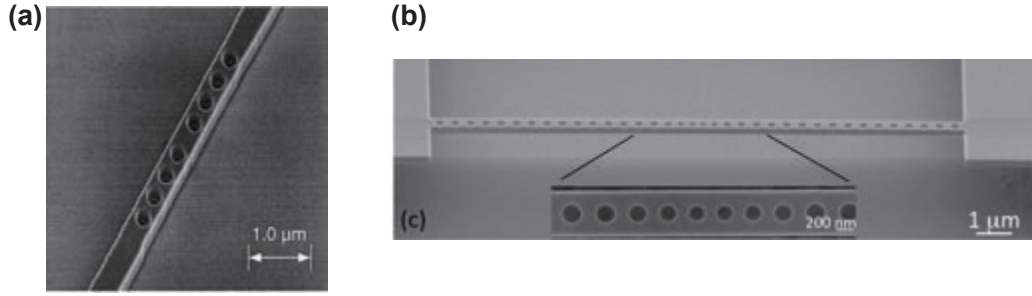
Fig. 1.7. (a) SEM image of a nanobeam cavity. [Reprinted with permission from J. S. Foresi, *et al.*, Nature **390**, 143-5 (1997)]. (b) SEM image of a nanobeam cavity with a tapered hole design. [Reprinted with permission from P. Deotare, *et al.*, Applied Physics Letters **94**, 12-5 (2009)].

formed in one dimension. Since a design proposal of a high $Q$ nanobeam cavity made of the relatively low-index material silicon nitride [82], there have been many demonstrations of nanobeam cavities made of various materials, such as silica [83, 84], polymer [85], silicon nitride [86, 87], and diamond [25]. In addition, the introduction of a deterministic strategy for high $Q$ designs is also an important factor in the widespread use of nanobeam cavities [88, 89]. The $Q/V$ values for nanobeam cavities made of different materials are summarized in Fig. 1.8.
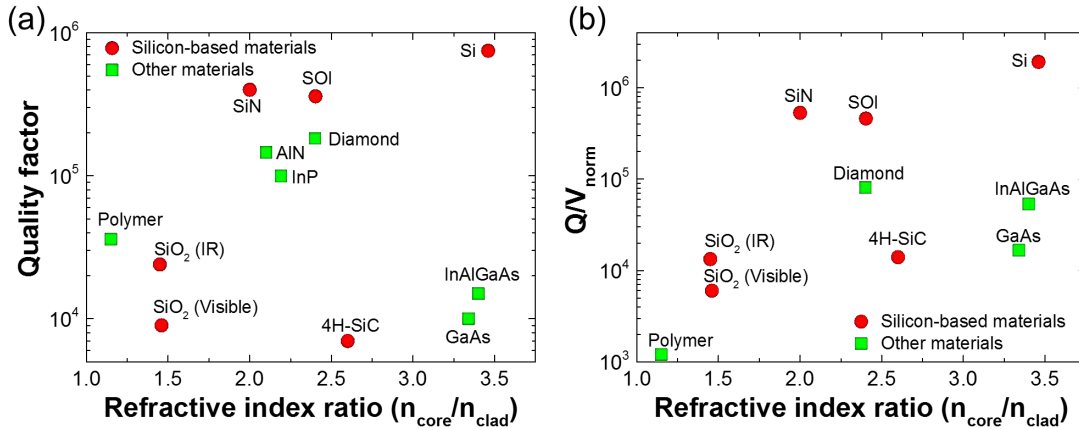


Fig. 1.8. (a) Refractive index ratio versus $Q$ factor. (b) Refractive index ratio versus $Q/V$ value (The plots with unknown normalized mode volumes are removed from (a)). References for the plots not included in the article are [90–94]

Recently, nanobeam cavities were also been fabricated using photolithographic processes [95]. In addition, it should be noted that the same design strategy were used for fabricating cavities in nanofibers, whereas mode volumes are not always small depending on the application [96–98].

The timeline of the improvement of the $Q$ factor of PhC nanocavities is shown in Fig. 1.9.
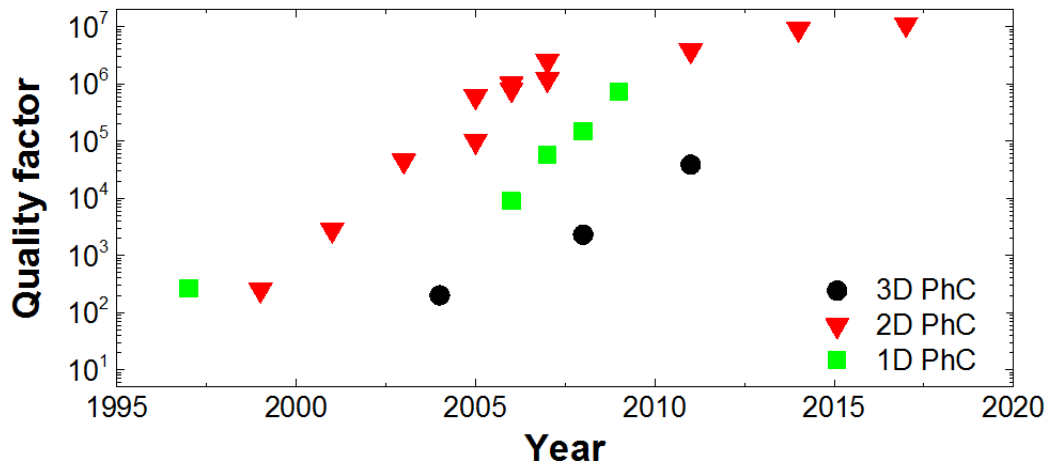
Fig. 1.9. Timeline of the improvement of the $Q$ factor of PhC nanocavities. The references are cited in the article.

## 1.2.3 Whispering gallery mode cavities

The notation "whispering gallery" is originated from places where whispered sound travels around by circularly reflecting from the walls and arrives back behind the whispering person, such as in St Paul's Cathedral in London [99, 100] (see Fig. 1.10(a)). Light is confined in WGM cavities owing to the total reflection, hence, a high $Q$ can be achieved if their surfaces are smooth. So far, cavities with ultra-high $Q$ exceeding $10^8$ have been demonstrated by accurate polishing methods [29, 30], surface melting processes [19, 26], and wet etching [28]. Although the surface roughness requirement for high $Q$ become crucial as the radius of a cavity become small, an ultra-high $Q$ of $10^8$ and a small mode volume of 200 $\mu m^3$ can be both achieved by a silica toroid microcavity, owing to its extremely smooth surface fabricated by a $CO_2$ laser reflow process [26] (see Fig. 1.10(b)). As a high $Q$ factor, compared to other nano- and microcavities was achieved earlier, the devices were used for the pioneering studies of nonlinear optics including optical Kerr frequency comb generation [101] and dynamic cooling and amplification of the mechanical oscillation in cavity opto-mechanical systems [102–104].

## 1.2.4 Semiconductor ring resonators

Ring resonators are fabricated on a chip using semiconductor processes. The light in the device is usually supported by index guiding of the waveguide, although it becomes more WGM-depending on the radius of the resonator. They can be integrated on chips with electrodes [21] (see Fig. 1.11(a)), similarly to PhC nanocavities. In addition, the trend of improvement of the $Q$ factor is also similar to that of PhC nanocavities (a $Q$ of $10^7$ was achieved for the devices very recently [27, 105, 106]), which is possibly because of the improvements are due to the progress of semiconductor fabrication techniques. The fundamental difference between PhC nanocavities and ring resonators is the amount of resonant modes and their dispersion. As ring resonators have multiple longitudinal modes over a wide wavelength range and with group velocity dispersion engineering a constant free spectral range (FSR) of the modes can be
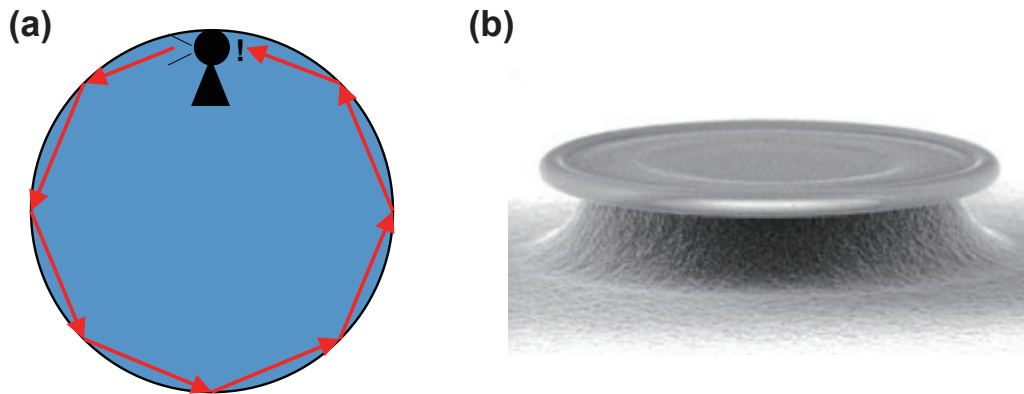
**(a)**

**(b)**



Fig. 1.10. (a) Schematic of a whispering gallery. The sound projected from a person (illustrated by a black circle and a black triangle) propagates along the inner circumference of the whispering gallery and comes back from behind him/her. (b) SEM image of a silica toroid microcavity.

achieved even with nonlinear processes in cavities, they are considered as promising platforms for optical Kerr comb generation. Recently, a wavelength division multiplexing (WDM) communication was demonstrated with Kerr comb, generated from this device [107, 108] (see Fig. 1.11(b)).

### 1.2.5 Methods for optical coupling

Achieving high coupling efficiency (CE) with an optical fiber is important for practical applications of optical nano- and microcavities. In this section, the methods used for coupling light between PhC nanocavities and optical fibers are reviewed.

There are several types of direct and indirect coupling methods as shown in Fig. 1.12.

Direct coupling methods couple light directly into PhC nanocavities. Its simplest form is free space coupling. It is a method to inject/correct light into/from a cavity using an objective lens. The CE is usually low for this method (a few percent) due to the poor overlap of optical modes between focused light and far-field pattern of cavities. On the other hand, there are several studies to improve the collection efficiency of this method by controlling the far-field patterns of the PhC nanocavities [109–111]. A high collection efficiency of 60% was achieved for an H1 type PhC nanocavity [111] (see Fig. 1.12(a)).

The other example of direct coupling methods is using a tapered nanofiber. A tapered nanofiber is an optical fiber thinned so that light leak evanescently around the fiber, and used as an efficient interface to couple light into cavity devices and optical waveguides [112–116] (see Fig. 1.12(b)). A high CE of almost 100% has been achieved for coupling with a WGM microcavity [113], and 94% for coupling with a PhC waveguide [114]. It is worth noting that the high CE was demonstrated even between the optical devices with large difference in material index, although a careful attention needs to be paid for satisfying a phase matching condition [117]. Tuning of the CE is also easy by changing the gap distance between the devices. On the other hand, the system is not stable compared to other methods described in this chapter.

Indirect coupling methods couple light into a rectangular waveguide, and then the coupled
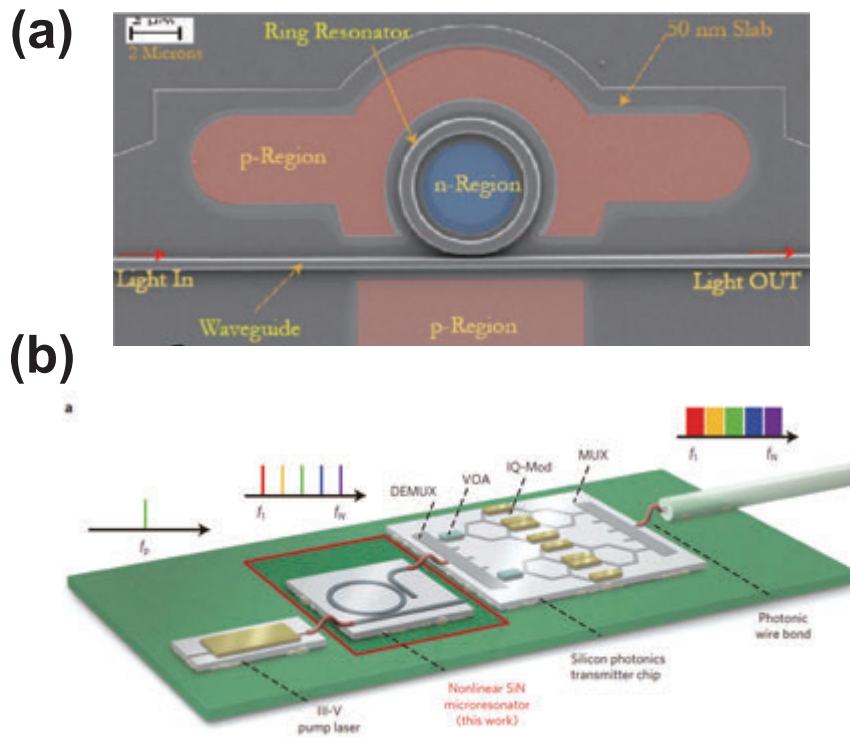
**(a)**

**(b)**



Fig. 1.11. (a) SEM image of an EO modulator based on a silicon ring. [Reprinted with permission from S. Manipatruni, *et al*., Optics Express **18**, 18235-42 (2010)]. (b) Schematic of optical WDM system based on ring resonator. DEMUX: de-multiplexer. VOA: variable optical attenuator. IQ-Mod: IQ-modulator. MUX: multiplexer. [Reprinted with permission from J. Pfeifle, *et al*., Nature Photonics **8**, 375-80 (2014)].

light transmits to a PhC waveguide and a nanocavity. A grating coupler (GC) is an example. It is an integrated device consisting of periodically placed dielectric materials. The light injected to the device couples to a connecting waveguide due to the diffraction caused by the periodic patterns. As the devices are based on periodic gratings, the wide bandwidth and the small polarization dependency are challenging to be implemented. A high CE of about 87% and a 3-dB bandwidth of 70 nm can be achieved with a grating coupler with a metal mirror underneath the device [118] (see Fig. 1.12(c)).

A spot size converter (SSC) is an interface to couple light from free space into an optical waveguide. The device is based on a inverse tapered waveguide covered with silica, and trenches are usually formed at the both side of the device. It is designed such that the guided mode of a waveguide adiabatically transits and matches the mode profile of the focused free space light. Efficient coupling with a CE of 89% has been demonstrated; however, a complex fabrication is required [119] (see Fig. 1.12(d)).

It should be noted that indirect coupling methods of GC and SSC suffer from additional insertion losses between a PhC waveguide and a rectangular waveguide, and a PhC waveguide and a PhC nanocavity. Therefore, the reduction of the insertion losses is required to maximize CE in a whole system. The insertion loss between a PhC waveguide and a rectangular waveguide will be more than 5 dB typically without the optimization of the interface between two

waveguides. It will be reduced to be around 0.5 dB with a careful design [120]). To reduce the insertion loss between a PhC waveguide and a PhC nanocavity, the control of a ratio between an intrinsic $Q$ and a coupling $Q$ is required as described in Chapter 2.2.3.

Considering the issues presented above, it is obvious that the nanofiber method is the most efficient for coupling the light with PhC nanocavities.
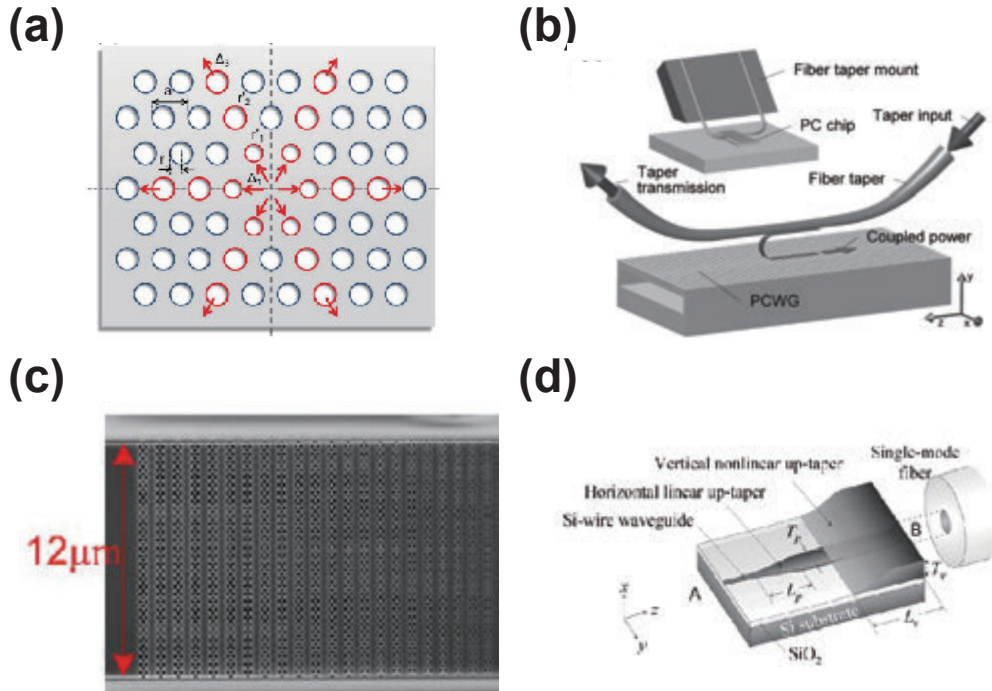


Fig. 1.12. Coupling methods and optical couplers. Schematic of (a) a H1 cavity for efficient free space coupling [111] and (b) evanescent coupling with a nanofiber [114], (c) a grating coupler [118], and (d) a spot size converter [119]. [Reprinted with permission from H. Takagi, *et al.*, Optics Express **20**, 28292-300 (2012), P. E. Barclay, *et al.*, Optics Letters **29**, 697-9 (2004), K. Shiraishi, *et al.*, Applled Physics Letters **91**, 141120 (2007), and Y. Ding, *et al.*, Optics Letters **39**, 5348-50 (2014).]

# 1.3 Applications of optical nano- and microcavities

## 1.3.1 Cavity quantum electrodynamics

Cavity QED is a study of the interaction between atoms or atom-like emitters and photons confined in optical cavities [121], which are the main target application in this study. The energy level of the emitters is usually described by the Jaynes–Cummings model in which a genuine two level system in an optical cavity is assumed (Fig. 1.13(a)). The state of the system

is evaluated by the coupling rate between a cavity and an emitter $g$, and is given by

$$g = \boldsymbol{d} \cdot \boldsymbol{E}(\boldsymbol{r})/\hbar = \sqrt{\frac{\mu^2 \omega}{2\hbar\epsilon_0\epsilon_r V}} \Phi(\boldsymbol{r}), \tag{1.6}$$

where $\boldsymbol{d}$, $\boldsymbol{E}$, $\mu$, $\omega$, $\hbar$, $\epsilon 0$, $\epsilon_r$, $V$, and $\Phi$ are the induced transition dipole of the emitter, electric field per photon, transition dipole moment of the emitter, resonant angular frequency of the cavity, reduced Planck constant, vacuum permittivity, relative permittivity, mode volume of the cavity, and mode function of the cavity, respectively.

When $g$ is larger than the cavity decay rate $\kappa$ and the decay rate of the emitter $\gamma$, the system is in the strong coupling regime. Then, the emission and the absorption of a photon takes place within any dissipative processes in the system coherently, which leads to the vacuum Rabi splitting of the system. This is an ideal state for the applications of the quantum information technology for two main reasons. First, the deterministic control of the emission of photons is possible through nonlinear processes such as the stimulated Raman transition by applying the external control field before the decay of the excited state of an emitter [122–124]. Generation of single-photon pulses with a probability exceeding 99% is predicted theoretically. Second, the emission process is reversible [125]. A photon emitted from a system can be efficiently absorbed by the identical system coherently because of the strong coupling between the optical field and the emitter. This can be applied for the another system with identical configuration when a time-reversed field of the emission is applied to the system. Thus, the coherent transfer of quantum states is possible between quantum nodes, which is important feature to realize the quantum information technology. Therefore, one of the main focus of the cavity QED is the control of quantum states of photons and emitters in the strong coupling regime.

On the other hand, the system is in the weak coupling regime when $g$ is smaller than $\kappa$ and $\gamma$. Then, the emission process is no longer a reversible process. However, the enhancement of spontaneous emission will happen owing to the higher density of state in the cavity compared to that in the vacuum. The enhancement factor is known as the Purcell factor and usually expressed as [126–128],

$$F_p = \xi^2 \frac{3Q_{\text{cav}}(\lambda/n)^3}{4\pi^2 V}, \tag{1.7}$$

where $\xi^2$, $Q_{\text{cav}}$, and $\lambda/n$ are the polarization factor, which is equal to 1/3 when the dipole is randomly oriented; the quality factor of the cavity; and the wavelength of light in the material, respectively. According to the Eq. (1.7), which is usually employed to express the factor, the spontaneous emission rate is proportional to the density of the state of $Q/V$. However, Eq. (1.7) assumes the condition in which the linewidth of the emitter is much narrower than that of the cavity. A more general form of the Purcell factor is as follows:

$$F_p = \xi^2 \frac{3(\lambda/n)^3}{4\pi^2 V} (Q_{\text{cav}}^{-1} + Q_{\text{em}}^{-1})^{-1}, \tag{1.8}$$

where the condition of $\delta\omega << \omega$ is assumed for the half width at half maximum (HWHM) of the linewidth of the emitter and the cavity of $\delta\omega$, and their angular frequency of $\omega$, which is

satisfied for most applications in the optical domain (details of the derivation of the equation are presented in Appendix B). Equation (1.8) means that the Purcell factor is limited by the lower $Q$ of either the emitter or the cavity and no longer depends on the cavity $Q$ when the linewidth of the emitter is much broader than that of the cavity. In addition, a poor spectral overlap between the cavity and the emitter means the poor CE between them (i.e., the emitted light cannot couple to the cavity without the spectral overlap) (Fig. 1.13(b)). Therefore, the critical coupling condition of $Q_{cav} = Q_{em}$ is an optimum condition to maximize the total photon correction rate.

As indicated by Eq. (1.6), the strong confinement of light in a tiny space is required to enhance the interaction between a cavity and an emitter. Therefore, optical nano/microcavities have been attractive platforms for the application owing to their high $Q/V$ value [129, 130]. In particular, PhC nanocavities are advantageous because of their small mode volume and integrated structures (Chapter 1.1.1). In fact, one of the main initial topics of research related to 3D PhCs was the control of spontaneous emission from atoms. Hence, the first pioneering studies on spontaneous emission control with PhCs have been demonstrated using the 3D ones [36, 131, 132]. 2D PhCs have been employed to form cavities containing quantum dots/wells since their integrated structures are suitable for it [133–136]. The strong coupling with a quantum dot in a PhC nanocavity was observed for a L3 cavity in which the quantum dots were located exactly at the loop of the optical mode Fig. 1.13(c) [137]. Note that the quantum dots are usually fabricated with a self-assembly method; however, they are formed in a substrate randomly and the control of their position is a big challenge. 1D nanobeam cavities are also promising platforms for cavity QED applicaitons [138]. In particular, they are employed to achieve coupling with emitters with visible emission wavelengths such as color centers in materials since the use of low-refractive-index materials is required owing to their small material absorption in the visible wavelength range [84, 139].

## 1.3.2 Optical signal processing

The optical signal processing is a method to control optical signals optically. This technology is expected to contribute to the reduction of energy consumption of large-capacity data communication, where the limit of electric signal processing is nearly reached in terms of information capacity and energy efficiency. Optical nano- and microcavities are promising platforms for this application, as strong light–matter interaction is required to control of optical signals. Optical cavities enhance the interaction efficiently and enable the application optical nonlinear effects for processing signals. For example, an optical switch [140] and adiabatic wavelength conversion [141] have been demonstrated by optical Kerr effect, using silica WGM cavities. In a cavity system of coupled WGM cavities, an optically tunable buffer [142] and isolation [143] have been demonstrated. By combining electrical control techniques, fast and energy efficient electric-optic modulation and optical switching can be achieved using silicon ring resonators [21] and PhC nanocavities [144–146], as well as photo-detection [147] (see Fig. 1.14(a)). These methods are also used for the adiabatic resonant wavelength tuning of a PhC nanocavity [148, 149]. As the large-scale integration of optical nano- and microcavities is achievable, a dense WDM has been demonstrated on a chip [150, 151] (see Fig. 1.14(b)). Random access memory [152, 153] and delay line [154] have also been demonstrated with cascaded PhC nanocavities.
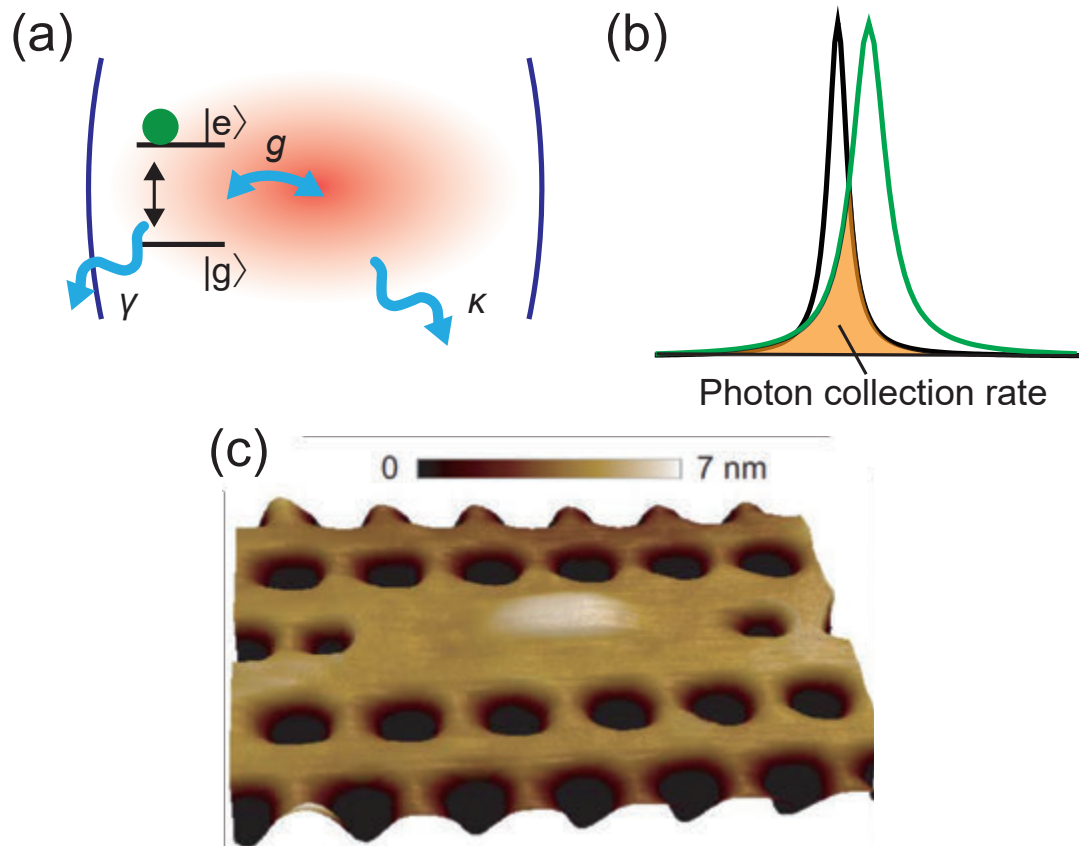
(a)



(b)



Photon collection rate

(c)

0 ◼◼◼◼◻◻◻ 7 nm



Fig. 1.13. (a) Schematic illustration of a Jaynes-Cummings model. An emitter with a two level system consisting of a ground state $|g>$ and an excite state $|e>$ couples with a cavity mode with a coupling rate $g$. $\kappa$ and $\gamma$ are the decay rate of the cavity mode and the emitter decay rate to modes other than the cavity mode, respectively. (b) Schematic illustration of a spectral overlap. (c) L3 PhC nanocavity includes a quantum dot [137]. The quantum dot is embedded at the center of the cavity. [Reprinted with permission from K. Hennessy, *et al.*, Nature **445**, 896-9 (2007)]

## 1.3.3   Cavity opto-mechanics

Cavity opto-mechanics is a discipline of interactions between mechanical and optical modes in an optical cavity system [155, 156]. The main focuses of the research are the opto-mechanical back-action cooling and parametric instability (mechanical amplification) as predicted by V. Bragincky [157]. Ultra-high-$Q$ cavities enabled the dynamic control of their mechanical motion with their strong radiation pressure worked to small structures [102–104]. A schematic of the system is shown in Fig. 1.15(a) and (b) to explain the fundamentals of the dynamic control. A Fabry–Perot (FP) cavity consisting of a fixed mirror and a movable mirror is used (see Fig. 1.15(a)) and the enhanced radiation pressure in the cavity pushes a movable mirror, which causing its oscillation. Then, an input light is modulated by the mechanical motion and sidebands are appearing at both sides of the input wavelength (see Fig. 1.15(b)). The fundamental idea is that the optical energy in the cavity is controlled by changing the detuning of the input wavelength from the resonant wavelength. When the detuning of the
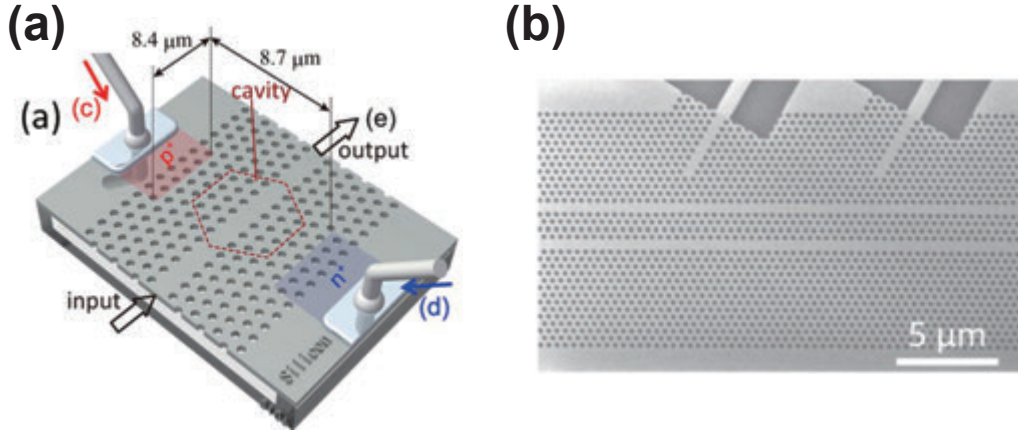
Fig. 1.14. (a) Optical modulator with p–i–n junction. [Reprinted with permission from T. Tanabe, *et al.*, Optics Letters **35**, 3895-7 (2010)] (b) A demultiplexer performed with PhC nanocavities. [Reprinted with permission from Y. Ooka, *et al.*, Optics Express **25**, 1521-8 (2017)].

input light is red-detuned, the optical energy in the cavity increases, thus the energy of the mechanical oscillation decreases owing to the conservation of energy in the system. On the other hand, the blue-detuned light causes a mechanical amplification, because the amount of optical energy decreases and that of the mechanical mode increases. Using this mechanism, several studies have been performed, such as ground state cooling [158, 159], optical induced transparency [160, 161], and sensing [162–164]. In addition, there are several works using enhanced optical forces for deforming structures [165–167]. Such approach can be extended to all kinds of optical mechanical control, like microelectromechanical systems.

## 1.4 Challenges of PhC nanocavities

Although PhC nanocavities are attractive platforms for nonlinear and quantum optics, there are certain challenges to be addressed. In this section, some of the important challenges for cavity QED applications are presented.

### 1.4.1 Small $V$ and tunability of $Q$

As indicated by Eq. (1.8), the Purcell factor increased with small $V$. In addition, the condition of $Q_{cav} = Q_{em}$ has to be satisfied to maximize the Purcell enhancement factor and the CE (not the coupling strength) between the cavity and the emitter simultaneously. As the accurate control of $Q_{cav}$ is difficult with fabrication, and the spectral linewidth depends on the types of emitters and the temperature, the tunablity of $Q_{cav}$ is required to provide the best platform for any cases.
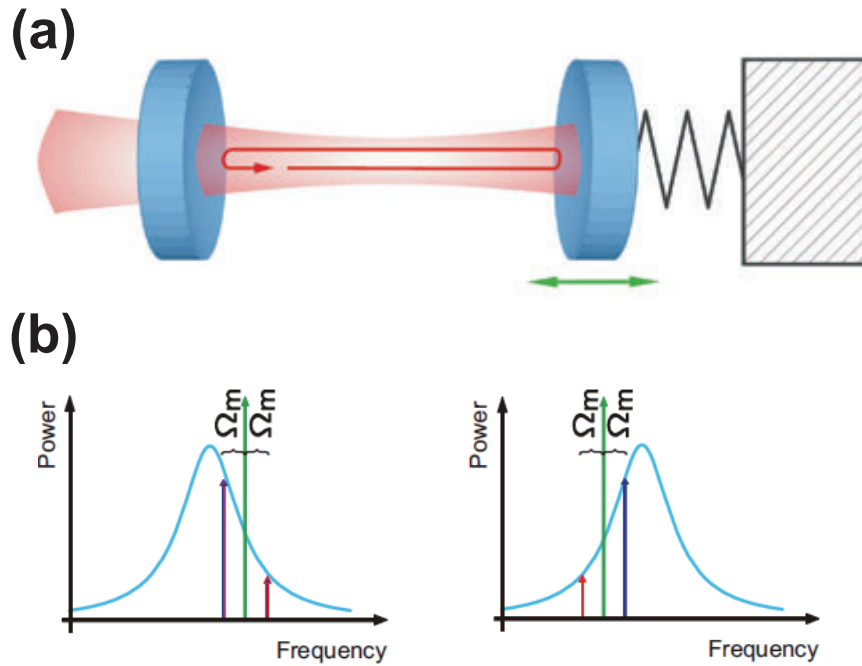
Fig. 1.15. (a) Cavity mechanical system consisting of a Fabry–Perot cavity with a har- monically bound end mirror. [155]. (b) Schematic illustration of the principal of mechanical amplification and cooling in a opto-mechanical system. The right and left figures show cavity resonances in frequency domain with blue and red detuned control light, respectively (illustrated with a green line). Mirror vibration with a mechanical frequency of $\Omega_m$ generates sidebands of the control light with asymmetric amplitudes owing to cavity enhancement of the Doppler scattering process (the sidebands are drawn by blue and red lines). This results in the energy transfer from the mechanical/optical mode to the optical/mechanical mode and causes the mechanical cooling/amplification. [Reprinted with permission from T. J. Kippenberg and K. J. Vahala, Optics Express **15**, 17172-205 (2007)]

### 1.4.2 Control of the resonant wavelength of the cavity

Since PhC nanocavities are sensitive to disorders, the accurate control of the resonant wavelength of the cavity is difficult with fabrication. However, increasing the spectral overlap between a cavity and an emitter is required for the cavity QED applications. Thus, post-tuning the resonant wavelength is performed for the efficient coupling with emitters (The focus in this study is tuning cavity resonances, although controlling emitter's spectrum is also powerful solution for this problem [168]). This tuning can be performed by controlling temperature [151]; however, the process has low energy efficiency and it also affects the emitter spectrum. The control by gas condensation can also be used for this purpose [169]; however, it affects all nanocavities simultaneously and it is not suitable for large-scale systems where wavelength control of individual cavities is needed. Fine and flexible tuning methods are required.

### 1.4.3 Large overlap between a cavity mode and an emitter

The coupling strength between a cavity and an emitter depends on the mode overlap between them. However, the fine control of the position of quantum emitters (quantum dots) is usually

difficult. A control method of the position of the cavity is required.

### 1.4.4 Polarization diversity

Although PBG works for light with any polarizations with the 3D PhC structure, its fabrication is difficult. Thus, 2D and 1D PhC structures are usually used for applications; however, they have strong polarization dependence compared to other integrated optical components. This is because the periodic structures are only formed in-plane and their effect is weak for the light with out-of-plane polarization. On the other hand, polarizations are important degrees-of-freedom of light and used for information processing in communication technologies (e.g., polarization multiplexing [170] and polarization entanglement [171]). In particular, they are indispensable for quantum communication due to the fact that various states (e.g., linear polarization for + and x-directions and circular polarizations) can be expressed even with one single photon. There are also studies for the effective uses of polarization-dependent electronic levels in materials (e.g., spins, valleys). To bridge the gap between communication technologies and PhC nanocavities, the achievement of a polarization independent resonance or a polarization diversity in PhC nanocavities fabricated in-plane is required.

## 1.5 Motivation

As described above, optical nano- and microcavities are attractive platforms in the fields of nonlinear and quantum optics and photonics. In particular, PhC nanocavities are promising due to their high $Q/V$ values and integrated structures as well. However, there are certain challenges to be addressed to provide ideal properties to cavity QED applications as listed below.

- Efficient coupling with an optical fiber

- Small $V$ and tunable $Q$

- Position selectivity (controllability of mode profile)

- Control of resonant wavelength

- Polarization diversity

The motivation of this study is to overcome these challenges. A post-tuning method of optical properties is the main focus of the study whereas proper cavity designs are also investigated. The tuning method is the use of the nanofiber for the index modulation of the cavity mode. It controls the position of a cavity and its resonant wavelength by changing the impact of the index modulation. In addition, the nanofiber helps realize efficient optical coupling, where the total loss in a cavity (loaded $Q$) can be also tuned.

To investigate the effectiveness of the method and ensure proper cavity design, two types of PhC nanocavities are studied. The first type of cavity is a fiber-coupled PhC cavity (FCPC), which is formed by the index modulation caused by a nanofiber and has both high $Q$ and high CE. In addition, it exhibits a resonant wavelength and position controllability. The characterization

of the cavity is discussed in Chapter 3 and its advanced use for the formation of a coupled cavity system is described in Chapter 4. The other cavity is a silica nanobeam cavity, chosen to satisfy the requirement of achieving polarization diversity, as two orthogonal modes are easily obtained at the same wavelength range. The high $Q$ of the two orthogonal modes and the control of coupling with them are demonstrated in Chapter 5. The discussion of the cavity with spectrally overlapped orthogonal modes is presented in Chapter 6. Finally, Chapter 7 gives a summary of each chapter and concludes the thesis.

# Chapter 2

# Theory and method

As described in the Chapter 1.2.2, PhC nanocavities are formed by introducing defects in PBG structures. The understanding of the basis of PBG and numerical methods are required to design a cavity with desired properties. In addition, one needs to be familiar with numerical and experimental techniques of efficient coupling interfaces of nanofibers for the experiment in this study. In this chapter, the basis of PhC and important numerical and experimental methods used in this research are presented. This chapter will help readers to understand the study in detail.

## 2.1 Theory of photonic crystal

### 2.1.1 Photonic bandgap

PBG is a fundamental concept of photonic crystal research. The formation of PBG will be discussed analytically [172].

First of all, Maxwell equations will be introduced which describe the propagation of electromagnetic waves in dielectric materials is as followed,

$$\nabla \cdot \boldsymbol{D} = \rho, \tag{2.1}$$

$$\nabla \cdot \boldsymbol{B} = 0, \tag{2.2}$$

$$\nabla \times \boldsymbol{E} = -\frac{\partial \boldsymbol{B}}{\partial t}, \tag{2.3}$$

$$\nabla \times \boldsymbol{H} = \mathbf{J} + \frac{\partial \boldsymbol{D}}{\partial t}, \tag{2.4}$$

where $\boldsymbol{D}$, $\boldsymbol{B}$, $\boldsymbol{E}$, $\boldsymbol{H}$, $\boldsymbol{J}$, $\rho$, and $t$ are electric flux density, magnetic flux density, electric field, magnetic field, current density, electric charge, and time, respectively. Each equation expresses Gauss's law, Gauss's law for magnetism, the Faraday's law of induction and the Ampere's circuital law. Relations between $\boldsymbol{D}$ and $\boldsymbol{E}$, and $\boldsymbol{B}$ and $\boldsymbol{H}$ are described using permittivity $\varepsilon$ and magnetic permeability $\mu$ as follows.

$$D = \varepsilon E(\mathbf{r}), \tag{2.5}$$

$$B = \mu H, \tag{2.6}$$

$$\varepsilon = \varepsilon_0 \varepsilon(\mathbf{r}), \tag{2.7}$$

$$\mu = \mu_0 \mu(\mathbf{r}), \tag{2.8}$$

where $\varepsilon_0$, $\varepsilon(\mathbf{r})$, $\mu_0$ and $\mu(\mathbf{r})$ are permittivity in vacuum, relative permittivity, permeability in vacuum and relative permeability respectively.

Here, the current density $J$ is assumed to be 0 since there are no current sources, and $\mu(\mathbf{r})$ is simplified to be 1 because magnetic response is very slow compared to periods of optical frequency. By submitting Eq. (2.5) and Eq. (2.6) into the Maxwell equations,

$$\nabla \cdot [\varepsilon(\mathbf{r})E(\mathbf{r},t)] = 0, \tag{2.9}$$

$$\nabla \cdot H(\mathbf{r},t) = 0, \tag{2.10}$$

$$\nabla \times E(\mathbf{r},t) + \mu_0 \frac{\partial H(\mathbf{r},t)}{\partial t} = 0, \tag{2.11}$$

$$\nabla \times H(\mathbf{r},t) - \varepsilon_0 \varepsilon(\mathbf{r}) \frac{\partial E(\mathbf{r},t)}{\partial t} = 0, \tag{2.12}$$

are obtained. Since $E$ and $H$ oscillate harmonically, they can be written as followed,

$$E(\mathbf{r},t) = E(\mathbf{r})e^{-j\omega t}, \tag{2.13}$$

$$H(\mathbf{r},t) = H(\mathbf{r})e^{-j\omega t}, \tag{2.14}$$

where $j$ is an imaginary number which satisfy $j^2 = -1$. By submitting Eq. (2.13) into Eq. (2.11), and Eq. (2.14) into Eq. (2.12) respectively following equations are obtained.

$$\nabla \times E(\mathbf{r}) - j\omega\mu_0 H(\mathbf{r}) = 0, \tag{2.15}$$

$$\nabla \times H(\mathbf{r}) + j\omega\varepsilon_0 \varepsilon(\mathbf{r})E(\mathbf{r}) = 0. \tag{2.16}$$

From Eq. (2.15) and Eq. (2.16),

$$\nabla \times \left(\frac{1}{\varepsilon(\mathbf{r})}\nabla \times H(\mathbf{r})\right) = \left(\frac{\omega}{c}\right)^2 H(\mathbf{r}), \tag{2.17}$$

is derived where $c = 1/\sqrt{\varepsilon_0\mu_0}$. Next, an operator $\Theta$ is defined as,

$$\Theta H(\mathbf{r}) \equiv \nabla \times \left(\frac{1}{\varepsilon(\mathbf{r})}\nabla H(\mathbf{r})\right), \tag{2.18}$$

$$\therefore \Theta H(\mathbf{r}) = \left(\frac{\omega}{c}\right)^2 H(\mathbf{r}). \tag{2.19}$$

In a periodic structure, such as a PhC, $H(\mathbf{r})$ can be assumed as a periodic function that has Bloch wavevector $\mathbf{k}$, on the basis of Bloch-Floquet theorem.

$$H(\mathbf{r}) = H_{\mathbf{k}}(\mathbf{r}) = e^{j\mathbf{k}\cdot\mathbf{r}} \cdot H_{n,\mathbf{k}}(\mathbf{r}), \tag{2.20}$$

$$H_{n,\mathbf{k}}(\mathbf{r}) = H_{n,\mathbf{k}}(\mathbf{r}+\mathbf{a}). \tag{2.21}$$

Here, $a$ is lattice constant of the structure and $n$ corresponds to the label number for primitive cells that is a part of a periodic structure. By submitting Eq. (2.20) and Eq. (2.21) into Eq. (2.17),

$$(\nabla + j\boldsymbol{k}) \times \frac{1}{\varepsilon(\boldsymbol{r})}(\nabla + j\boldsymbol{k}) \times \boldsymbol{H}_{n,\boldsymbol{k}}(\boldsymbol{r}) = (\frac{\omega_n(\boldsymbol{k})}{c})^2 \boldsymbol{H}_{n,\boldsymbol{k}}(\boldsymbol{r}), \tag{2.22}$$

is obtained. The Coefficient of $\boldsymbol{H}_{n,\boldsymbol{k}}(\boldsymbol{r})$ at the right side of Eq. (2.22) is eigenvalue in this Schrödinger equation, and here, $\omega_n v(\boldsymbol{k})$ are functions of $\boldsymbol{k}$. The relation between $\omega_n(\boldsymbol{k})$ and $\boldsymbol{k}$ express dispersion of the system. Since $\boldsymbol{H}(\boldsymbol{r})$ is a Bloch function as described in Eq. (2.21), it satisfies a condition below, where wavevector $\boldsymbol{k}'$ is assumed to be $\boldsymbol{k}' = \boldsymbol{k} + 2\pi/a$

$$\boldsymbol{H}_{\boldsymbol{k}}(\boldsymbol{r}) = e^{j(k'-\frac{2\pi}{\boldsymbol{a}})\cdot\boldsymbol{r}} \cdot \boldsymbol{H}_{n,\boldsymbol{k}}(\boldsymbol{r}) = e^{jk'\boldsymbol{r}} \cdot \boldsymbol{H}_{n,\boldsymbol{k}}(\boldsymbol{r}) e^{-j\frac{2\pi}{\boldsymbol{a}}\cdot\boldsymbol{r}}. \tag{2.23}$$

Since $\boldsymbol{H}_{n,\boldsymbol{k}}(\boldsymbol{r}) e^{-jk'\frac{2\pi}{\boldsymbol{a}}\cdot\boldsymbol{r}} = \boldsymbol{H}_{n,\boldsymbol{k}}(\boldsymbol{r}+\boldsymbol{a}) e^{-jk'\frac{2\pi}{\boldsymbol{a}}\cdot(\boldsymbol{r}+\boldsymbol{a})}$, the following equations are obtained.

$$\boldsymbol{H}_{n,\boldsymbol{k}'}(\boldsymbol{r}) = \boldsymbol{H}_{n,\boldsymbol{k}}(\boldsymbol{r}) e^{-j\frac{2\pi}{\boldsymbol{a}}\cdot\boldsymbol{r}},. \tag{2.24}$$

As shown in Eq. (2.24), $\boldsymbol{H}_{\boldsymbol{k}}(\boldsymbol{r})$ is a periodical function of $2\pi/a$, and therefore, the eigenvalue $\omega_n(\boldsymbol{k})$ also have same periodicity. So, we only need to know the dispersion relation in the range of $-\pi/a \leq k \leq \pi/a$. This range is called the first Brillouin zone. Only half of the range of $0 \leq k \leq \pi/a$ is considered in general since time-reversal symmetry is satisfied for most cases.
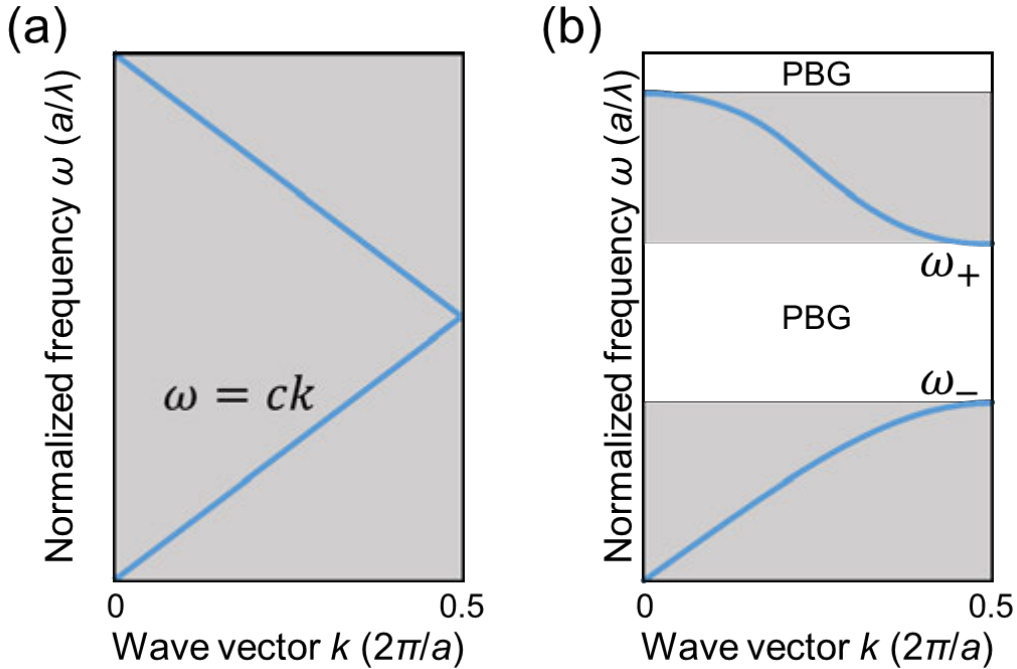


Fig. 2.1. Schematic of (a) Photonic band diagram for uniform medium. (b) Photonic band diagram for periodic dielectric structures.

Next, we will look at a dispersion diagram. Assuming the system is one-dimensional and $\varepsilon(r) = 1$, Eq. (2.22) has eigenvalues of $\omega = ck$ as shown in Fig. 2.1(a). On the other hand, if

periodical perturbation in dielectric constant of $\varepsilon(r) = 1 + \Delta \cdot \cos(2\pi r/a)$ is assumed, following two eigenvalues at $k = \pi/a$ proportional to $\cos(\pi r/a)$ or $\sin(\pi r/a)$ are obtained.

$$\omega_{+,k=\pi/a} \propto |\boldsymbol{H}_+|^2 \propto 4\cos^2\frac{\pi r}{a}, \tag{2.25}$$

$$\omega_{-,k=\pi/a} \propto |\boldsymbol{H}_-|^2 \propto 4\sin^2\frac{\pi r}{a}. \tag{2.26}$$

Equation (2.25) and Eq. (2.26) shows two different eigenvalues existing at $k = \pi/a$, which is the origin of PBG (see Fig. 2.1 (b)). Light with wavelength within the PBG cannot exist in the medium, so the PhC structure works as a forbidden band for photons. This derivation can expand for two and three dimensional cases.

### 2.1.2 Strategy to form a cavity

To form a PhC nanocavity, the introduction of a defect into the PBG structure is required. Figure 2.2 shows the photonic band diagram of two PhC structures. Figure 2.2(a) shows a band diagram of PhC without a defect and Fig. 2.2(b) shows that of a PhC with a defect where the defect is introduced by burying an air hole. The orange shaded region shows the area where PhC modes exist and the gray shaded region indicates the area above the light line where modes radiate out of plane. In Fig. 2.2(a), PBG was observed around a normalized frequency of 0.25 to 0.33. On the other hand, two modes appear in the PBG when the defect is introduced as shown in Fig. 2.2(b). The mode profiles of them show that the modes are confined in the defect (see Figs. 2.2(c) and (d)). So, a cavity is formed if the lattice in Fig. 2.2(a) is sandwiched between that in Fig. 2.2(a), where light can exist in the defect but cannot propagate into the PBG structure. Note that precise tuning of the defect size is performed to reduce radiation loss in practical. Formation of a waveguide is also possible by connecting defects.

Types of PhC nanocavities are roughly categorized into two different types. One is bandgap type and the other is modegap type. Bandgap cavities are introduced by forming a defect in PhC (e.g., L3 and H0 cavities). Since a small defect can be formed, their mode volume tend to be smaller than those of modegap cavities. Modegap cavities are formed in a PhC waveguide by modulating its guided modes (e.g., width-modulated and multi-hetero cavities). Modegap cavities usually have higher $Q$ than bandgap cavities since it based on guided mode with small out-of-plane radiation.

## 2.2 Numerical methods

### 2.2.1 Plane wave expansion method

Plane wave expansion (PWE) method is an effective way to calculate eigenmodes in periodic structures and are commonly used to compute photonic band diagrams [173, 174]. It employs expanded plane waves to form eigenvalue equations, which is the origin of its name. In this study, the method is used with a free software package of MPB [175]. Here, introduction of the eigenvalue equation is described. As described in Chapter 2.1.1, the magnetic field is
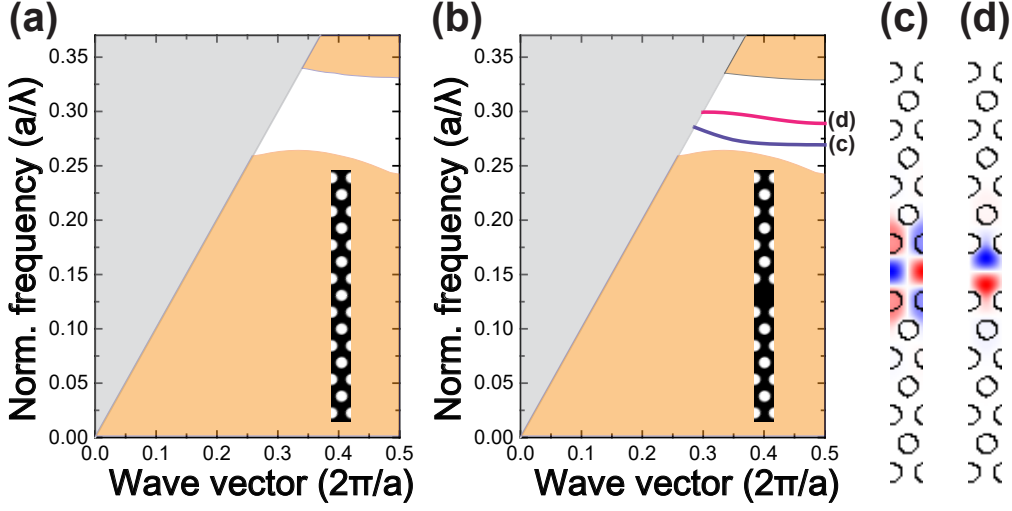
Fig. 2.2. Photonic band diagram of PhC (a) without defect. (b) with defect. The orange shaded region indicate PhC modes and the gray shaded region indicates radiation mode above light line. Inset shows unit cell used for the band calculation. Mode profile of Hz field of guided mode with (c) even symmetry and (d) odd symmetry.

expressed through the deformed Maxwell equation of,

$$\Theta \boldsymbol{H}(\boldsymbol{r}) = (\frac{\omega}{c})^2 \boldsymbol{H}(\boldsymbol{r}). \tag{2.19}$$

This is used for constructing eigenvalue equations later. By assuming a periodic structure with period of $\Lambda$, a dielectric constant satisfies condition of

$$\varepsilon(\boldsymbol{r} + \Lambda) = \varepsilon(\boldsymbol{r}). \tag{2.27}$$

Fourier transformation of inverse of dielectric constant is

$$\frac{1}{\varepsilon(\boldsymbol{r})} = \sum_G \xi(\boldsymbol{G}) \exp(j\boldsymbol{G} \cdot \boldsymbol{r}), \tag{2.28}$$

where $\boldsymbol{G}$ is a reciprocal vector, which satisfies $\exp(j\boldsymbol{G} \cdot \Lambda) = 1$ and $1/\varepsilon(\boldsymbol{r} + \Lambda) = 1/\varepsilon(\boldsymbol{r})$, and $\xi(\boldsymbol{G})$ is Fourier coefficient. By multiplying both side of Eq. (2.28) with $\exp(-j\boldsymbol{G} \cdot \boldsymbol{r})$ and integrating for unit cell,

$$\int \frac{1}{\varepsilon(\boldsymbol{r})} \exp(-j\boldsymbol{G} \cdot \boldsymbol{r}) dV = \sum_{G'} \xi(\boldsymbol{G'}) \int \exp(j(\boldsymbol{G'} - \boldsymbol{G}) \cdot \boldsymbol{r}) dV \tag{2.29}$$

$$= \sum_{G'} \xi(\boldsymbol{G'}) V_f \delta_{G,G'} \tag{2.30}$$

$$= V_f \xi(\boldsymbol{G}), \tag{2.31}$$

is obtained. So, the Fourier coefficient is expressed as,

$$\xi(\boldsymbol{G}) = \frac{1}{V_f} \int \frac{1}{\varepsilon(\boldsymbol{r})} \exp(-j\boldsymbol{G} \cdot \boldsymbol{r}) dV. \tag{2.32}$$

35

The magnetic field of Eq. (2.19) is expanded with plane wave of $\exp(j\boldsymbol{k} \cdot \boldsymbol{r})$ in the first Brillouin zone. Since the magnetic field is modulated by the periodicity of structures of $\exp(j\boldsymbol{G} \cdot \boldsymbol{r})$, it is written as,

$$\boldsymbol{H}(\boldsymbol{r}) = \sum_{G} \boldsymbol{h}_k(\boldsymbol{G})\exp\{j(\boldsymbol{k} + \boldsymbol{G}) \cdot \boldsymbol{r}\}, \tag{2.33}$$

where $\boldsymbol{h}_k(\boldsymbol{G})$ is a coefficient for plane wave expansion and its subscript $\boldsymbol{k}$ means that it is dependent on wave vector. The magnetic field also satisfies the Bloch condition of

$$\boldsymbol{H}(\boldsymbol{r} + \boldsymbol{\Lambda}) = \boldsymbol{H}(\boldsymbol{r})\exp\{j(\boldsymbol{k} + \boldsymbol{G}) \cdot \boldsymbol{\Lambda}\} = \boldsymbol{H}(\boldsymbol{r})\exp(j\boldsymbol{k} \cdot \boldsymbol{\Lambda}). \tag{2.34}$$

So, only the first Brillouin zone is necessary for describing all systems. By submitting Eq. (2.28) and Eq. (2.33) into Eq. (2.19),

$$\sum_{G'} \sum_{G''} \nabla \times [\xi(\boldsymbol{G''})\exp(j\boldsymbol{G''} \cdot \boldsymbol{r})\nabla \times \boldsymbol{h}_{k'}(\boldsymbol{G'})\exp\{j(\boldsymbol{k} + \boldsymbol{G'}) \cdot \boldsymbol{r}\}]$$

$$= \sum_{G} (\frac{\omega_k}{c})^2 \boldsymbol{h}_k(\boldsymbol{G})\exp\{j(\boldsymbol{k} + \boldsymbol{G}) \cdot \boldsymbol{r}\}, \tag{2.35}$$

is obtained. The left side of the Eq. (2.35) is deformed as followed using the relation of $\nabla \times \boldsymbol{h}_{k'}(\boldsymbol{G'})\exp\{j(\boldsymbol{k} + \boldsymbol{G'}) \cdot \boldsymbol{r}\} = j(\boldsymbol{k} + \boldsymbol{G'}) \times \boldsymbol{h}_{k'}(\boldsymbol{G'})\exp\{j(\boldsymbol{k} + \boldsymbol{G'}) \cdot \boldsymbol{r}\}$,

$$\sum_{G'} \sum_{G''} \nabla \times [\xi(\boldsymbol{G''})j(\boldsymbol{k} + \boldsymbol{G'}) \times \boldsymbol{h}_{k'}(\boldsymbol{G'})\exp\{j(\boldsymbol{k} + \boldsymbol{G'} + \boldsymbol{G''}) \cdot \boldsymbol{r}\}]$$

$$= \sum_{G} (\frac{\omega_k}{c})^2 \boldsymbol{h}_k(\boldsymbol{G})\exp\{j(\boldsymbol{k} + \boldsymbol{G}) \cdot \boldsymbol{r}\}. \tag{2.36}$$

The meaning of Eq. (2.36) is briefly discussed. On the left side of the equation, $\boldsymbol{k} + \boldsymbol{G'}$ means phase of incident light and $\boldsymbol{G''}$ expresses reciprocal vector of the periodic structure which produces diffraction components with form of basis vector of reciprocal space of $\boldsymbol{b}$ multiplied by integer. The last term on the left side indicates incident light diffracted by the periodic structure. To avoid extinction of the diffracted light, phase components in exponential on both sides of the equation must be equal. Therefore, condition of

$$\boldsymbol{G''} = \boldsymbol{G} - \boldsymbol{G'}, \tag{2.37}$$

is required. This corresponds to condition of the Bragg diffraction. By submitting Eq. (2.37) into Eq. (2.36)),

$$\sum_{G'} \nabla \times [\xi(\boldsymbol{G} - \boldsymbol{G'})j(\boldsymbol{k} + \boldsymbol{G'}) \times \boldsymbol{h}_{k'}(\boldsymbol{G'})\exp\{j(\boldsymbol{k} + \boldsymbol{G}) \cdot \boldsymbol{r}\}]$$

$$= (\frac{\omega_k}{c})^2 \boldsymbol{h}_k(\boldsymbol{G})\exp\{j(\boldsymbol{k} + \boldsymbol{G}) \cdot \boldsymbol{r}\}, \tag{2.38}$$

is derived. Then, calculating the rotation on the left side, the equation is deformed to be,

$$-\sum_{G'} \xi(G - G')(k + G) \quad \times \quad \{(k + G') \times h_{k'}(G')\} \exp\{j(k + G) \cdot r\}$$

$$= \quad (\frac{\omega_k}{c})^2 h_k(G) \exp\{j(k + G) \cdot r\}. \tag{2.39}$$

Finally, the common denominator of $\exp\{j(k+G) \cdot r\}$ is deleted from both sides of the equation and

$$-\sum_{G'} \xi(G - G')(k + G) \times \{(k + G') \times h_{k'}(G')\} = (\frac{\omega_k}{c})^2 h_k(G), \tag{2.40}$$

is obtained. This is a eigenvalue equation of simultaneous linear equations with many unknowns for infinite number of expansion coefficient of $h_k$. Since Eq. (2.40) is derived from Eq. (2.19) and $\Theta$ is a the Hermitian operator, the equations possess eigenvalues of real numbers. In addition, diagonalization of Hermitian matrix is not complicated, so the eigenvalues and vectors are easily calculated. The electric field is calculated with the following equation.

$$E(r) = -\frac{j}{\omega \varepsilon(r)} \nabla \times H(r). \tag{2.41}$$

The method above is called plane wave expansion method. For the actual calculation, the number of plane waves are reduced to be a finite number as far as eigenvalues converge.

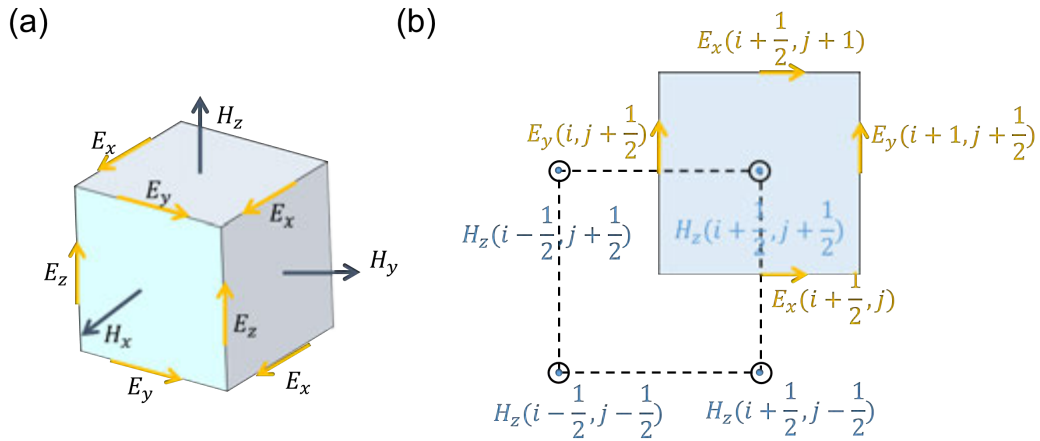### 2.2.2 Finite differential time domain (FDTD) method



Fig. 2.3. (a) Three dimensional arrangement of electric and magnetic fields in a Yee cell. (b) Two dimensional arrangement of electric and magnetic fields in a Yee cell. Arrows indicate positive directions for each coordinate.

Finite-difference time-domain (FDTD) method is used for describing propagation of light in dielectric materials [176]. It is a useful way to predict characterization of PhCs accurately both in frequency and time domain. This method employs a lattice consisting of tiny cells called the Yee cell for calculating electric and magnetic field distribution. In the Yee cell, electric and magnetic fields are placed at different positions with a spatial difference of half of

the lattice constant. 3D and 2D arrangement of both fields are displayed in Figs. 2.3(a) and (b) respectively. FDTD divides time into tiny sections and each field components are calculated from fields around them at previous time section. The light propagation is determined by repeating this process sequentially in time and space. The algorithm is summarized in Fig. 2.4.
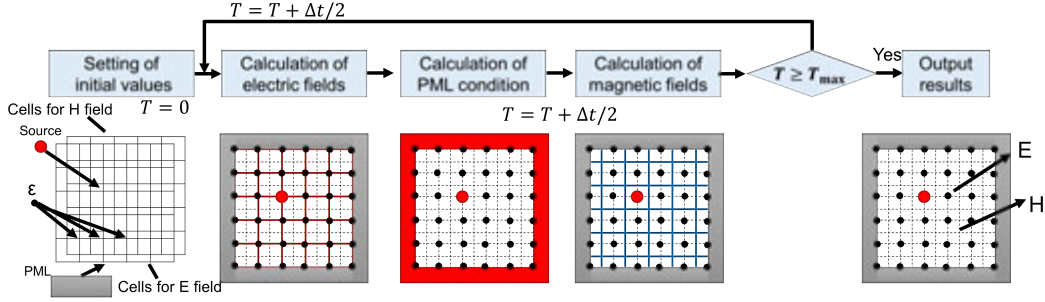


Fig. 2.4. Schematic of Algorithm of FDTD method. $T_{max}$ specifies calculation time.

To demonstrate FDTD method, time and spatial discretization of Maxwell's equations is required. It is performed with the following transformation of partial differential form of the field $\boldsymbol{F}$ using central difference.

$$\frac{\partial \boldsymbol{F}}{\partial t} \rightarrow \frac{\boldsymbol{F}(x, y, t + \Delta t/2) - \boldsymbol{F}(x, y, t - \Delta t/2)}{\Delta t}, \tag{2.42}$$

Although the above equation is an example of discretization in time domain, transformation for space is also performed in the same way. For simplicity, the following expression is introduced for the field at position and time of $(x, y, z, t) = (i\Delta x, j\Delta y, k\Delta z, n\Delta t)$,

$$\boldsymbol{F}(x, y, z, t) = \boldsymbol{F}^n(i, j, k), \tag{2.43}$$

where $\Delta x, \Delta y, \Delta z, \Delta t$ are infinitesimal differences for each components and $i, \quad j, \quad k, \quad n$ are integers.

First, the general way of the sequent calculation in time domain is presented. Maxwell's equations of Eq. (2.3) and Eq. (2.4) is deformed as follows with relationship of Eq. (2.5) and Eq. (2.6) by assuming uniform and non-dispersive medium,

$$\frac{\partial \boldsymbol{E}}{\partial t} = -\frac{\sigma}{\varepsilon}\boldsymbol{E} + \frac{1}{\varepsilon}\nabla \times \boldsymbol{H}, \tag{2.44}$$

$$\frac{\partial \boldsymbol{H}}{\partial t} = -\frac{1}{\mu}\nabla \times \boldsymbol{E}, \tag{2.45}$$

where $\sigma$ is conductivity which have relation of $\boldsymbol{J} = \sigma\boldsymbol{E}$. If an electric field is calculated at time of $t = n\Delta t$, whereas magnetic field is at $t = (n - 1/2)\Delta t$ ($n$ is integer), the discrete forms of each field are

$$\left.\frac{\partial \boldsymbol{E}}{\partial t}\right|_{t=(n-1/2)\Delta t} = \frac{\boldsymbol{E}^n - \boldsymbol{E}^{n-1}}{\Delta t}, \tag{2.46}$$

$$\left.\frac{\partial \boldsymbol{H}}{\partial t}\right|_{t=n\Delta t} = \frac{\boldsymbol{H}^{n+1/2} - \boldsymbol{H}^{n-1/2}}{\Delta t}. \tag{2.47}$$

Therefore, Eq. (2.44) and Eq. (2.45) are deformed to be followings by submitting Eq. (2.46) and Eq. (2.46) into them,

$$\frac{\boldsymbol{E}^n - \boldsymbol{E}^{n-1}}{\Delta t} = -\frac{\sigma}{\varepsilon}\boldsymbol{E}^{n-1/2} + \frac{1}{\varepsilon}\nabla \times \boldsymbol{H}^{n-1/2}, \tag{2.48}$$

$$\frac{\boldsymbol{H}^{n+1/2} - \boldsymbol{H}^{n-1/2}}{\Delta t} = -\frac{1}{\mu}\nabla \times \boldsymbol{E}^n. \tag{2.49}$$

Then, the approximation of $\sigma\boldsymbol{E}^{n-1/2} \approx \sigma\frac{\boldsymbol{E}^{n-1}+\boldsymbol{E}^n}{2}$ is applied and $\boldsymbol{E}^n$ and $\boldsymbol{H}^{n+1/2}$ are deformed to be,

$$\boldsymbol{E}^n = \frac{1 - \frac{\sigma\Delta t}{2\varepsilon}}{1 + \frac{\sigma\Delta t}{2\varepsilon}}\boldsymbol{E}^{n-1} + \frac{\Delta t/\varepsilon}{1 + \frac{\sigma\Delta t}{2\varepsilon}}\nabla \times \boldsymbol{H}^{n-1/2}, \tag{2.50}$$

$$\boldsymbol{H}^{n+1/2} = \boldsymbol{H}^{n-1/2} - \frac{\Delta t}{\mu}\nabla \times \boldsymbol{E}^n. \tag{2.51}$$

According to Eq. (2.50) and Eq. (2.51), both $\boldsymbol{E}$ and $\boldsymbol{H}$ are obtained from the last time section. This is the basis of the sequential computing of fields in FDTD in time domain.

Next, discrete forms of Maxwell equations for spatial sequential calculation are presented. Here, the equations for TE wave in a 2D are described by employing a Yee cell as shown in Figure 2.3 (b) for simplicity. Note that the field arrangement of the Yee cell is possible because an electric field is expressed with the rotation of a magnetic field and vice versa. Since TE waves consist of $E_x$, $E_y$, and $H_z$ in 2D field and $\partial/\partial z = 0$, electric fields are written as follows using Eq. (2.50).

$$E_x^n = \frac{1 - \frac{\sigma\Delta t}{2\varepsilon}}{1 + \frac{\sigma\Delta t}{2\varepsilon}}E_x^{n-1} + \frac{\Delta t/\varepsilon}{1 + \frac{\sigma\Delta t}{2\varepsilon}}\frac{\partial H_z^{n-1/2}}{\partial y}, \tag{2.52}$$

$$E_y^n = \frac{1 - \frac{\sigma\Delta t}{2\varepsilon}}{1 + \frac{\sigma\Delta t}{2\varepsilon}}E_y^{n-1} + \frac{\Delta t/\varepsilon}{1 + \frac{\sigma\Delta t}{2\varepsilon}}\frac{\partial H_z^{n-1/2}}{\partial x}. \tag{2.53}$$

By taking the location of electric fields into account, the partial differential equations for magnetic fields are expressed as,

$$\frac{\partial H_z^{n-1/2}}{\partial y}\Big|_{i+1/2,j} = \frac{H_z^{n-1/2}(i + 1/2, j + 1/2) - H_z^{n-1/2}(i + 1/2, j - 1/2)}{\Delta y}\text{and,} \tag{2.54}$$

$$\frac{\partial H_z^{n-1/2}}{\partial y}\Big|_{i,j+1/2} = \frac{H_z^{n-1/2}(i + 1/2, j + 1/2) - H_z^{n-1/2}(i - 1/2, j + 1/2)}{\Delta x}. \tag{2.55}$$

Therefore, Eq. (2.52) and Eq. (2.53) are deformed as followed with Eq. (2.54) and Eq. (2.55),

$$\begin{aligned} E_x^n(i + 1/2, j) &= C_{EX}(i + 1/2, j)E_x^{n-1}(i + 1/2, j) \\ &+ C_{EXLY}(i + 1/2, j)\{H_z^{n-1/2}(i + 1/2, j + 1/2) - H_z^{n-1/2}(i + 1/2, j - 1/2)\}, \end{aligned} \tag{2.56}$$

$$\begin{aligned} E_y^n(i, j + 1/2) &= C_{EY}(i, j + 1/2)E_y^{n-1}(i, j + 1/2) \\ &- C_{EYLX}(i, j + 1/2)\{H_z^{n-1/2}(i + 1/2, j + 1/2) - H_z^{n-1/2}(i - 1/2, j + 1/2)\}, \end{aligned} \tag{2.57}$$

where,

$$C_{\text{EX}}(i + 1/2, j) \quad = \quad \frac{1 - \frac{\sigma(i+1/2,j)\Delta t}{2\varepsilon(i+1/2,j)}}{1 + \frac{\sigma(i+1/2,j)\Delta t}{2\varepsilon(i+1/2,j)}}, \tag{2.58}$$

$$C_{\text{EXLY}}(i + 1/2, j) \quad = \quad \frac{\Delta t/\varepsilon(i + 1/2, j)}{1 + \frac{\sigma(i+1/2,j)\Delta t}{2\varepsilon(i+1/2,j)}} \frac{1}{\Delta y}, \tag{2.59}$$

$$C_{\text{EY}}(i, j + 1/2) \quad = \quad \frac{1 - \frac{\sigma(i,j+1/2)\Delta t}{2\varepsilon(i,j+1/2)}}{1 + \frac{\sigma(i,j+1/2)\Delta t}{2\varepsilon(i,j+1/2)}}. \tag{2.60}$$

$$C_{\text{EYLX}}(i, j + 1/2) \quad = \quad \frac{\Delta t/\varepsilon(i, j + 1/2)}{1 + \frac{\sigma(i,j+1/2)\Delta t}{2\varepsilon(i,j+1/2)}} \frac{1}{\Delta y}. \tag{2.61}$$

The magnetic field is determined with Eq. (2.51) as,

$$H_{\text{z}}^{n+1/2} \quad = \quad H_{\text{z}}^{n-1/2} - \frac{\Delta t}{\mu}(\frac{\partial E_{\text{y}}^n}{\partial x} - \frac{\partial E_{\text{x}}^n}{\partial y}). \tag{2.62}$$

Since $H_{\text{z}}$ is located at $(x, y) = (i + 1/2, j + 1/2))$, the partial differential equations in Eq. (2.62) are

$$\frac{\partial E_{\text{y}}^n}{\partial x}\bigg|_{i+1/2,j+1/2} \quad = \quad \frac{E_{\text{y}}^n(i + 1, j + 1/2) - E_{\text{y}}^n(i, j + 1/2)}{\Delta x}, \tag{2.63}$$

$$\frac{\partial E_{\text{x}}^n}{\partial x}\bigg|_{i+1/2,j+1/2} \quad = \quad \frac{E_{\text{y}}^n(i + 1/2, j + 1) - E_{\text{y}}^n(i + 1/2, j)}{\Delta y}. \tag{2.64}$$

Therefore, following equation is obtained.

$$\begin{aligned} H_{\text{z}}^{n+1/2}(i + 1/2, j + 1/2) = \; & H_{\text{z}}^{n-1/2}(i + 1/2, j + 1/2) \\ & - C_{\text{HZLX}}(i + 1/2, j + 1/2)\{E_{\text{y}}^n(i + 1, j + 1/2) - E_{\text{y}}^n(i, j + 1/2)\} \\ & + C_{\text{HZLY}}(i + 1/2, j + 1/2)\{E_{\text{x}}^n(i + 1/2, j + 1) - E_{\text{y}}^n(i + 1/2, j)\}, \end{aligned} \tag{2.65}$$

where,

$$C_{\text{HZLX}}(i + 1/2, j + 1/2) = \frac{\Delta t}{\mu(i + 1/2, j + 1/2)} \frac{1}{\Delta x}, \tag{2.66}$$

$$C_{\text{HZLY}}(i + 1/2, j + 1/2) = \frac{\Delta t}{\mu(i + 1/2, j + 1/2)} \frac{1}{\Delta y}. \tag{2.67}$$

Next, field distribution is determined with Eq. (2.56), Eq. (2.57) and Eq. (2.65). Derivation of the equations for transverse magnetic (TM) wave is also possible in the similar way (TM wave consists of $H_{\text{x}}$, $H_{\text{y}}$, and $E_{\text{z}}$). In general, absorption boundaries are placed at the edges of the calculation area to avoid reflection. Perfect matching layer (PML) is the most standard condition applied for this purpose [176, 177].

Note that the Courant-Friedrichs-Lewy condition must be satisfied to ensure the stability of the calculation.

$$v\Delta t \leq \frac{1}{\sqrt{(\frac{1}{\Delta x})^2 + (\frac{1}{\Delta y})^2 + (\frac{1}{\Delta z})^2}}. \tag{2.68}$$

FDTD is a common numerical tool for optics and photonics research, so there are many different types of commercial and free software available. In this study, a free software package develped by MIT called MEEP was used [178] .

### 2.2.3 Coupled mode theory

Coupled mode theory (CMT) [179–181] is a powerful method for modeling a flow of light in systems consisting of optical components. CMT focuses only on amplitudes of a mode of each optical component in a system which can be expressed with a small matrix, so time and computational costs are much smaller compared to other numerical methods such as FDTD and finite element method (FEM). In those days, CMT was used to model the interaction between adjacent waveguides. However, recent applications of CMT have been used to, for example, design optical circuits which contain optical microcavities [182]. Here, three CMT models have been developed for configurations of a side-coupled ring-type cavity, a direct-coupled FP-type cavity and a side-coupled FP-type cavity (see Fig. 2.5). Initially, the transmission spectrum of a ring cavity coupled with a waveguide is considered (see Fig. 2.5 (a)).
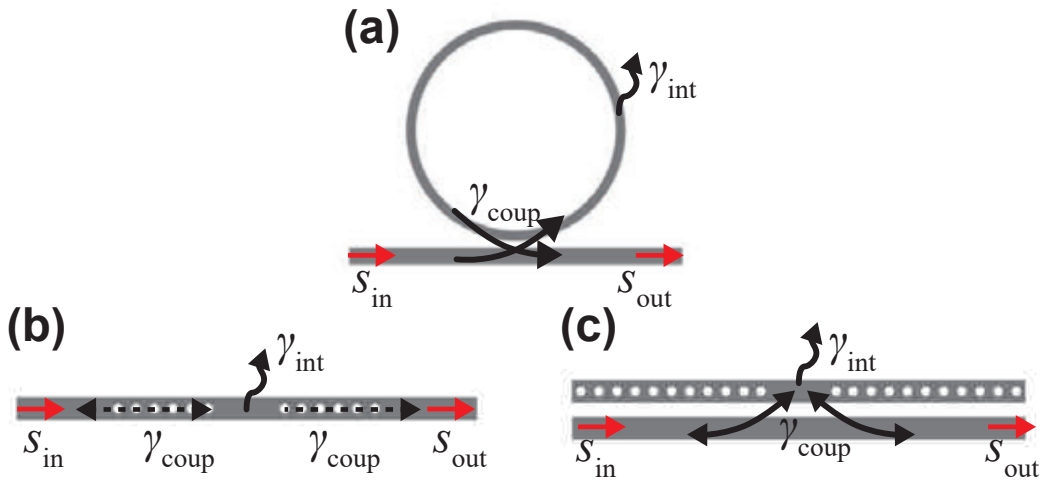


Fig. 2.5. Schematic diagrams of coupling configurations. (a) Side coupled ring-type cavity. (b) Direct coupled FP-type cavity. (c) Side coupled FP-type cavity.

CMT starts from the following master equation [179, 180];

$$\frac{\mathrm{d}a}{\mathrm{d}t} = \left(j\omega_0 - \frac{\gamma}{2}\right)a + j\sqrt{\gamma_{\text{coup}}}s_{\text{in}}, \tag{2.69}$$

where $a$, $s_{\text{in}}$, $j$, $\omega_0$ are the amplitudes of the modes in the microcavity, that of the input, an imaginary number which satisfy $j^2 = -1$, and the resonant angular frequency of the cavity,

respectively. Note that the light energy $U_{\text{cavity}}$ and the input power $P_{\text{in}}$ are expressed by $U_{\text{cavity}} = |a|^2 = aa^*$ and $P_{\text{in}} = |s_{\text{in}}|^2 = s_{\text{in}}s_{\text{in}}^*$. Therefore, $a$ and $s_{\text{in}}$ have dimensions of $J^{1/2}$ and $W^{1/2}$.

Equation (2.69) expresses a differential equation for a mode which oscillates with the angular frequency of $\omega_0$. The cavity decay rate $\gamma$ is expressed by $\gamma = \gamma_{\text{int}} + \gamma_{\text{coup}}$, where $\gamma_{\text{int}}$ and $\gamma_{\text{coup}}$ are the intrinsic cavity decay rate and the coupling rate between the cavity and the waveguide, respectively (see Fig. 2.5). Thus, the mode amplitude in the cavity will decay exponentially to the sum of the two decay rates. Note that the decay rates have the following relation with $Q$ factor of

$$\gamma = \omega_0/Q. \tag{2.70}$$

The last term on the right side of Eq. (2.69) describes the amplitude of input light $s_{\text{in}}$ couples into the cavity at a rate of $j\sqrt{\gamma_{\text{coup}}}$, respectively (This term needs to be a pure imaginary number for satisfying the energy conservation and the time-reversal symmetry [179]). Since the unit of input amplitude $s_{\text{in}}$ is $W^{1/2} = J/s^{1/2}$, its coupling rate into the cavity mode is the square root of $\gamma_{\text{coup}}$.

The output mode amplitude $s_{\text{out}}$ can be written as

$$s_{\text{out}} = s_{\text{in}} + j\sqrt{\gamma_{\text{coup}}}a, \tag{2.71}$$

As seen in Eq. (2.71), the output amplitude $s_{\text{out}}$ is determined as a result of interference between the cavity mode $a$ and the input mode $s_{\text{in}}$. For ring-type cavity in side coupled configuration, this interference enables us to have a condition where all light couples to the cavity as described in later, which is the clear advantage of the system compared to direct couple ones [183]. If a static condition ($a, s_{\text{in}}, s_{\text{out}} \propto \exp(j\omega t)$) is assumed, the relation between $a$ and $s_{\text{in}}$ is given as

$$a = \frac{j\sqrt{\gamma_{\text{coup}}}}{j(\omega - \omega_0) + \gamma/2}s_{\text{in}}. \tag{2.72}$$

Therefore, the relationship between $s_{\text{out}}$ and $s_{\text{in}}$ is obtained by substituting Eq. (2.72) into Eq. (2.71),

$$s_{\text{out}} = \left[\frac{j(\omega - \omega_0) + (\gamma_{\text{int}} - \gamma_{\text{coup}})/2}{j(\omega - \omega_0) + (\gamma_{\text{int}} + \gamma_{\text{coup}})/2}\right]s_{\text{in}}. \tag{2.73}$$

Note that $\gamma = \gamma_{\text{int}} + \gamma_{\text{coup}}$ is used. Finally, the transmittance $Tr = P_{\text{out}}/P_{\text{in}} = |s_{\text{out}}/s_{\text{in}}|^2$ is written as

$$Tr_{\text{side,ring}} = \frac{(\omega - \omega_0)^2 + (\gamma_{\text{int}} - \gamma_{\text{coup}})^2/4}{(\omega - \omega_0)^2 + (\gamma_{\text{int}} + \gamma_{\text{coup}})/4}. \tag{2.74}$$

On the other hand, transmittance of FP-type cavities coupled with waveguides in side and direct coupling configurations are obtained by performing deformation in the same way as that of side coupled ring-type cavity as follows.

$$Tr_{\text{side,FP}} = (\frac{1}{1 + \gamma_{\text{coup}}/\gamma_{\text{int}}})^2, \tag{2.75}$$

$$Tr_{\text{direct,FP}} = (\frac{1}{1 + \gamma_{\text{int}}/\gamma_{\text{coup}}})^2, \tag{2.76}$$

where $\gamma = \gamma_{\text{int}} + 2\gamma_{\text{coup}}$ is employed in Eq. (2.69) and $s_{\text{out}} = -j\sqrt{\gamma_{\text{coup}}}a$ is used for calculating the transmittance for the direct coupling system. For all systems, phase differences between the input and the output light $\theta$ were obtained from $\theta = \arg(s_{\text{out}})$. $\theta$ will be non-zero for coupled light with longer and shorter wavelengths than a resonant wavelength since the cavity length does not fit it.

For a side coupled ring-type cavity, the transmittance takes the smallest value when the input frequency is matched to the resonant frequency (i.e., $\omega - \omega_0 = 0$). This is due to the fact that the phase of input wave and wave releasing from the cavity is inverted, and then destructive interference occurs when the cavity is on resonance (see Fig. 2.6). Interestingly, the transmittance drops to zero when the loss ratio of the cavity and coupling are equal (i.e., the critical coupling condition of $\gamma_{\text{int}} = \gamma_{\text{coup}}$), which is a specific phenomena observed only in side coupled ring-type cavity. In this condition, the amplitude of the mode transmitted through the waveguide is the same as the amplitude of the mode coupled from the cavity, thus the output wave completely disappears. Meanwhile, the name of condition where $\gamma_{\text{int}} < \gamma_{\text{coup}}$ ($Q_{\text{int}} > Q_{\text{coup}}$) is over coupling and condition with $\gamma_{\text{int}} > \gamma_{\text{coup}}$ ($Q_{\text{int}} < Q_{\text{coup}}$) is under coupling.

The trend of the phase difference $\theta$ of the over-coupled ring-type cavity is different from that of an under-coupled ring-type cavity as shown in Fig. 2.6(a) and (b). This relation needs to be taken into account for considering the interference between multiple modes, such as coupled cavity systems.
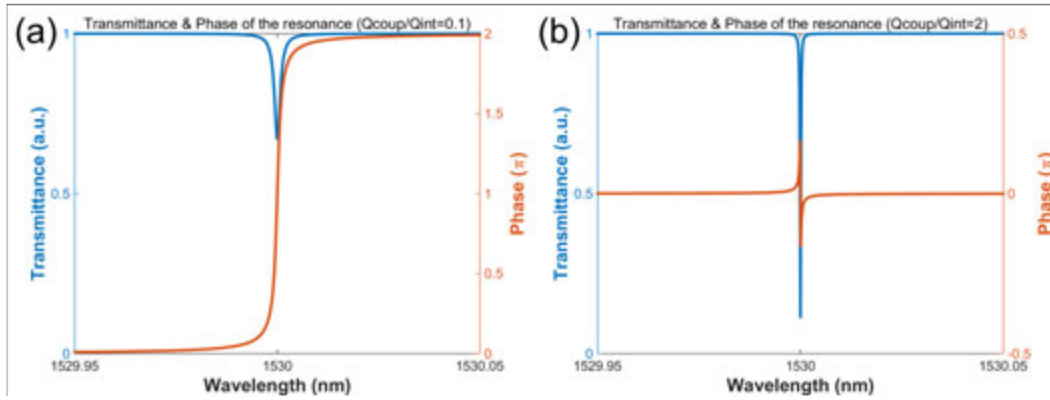


Fig. 2.6. (a) Transmission spectrum and relative phase of side coupled ring-type cavity in over-coupling regime ($Q_{\text{coup}} = 1 \times 10^5$ and $Q_{\text{int}} = 1 \times 10^6$). (b) Transmission spectrum and relative phase of side coupled ring-type cavity in under-coupling regime ($Q_{\text{coup}} = 2 \times 10^6$ and $Q_{\text{int}} = 1 \times 10^6$).

Figure 2.7(a) and (b) shows transmission spectrum and relative phase of FP-type cavity in direct and side coupled configurations (see Fig. 2.5 (b) and (c)). The condition of $\gamma_{\text{int}} < \gamma_{\text{coup}}$ ($Q_{\text{int}} > Q_{\text{coup}}$) is required to maximize/minimize the transmittance at a resonant wavelength for a direct/side coupled system, although it does not rise/drop to one/zero with either a finite intrinsic quality factor or a non-zero coupling quality factor as described by Eq. (2.75) and Eq. (2.76).

In order to compare a FP-type cavity and a ring-type cavity in side-coupled configurations, the transmittance dependence versus ratio of $Q_{\text{coup}}$ and $Q_{\text{int}}$ is summarized in Fig. 2.8. For both cases, the small transmittance corresponds high CE (i.e., CE $= 1 - Tr$). As mentioned, the transmittance of a ring-type cavity drops to 0 with the critical coupling condition of

$Q_{\text{int}}^{-1} = Q_{\text{coup}}^{-1}$, whereas that of a FP-type cavity is 0.25 with the critical coupling condition of $Q_{\text{int}}^{-1} = 2Q_{\text{coup}}^{-1}$ (Note that the critical coupling indicates the condition where the intrinsic cavity loss equals to the total coupling loss, and the total coupling loss is defined as $2Q_{\text{coup}}^{-1}$ for a FP-type cavity here). On the other hand, the transmittance of a FP-type cavity goes below 0.1 and approaches 0 with $Q_{\text{coup}}/Q_{\text{int}}$ less than 1.
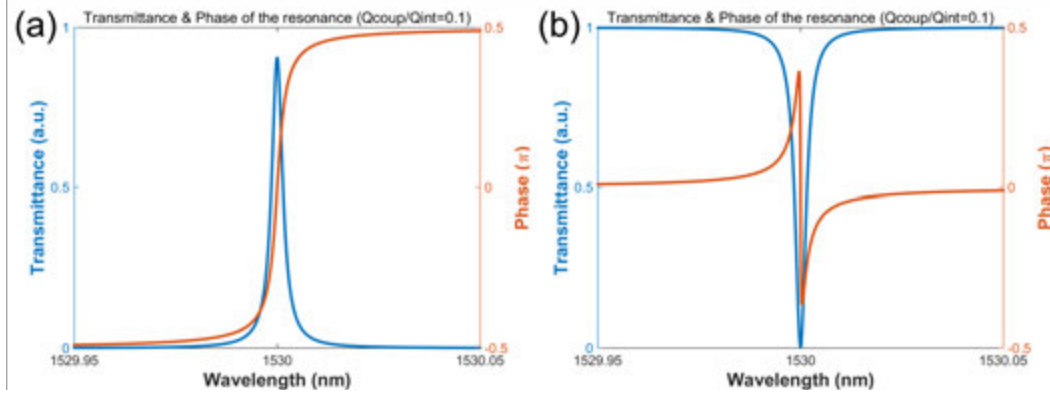


Fig. 2.7. (a) Transmission spectrum and phase of direct coupled FP-type cavity (b) Transmission spectrum and phase of side coupled FP-type cavity. ($Q_{\text{int}} = 1 \times 10^7$ and $Q_{\text{int}} = 1 \times 10^6$).

## 2.3 Nanofiber technology

### 2.3.1 Propagation modes in a nanofiber

A nanofiber is a thinned optical fiber which is used as an interface to couple light efficiently into other optical devices [112]. It is usually fabricated by heating and stretching a standard optical fiber. The radius at the thinnest point is usually less than 1 $\mu$m, thus it is called nanofiber (see Fig. 2.9). For the efficient coupling, satisfying the phase matching condition and obtaining large overlap between optical modes of a nanofiber and target optical devices are important since the coupling rate is determined by the following equations [184, 185].

$$\tilde{\kappa} = \int \kappa(z)e^{j\Delta\beta z}\mathrm{d}z, \tag{2.77}$$

$$\kappa(z) = \frac{1}{2}(n^2 - n_0^2)\frac{k_0^2}{\beta} \iint \boldsymbol{E}_1(x, y, z) \cdot \boldsymbol{E}_2(x, y, z)\mathrm{d}x\mathrm{d}y, \tag{2.78}$$

where $\Delta\beta$ and $\kappa$ indicate the phase mismatching and the mode overlap between two optical modes, respectively. In Eq. (2.77) and Eq. (2.78), $j$, $n$, $n_0$, $k_0$, $\beta$ and $\boldsymbol{E}$ are an imaginary number which satisfies $j^2 = -1$, a refractive index of core, a refractive index of clad, a wave number in air, a propagation constant and electric field, respectively.

Here, optical modes and their propagation constant in a nanofiber are analytically calculated as followed. The $z$-component of the electric and the magnetic fields in the nanofiber are [186, 187],

$$\left[\frac{\partial^2}{\partial r^2} + \frac{1}{r}\frac{\partial}{\partial r} + \frac{1}{r^2}\frac{\partial^2}{\partial \phi^2} + (k^2 - \beta^2)\right]\begin{bmatrix} E_{\text{z}} \\ H_{\text{z}} \end{bmatrix} = 0. \tag{2.79}$$
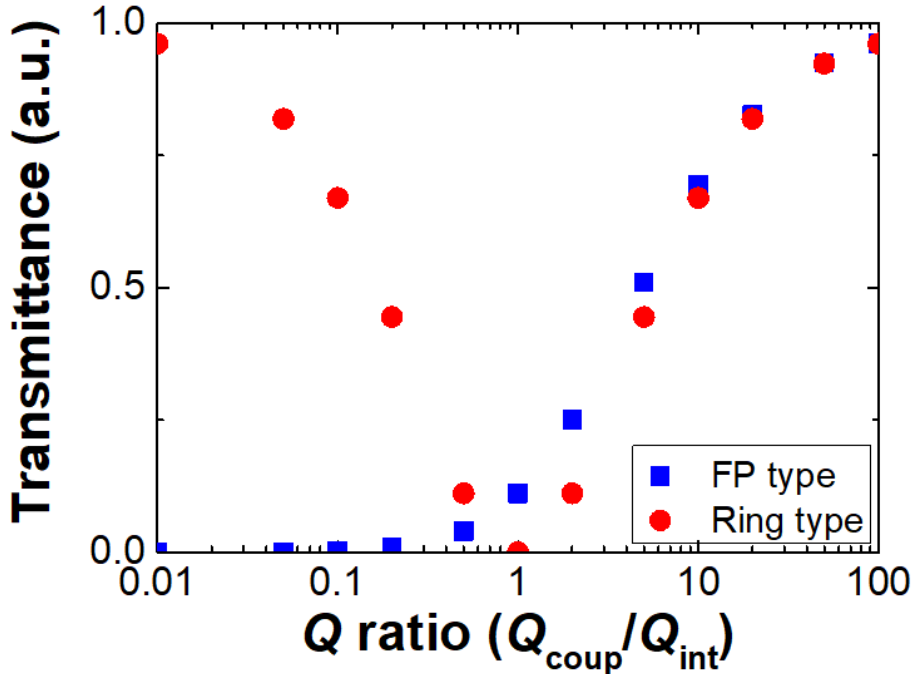
Fig. 2.8. Ratio of $Q_{\text{coup}}$ and $Q_{\text{int}}$ versus transmittance dependence at dip for side coupled FP-type and ring-type cavity.

where $r$, $\phi$, $z$ indicate radial, azimuth and axis direction in a cylindrical coordinate system. By applying a variable-separation method to Eq. (2.79), $E_z$ and $H_z$ are deformed as followed,

$$\begin{bmatrix} E_z \\ H_z \end{bmatrix} = \Psi(r)\exp(\pm jl\phi). \tag{2.80}$$

Then, by substituting Eq. (2.80) into Eq. (2.79), the Bessel differential equation is given as

$$\frac{\partial^2\Psi}{\partial r^2} + \frac{1}{r}\frac{\partial\Psi}{\partial r} + \left(k^2 - \beta^2 - \frac{l^2}{r^2}\right)\Psi = 0. \tag{2.81}$$

The solution for Eq. (2.81) depends on the sign of $h^2 = k^2 - \beta^2$. Note that the condition $n_{\text{core}}k_0 > \beta > n_{\text{clad}}k_0$ must be satisfied to obtain propagation modes. If the radius of the
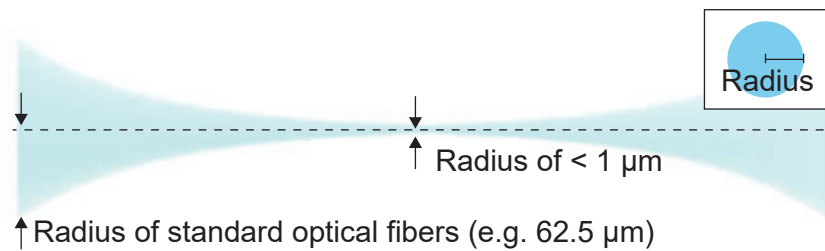


Fig. 2.9. Schematic of a tapered nanofiber. The shape of its cross section is circle (ideally) as shown in the inset.

45

nanofiber of $r_{\text{taper}}$ is smaller than $r$ ($r > r_{\text{taper}}$), $h^2$ takes a negative value. In this situation, the solution of Eq. (2.81) is a linear combination of the $l$-th modified Bessel function of the first kind $I_l(qr)$ and the $l$-th modified Bessel function of the second kind $K_l(qr)$ where $q^2 = -h^2$ is employed. With the condition $\Psi(r = \infty) = 0$, the electric and magnetic fields in the clad become as followed,

$$E_z = A_{0,\text{clad}} K_l(qr) \exp\left[j(\omega t + l\phi - \beta z)\right], \tag{2.82}$$

$$H_z = B_{0,\text{clad}} K_l(qr) \exp\left[j(\omega t + l\phi - \beta z)\right]. \tag{2.83}$$

On the other hand, when $h^2 > 0$, the solution of Eq. (2.81) is a linear combination of the $l$-th Bessel function of the first kind $J_l(hr)$ and the $l$-th Bessel function of the second kind $Y_l(hr)$. Since $Y_l(hr)$ diverse at $r = 0$, the z-component of the electric and magnetic fields in the core are given as

$$E_z = A_{0,\text{core}} J_l(hr) \exp\left[j(\omega t + l\phi - \beta z)\right], \tag{2.84}$$

$$H_z = B_{0,\text{core}} J_l(hr) \exp\left[j(\omega t + l\phi - \beta z)\right]. \tag{2.85}$$

Other components are calculated directly from $E_z$ and $H_z$, as

$r < r_{\text{taper}}$ :

$$\begin{pmatrix} E_r \\ E_\phi \\ H_r \\ H_\phi \end{pmatrix} = \frac{-j\beta}{h^2} \begin{bmatrix} A_{0,\text{core}} h J_l'(hr) + \dfrac{j\omega\mu l}{\beta r} B_{0,\text{core}} J_l(hr) \\[2mm] \dfrac{jl}{r} A_{0,\text{core}} J_l(hr) - \dfrac{\omega\mu}{\beta} B_{0,\text{core}} h J_l'(hr) \\[2mm] B_{0,\text{core}} h J_l'(hr) - \dfrac{j\omega\varepsilon_1 l}{\beta r} A_{0,\text{core}} J_l(hr) \\[2mm] \dfrac{jl}{r} B_{0,\text{core}} J_l(hr) + \dfrac{\omega\varepsilon_1}{\beta} A_{0,\text{core}} h J_l'(hr) \end{bmatrix} e^{j(\omega t + l\phi - \beta z)}, \tag{2.86}$$

$r > r_{\text{taper}}$ :

$$\begin{pmatrix} E_r \\ E_\phi \\ H_r \\ H_\phi \end{pmatrix} = \frac{j\beta}{q^2} \begin{bmatrix} A_{0,\text{clad}} q J_l'(qr) + \dfrac{j\omega\mu l}{\beta r} B_{0,\text{clad}} J_l(qr) \\[2mm] \dfrac{jl}{r} A_{0,\text{clad}} J_l(qr) - \dfrac{\omega\mu}{\beta} B_{0,\text{clad}} q J_l'(qr) \\[2mm] B_{0,\text{clad}} q J_l'(qr) - \dfrac{j\omega\varepsilon_1 l}{\beta r} A_{0,\text{clad}} J_l(qr) \\[2mm] \dfrac{jl}{r} B_{0,\text{clad}} J_l(qr) + \dfrac{\omega\varepsilon_1}{\beta} A_{0,\text{clad}} q J_l'(qr) \end{bmatrix} e^{j(\omega t + l\phi - \beta z)}. \tag{2.87}$$

The value of $\beta$ is necessary to draw the mode profile of propagation modes. It is obtained from the following characteristic equation derived from the boundary condition of the electric and magnetic fields at $r = r_{\text{taper}}$ (i.e., field components parallel to the surface are continuous at the boundary),

$$\left(\frac{J_l'(ha)}{ha J_l(ha)} + \frac{K_l'(qa)}{qa K_l(qa)}\right)\left(\frac{n_1^2 J_l'(ha)}{ha J_l(ha)} + \frac{n_1^2 K_l'(qa)}{qa K_l(qa)}\right) = l^2 \left[\left(\frac{1}{qa}\right)^2 + \left(\frac{1}{ha}\right)^2\right]^2 \left(\frac{\beta}{k_0}\right)^2. \tag{2.88}$$

Then, the relationship between the effective refractive index and the radius of the nanofiber is calculated for the light with the wavelength of 1.55 $\mu$m in Fig. 2.10(a). There are four types of propagation modes ($HE_{l,m}$, $TE_{l,m}$, $TM_{l,m}$, and $EH_{l,m}$). The integer $l$ and $m$ indicate the number of peaks along azimuth and radial directions, respectively. The modes of $HE_{l,m}$ and $EH_{l,m}$ are basically hybrid modes which hold all six components of the electric and the magnetic fields. However, $HE_{1,1}$ mode corresponds the lowest order linearly polarized mode of $LP_{0,1}$, which holds one-directional linearly polarized light in the fiber cross section. Higher order linearly polarized modes are obtained with the degeneration of HE and EH modes.

The cutoffs of the propagation modes except $HE_{1,1}$ ($LP_{0,1}$) are observed at the nanofiber radius larger than 600 nm. In other words, only the $HE_{1,1}$ mode will exist in a nanofiber with a radius less than 600 nm (the diameter of $D = 2.405\lambda/\pi\sqrt{n^2 - 1}$ is the cutoff for the light with wavelength of $\lambda$ in general [187, 188]). Finally, The mode profile of electric field of $HE_{1,1}$ mode is simulated in Fig. 2.10(b). It has a single peak at the center of the nanofiber. The propagation constant $\beta$ can be determined with $n_{\text{eff}}$ from the equation of $\beta = n_{\text{eff}}k_0$.
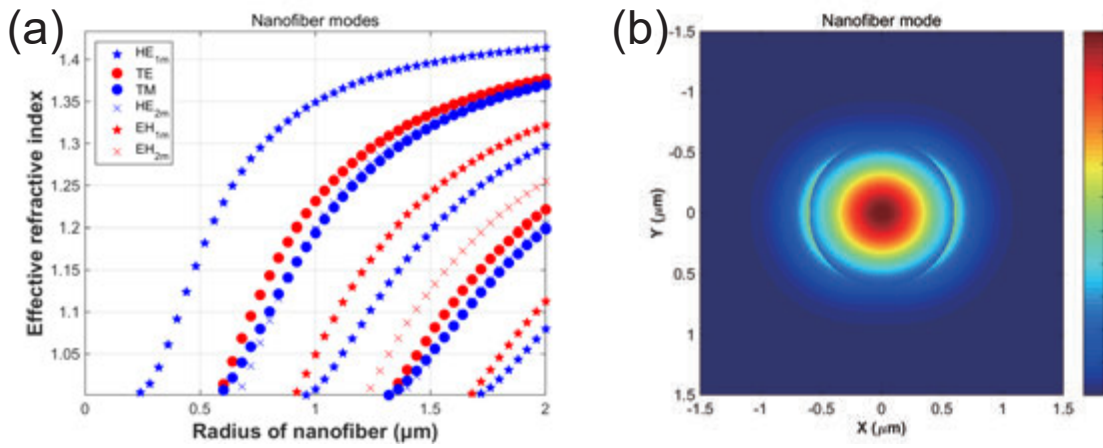


Fig. 2.10. (a) The effective refractive index dependence versus the nanofiber radius. (b) Mode profile of intensity of the electric field in the nanofiber with a radius of 600 nm.

### 2.3.2 Fabrication techniques of nanofibers

As mentioned, a tapered nanofiber is usually fabricated by heating and stretching a standard optical fiber and used for the optical coupling. It exhibits extremely small insertion loss owing to adiabatic transition of mode profile of the guided mode if fabricated properly. Surprisingly, ultra high transmittance of 99.7% at a wavelength of 852 nm was reported in [189].

Here, its fabrication procedure is described as followed. First, a commercial single mode optical fiber is cut off to be about 1 m and its coating is stripped at around the center for 2 cm with a fiber stripper. The stripped region is carefully cleaned with ethanol since residual coating is a cause of excessive loss and fabrication error. Next, the cut fiber is fixed to a homemade zig attached to the nanofiber fabrication system (see Fig. 2.11(a)). Then, mixed gas of $C_3H_8$ and $O_2$ was sent to torch and lighted. After the stabilization of the fire, heating of the fiber starts.

The heating process is operated by swinging a torch along the central axis of the fiber. The stretching process starts a few seconds after the heating starts. During the stretching process, transmittance of the fiber is monitored (see Fig. 2.11(b)). The fiber experiences roughly three transition stages; Stage 1: initial single mode, Stage 2: multimode and Stage 3: single mode owing to a sufficiently small radius. We can clearly observe each stage in the change in the transmittance because it fluctuates widely when the fiber is in multimode stage due to the interference of guided modes. The fabrication process is stopped manually several seconds after entering the third stage. Necessary time for the third stage is different depending on the required diameter of nanofibers.
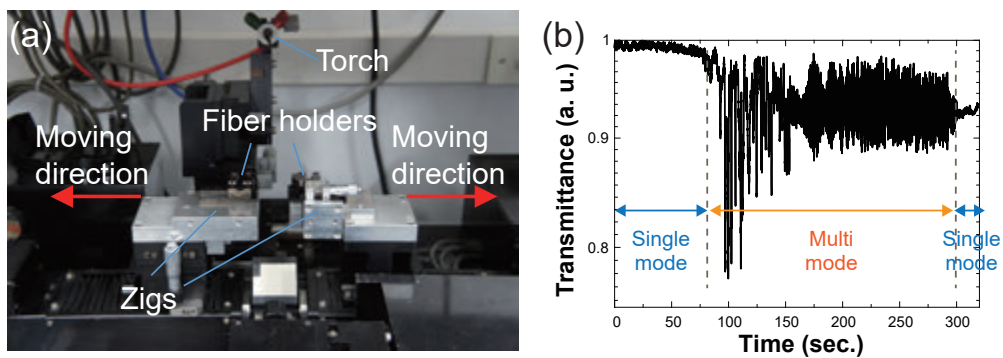


Fig. 2.11. (a) Tapered fiber fabrication system. (b) Typical transmittance during fiber tapered process.

The fabricated nanofiber can be used for the optical coupling with optical cavities out of chips (e.g., bottle-type resonators). However, a mechanical interference between a nanofiber and a substrate usually occur at the edge of the substrate when an optical coupling is performed for a cavity integrated on a chip (see Fig. 2.12). This is due to the fact that the diameter of the nanofiber is thicker at the edge of the substrate than that at the cavity. A dimpled tapered naanofiber, which is locally bent nanofiber proposed in [116], is effective way to access the cavity at arbitrary place on a substrate (see Fig. 2.12).

It is fabricated with post-process of fabrication of a tapered nanofiber as shown in Fig. 2.13. After fabricating a nanofiber, a mold fiber is brought into contact with it. The mold is coated with graphite, which is a key process to avoid tight sticking between the nanofiber and the mold after followed heating process. Then, the mold was moved downward by several hundred micro meters from the contact position to make nanofiber dimpled (the tension of the nanofiber is slightly loosen before the process). Then, the contact point is heated with a lighter. This process fixes the shape of the nanofiber. Next, the mold was removed carefully not to break the nanofiber. The coated graphite plays a role to raise the success rate of this process since the mold is easily detached from the nanofiber if the graphite is located between the nanofiber and the mold (the fusion of the two glass structures is the main cause of the failure). Note that removing all graphite through the burning process is not always easy and it results in an increase of insertion loss of the nanofiber. Removal of the residual graphite by sweepng with another clean optical fiber is effective to reduce the loss. Finally, the tension of the nanofiber is adjusted and dimpled shape is formed.
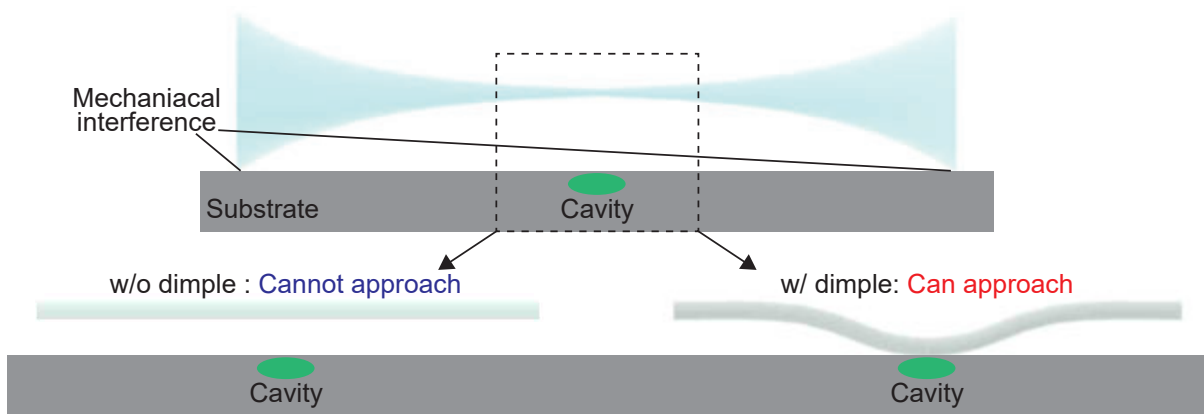
Fig. 2.12. Schematic diagram of the optical coupling between a nanofiber and an integrated optical cavity. Mechanical interference will occur at the edge of the substrate when a nanofiber without dimple is employed.

## 2.4 Summary

In this chapter, the important basic materials for the study are presented. The principal of the PBG and the formation of PhC nanocavities are explained. Then, the theories of PWE, FDTD method, and CMT are introduced. Finally, the analytical calculation of the propagation modes of a nanofiber and its experimental fabrication are described.

**1. Fabricate a nanofiber**

Nanofiber

**2. Prepare a mold**

Mold fiber

**3. Bring the mold into contact with the nanofiber**

**4. Heat up the contact point with a lighter**

**5. Remove the mold**
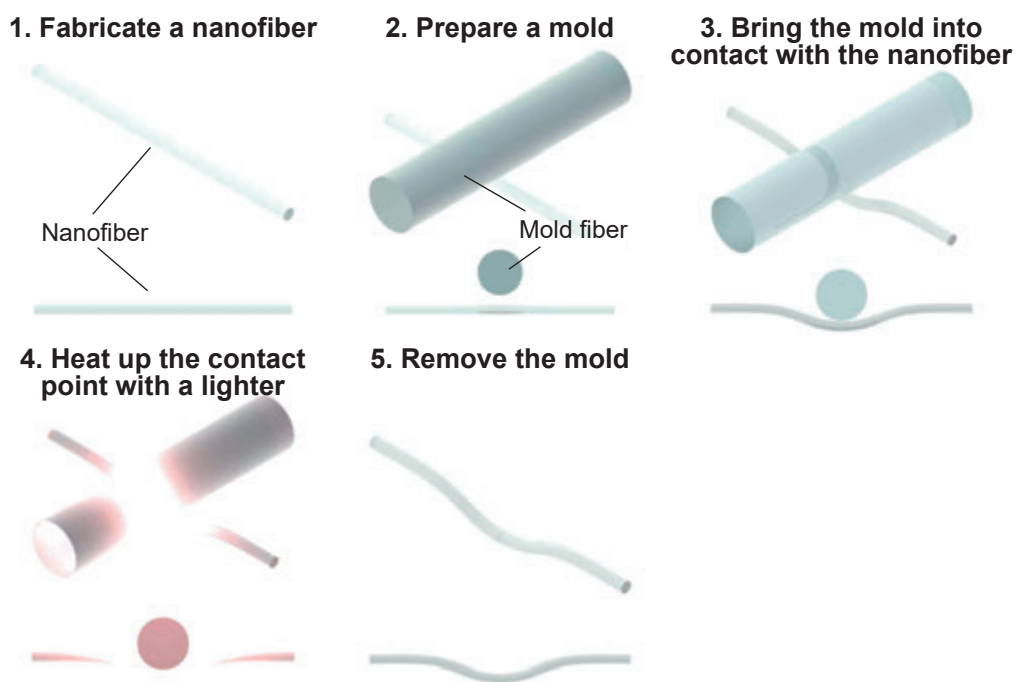
Fig. 2.13. Fabrication procedure of a dimpled nanofiber. Top and bottom figures are structures observed from different points.

# Chapter 3

# Fiber-coupled photonic crystal (PhC) cavity

Because PhC nanocavities are sensitive to changes in their surrounding environment, they have been employed for optical sensing [190–192]. However, this means that their resonances are affected by disorder in their structures. Thus, resonant wavelength post-tuning methods have been studied to compensate for fabrication errors. There have been some demonstrations of such methods, including the oxidation of silicon using atomic force microscopy [193] and index modulation using droplets [194]. Fiber-coupled PhC cavities (FCPCs), which were initially proposed and demonstrated by Yong-Hee Lee's group at KAIST [195,196], are one of the most promising approaches. These cavities are formed at arbitrary positions on the PhC platform by introducing defects with an effective index modulation caused by a nanofiber. Therefore, the cavities allows for controllability of the resonant wavelength and position selectivity. In addition, this technique is superior to using other reconfigurable cavities in terms of CE with an optical fiber. The expected CE was considerably high (over 90%), and the theoretical $Q$ factor was high as well. However, both a high CE and high $Q$ have not been achieved experimentally mainly because of the absorption loss of quantum dots in InGaAsP/InP PhCs.

In this chapter, a FCPC based on a silicon PhC waveguide is explored to demonstrate resonant modes with high $Q$ and high CE. Because the material absorption of our silicon layer is small compared to the expected quality factor of the cavity, which is of the order of $10^5$, the possible $Q$ and CE values of the FCPC were measured experimentally. Fine tuning of the resonant wavelength was also performed.

## 3.1 Principal and numerical analysis

First, the principle of cavity formation for an FCPC is described. Figure 3.1(a) shows the photonic band diagram of the guided mode of a PhC waveguide. When a nanofiber is brought into contact with a PhC waveguide from the top of the slab, the effective refractive index of the waveguide increases, which results in a down shift of the cutoff frequency of its guided mode. Thus, a mode gap is formed at the contact region. This principle is effectively the same as that of width-modulated PhC nanocavities [61,63]. To confirm the formation of the cavity, the mode profile of the cavity was calculated using the 3D FDTD method. A dimpled

nanofiber was modeled with a curvature radius of 125 $\mu$m and a diameter of 1000 nm. When the fiber was brought into contact with a W0.98 PhC waveguide (a waveguide with a width of $w = 0.98\sqrt{3}a$), a mode profile as the one shown in Fig. 3.1 (b) was obtained. The $Q$ value was $1.4 \times 10^7$ and the mode volume was $1.9(\lambda/n)^3$.
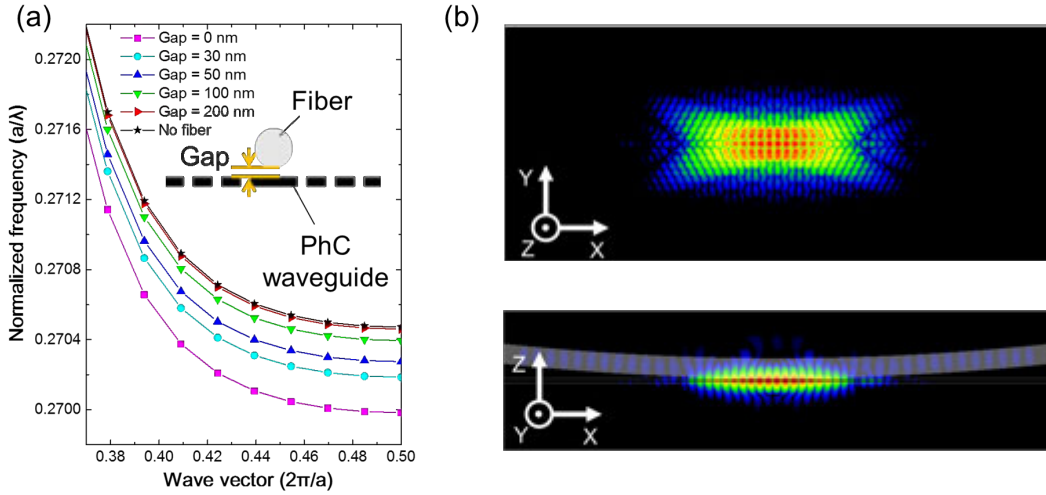


Fig. 3.1. (a) Photonic band diagram of the guided mode of a photonic crystal waveguide. Lattice constant $a = 420$ nm, waveguide width $w = 0.98\sqrt{3}a$ (W0.98), hole radius $r = 0.30a$, slab thickness $t = 0.50a$ and refractive index of silicon $n_{Si} = 3.47$. The diameter of the silica fiber was 500 nm ($n_{SiO_2} = 1.45$) (b) Mode profile of the Ey component of the FCPC mode. The upper and lower figures are views from the top and the side, respectively. The positions of the nanofiber and the PhC are overlaid in bottom figure.

## 3.2 Experimental characterization of a FCPC

### 3.2.1 Sample and method

In this section, the details of the samples and experimental methods used are presented. PhC waveguides were fabricated using photolithography with a KrF excimer laser at a silicon photonics foundry in Singapore (IME, Singapore) [71]. Because the original structure was covered with silica, it was removed by wet etching with a 20% HF solution. Schematic illustration of the overview of the PhC waveguides are shown in Fig. 3.2(a). The length of the PhC waveguides were 100 $\mu$m. Although silicon waveguides were connected to the PhC waveguides at the initial state, they were made drooping or broken and flown away during the etching. SEM images of the structures are shown in Figs. 3.2(b) and (c). In Fig. 3.2(b), the design parameters of the PhC are indicated. All the PhCs used in these experiments were formed in a silicon slab with a thickness of 210 nm by arranging air holes in a triangular grid with a lattice constant of 420 nm. The width of the waveguides and the diameter of the air holes were variable. As shown in Fig. 3.2(c), the surface of the structure was not perfectly smooth due to contaminations introduced before and after wet etching. It was confirmed that the original surface was smooth by observing the surfaces of other samples which were procured by the post-processes performed more carefully.
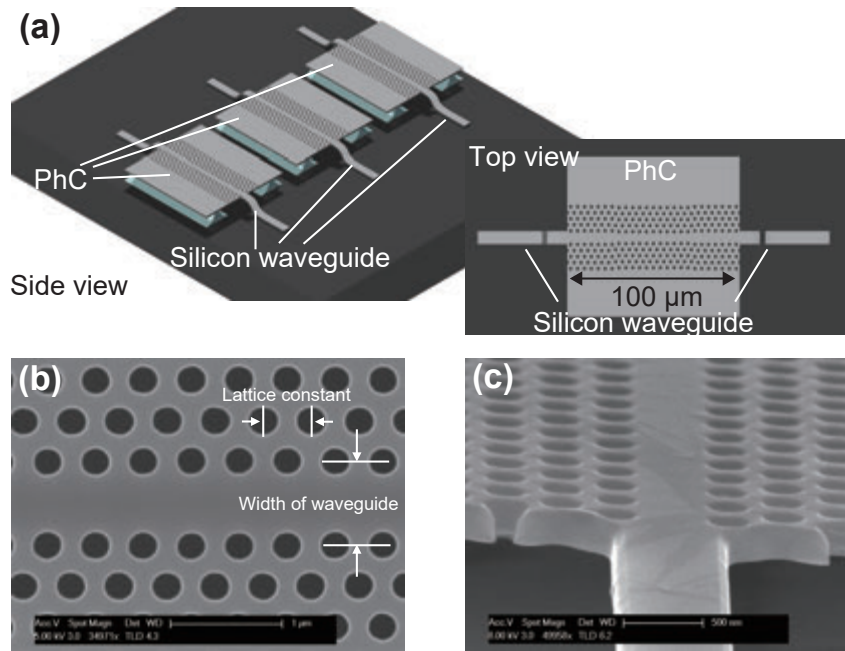
Fig. 3.2. (a) Schematic illustration of the overview of the PhC waveguides. Silicon waveguides connected to the PhC waveguides were not available. SEM images of the PhC structures after HF etching taken from (b) the top and (c) the side of the structure.

The diameters of the holes of the PhC were measured with an SEM with a magnification of 250,000, with an image resolution of 1.17 nm per pixel. The diameters of 15 to 25 holes were obtained by fitting circles using the built-in function NI-IMAQ in LabVIEW 2016 (fitting results are shown in Fig. 3.3(b)) and their average was taken as the measured value. The measured values for the diameter of various holes that were specifically designed in the PhC are summarized in Fig. 3.3(a). As shown in the figure, the actual diameters of the holes for this sample were much larger than in the original design. However, this trend is different for other samples on different chips, even for those that were fabricated at the same time. Thus, the diameters of the holes on each sample were evaluated individually and each measured value is displayed hereafter.

The experimental setup is shown in Fig. 3.4(a). A dimpled tapered nanofiber was fabricated with the method described in Chapter 2.3.2 and brought into contact with the PhC waveguide. Microscope images taken from the side and the top are shown in Figs. 3.4(b) and (c). The transmission spectrum was recorded by sweeping the input wavelength using a tunable laser diode (TLD; Santec TSL-710) and the corrected transmittance was measured with a power meter (PM; Keysight Technologies 8163B Lightwave Multimeter). The power and polarization of the input light were controlled using a polarization controller (PC; Alnair Labs MLC series) and a variable optical attenuator (VOA; OZ Optics DA-100-3A), respectively. The position of the sample was controlled with XY and Z stages (Sigma Tech. FS-1020PX and FS-1010PZ).
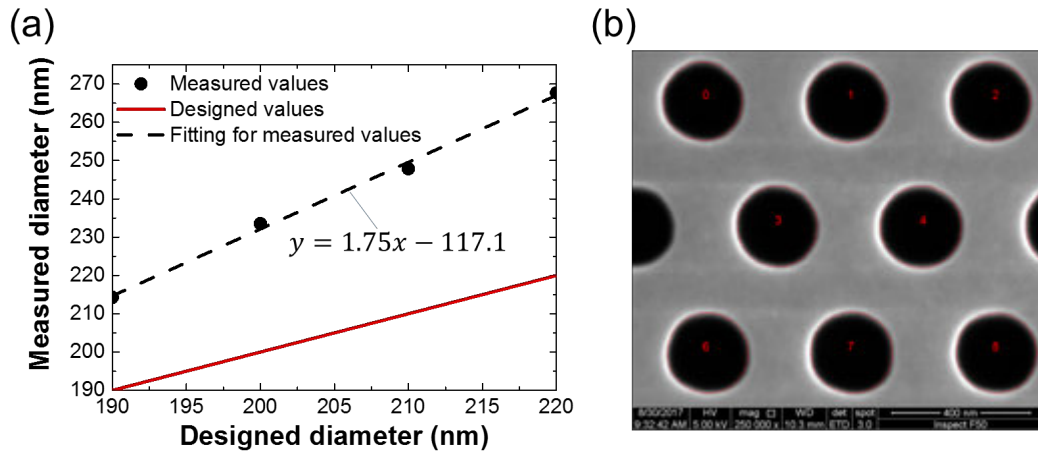
Fig. 3.3. (a) Summary of the measurement of the diameters of holes on the PhC. Linear fitting of the measured plots is displayed with a dashed line. (b) Image of the fitted holes generated using LabVIEW. Red circles show the fitting results.
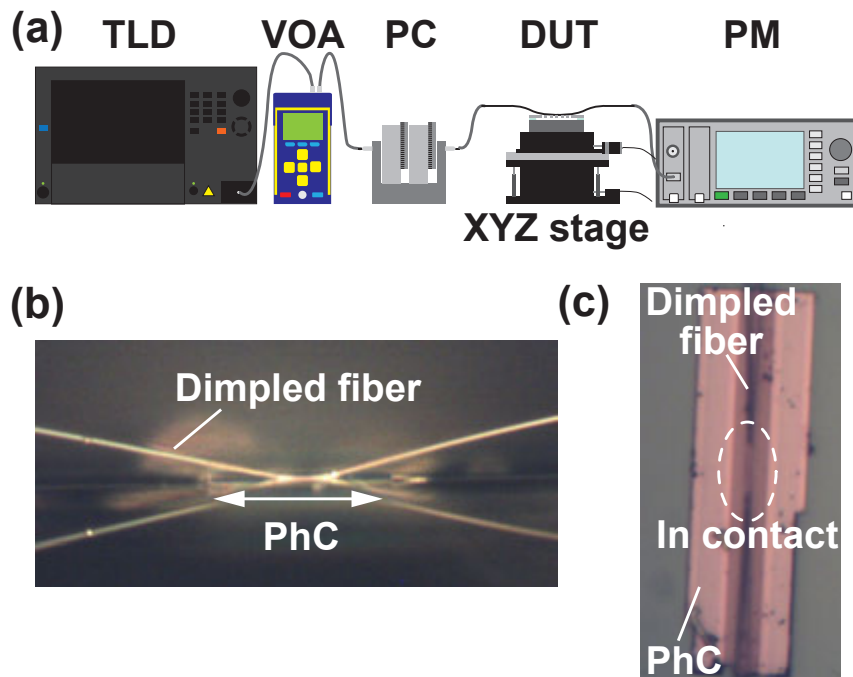


Fig. 3.4. (a) Schematic of the experimental setup. TLD: Tunable laser diode. VOA: Variable optical attenuator. PC: Polarization controller. DUT: Device under test. PM: Power monitor. (b) Microscope image of the side view of the FCPC. (c) Microscope image of the top view of the FCPC. White dotted line shows the contact region.

### 3.2.2 Characteristics of the obtained resonant mode

The characteristics of the obtained resonance are presented in this section. The measured transmission spectrum for the PhC waveguide with a width of $0.98 \times \sqrt{3}a$ (W0.98) and a hole

diameter of 248 nm is shown in Fig. 3.5(a). Although some resonant peaks were observed in the spectrum, one of the dips is characterized in this section (the origin of the multiple modes is discussed in Appendix C). Figure 3.5(b) shows the Lorentzian fitting to a dip with a high $Q_{\text{load}}$ of $5.1 \times 10^5$ ($Q_{\text{int}} = 9.2 \times 10^5$, $Q_{\text{coup}} = 1.2 \times 10^6$). This value is as high as that of a width-modulated cavity fabricated through the same process [71], which means that the $Q$ was limited by the fabrication imperfection. In addition, a high CE of 31% was obtained, which can be expressed as followed.

$$\text{CE} = 1 - Tr, \tag{3.1}$$

where $Tr$ is the transmittance at a resonant dip.

The localization of the cavity mode was confirmed by observing IR images (using Goodrich SU320KTS-1.7RT) and the bi-stable behavior of the resonance caused by the thermo-optic (TO) effect. Figure 3.6(a) shows IR images of the FCPC mode. The bright spot was observed at the contact point of the nanofiber only when the input wavelength was on-resonance. This is proof that the mode was localized in the waveguide. Figure 3.6(b) shows the results of the investigation of the TO effect. As the input power increased, the resonance shifted toward longer wavelengths and showed an inverse triangular shape at a certain point. This is evidence for TO bi-stability, which indicates that light is confined in a tiny space.

Finally, the controllability of the resonant wavelength was examined. Figure 3.7(a) shows the experimental method used. The stage was moved downward by 100 nm from the initial contact position, while the position of the nanofiber was fixed. The contact state of the PhC and the nanofiber was maintained due to electric static force, but because the contact length decreased along with the displacement of the stage, a shift in the resonant wavelength was observed (Figure 3.7(b)). This is due to a decrease in the impact of the effective index modulation caused by the nanofiber. The tuning resolution was 27 pm for a 100-nm displacement of the stage, which result in the tunability of 0.27 pm for a 1 nm displacement of the stage. Note that the resolution of the stage is 10 nm and the amount of the shift is different from each mode. The maximum tunable range will be 2.7 nm since the nanofiber is usually detached from the PhC waveguide with the displacement of 100 $\mu$m, where the range is smaller than the amount of longer shift of cutoff wavelength of about 3 nm caused by the effective index modulation.
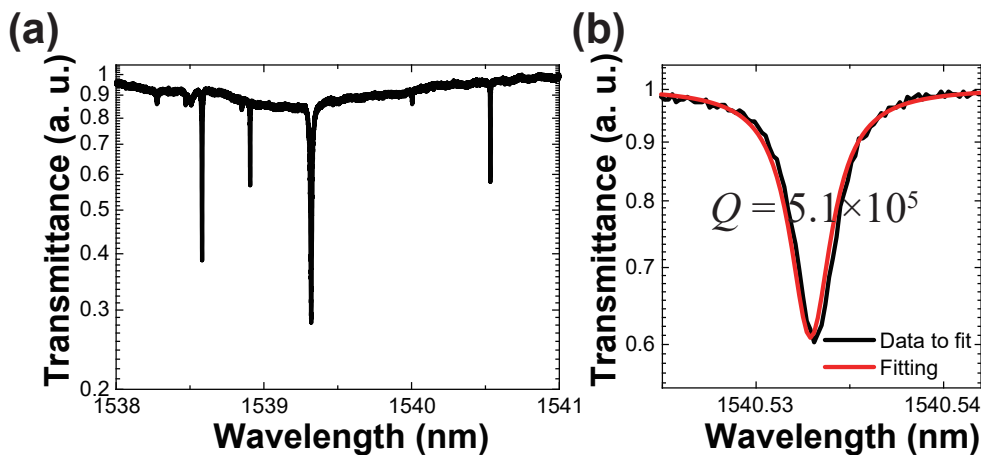


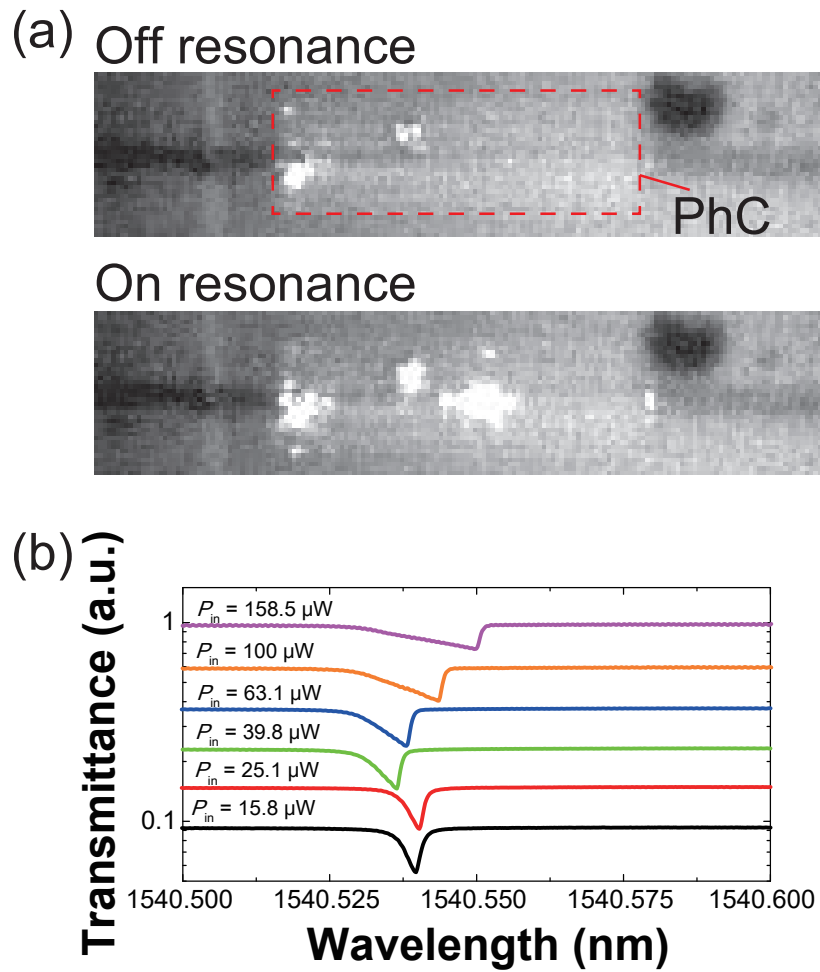Fig. 3.5. (a) Transmission spectrum of the FCPC. (b) Lorentzian fitting of a dip.

Fig. 3.6. (a) IR image of an FCPC resonance. Input was off-resonance in the top picture and on-resonance in the bottom picture. (b) Bi-stability caused by the TO effect. The shorter shift of resonant wavelength will be due to either the fluctuation of the contact length of the nanofiber or the Carrier plasma effect.
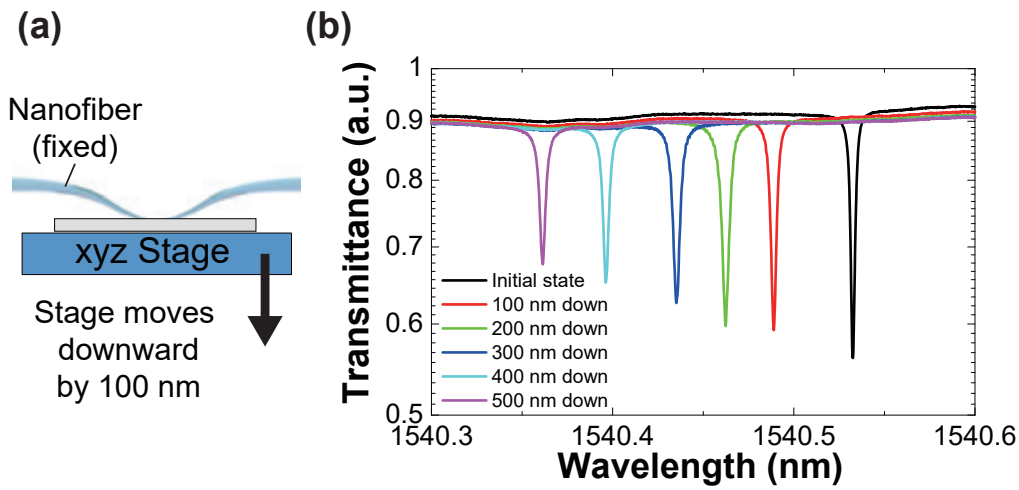
Fig. 3.7. (a) Schematic of the experimental method for resonant wavelength tuning. (b) Resonant wavelength tuning of a resonant mode of the FCPC.

### 3.2.3 Analysis of the optimum coupling condition

Analyzing the coupling conditions is necessary to achieve both efficient coupling and the tuning of loaded $Q$. The CE depends on the phase-matching condition and the mode overlap between a cavity and a nanofiber; both can be controlled by changing the diameter of nanofibers (see Chapter 2.3.1).

To address this issue, a measurement using a straight nanofiber (not a dimpled one) was demonstrated. Since the diameters of nanofibers are different depending on the position of contact, the dependence of CE and wavelength on diameter can easily be measured with a single nanofiber if it is not dimpled. Note that the straight nanofiber does not form cavities since they modulate the guided mode of the waveguide uniformly. One issue that needs to be solved for this measurement is removing the physical barrier at the edges of substrate. A nanofiber cannot get close to a PhC waveguide without a dimple, because the substrate will interfere with the nanofiber at its edges, where the diameter of the nanofiber is thick (see Fig. 2.12 which illustrates the situation). To carry out the experiment, the silicon substrate layer of the sample used for the measurement shown in Fig. 3.5 was partially etched using the method shown in Fig. 3.8(a). Resist with high viscosity was applied only on the PhC waveguides using a writing brush by hand. Then, the PhC waveguide was protected from being attacked by the $XeF_2$ gas during the etching process whereas the silicon substrate was etched (see Fig. 3.8(b)). The etching process increased the height difference between the surface of the PhC waveguides and the edges of the substrate, which enabled the nanofiber to be brought into contact with the PhC waveguide Fig. 3.9(a).

The bandwidth and the maximum and minimum cutoff wavelengths of coupled light were evaluated for various diameters of nanofiber using the definition shown in Fig. 3.9 (b). The diameter of the nanofibers was roughly estimated by extracting pixel values of grayscale microscope images (Fig. 3.10 (a)). The position dependence on the diameter of the nanofiber is shown in Fig. 3.10(b).
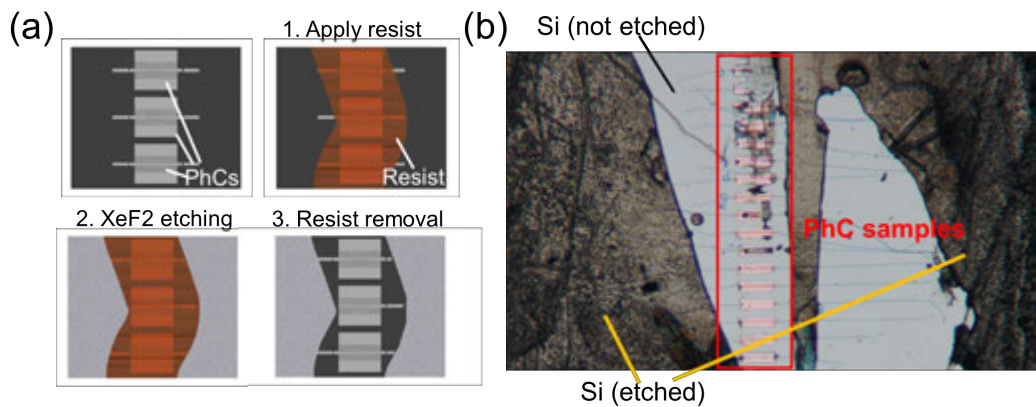
Fig. 3.8. (a) Fabrication procedure of a partially etched sample. (b) Microscope image of the fabricated sample.
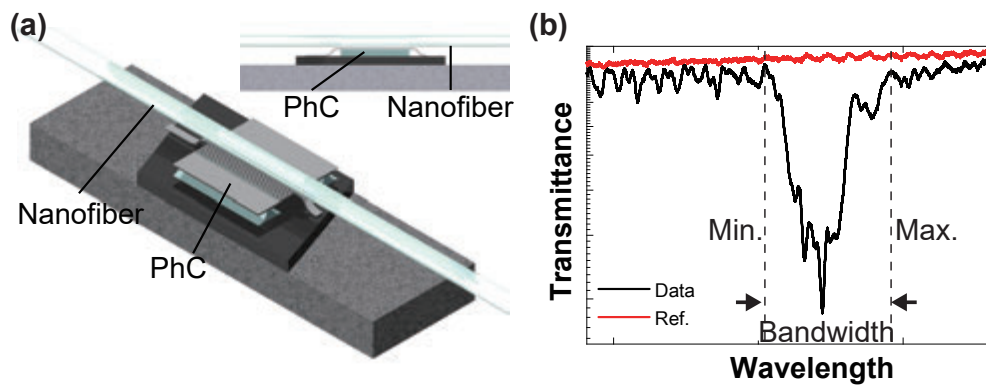


Fig. 3.9. (a) Schematic of the experimental method. (b) Definition of the measured minimum and maximum wavelengths of coupled light. Bandwidth was calculated from the difference of the values.
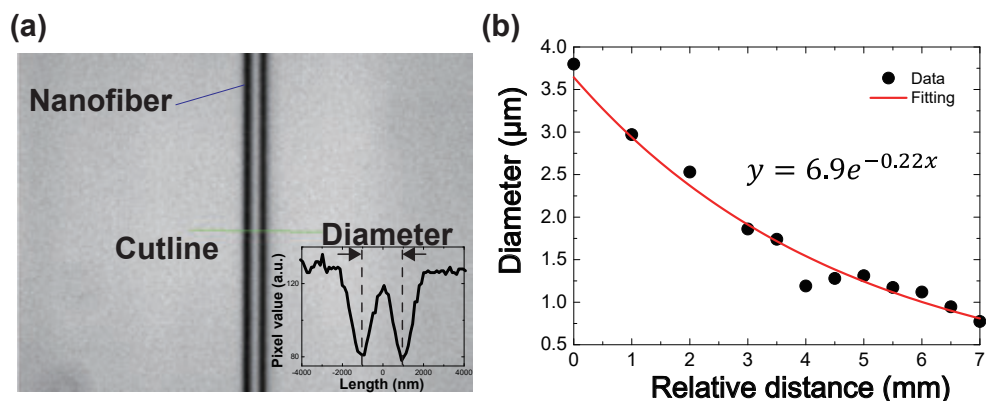


Fig. 3.10. (a) Microscope image of a nanofiber. The inset shows the extracted pixel values along a green cut line. The resolution of the image is 108 nm/pixel. (b) Summary of the diameter measurements.

Examples of the results are displayed in Fig. 3.11(a) and (b). In Fig. 3.11(a), the nanofiber

with the thinner diameter is coupled with the guided mode with a shorter wavelength. Figure 3.11(b), on the other hand, shows the PhC design versus the transmission spectrum. The PhC waveguide with a larger hole diameter had the coupling band at a shorter wavelength. Both results showed a clear dependence of the coupled wavelength on diameter and design. A summary of the results is shown in Fig. 3.12. Figures 3.12(a) and (b) present the minimum and the maximum coupled wavelengths for various diameters of nanofibers. As the diameter increases, the minimum coupled wavelength increases, and though the maximum frequency shows the same tendency, it gets saturated at the cutoff wavelength of the waveguide. Figure 3.12(c) shows the bandwidth versus the nanofiber diameters. The bandwidth became smaller as the diameter of nanofiber increased due to the saturation of the maximum coupled wavelength. The maximum bandwidth was about 30 nm.

The strong dependence of the coupled wavelength on the nanofiber diameter is related to the phase-matching condition between a fiber mode and a PhC guide mode [117]. Figure 3.13(a) shows a photonic band diagram of the guided modes of a PhC waveguide and nanofibers. As shown in the graph, the nanofibers with larger diameters shows a larger bending of the bands, which results in phase matching with a PhC guided mode at lower frequencies (longer wavelength). This is in good agreement with the experimental results as shown in Fig. 3.13(b). The trend of the shift of measured minimum coupled wavelength matched that of the phase matching points in Fig. 3.13(a) where small difference could be due to the inaccuracy in the measurement of the nanofiber diameters and air hole diameters of PhCs. Since the resonant wavelengths of the FCPC are close to the cutoff wavelengths of the PhC waveguides, the nanofiber diameters with saturated maximum cutoff wavelengths can be good indicators of the optimum diameters for efficient coupling to the cavities. For example, the nanofiber with a diameter of > 1200 nm will couple to the cavities on the PhC waveguide with diameters of 214 nm (indicated by black dots in Fig. 3.12(b)). Note that the nanofibers will be in multi-mode operation for diameters larger than 1200 nm (see Chapter 2.3.1), and this may also be the reason for the decrease in CE observed in Figure 3.11(a) in addition to the decrease in mode overlap due to the small evanescent field.
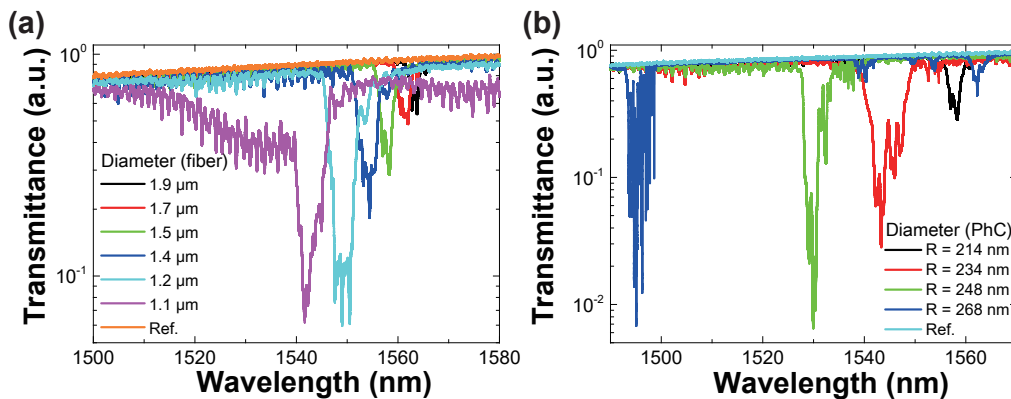


Fig. 3.11. (a) Transmission spectrum of a PhC waveguide with a width of $0.98 \times \sqrt{3}a$ and a diameter of 203 nm. Lines with different colors correspond to results measured with nanofibers with different diameters. (b) Transmission spectrum of a PhC waveguide measured with a nanofiber with a diameter of 1.7 $\mu$m. Lines with different colors correspond to results for PhC waveguides with a width of $0.98 \times \sqrt{3}a$ but different diameters.

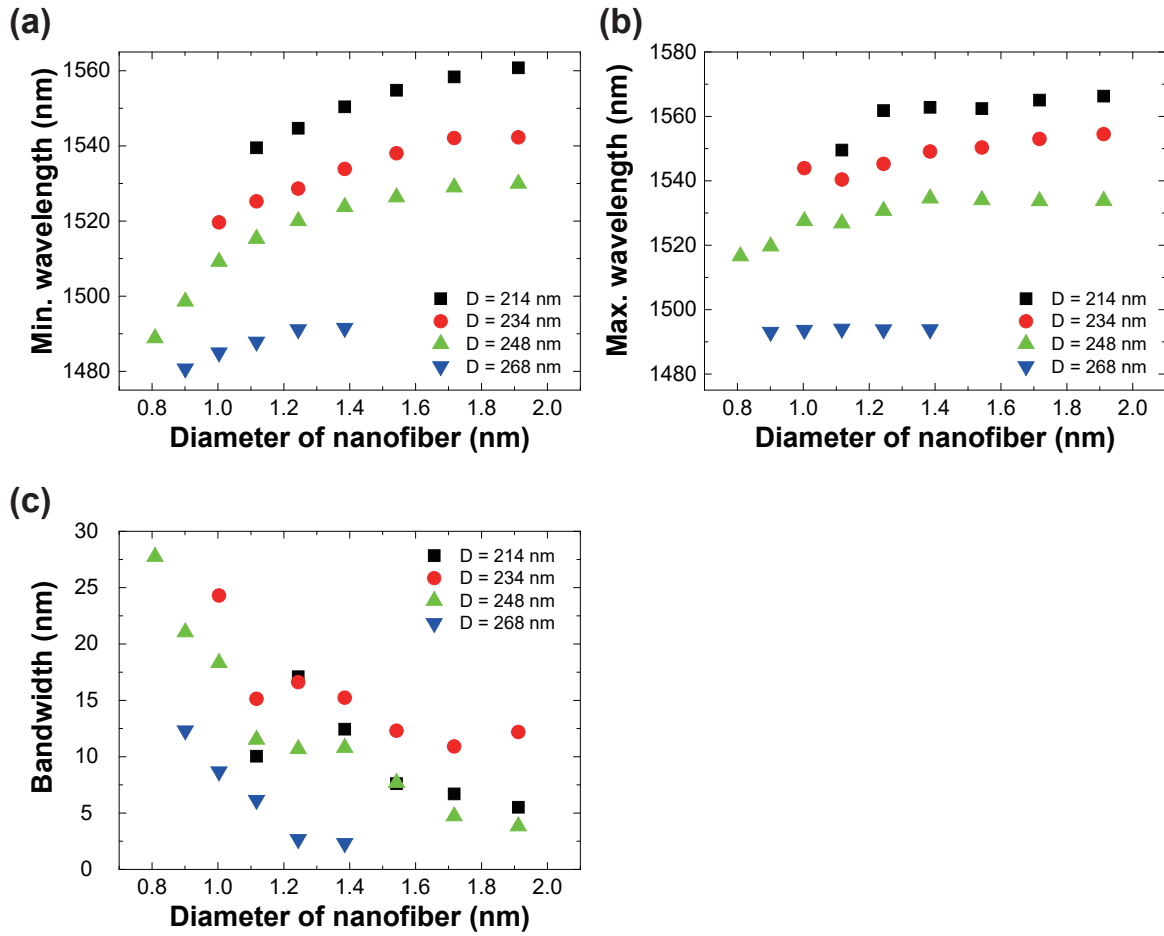**(a)**



**(b)**



**(c)**



Fig. 3.12. Summary of the coupling analysis. (a) Fiber diameter vs. minimum coupled wavelength. (b) Fiber diameter vs. maximum coupled wavelength. (c) Fiber diameter vs. bandwidth of the coupled wavelength.
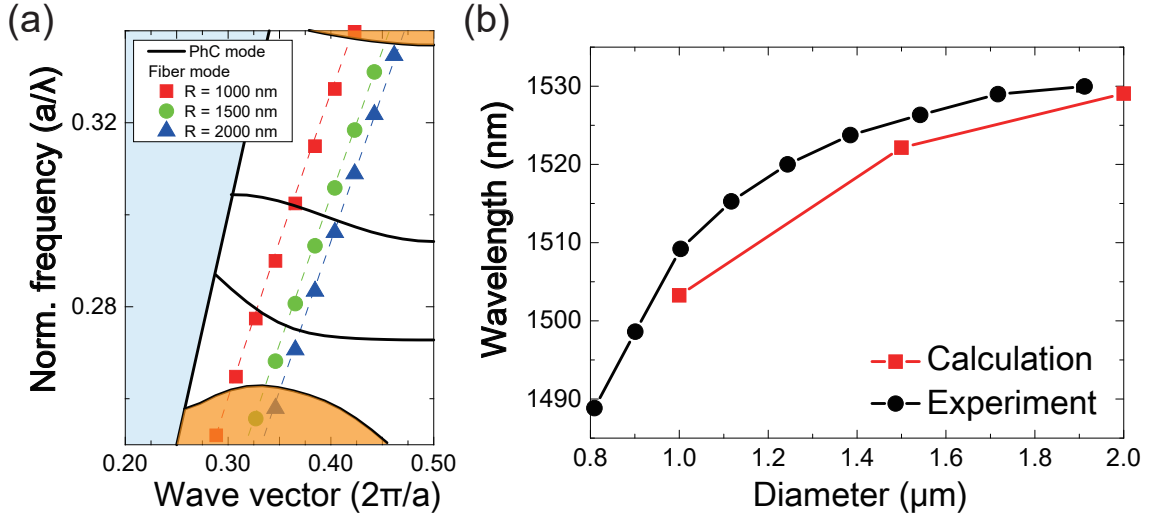
Fig. 3.13. (a) Photonic band diagram of nanofibers and a PhC waveguide with a width of $0.98 \times \sqrt{3}a$ and a diameter of 248 nm. The bands for the nanofibers were calculated using FDTD. Blue and red shaded regions indicate the radiation mode above a light line and eigenmodes in the PhC, respectively. (b) Fiber diameter vs. minimum coupled wavelength for a PhC waveguide with a width of $0.98 \times \sqrt{3}a$ and a diameter of 248 nm. Calculation result shows the wavelength at the cross point of the PhC waveguide's and nanofibers's lower guided band in (a).

Finally, the coupling with the nanocavities was performed with a nanofiber with a proper diameter. The results obtained are shown in Fig. 3.14. As shown in Fig. 3.14(a), high CEs were successfully obtained for multiple resonant modes with polarization dependence. Note that most resonant modes were formed due to the randomness of the structure and not because of the index modulation with the nanofiber (the discussion about the origin of these modes is presented in Appendix C, and the identification of a resonant mode formed with a nanofiber is performed in Chapter 4.2). By measuring the $Q$ and CE for a resonant dip, we verified that a high CE of 99.6% was obtained with a $Q_{\text{load}}$ of $6.1 \times 10^3$ ($Q_{\text{int}} = 9.6 \times 10^4$, $Q_{\text{coup}} = 6.5 \times 10^3$) as shown in Fig. 3.14(b), which is a record-setting CE value for coupling with PhC nanocavities. A remarkable point to be taken is that the loss of the nanocavity (loaded $Q$) can be controlled within a tunable in the order of $10^3$ to $10^5$ by changing the coupling with the nanofiber, because increasing $Q_{\text{coup}}$ is easy by changing the contact position (diameter of the nanofiber). This feature is effective in cavity QED applications, as it allows the user to tune a resonant spectrum into the spectrum of an emitter. It is obvious that such a high CE will also increase the photon collection ratio from the emitter (i.e., if an emitter is placed in a cavity, about 100% of photon will be collected by the nanofiber). A discussion about the collection efficiency and cavity-mediated coupling between a PhC waveguide and a nanofiber is performed in Appendix D. In addition, the amount of the reflectance from a PhC waveguide was measured experimentally and is described in Appendix E.
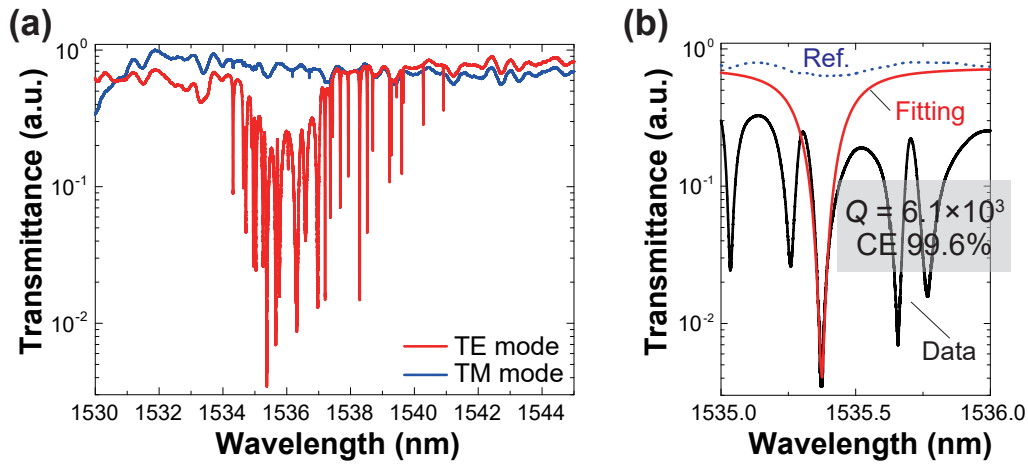
Fig. 3.14. (a) Obtained multiple resonant dips. Polarization dependence was clearly observed. (b) The resonant mode with highest CE.

## 3.3 Summary

In this chapter, the characteristics of the resonant modes in the FCPC platform are presented. A $Q_{\text{load}}$ of $5.1 \times 10^5$ with a CE of 31% was obtained. The optical properties of this mode are described, including the TO nonlinearity and the controllability of resonant wavelength with resolution of 27 pm. The highest CE value obtained was 99.6% with a $Q_{\text{load}}$ of $6.1 \times 10^3$, which is the highest recorded value for the coupling to PhC nanocavities. Although it is unclear whether the demonstrated resonant modes were formed by index modulation with a nanofiber, they are optically and efficiently coupled with nanofibers and control of the resonant wavelength is possible using nanofibers. In such broad sense, they are "fiber-coupled modes", and the characteristics shown in this work will be useful for the applications such as cavity QED. Further discussion is presented in Chapter 4 and Appendix C.

# Chapter 4

# Coupled cavity formation on the FCPC platform

In the previous chapter, the controllability of the resonant wavelength was discussed. This feature can be effectively used to tune a resonant mode into another one. In this chapter, methods to form coupled resonant modes are described. These methods will be useful for increasing the spectral and spatial overlap between an optical mode and an emitter in cavity QED applications.

## 4.0.1 Tunability of the resonant wavelength

As shown in Chapter 3.2.2, fine tuning of the resonant wavelength is possible in the FCPC configuration. In this section, tuning for multiple resonant modes is discussed. Figure 4.1 shows the result of tuning for multiple resonant modes in the PhC. It is worth noting that the amount of shift differs for different dips. This is due to the dependence of the resonant wavelength shift on position. Figure 4.2(a) shows the numerical model used to clarify the background of this effect. There are two bumps on the PhC waveguide (indicated as Bump 1 and Bump 2). The height of the bumps is the same whereas the widths are different. The distance between the bumps is 5 $\mu$m. This is a simple model of a randomly and bumpy surface in Fig. 3.2(c). When a nanofiber is brought into contact with the surface of the bumps, resonant modes are formed at the bumps since the effective indices at these regions are initially slightly high. Figures 4.2(b) and (c) show the mode profiles of the resonant modes. The mode profile of the resonance at Bump 1 is larger than that of Bump 2 because the potential well is shallow due to the large width of the bump. This also results in differences in the resonant wavelength between the two modes. Figure 4.2(d) shows the transmission spectrum obtained at Bump 1 and Bump 2 (indicated as Mode 1 and Mode 2, respectively). The resonant modes can be clearly observed in the spectrum, however, at different frequencies. In addition, the amount of frequency shift of the two modes when the contact length of the nanofiber is controlled is different. Mode 1 does not shift when the contact length changes because this mode is located at the center of the contact region of the nanofiber and does not react to the change. On the other hand, Mode 2 moves toward higher frequencies as the contact length decreases. This is because the mode is located at the edge of the nanofiber contact region and is strongly affected by changes in its length. This is the reason for the different amounts of wavelength shift for the
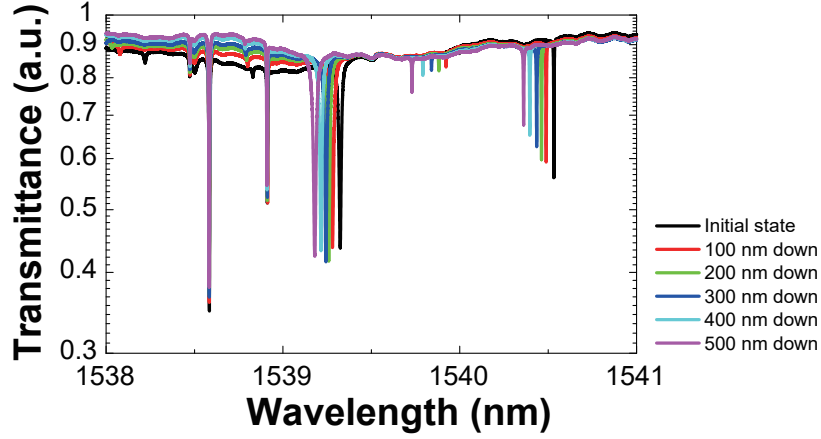
63

different modes.



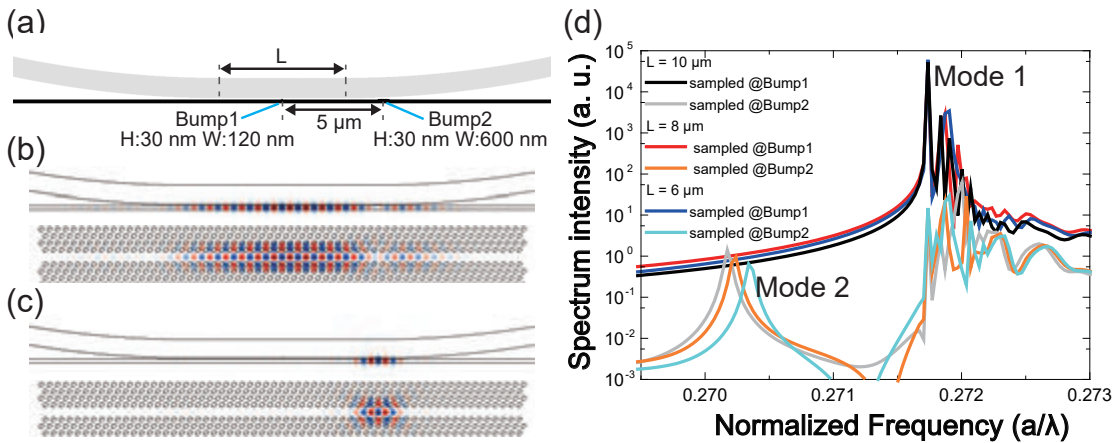Fig. 4.1. Resonant wavelength tuning of multiple resonant dips.



Fig. 4.2. (a) Schematic diagram of the computing model. (b) Mode profile of Mode 1. Ey field is presented. (c) Mode profile of Mode 2. Ey field is presented. (d) Transmission spectrum of PhC nanocavities for different contact lengths of a nanofiber calculated by the Fourier transformation of the temporal waveform of the Ey field sampled in the Bump 1 and the Bump 2.

## 4.1 Coupled cavity formation

### 4.1.1 Experimental demonstration

The feature observed in Fig. 4.1 was used to demonstrate the formation of coupled resonances. There are two modes in the transmission spectrum shown in Fig. 4.3. The amount of wavelength shift of one cavity (Mode 1, whose $Q_{load} = 4.6 \times 10^5$) is larger than that of the other cavity (Mode 2, whose $Q_{load} = 6.0 \times 10^5$). Thus, tuning the resonant wavelength of Mode 1 into that

of Mode 2 is possible, which leads to the formation of a coupled resonance. In fact, a clear anti-crossing with a mode splitting of $g/2\pi = 0.94$ GHz was observed, which is evidence of the presence of coupling between the two modes.

Interestingly, a sudden split of resonant dip was observed in another experiment, as shown in Fig. 4.4. The width of the split was 1.8 GHz, where the strong coupling condition was satisfied (i.e., the cavity decay rate $\kappa$ of about 0.5 GHz was smaller than the coupling rate $g$ of 1.8 GHz). This coupling was formed between a cavity coupled with the nanofiber and a cavity isolated from the nanofiber. Numerical results for this are presented in the next chapter.
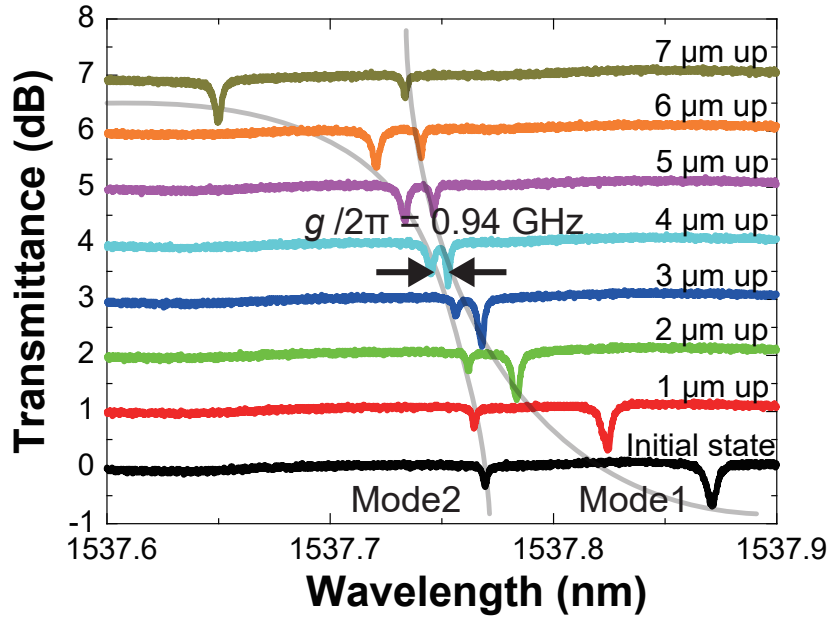


Fig. 4.3. Demonstration of coupled cavity formation. The lines correspond to the results of different contact conditions and are plotted with offsets.

## 4.1.2 Numerical analysis using coupled-mode equations

Coupled mode analysis was performed to understand the physics behind the formation of the coupled resonances presented in the previous chapter. Figure 4.5 shows the numerical model used, where $a$ is the amplitude of light in the cavity, $\omega$ is the angular resonant frequency of the cavity mode, $\gamma$ is the decay rate, $s_{\mathrm{in}}$ is the input power, and $\mu$ is the direct-coupling rate between the two cavities. The numbers in subscript are the identifications of the cavities. The meaning of the letters are as follows: i: intrinsic and c: coupled to a nanofiber. There are two paths for energy exchange between cavities in this system; one is through a fiber and the other is the direct coupling between the cavities. Therefore, the coupled-mode equations can be expressed as follows.
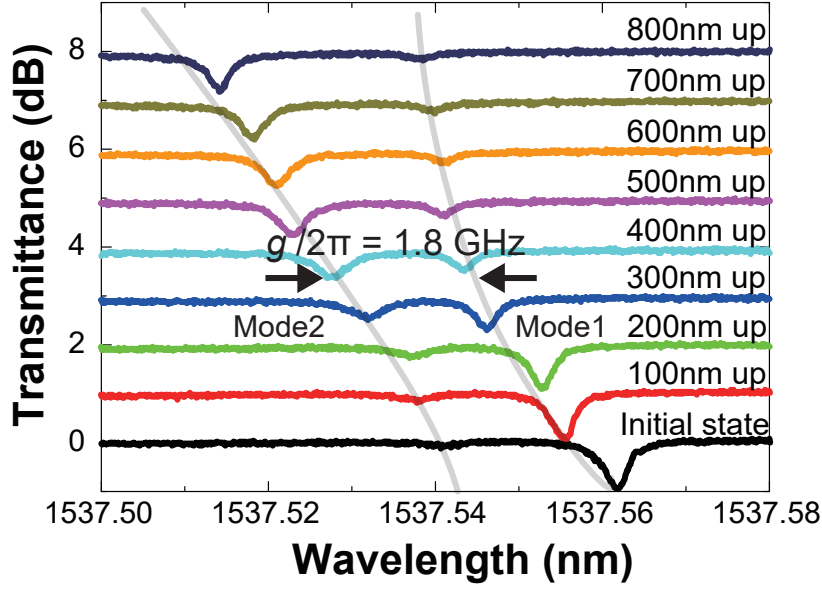
Fig. 4.4. Sudden split of a resonant dip. The lines correspond to the results of different contact conditions and are plotted with offsets.

$$\frac{\mathrm{d}a_1}{\mathrm{d}t} = (j\omega_0 - \frac{\gamma_{1\mathrm{i}} + 2\gamma_{1\mathrm{c}}}{2})a_1 + j\sqrt{\gamma_{1\mathrm{c}}}s_{\mathrm{in}} + \sqrt{\gamma_{2\mathrm{c}}\gamma_{1\mathrm{c}}}a_2 + j\frac{\mu}{2}a_2, \tag{4.1}$$

$$\frac{\mathrm{d}a_2}{\mathrm{d}t} = (j\omega_0 - \frac{\gamma_{2\mathrm{i}} + 2\gamma_{2\mathrm{c}}}{2})a_2 + j\sqrt{\gamma_{2\mathrm{c}}}s_{\mathrm{in}} + \sqrt{\gamma_{1\mathrm{c}}\gamma_{2\mathrm{c}}}a_1 + j\frac{\mu}{2}a_1, \tag{4.2}$$

$$s_{\mathrm{out}} = s_{\mathrm{in}} + j\sqrt{\gamma_{1\mathrm{c}}}a_1 + j\sqrt{\gamma_{2\mathrm{c}}}a_2. \tag{4.3}$$

An anti-crossing will be obtained when the total coupling rate through the nanofiber and the PhC waveguide exceeds the decay rate of the cavity. Then, the equations were solved by applying the experimental parameters. The resonant wavelengths of the Mode 1 and Mode 2 were tuned from the initial to the final wavelengths obtained in the experiment discretely. The amount of the wavelength shift at each step was determined by dividing the total amount of the shift by the number of the tuning processes in the experiment. Equation (4.1) and Eq. (4.2) were solved at the each step. The results are displayed in the same graph with offsets for the y axis as shown in Fig. 4.6(a). The anti-crossing with coupling rate of $g = 0.94$ GHz was observed when the direct-coupling rate between the cavities assumed to be $\mu/2\pi = 0.92$ GHz ($Q_\mu = 2.1 \times 10^5$) (see Fig. 4.6(b)). This value was about 337 times larger than the coupling rate through the nanofiber of $\sqrt{\gamma_{1\mathrm{c}}\gamma_{2\mathrm{c}}}/2\pi = 0.025$ GHz ($Q_{\mathrm{fiber}} = 7.7 \times 10^6$), which means that the dominant path for energy exchange was direct coupling between the cavities. Next, we carried out an analysis of the results shown in Fig. 4.3. Because the resonant mode Mode 2 was not observed during the initial state, the coupling between the cavity and the nanofiber was assumed to be very weak, with a coupling $Q$ of $10^{10}$. On the other hand, the other parameters were set according to the results shown in Fig. 4.4. The calculated result is shown in Fig. 4.7(a). A clear anti-crossing and a sudden split of the resonant peaks was observed in the same way as
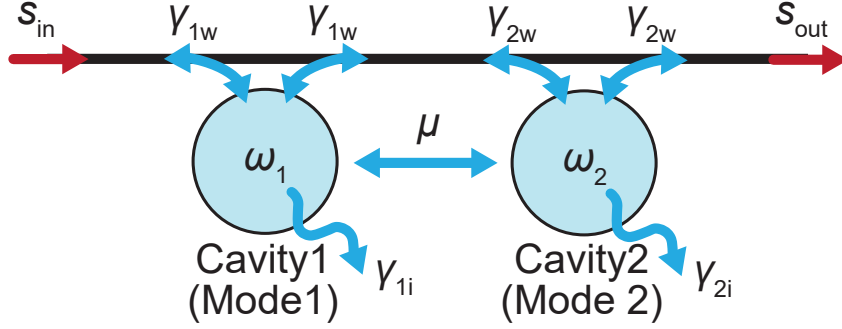
Fig. 4.5. Numerical model of coupled-mode analysis.

shown in Fig. 4.4. The amount of splitting was 1.7 GHz (see Fig. 4.7(b)), which agreed well with the experimental result. The direct coupling rate between the cavities of $\mu = 1.7$ GHz ($Q_\mu = 1.1 \times 10^5$) was obviously much larger than the coupling rate through the nanofiber of $\sqrt{\gamma_{1c}\gamma_{2c}}/2\pi = 9.6$ MHz ($Q_{\text{fiber}} = 1.3 \times 10^8$), which also indicates that the energy was exchanged through the direct coupling between the cavities.
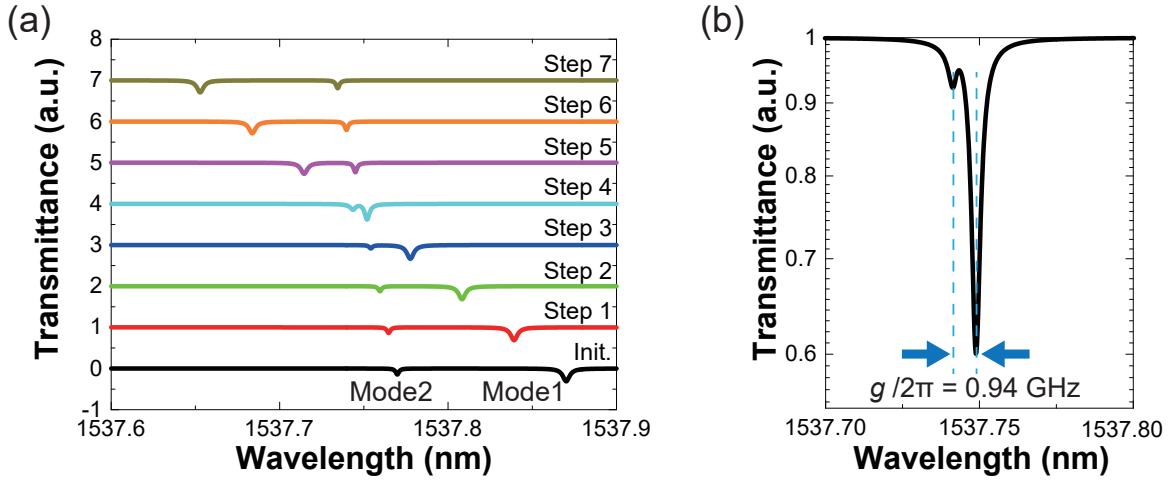


Fig. 4.6. (a) Coupled-mode analysis for the results shown in Fig. 4.3. (b) Enlarged view of mode splitting when the resonant wavelengths of the two modes are equal. Parameters used for the comuputing are as followed: $\gamma_{1i}/2\pi = 0.51$ GHz ($Q_{1i} = 3.9 \times 10^6$), $\gamma_{1c}/2\pi = 0.049$ GHz ($Q_{1c} = 3.9 \times 10^6$), $\gamma_{2i}/2\pi = 0.27$ GHz ($Q_{2i} = 7.1 \times 10^5$), $\gamma_{2c}/2\pi = 0.013$ GHz ($Q_{2c} = 1.5 \times 10^7$), $\mu/2\pi = 0.92$ GHz ($Q_\mu = 2.1 \times 10^5$).

## 4.2 Position control of resonant modes

In this section, the control of the position of the resonances is discussed. Controllability of position is important for increasing the spatial overlap between an optical mode and other materials or emitters as well as for forming a coupled resonance. The FCPC will provide such controllability in principle, however, its effects have not been evidenced by the results
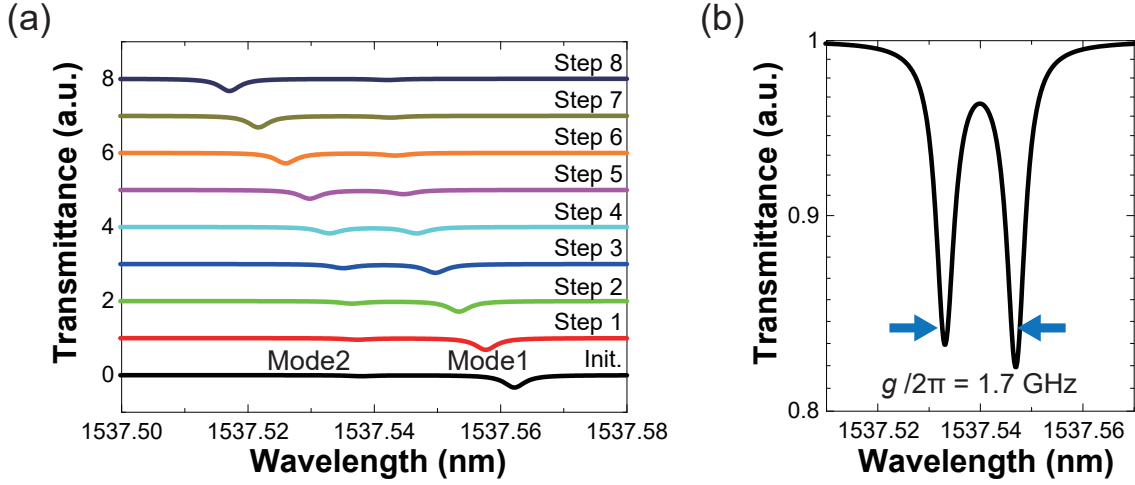
Fig. 4.7. (a) Coupled-mode analysis for the results shown in Fig. 4.4. (b) Enlarged view of mode splitting when the resonant wavelengths of the two modes are equal. Parameters used for the comuputing are as followed: $\gamma_{1i}/2\pi = 0.38\,\text{GHz}\,(Q_{1i} = 5.0{\times}10^5)$, $\gamma_{1c}/2\pi = 0.049\,\text{GHz}\,(Q_{1c} = 3.9{\times}10^6)$, $\gamma_{2i}/2\pi = 0.65\,\text{GHz}\,(Q_{2i} = 3.0{\times}10^5)$, $\gamma_{2c}/2\pi = 0.019\,\text{MHz}\,(Q_{2c} = 1.0\times10^{10})$, $\mu/2\pi = 1.7\,\text{GHz}\,(Q_\mu = 1.1\times10^5)$.

presented in the previous chapter. This was because the presence of multiple randomly formed resonances made it difficult to distinguish the resonance formed with the nanofiber from others (see Appendix C). To address this issue, a sample, illustrated in Fig. 4.8(a) was employed. It was fabricated via partial etching of the silica clad using HF, which is necessary to prevent silicon wires and SSCs from being broken and flown away during the etching. The sample enabled the measurement in both both direct and side-coupling configurations. Note that the nanofiber was absent when the direct coupling measurement was demonstrated; during this measurement, light was focused using focusing lenses (Focusing Module, Optoquest Co., Ltd.) and coupled to the SSC. Then, a sample, illustrated in Fig. 4.8(b) was measured. The lattice constant $a$ of the PhC with the 2D triangular lattice was 420 nm. A width-modulated PhC nanocavity was formed in a W0.98 waveguide (a waveguide with a width of $w = 0.98\sqrt{3}a$) which was sandwiched between W1.05 waveguides (waveguides with widths of $w = 1.05\sqrt{3}a$). As the number of barrier layers at both sides of the nanocavity of nine was small enough to avoid the formation of random modes, no resonance was observed except for the intrinsic mode of our design (the transmission spectrum obtained in a direct coupling measurement is shown in Fig. 4.9(a)). Thus, an FCPC mode can be easily found if it is formed in the W0.98 waveguide, though a small contact length is required. Figure 4.8(c) shows the dimpled nanofiber used for the experiment. The dimple was formed so that its curvature was small to obtain a small contact length (the contact length was about 10 $\mu$m for the nanofiber). Furthermore, the PhC sample was angled to reduce the contact length of the nanofiber. Figures 4.8(d) and (e) show microscope images of the sample in contact with the nanofiber with tilt angles from the nanofiber axis direction of 0 and 15 degrees, respectively. Figure 4.9(a) shows the transmission spectrum for the contact conditions displayed in Figs. 4.8(d) and (e). As previously mentioned, only a single peak was detected in the PBG of the W0.98 waveguide in the direct coupling measurement. This peak was the designed one and no other resonances existed on the W0.98 waveguide. This resonance was observed in the side coupling configuration without a tilt angle

(Fig. 4.8(d)) as shown in Fig. 4.9(b). On the other hand, two resonant dips (Mode 1t and Mode 2t) were measured for the sample with a tilt angle of 15 degrees (Fig. 4.9(b)). Both resonances show the clear nonlinearity of the TO effect as shown in Fig. 4.10(a) and (b), which are evidence of the strong localization of the modes in a small space. Because the resonant wavelengths of the two modes were between the cutoff wavelengths of the W0.98 and W1.05 waveguides, they must be located at the W0.98 waveguide (i.e., the W1.05 waveguide supports the guided mode at the resonant wavelength, so the formation of cavities in the waveguide is impossible). This implies that the resonance was formed by the index modulation of the nanofiber.
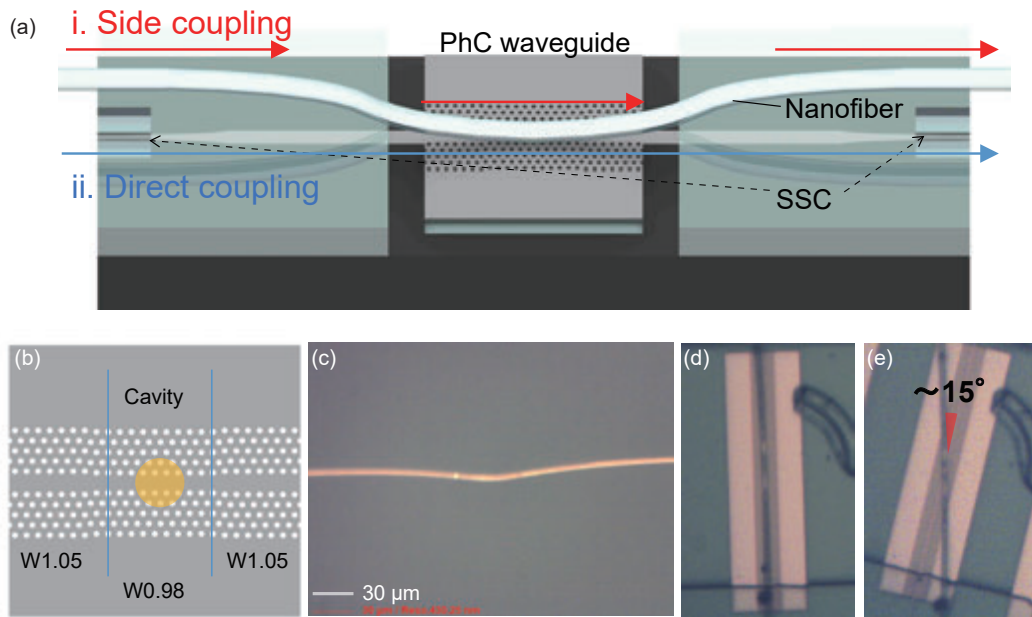


Fig. 4.8. (a) Schematic of a PhCs of which silica clad was partially etched. (b) Schematic of a PhC nanocavity sandwiched between two W1.05 waveguides. A cavity was formed in a W0.98 waveguide by modulating its width. The number of barrier layers was 9. (c) A dimpled nanofiber. (d) The PhC waveguide making contact with a dimpled nanofiber without a tilt angle and (e) with a tilt angle of about 15 degrees.

To clarify this, an observation of the localized mode was performed using an IR camera. Figure 4.11 shows the results. The position of the sample was repeatedly moved 1 $\mu$m along the vertical direction as indicated by the red arrow. IR images were taken at each moving step for both modes. The red dashed lines are drawn as indicators of the initial positions of the left-upper corner of the PhC, a dust particle on the nanofiber, and the cavity resonance. The position of the resonant mode of Mode 1t did not move as the sample position changed (see Figure 4.11(a)). This means that the resonance was located right below the nanofiber, because the position of the nanofiber was constant as shown by the position indicator of the dust particle. On the other hand, the position of the resonant mode of Mode 2t moved along with the sample (see Figure 4.11(b)). This means that the resonance was embedded in the sample, and thus this must be the intrinsic resonant mode of the sample. From these results, it can be inferred that Mode 1t is an FCPC mode formed by the presence of the nanofiber.

Figure 4.12 and Fig. 4.13 show the change of the resonant wavelength and the quality factors
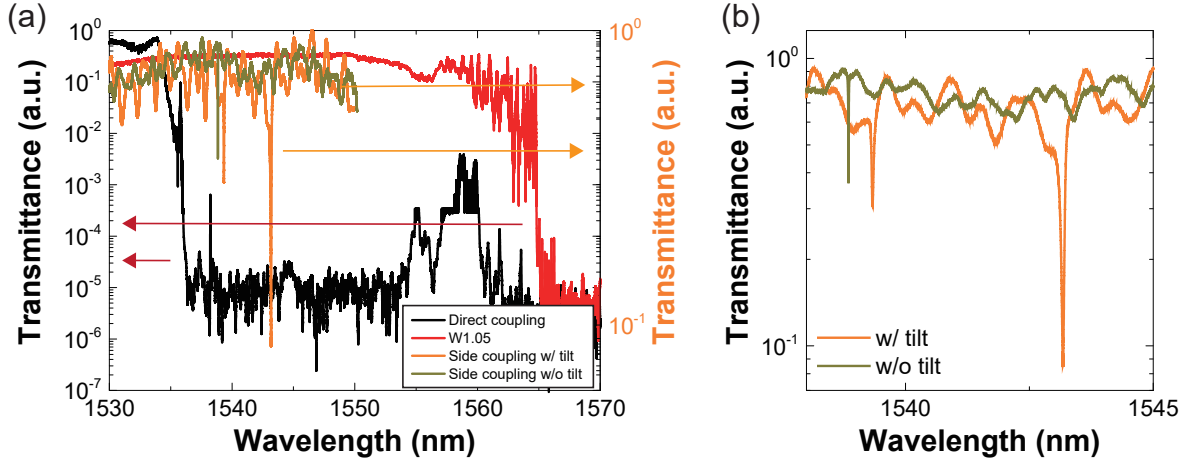
Fig. 4.9. Transmission spectra of a PhC nanocavity measured in the direct coupling configuration and the side coupling configuration shown in Fig. 4.8(e) and (f). (b) Enlarged view of (a).
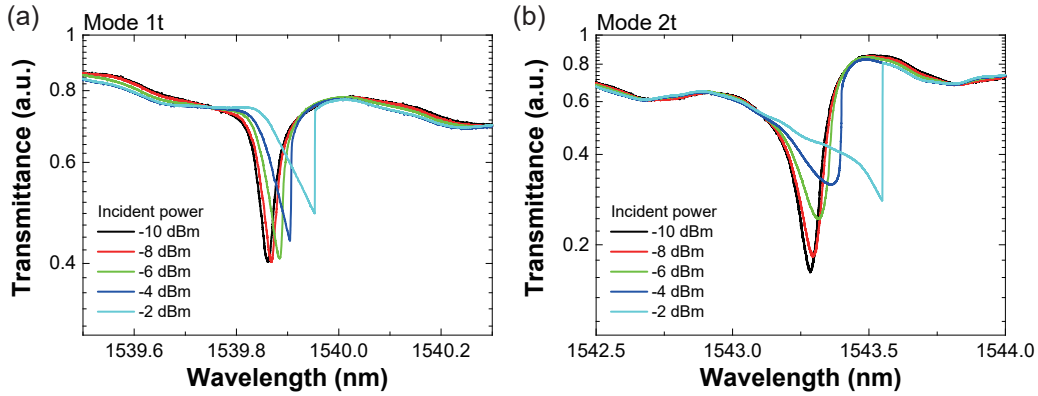


Fig. 4.10. Thermo-optic bistability observed for (a) Mode 1t, and (b) Mode 2t. The incident power is calculated by taking into account the transmittance of the nanofiber and the amount of the attenuation.

along with the change of the position of the sample, respectively. As shown in Fig. 4.12, the resonant wavelength of Mode 1t approached the cutoff wavelength of the W0.98 waveguide whereas that of Mode 2t approached the resonant wavelength of the intrinsic mode. Because the effects of the index modulation with the nanofiber become smaller for large displacements, they show the original wavelength of each mode. In other words, we assume that Mode 1t was a modulated guided mode of the W0.98 waveguide, and Mode 2t was the intrinsic mode of the design. $Q$ was almost constant for Mode 1t (see Fig. 4.13(a)), whereas that of Mode 2t increased as the effect of the nanofiber became smaller (see Fig. 4.13(b)). The tendency of the change in the resonant wavelength and $Q$ is also in good agreement with what could be expected from the experimental results shown in Fig. 4.11.

From the results mentioned above, I concluded that Mode 1t was formed by the effective index modulation caused by the nanofiber whereas Mode 2t was the intrinsic mode of the design. The results shows the controllability of position and the mode profile of the FCPC.
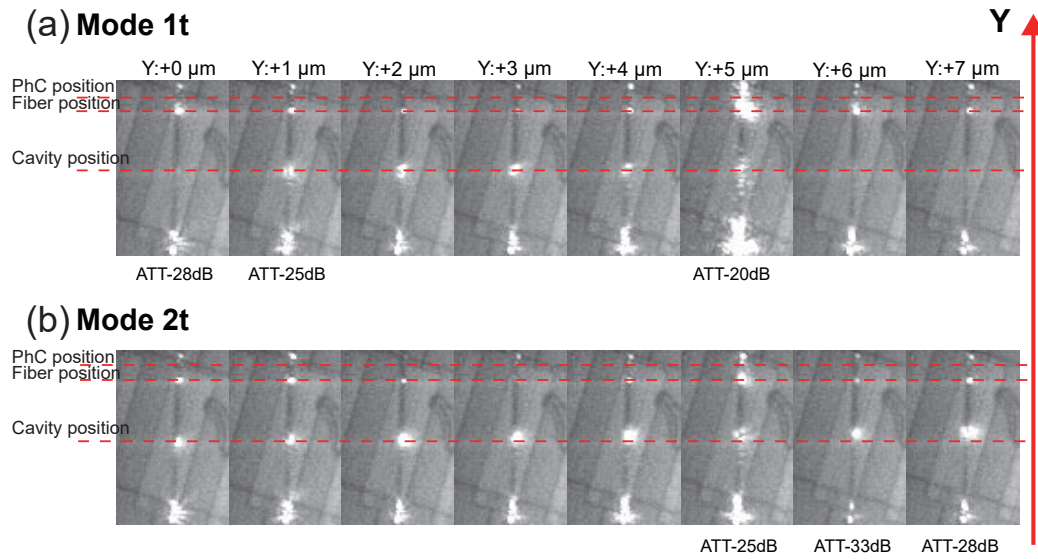
Fig. 4.11. Cavity position dependence on the displacement of the position of the PhC for (a) mode 1t and (b) mode 2t. Red dashed lines indicate the initial positions of the left upper corner of the PhC, a dust particle on the nanofiber, and cavities. The attenuation values of the VOA are shown if they were changed from the initial setting (-28 dB).

## 4.3 Summary

The experimental formation of coupled resonances was demonstrated by exploiting the resonant wavelength controllability of an FCPC. Coupling rates of 0.97 GHz and 1.8 GHz were obtained experimentally, which are in the strong coupling conditions. Numerical analysis was performed using coupled-mode equations. These results support the experimental results and they show that in the coupling mechanism the dominant path for energy exchange was the direct coupling between the cavities. The demonstrated control will be useful to tune an FCPC mode into a coupling mode with an emitter ' s spectrum and to form coupled resonance. In addition, position control of the cavity was demonstrated. A resonance was formed through index modulation using a nanofiber, and its origin was investigated via a multi- faceted approach. The characteristics of this position control can effectively strengthen the coupling with an emitter by increasing the spatial overlap between the optical mode and the emitter.
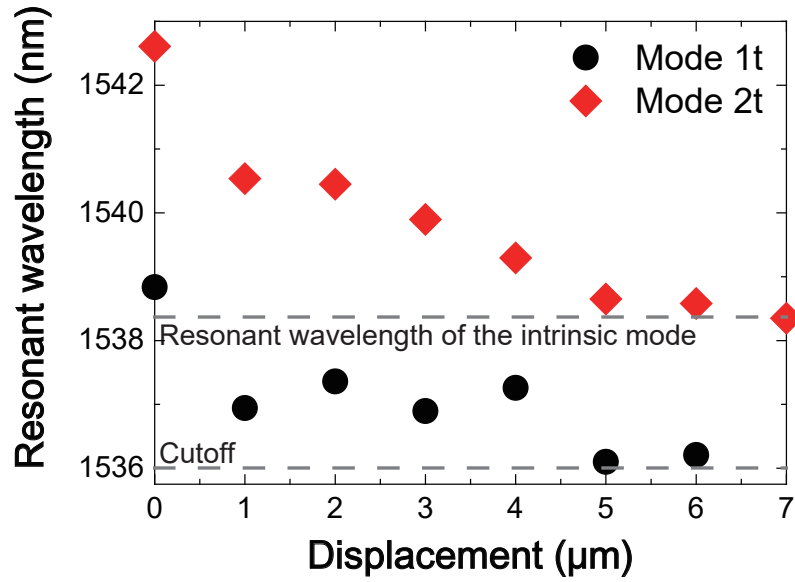
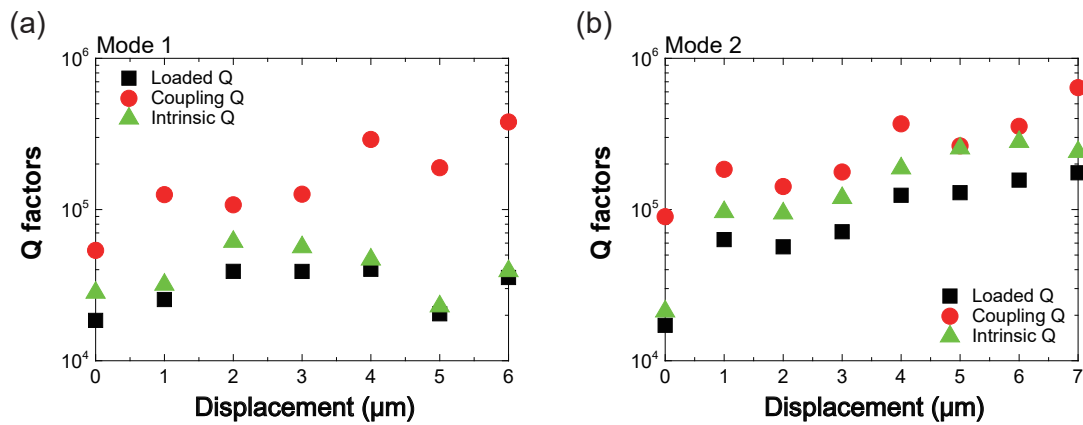Fig.  4.12.  Resonant wavelength dependence on contact position displacement.



Fig.  4.13.  Quality factor dependence on contact position displacement.

# Chapter 5

# High-$Q$ silica nanobeam cavity

Silica is an indispensable material to optical applications owing to its extremely small absorption loss over a wide wavelength range. Thus, it is used as a material for optical fibers, which are the key components of long-distance communication technologies [197]. Although the nonlinear coefficient of silica is not large, nonlinear applications have been demonstrated using ultra-high-$Q$ micro-cavities or long optical fibers [198–200]. In addition, the so-called sol-gel process, a convenient method of forming solid materials, enables the fabrication of active silica devices including micro-cavity lasers [201–203]. These properties make silica widely used in optical applications and an attractive material for cutting-edge researches. Despite the attractive material properties, silica has been rarely used for the fabrication of PhC nanocavities, as due to its low refractive index, achieving high $Q$ is challenging. In other words, the silica is not suitable for opening a wide PB, which is a condition required to obtain high-$Q$ cavities. On the other hand, the narrow PB causes a small modulation of the dispersion curves of each mode in the cavity, leading to a uniform cavity design with regard to polarizations where the dispersion curves of the orthogonal modes (TE and TM modes) are close to being equal. In this study, a silica nanobeam cavity, with spectrally overlapped orthogonal modes is explored. This chapter discusses the development of fabrication and experimental techniques of a silica nanobeam cavity. First, the design of a high $Q$ cavity is presented. Then, the fabrication techniques of the cavity are described. Finally, investigation of the condition to maximize the CE with a nanofiber is demonstrated. Although all experiments are performed in a telecommunication range, extension of the design to the visible range is possible by applying the scaling law of PhC [172].

## 5.1   Design of the cavity

As the formation of 2D PBG with low refractive index materials is difficult, usually a 1D nanobeam configuration is adapted for PhC nanocavities made of such materials. Following the conventional strategy, a design for a silica nanobeam cavity in a 1D configuration is presented here. A beam structure with a rectangular air hole inside was adapted as a unit cell of the cavity. Figure 5.1(a) shows the dispersion relation of the unit cell with lattice constant $a$, width $w$ 2.6$a$, hole depth $h_x = 0.5a$, hole width $h_y = 0.7a$, and thickness $t = 1.1a$. Although the complete PB is absent for both TE and TM modes, the possible formation of a

high *Q* mode-gap cavity is expected, because the separation between the fundamental and the second order modes is large and the edge of fundamental mode (at $k = 0.5$) is sufficiently far from the light line. A cavity was formed by modulating the lattice constant of the unit cell. Figure 5.1(b) shows a schematic of the whole nanobeam structure and Fig. 5.1(c) shows the modulation profile of the lattice constant. As can be seen, the region with the modulated air holes, called the cavity region, is sandwiched between regions containing holes with a constant spacing, referred to as barrier layers (holes). In the cavity region, the lattice constant between the holes is gradually reduced toward the center of the cavity, causing a slight upshift of the cutoff frequency of the first band, leading to the formation of a mode-gap by an equivalent potential well. Following the strategy reported elsewhere [83, 84], a Gaussian modulation was adopted. Then, a numerical analysis of the resonant modes was performed by 3D FDTD using the software MEEP. The transmission spectra are shown in Fig. 5.2(a). Four peaks were found; two were obtained from the Ey component (TE mode), while the other two were obtained from the Hy component (TM mode). They correspond to the fundamental and second-order longitudinal modes of the TE and TM modes, respectively, according to their mode profiles (see Fig. 5.2(b)). The TM resonant modes were observed close to those of the TE modes by using a standard cavity design only, which was initially expected from the photonic band diagram Fig. 5.1(a). The *Q* and *V* values of the fundamental modes were $Q_{TE} = 1.1 \times 10^5$, $V_{TE} = 1.1(\lambda/n_{eff})^3$ and $Q_{TM} = 4.7 \times 10^4$, $V_{TM} = 2.1(\lambda/n_{eff})^3$, respectively, with 36 barrier holes on each side of the cavity region. Hence, the high *Q* design was confirmed numerically.
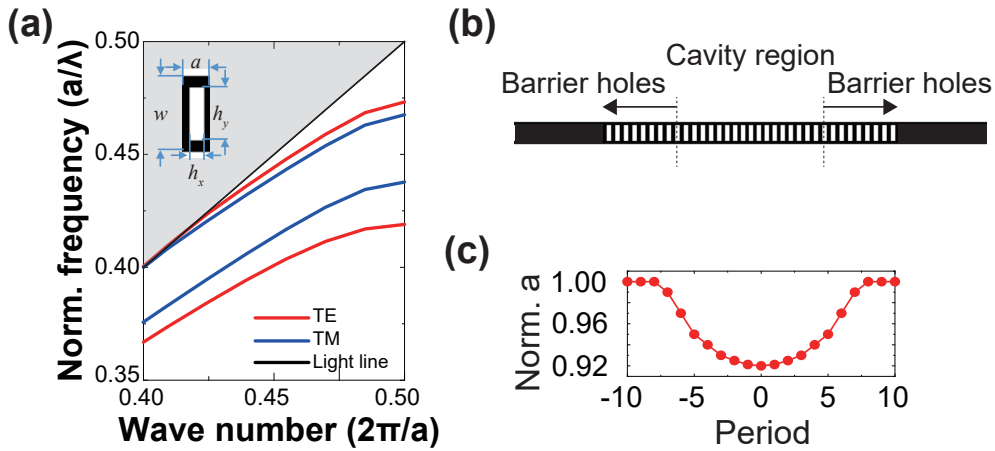


Fig. 5.1. (a) Photonic band diagram of a unit cell of the cavity calculated by MPB. The inset shows a schematic of the unit cell. (b) Schematic illustration of the cavity structure. (c) Modulation profile of the lattice constant with the normalized lattice constant.
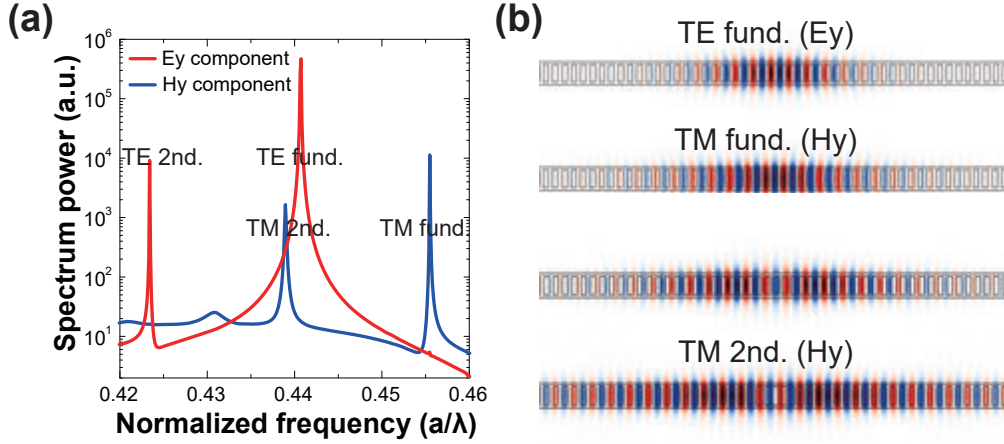
Fig. 5.2. (a) Spectra of the designed cavity calculated by FDTD, calculated by the Fourier transformation of the temporal waveforms of the Ey and Hy components, sampled in the cavity region. (b) Mode profiles of the cavity. The Ey/Hy components are displayed for TE/TM modes.

## 5.2 Fabrication of the cavity

The fabrication of the cavity structure was demonstrated by the method shown in Fig. 5.3. The most challenging process in the fabrication of a PhC nanocavity in the telecommunication wavelength range is etching the thick film of the material. In general, fabrication of a high-$Q$ cavity in a longer wavelength range is easier than that in a shorter wavelength range, due to the strong wavelength dependence of the scattering losses due to the line edge roughness (LER) of the patterns that defines the cavity (roughly speaking, the LER has to be one quarter if the operational wavelength become one half for the same scattering loss [204]). However, the thick device layer required for our design ($\sim$ 760 nm) exhibits additional challenges to fabrication as the LER can be deteriorated as the etching depth is increased. Furthermore, a thick organic resist mask may itself degrade the resolution of the patterns due to the increased electron scattering. In order to achieve deep high-resolution etching of the device layer, a tri-layer mask approach was used. In this approach, the structure was firstly defined in a thin organic resist with a small LER, and then sequentially transferred to the dielectric hard masks by using appropriate etch chemistries, which eventually allow us to obtain sufficient etching selectivity to the device layer, despite the complexity of the process.

For the design, resonant wavelengths in the telecommunication wavelength range, $a$, were used with a barrier layer of 690 nm, which determined the dimensions of other parameters, such as the beam width of 1794 nm, the rectangular hole size of 345 nm $\times$ 1256 nm, and the beam thickness of 759 nm. In addition, two types of test patterns were used to assess the quality of the fabrication techniques. One is a "line and space" pattern, where rectangular structures with a width of 200 nm are placed repeatedly with a spacing of 200 nm (see Fig. 5.7(a)). The other is a cross structure with a size of 3 $\mu$m $\times$ 3 $\mu$m, where the width of the cross lines is 1 $\mu$m (see Fig. 5.7(b)). It should be noted that the size of the designed cavity is between those of the two test patterns.

The test patterns fabricated in each fabrication step are shown in Fig. 5.4 to Fig. 5.8. The process starts with a substrate with a thermal oxide $SiO_2$ film with a thickness of approximately 1000 nm on Si (CZ-P type, Silicon Technology Corp.). Firstly, $SiO_2$ was etched with HF solution such that its thickness became approximately 760 nm (see Fig. 5.3). Following the process, the thickness was confirmed by using a spectroscopic ellipsometer (AutoSE HORIBA, Ltd.). Then, a ~550 nm thick amorphous silicon (a-Si) layer (Canon Anelva EB1100) was deposited by sputtering and a ~100 nm-thick tetraethyl orthosilicate (TEOS) $SiO_2$ layer was formed on the substrate by plasma-enhanced chemical vapor deposition (CVD) (Samco PD-220NLJ). The thicknesses of the Si and TEOS layers were determined from the selection ratios of the following etching processes. Next, a resist (ZEON ZEP520A) was spin coated and the patterns were defined using EB lithography (JEOL JBX-9500FSZ) (see Fig. 5.4(a) and (b)). A TEOS mask layer was then etched by using inductively coupled plasma (ICP) etching with $CF_4$ and Ar gases (Samco RIE-101iPHJF), as shown in Fig. 5.5(a) and (b). After removing the EB resist (see Fig. 5.6), ICP etching of the Si mask layer was performed with $Cl_2$ gas (Samco RIE-140iPJ), where the TEOS layer served as a mask (see Fig. 5.7(a) and (b)). Then, the $SiO_2$ device layer was etched using an a-Si mask by ICP etching with $CHF_3$ and Ar gases (Samco RIE-101iPHJF) (see Fig. 5.8(a) and (b)). As shown in Fig. 5.4 to Fig. 5.8, the defined patterns were successfully transferred to the other layers step-by-step. Finally, an air-bridge structure was formed by etching a Si sacrificial layer with $XeF_2$ (Samco VPE-4F), where the Si mask layer was also removed.
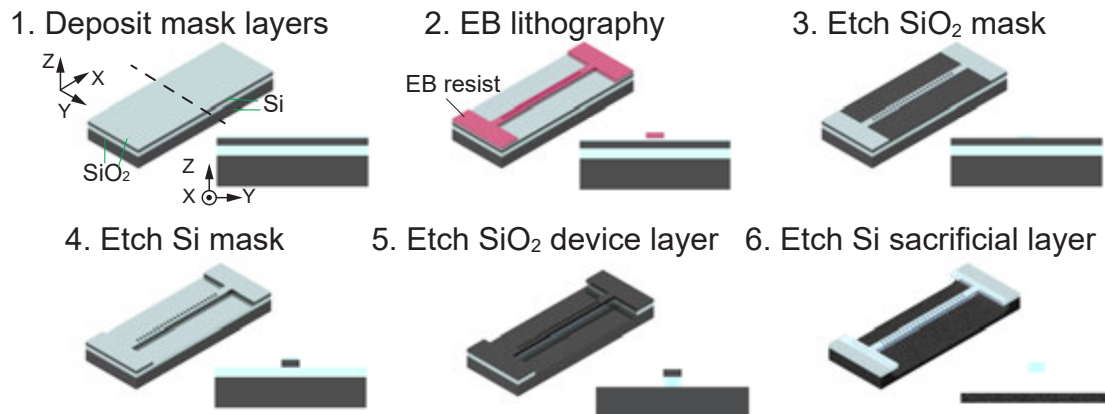


Fig.  5.3. Fabrication procedure

Although a relatively large mask erosion of the Si mask was observed in Fig. 5.7 and Fig. 5.8, it does not seem to critically affect the verticality of a fabricated silica beam pattern, as shown in Fig. 5.8(b) and Fig. 5.9(a) (Figure 5.9(a) shows that under-etching was not observed at the boundary between the Si and $SiO_2$ device layers). On the other hand, the hole size enlarged by ~60 nm, as shown in Fig. 5.9(b). The SEM images of the side view of the fabricated structure are shown in Figs. 5.10(a) and (b). Figure 5.10(a) shows that the air-bridged structure was slightly (sometimes severely) warped, because it was released from the tensile force of the silicon sacrificial layer, while its effect on optical characteristics of the cavity was not

observed in experiments. The surface of the fabricated structure appeared smooth, as shown in Fig. 5.10(a) and Fig. 5.10(b).
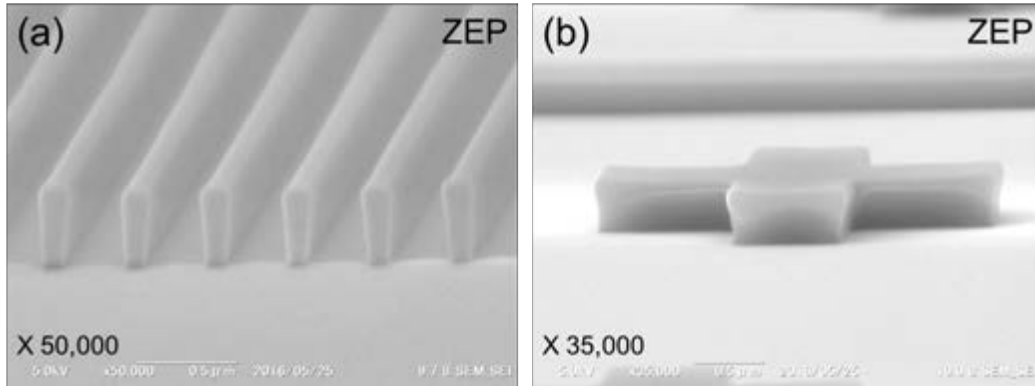


Fig. 5.4. SEM images of fabricated test patterns of the ZEP mask layer. (a) "Line and space" pattern with line width of 200 nm. (b) Cross structure.
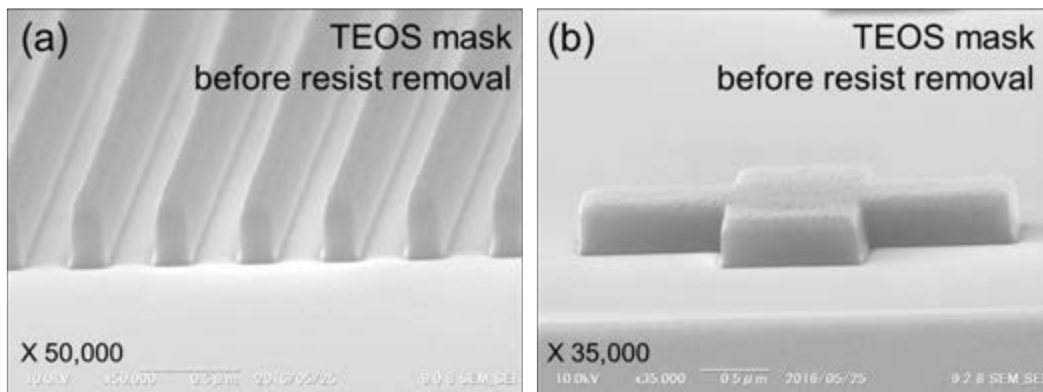


Fig. 5.5. SEM images of the fabricated test patterns of the TEOS mask layer before the removal of the resist. (a) "Line and space" pattern with a line width of 200 nm. (b) Cross structure.
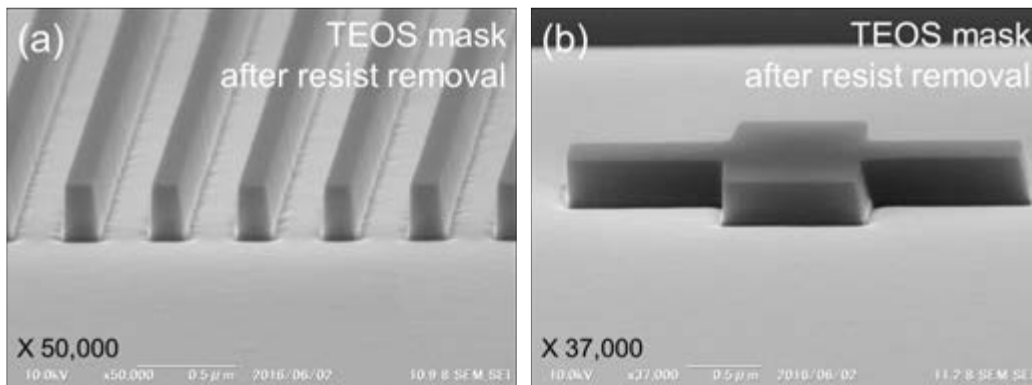


Fig. 5.6. SEM images of fabricated test patterns of the TEOS mask layer after removal of the resist. (a) "Line and space" pattern with line width of 200 nm. (b) Cross structure. A thin Au layer of ~10 nm was coated to avoid charging the electrons.
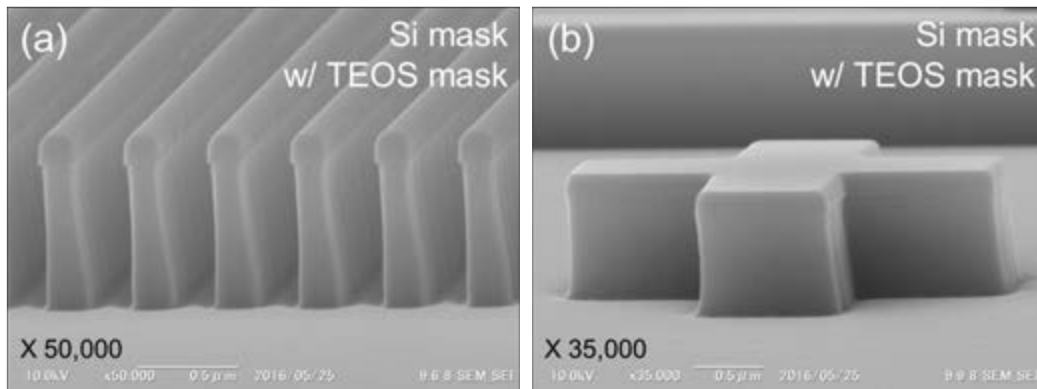
Fig. 5.7. SEM images of fabricated test patterns of the Si mask layer. (a) "Line and space" pattern with line width of 200 nm. (b) Cross structure.
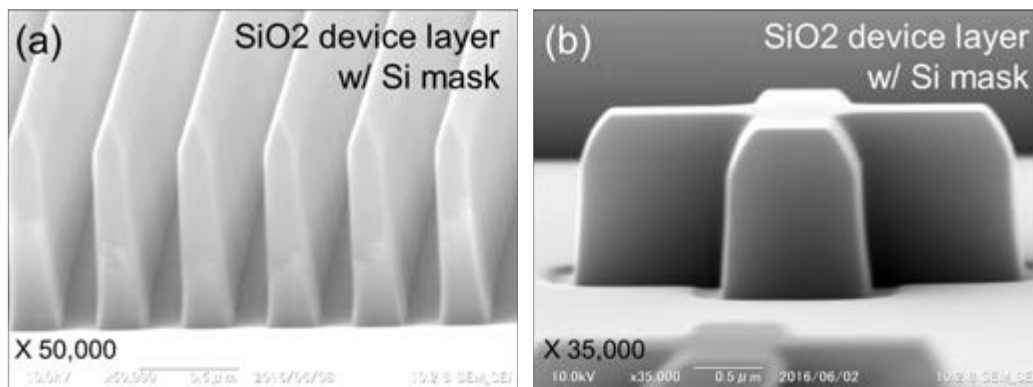


Fig. 5.8. SEM images of fabricated test patterns of the SiO$_2$ device layer. (a) "Line and space" pattern with line width of 200 nm. (b) Cross structure.
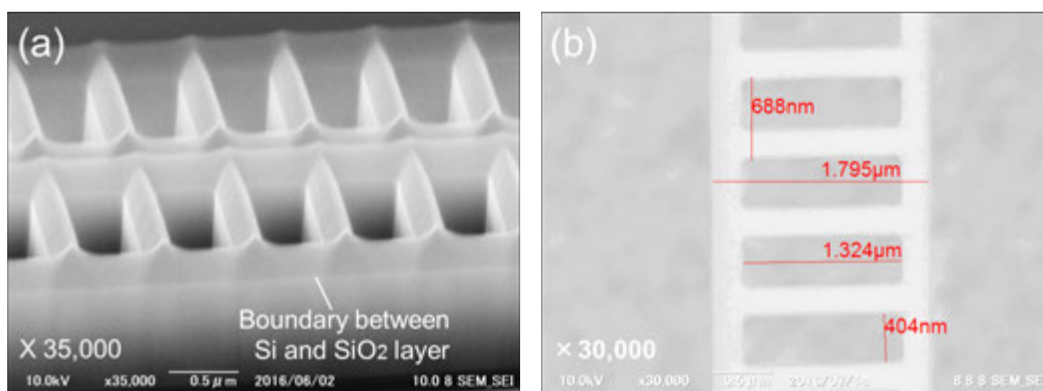


Fig. 5.9. SEM images of (a) enlarged view of the boundary between the Si mask and the silica device layer and (b) top view of the air-bridged silica beam structure. The measured lengths are written in red letters, the resolution of the image is 5.6 nm/pixel.
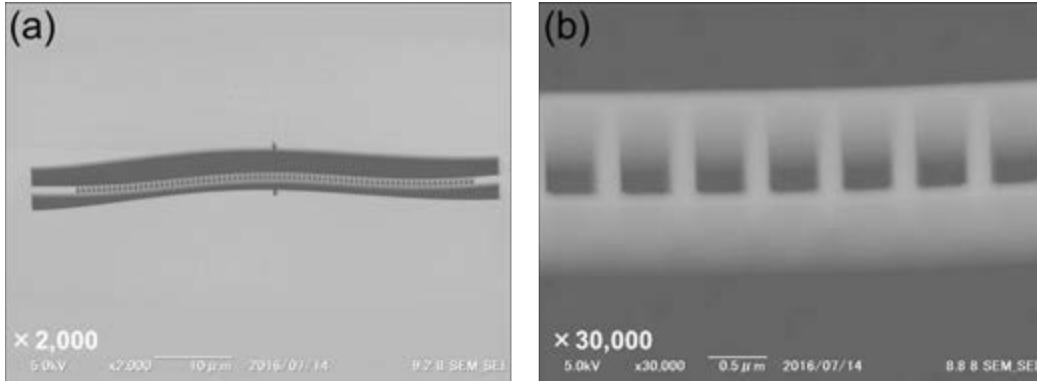
Fig. 5.10. SEM images of the side view of the fabricated beam structures (a) observed with a magnification of 2000× and (b) observed with a magnification of 30000× .

## 5.3 Experimental characterization of the cavity

In this section, the optical properties of the fabricated cavity are characterized. The experimental setup is shown in Fig. 5.11. A laser light was emitted from a narrow-linewidth tunable laser diode (Santec TSL-710) into the optical fiber. The power and polarization of the input light were controlled by a variable optical attenuator (OZ Optics DA-100-3A) and a polarization controller (Alnair Labs MLC series), respectively. The light was evanescently coupled to the nanocavity using a dimpled taper nanofiber [116]. The position of the nanocavity was changed by XY- and Z-stages (Sigma Tech. FS-1020PX and FS-1010PZ) and the coupling between the cavity and the nanofiber was controlled. The transmitted light was recorded by a power meter (Keysight Keysight8163b). The transmission spectrum of the device was measured by sweeping the input wavelength of the light. The transmission spectra observed for the two orthogonal polarizations are shown in Fig. 5.12(a). Both TE and TM modes were observed, as predicted by the calculation shown in Fig. 5.2(a). It should be noted that the resonant wavelengths obtained were slightly shorter than those in the FDTD due to the enlarged air holes, as shown in Fig. 5.9(b) ($\lambda_{TE,Exp}$ = 1531 nm, $\lambda_{TM,Exp}$ = 1488 nm. $\lambda_{TE,FDTD}$ = 1566 nm (normalized frequency of 0.4407), $\lambda_{TM,FDTD}$ = 1515 nm (normalized frequency of 0.4555)). The orthogonality of the two modes is confirmed in Fig. 5.12(b), where the radial direction represents the dip depths of the respective resonances, while the azimuthal direction corresponds to the polarization rotation angle of the incident light. The wavelength separation between the two orthogonal fundamental modes was 43 nm and only 14 nm between the fundamental TE and second order TM modes. These values are closer than that for a silicon dual polarized cavity of 50 nm, reported in [205].

We also examined the effect of the barrier layer length. Figure 5.13 shows the dependence of the calculated intrinsic $Q$ factor ($Q_{int}$) on the number of barrier holes by using the following equations:

$$Q_{int}^{-1} = Q_{load}^{-1} - Q_{coup}^{-1}, \tag{5.1}$$

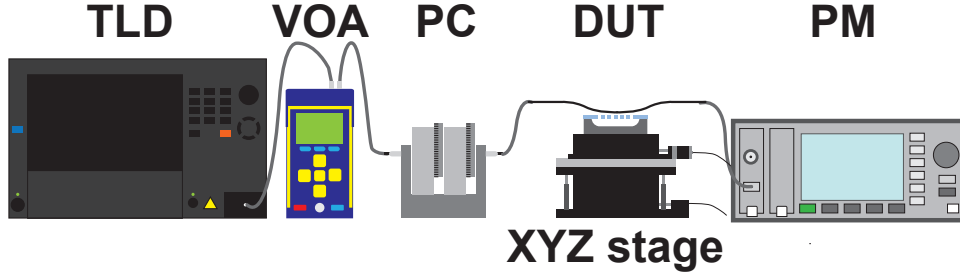$$Q_{coup} = \frac{Q_{load}}{1 - \sqrt{Tr}}, \tag{5.2}$$

Fig. 5.11. (a) Schematic of the experimental setup. TLD: Tunable laser diode. VOA: Variable optical attenuator. PC: Polarization controller. DUT: Device under testing. PM: Power monitor.
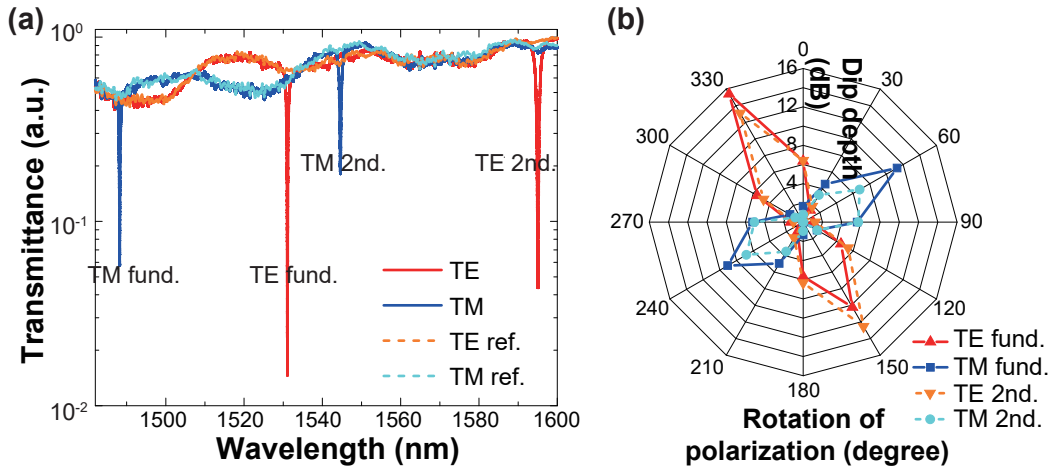


Fig. 5.12. (a) Transmission spectrum of the fabricated silica nanobeam cavity. (b) Polarization dependence of the fabricated silica nanobeam cavity.

where $Q_{\text{load}}$ and $Q_{\text{coup}}$ are the loaded and coupling $Q$ factors, respectively, and $Tr$ is the transmittance at the resonant wavelength [181]. As shown in the figure, $Q_{\text{int}}$ saturates above the number of 24 holes for both polarizations, and this is in reasonably good agreement with the FDTD predictions, indicating the way the modal tail extends out of the cavity region. Figures 5.14(a) and (b) show the fitting results for the resonance profiles of the fundamental modes with the highest $Q_{\text{load}}$ values, using 36 barrier holes. The calculated $Q_{\text{int}}$ values ($2.4 \times 10^4$ for the TE mode and $1.0 \times 10^4$ for the TM mode) well exceed the previously reported values for silica based materials [83, 84], and are even comparable to those of the silicon nanobeam cavity with dual polarization designs ($Q_{\text{TE}} = 2.8 \times 10^4$, $Q_{\text{TM}} = 1.9 \times 10^4$) [205], demonstrating that it is possible to realize high-$Q$ nanobeam cavities using a low index material. In addition, the highest loaded $Q_{\text{load}}$ values for the second order modes were $Q_{\text{TE2}} = 8.2 \times 10^3$ and $Q_{\text{TM2}} = 4.2 \times 10^3$, respectively, with 36 barrier holes. These are still as high as the highest value for silica PhC nanocavities, despite the larger out-of-plane radiation due to the larger propagation angle of the higher order modes, predicted by the FDTD ($Q_{\text{TE2,FDTD}} = 3.4 \times 10^4$ and $Q_{\text{TM2,FDTD}} = 1.0 \times 10^4$).
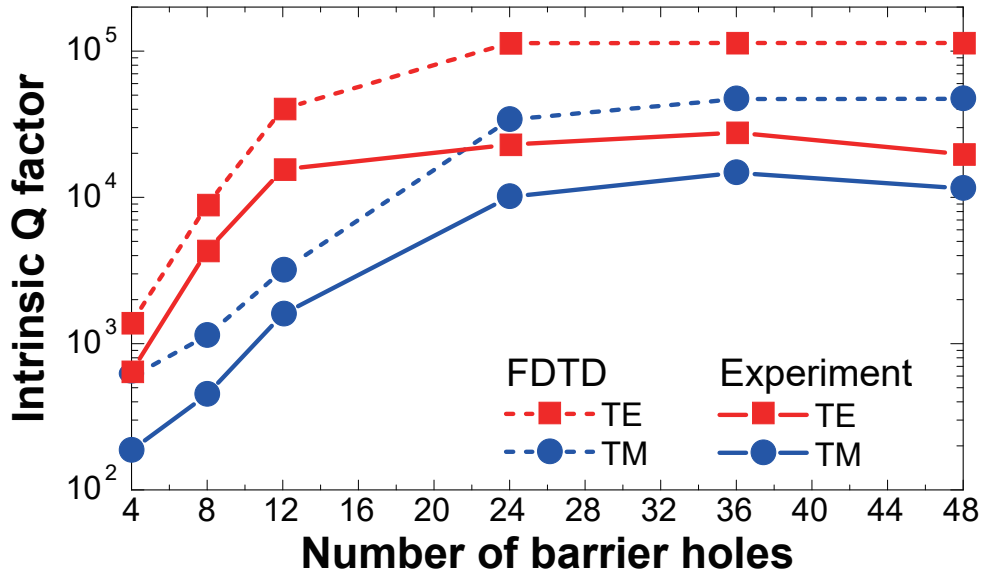
Fig. 5.13. Intrinsic $Q$-dependence versus number of barrier holes in each side of the cavity region. The intrinsic $Q$ increases until the loss to the directly coupled waveguide (coupling $Q$ to the waveguide) close to being equal to that of the vertical radiation.
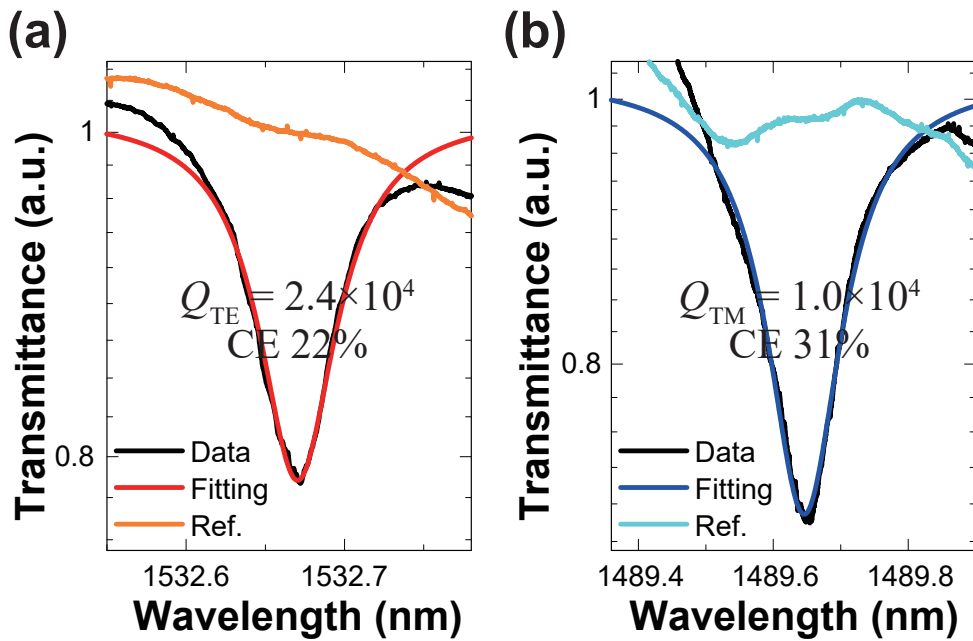


Fig. 5.14. (a), (b) Highest loaded $Q$ of TE and TM modes using 36 barrier holes.

## 5.4  Investigation of the coupling condition

Achieving high CE with an optical fiber is important for practical applications. In addition, the control of coupling results in the control of loaded $Q$ (loss) of cavities, which is important for cavity QED applications. In this section, the investigation of the optimum coupling condition is discussed. As a side-coupled configuration with an FP-type cavity was used, the transmittance of each configuration is described by the following equations (see Chapter 2.2.3):

$$Tr = (\frac{1}{1 + Q_{\text{int}}/Q_{\text{coup}}})^2, \tag{5.3}$$

$$CE = 1 - Tr. \tag{3.1}$$

It should be noted that a small $Tr$ indicates a large CE, therefore, $Q_{\text{int}}$ must be larger than $Q_{\text{coup}}$ to achieve a high CE. However, a degradation of $Q_{\text{int}}$ is expected when the gap between the nanofiber and the cavity is small, as the effect of the perturbation caused by the presence of the nanofiber can become large. Obviously, this effect is undesirable in the process of achieving a high CE. Thus, a large obtained $Q_{\text{coup}}$ with large gap distance is required. To explore this issue, an experiment was performed as follows.

The experimental setup was the same as in Fig. 5.11(a). The Z-stage was moved upwards to reduce the distance between the cavity and the nanofiber, and then the transmission spectra were measured at every 100 nm. It was difficult to determine the actual gap distance, as the measurement of the origin (gap = 0) was difficult due to the deformation of the dimpled nanofiber caused by the electrostatic force acting between the nanofiber and the cavity. The resonant dips observed were analyzed with the LabVIEW software and each $Q$ component was obtained. The data points with too shallow (or distorted) dips were excluded, for fitting the data to a Lorentzian curve with appropriate quality. This measurement was performed with four nanofibers with different diameters. The diameters of the nanofibers were measured using the following method.
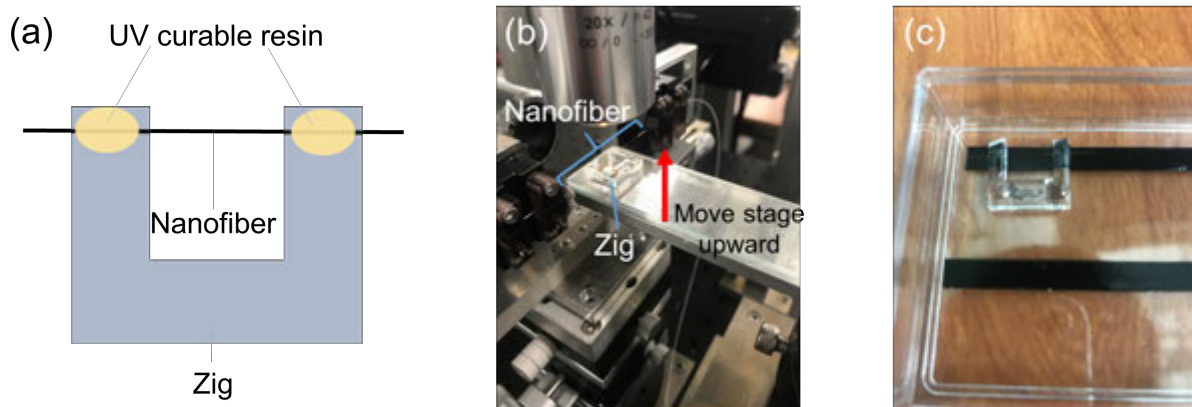


Fig. 5.15. (a) Schematic drawing of the fastened nanofiber. (b) Image of the setup for the fiber fasting process. (c) Fixed nanofiber.

The nanofibers used in the experiments were anchored to acrylic U-shaped zigs to transfer them into a chamber for SEM observation (a schematic of the zig is shown in Fig. 5.15(a)).

A UV-curable resin was used to fix the position of the nanofibers, which were brought into the adhesive by a high-precision stage (see Fig. 5.15(b)). The nanofibers were cut at outsides of the both fixing points. An image of fixed nanofiber is shown in Fig. 5.15(c). After the anchoring process, the nanofibers were observed by SEM. The obtained SEM pictures are shown in Fig. 5.16. Finally, fiber diameters at the dimpled points, which were exact parts used for the optical coupling, were measured.
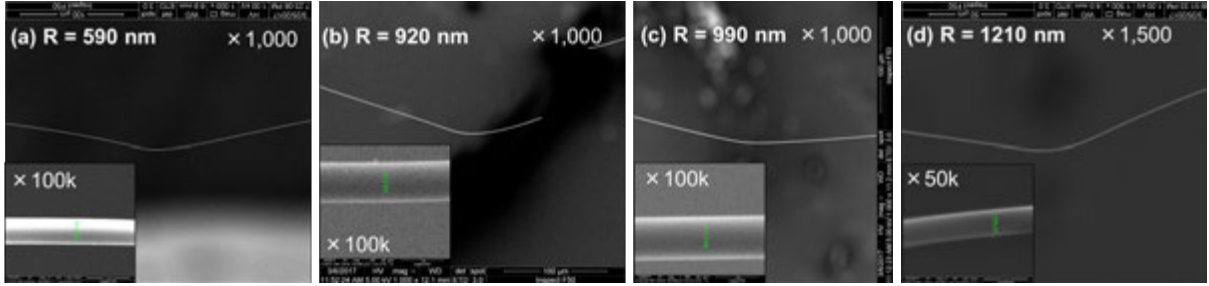


Fig. 5.16. SEM images of the dimpled tapered nanofibers with diameters of (a) 590 nm, (b) 920 nm, (c) 990 nm, and (d) 1210 nm, respectively. The insets show images observed with grater magnification.

The experimental results for the nanofiber with a diameter of 920 nm is shown in Fig. 5.17(a). For both TE and TM modes, $Q_{coup}$ decays exponentially over the measurement range, exhibiting a reasonably good linearity of the stage as well as a negligible deformation of the dimple. On the other hand, $Q_{int}$ starts to decay as the gap distance becomes small (displacement > 800 nm), and this can be attributed to the fact that the effective cladding index of the nanobeam cavity is increased. This modifies the potential profile of the cavity region. As the cavity was initially designed to achieve a high $Q_{int}$, the resultant $Q_{int}$ due to the presence of the nanofiber can to be degraded. Figures 5.17(b) and (c) show that the fitting for the TE and TM modes with the highest CE on the loaded $Q$ condition was over $10^4$. The CEs were 87% and 31% for TE and TM modes, respectively.



Fig. 5.17. Experimental results measured with a nanofiber with a diameter of 920 nm (see Fig. 5.16(b)). (a) $Q$ factor dependence versus displacement of the Z-stage. The R-squared values of the fitted lines are 0.995 for coupling $Q$ of the TE mode, 0.955 for that of TM mode, and 0.992 for the decay rate of the intrinsic $Q$ of the TE mode. (b) Fitting for the TE mode obtained with a displacement of 800 nm. The loaded $Q$ is $1.1 \times 10^4$ and CE is 87%. (c) Fitting for the TM mode obtained with a displacement of 400 nm. the loaded $Q$ is $1.0 \times 10^4$ and the CE is 31%.

The degradation effect of the intrinsic $Q$ became noticeable when a thicker nanofiber with a diameter of 1210 nm was used, as shown by the results in Fig. 5.18(a). Even at the initial point, where the dip first appeared, the intrinsic $Q$ decreased to the order of $10^3$. This means that coupling did not occur until the gap became small enough to cause the degradation of the intrinsic $Q$. This is possible due to the short evanescent tail and the larger effective index of the nanofiber. Figure 5.18(b) shows highest the CE obtained, which was 40% with a $Q_{load}$ of $3.5 \times 10^3$. The TM mode was not observed clearly in this experiment. It should be noted that there might be multi-modes in the nanofiber, as the cutoff of the nanofiber diameter for a single mode is approximately 1200 nm (see Chapter 2.3), which may also result in a low CE.
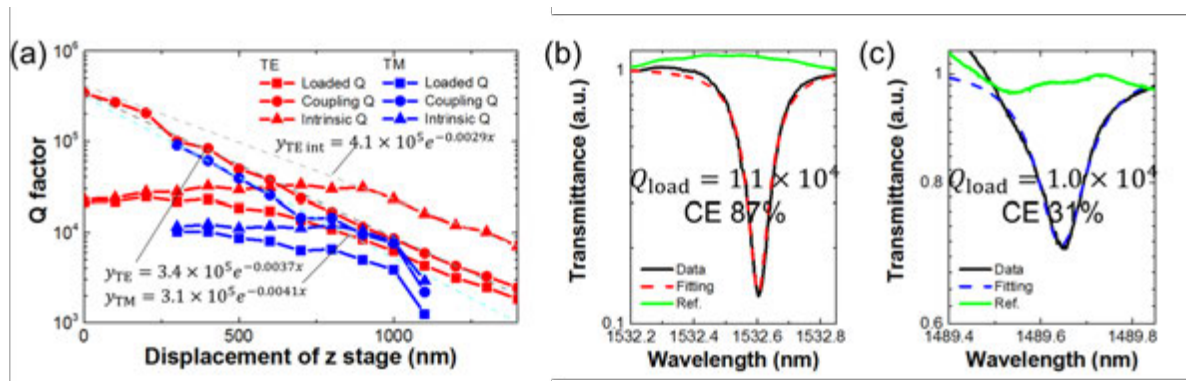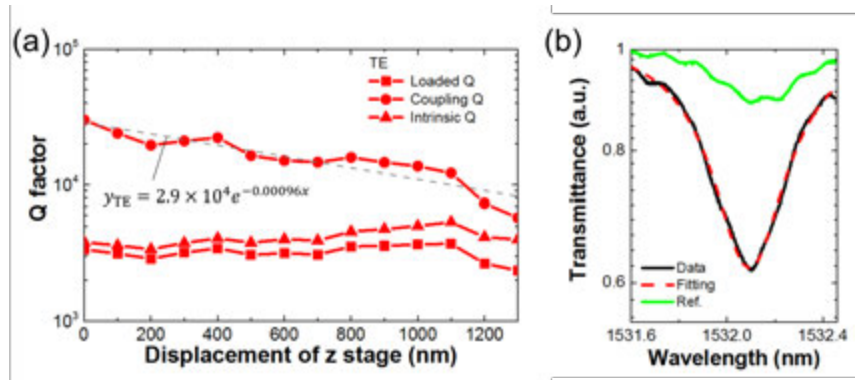


Fig. 5.18. Experimental results measured with a nanofiber with a diameter of 1210 nm (see Fig. 5.16(d)). (a) $Q$ factor dependence versus displacement of the Z-stage. The R-squared value of the fitted lines is 0.842 for coupling $Q$ of the TE mode. (b) Fitting for the TE mode obtained with a displacement of 800 nm. The loaded $Q$ is $3.5 \times 10^3$ and the CE is 40%.

On the other hand, the degradation of the intrinsic $Q$ was not observed in the experiment performed with a nanofiber with a diameter of 590 nm, as can be seen from the results in Fig. 5.19(a). As the gap became small, coupling $Q$ decays exponentially, whereas the intrinsic $Q$ remains constant. This is due to the large evanescent tail of the nanofiber, as well as the smaller impact of the modulation of the effective index. Although the CE for the TE mode was 73% when the loaded $Q$ was over $10^4$ (see Fig. 5.19(b)), a CE of 96% was obtained for the TE mode with a $Q$ of $1.1 \times 10^3$. A high CE of 72% for the TM mode was also achieved with a $Q$ of $3.2 \times 10^3$ (see Fig. 5.19(c)).

Finally, the experiments with a nanofiber with a diameter of 990 nm is discussed to study the reproducibility of the results by comparing them with the results obtained from a nanofiber with a diameter of 920 nm (see Fig. 5.20(a)). For the TE mode, the decay rate of coupling $Q$ and intrinsic $Q$ were slightly higher than those for the nanofiber with a diameter of 920 nm shown in Fig. 5.17(a) (It should be noted that the x-axis does not indicate the same gap distance, but a relative displacement.) This agrees well with the intuitive expectation, as the effect of the modulation of the effective index is greater if the diameter becomes larger. The obtained CEs were almost the same for both TE and TM modes (when $Q$ is greater than $10^4$). At the same time, a fluctuation of the measured values was observed when the gap became small. This may be due to the small vibration of nanofiber caused by electric static force or optical force. Figures 5.20(b) and (c) show fittings for the TE mode with a loaded $Q$ of $1.1 \times 10^4$ and a CE of 73%, and for the TM mode with a loaded $Q$ of $2.2 \times 10^3$ and a CE of 22%.
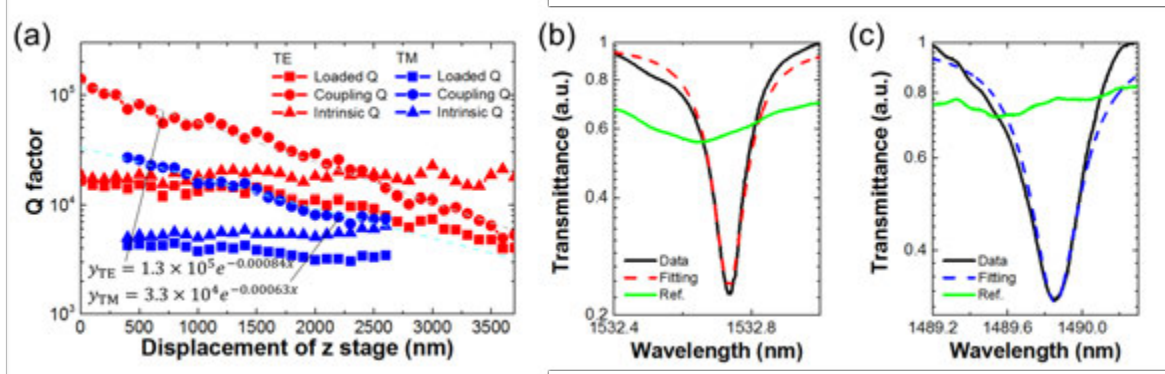
Fig. 5.19. Experimental results measured with a nanofiber with a diameter of 590 nm (see Fig. 5.16(a)). (a) $Q$ factor dependence versus displacement of the Z-stage. The R-squared values of fitted lines are 0.982 for coupling $Q$ of the TE mode and 0.962 for that of the TM mode. (b) Fitting for TE mode obtained with a displacement of 2400 nm. The loaded $Q$ is $1.0 \times 10^4$ and the CE is 73%. (c) Fitting for the TM mode obtained with a displacement of 2400 nm. The loaded $Q$ is $3.2 \times 10^3$ and the CE is 72%.

A summary of each experiment is shown in Tab. 5.1. The highest CE values shown for the condition when the loaded $Q$ is greater than $10^3$ and $10^4$ for the experiments performed with different nanofibers. Interestingly, the highest CE was obtained with the nanofiber with a diameter of 990 nm for both modes; however, a degradation of $Q_{int}$ was observed. This means that a nanofiber with a diameter of less than $1\,\mu$m is thin enough to have a high CE for the silica nanobeam cavity demonstrated here. These results are useful to understand the tunable ranges of the CE, as well as the intrinsic and loaded $Q$ factors.

Table. 5.1: Obtained CEs for each nanofiber.

| Diameter | CE under condition of $Q_{load} > 10^4$ | | CE under condition of $Q_{load} > 10^3$ | |
|---|---|---|---|---|
| | TE | TM | TE | TM |
| 590 nm | 68% w/ $Q_{load} = 1.1 \times 10^4$ | - | 96% w/ $Q_{load} = 1.1 \times 10^3$ | 72% w/ $Q_{load} = 3.2 \times 10^3$ |
| 920 nm | 88% w/ $Q_{load} = 1.1 \times 10^4$ | 31% w/ $Q_{load} = 1.0 \times 10^4$ | 94% w/ $Q_{load} = 2.5 \times 10^3$ | 82% w/ $Q_{load} = 1.2 \times 10^3$ |
| 990 nm | 73% w/ $Q_{load} = 1.1 \times 10^4$ | 37% w/ $Q_{load} = 1.1 \times 10^4$ | 98% w/ $Q_{load} = 1.0 \times 10^3$ | 92% w/ $Q_{load} = 2.4 \times 10^3$ |
| 1210 nm | - | - | 35% w/ $Q_{load} = 2.4 \times 10^3$ | - |

## 5.5 Investigation of tunability of resonant wavelength

Finally, the tunability of the resonant wavelength of the nanobeam cavity by using a nanofiebr is discussed. As demonstrated in the Chapter 3 and Chapter 5.4, the presence of the nanofiber will modulate the effective index of cavities, which will effect the resonant wavelength of the silica nanobeam cavity.

Figure 5.21 shows the resonant wavelength versus the displacement of the stage, which is measured in the experiment in the previous section (see Fig. 5.17 and Fig. 5.19). Interestingly, two results with different trends of the wavelength shift were obtained. Figure 5.21(a) shows
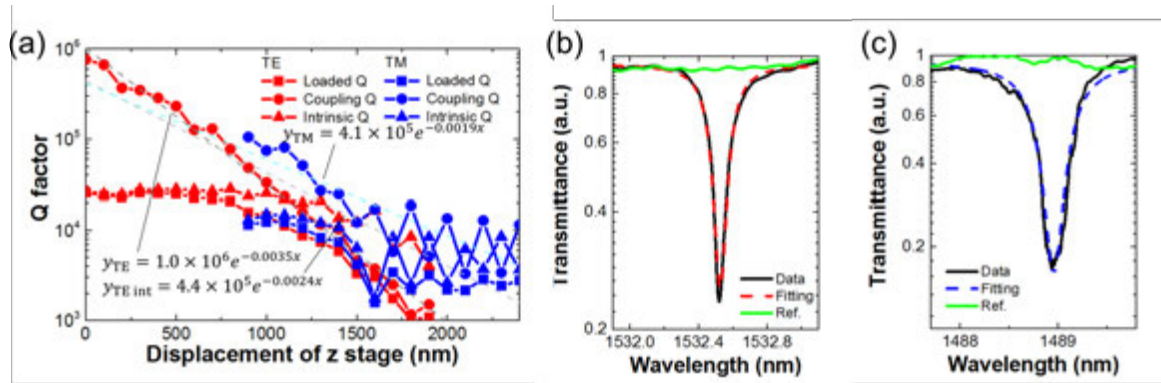
Fig. 5.20. Experimental results measured with a nanofiber with a diameter of 990 nm (see Fig. 5.16(c)). (a) $Q$ factor dependence versus displacement of Z-stage. The R-squared values of the fitted lines are 0.991 for coupling $Q$ of the TE mode, 0.708 for that of the TM mode and 0.761 for the decay rate of the intrinsic $Q$ of the TE mode. (b) Fitting for TE mode obtained with displacement of 1100 nm. The loaded $Q$ was $1.1 \times 10^4$ and the CE was 73%. (c) Fitting for the TM mode obtained with a displacement of 1800 nm. The loaded $Q$ was $2.2 \times 10^3$ and the CE is 22%.

the results measured with the nanofiber with the diameter of 920 nm. The resonant wavelength shifted toward shorter wavelength in this case, although the cutoff wavelength of the nanobeam cavity will shift longer wavelength by the modulation caused by the nanofiber in the same way as shown in Fig. 3.1(a). On the other hand, the resonant wavelength moves toward longer wavelength in the measurement using the nanofiber with the diameter of 590 nm (see Fig. 5.21(b)). This difference in the trend of the wavelength shift can be come from the difference in the effect of modulation. For example, the cavity length will become short when the effective index modulation affects the entire potential of a cavity (see inset of Fig. 5.21(a)). This will lead to the shorter shift of the resonant wavelength. A thick dimpled nanofiber with a large curvature will be required for this wavelength control. On the other hand, the longer shift of the resonant wavelength will be observed if the effective index modulation effects the cavity potential in the limited region (see inset of Fig. 5.21(b)). Then, the cutoff frequency shift will directly lead to the wavelength shift while the cavity length is kept almost constant. A thin dimpled nanofiber with a small curvature will be required for this wavelength control.

Note that the amount of the resonant wavelength shift of TM mode was larger than that of TE mode for both cases. This is because of the lager amount of the evanescent tail of the electric field of the TM mode. The minimum resolutions and the tunable range of the wavelength shift were as follows: TE (920 nm); resolution of 3 pm, range of 310 pm. TM (920 nm); resolution of 7 pm, range of 330 pm. TE (590 nm); resolution of 3 pm, range of 760 pm. TM (590 nm); resolution of 4 pm, range of 280 pm. The demonstrated tunability of the wavelength will be useful to tune a resonance into other mode in the frequency domain although the trends of the shift were not linear but exponential.
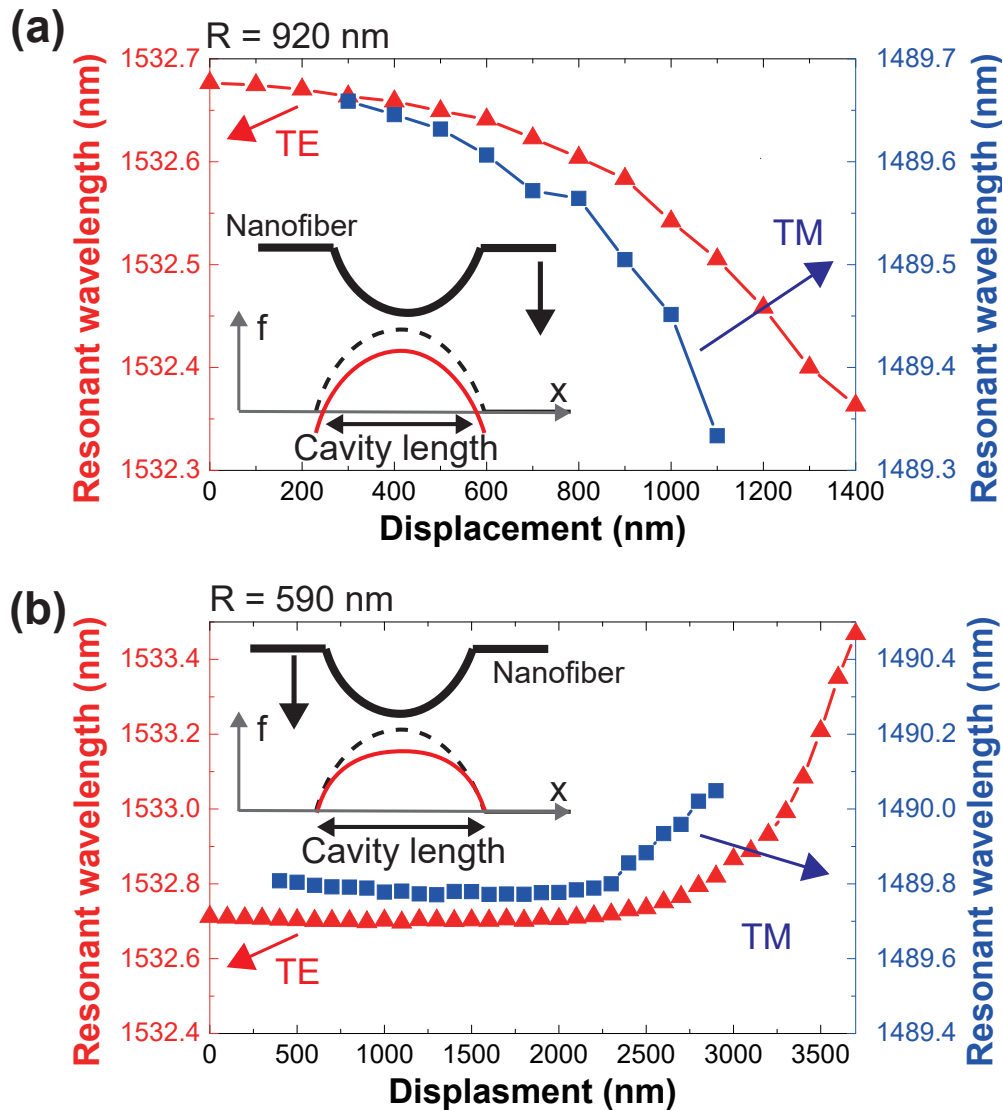
**(a)**



**(b)**



Fig. 5.21. Resonant wavelength shift observed in the measurement in Chapter 5.4. (a) Result for the nanofiber with diameter of 920 nm. (b) Result for nanofiber with diameter of 590 nm. Insets show the schematic illustration of the potential well (modulated frequency) for the cavity formation.

## 5.6 Summary

In this chapter, the fabrication of a silica nanobeam cavity and its experimental characterization were presented. By using tri-layer masks, a fine structure was fabricated and high loaded $Q$ values of $2.4 \times 10^4$ and $1.0 \times 10^4$ were obtained for the TE and TM modes, respectively. In addition, the optimum coupling condition with a nanofiber was investigated. Although the degradation of the intrinsic $Q$ of the cavity was observed when a thick nanofiber was used for the measurement, a thin nanofiber with a diameter of less than 1 $\mu$m enabled us to avoid the effect and obtain a high CE over 95% for the TE mode and 73% for the TM mode. This result indicates that for nanocavities made of low-index materials, such as a silica nanobeam

cavity, compared to the target device, a sufficiently thin fiber is required to achieve a high CE. However, it should be noted that the highest CE values were achieved in the experiment with a slightly thicker nanofiber with a diameter of 990 nm, thus the small degradation effect was negligible. In addition, the demonstrated controllability of the quality factors and the resonant wavelengths of the cavity are useful to increase the spectral overlap between the spectra of the cavities and the emitters.

# Chapter 6

# Silica nanobeam cavity with spectrally overlapped orthogonal modes

Followed by Chapter 5, a silica nanobeam cavity with spectrally overlapped orthogonal modes is discussed in this chapter. Main focuses are the design and the numerical analysis of optical properties of the cavity. The designed cavity will confine both TE and TM resonant modes at same resonant wavelength as well as circularly polarized light propagating along nanobeam structure. Such cavity is necessary for the applications which require polarization diversity.

## 6.1   Strategy for cavity design

First of all, the design strategy for the cavity with spectrally overlapped TE and TM modes is described. Electric fields of TE and TM modes in a nanobeam cavity are shown in Fig. 6.1 and Fig. 6.2. The dominant (strongest) electric component of TE and TM modes are Ey and Ez, respectively. Note that the two components localize at the same place in the beam structure, thus, the electric field at the place will be given by the vectorial sum of Ey and Ez components when the resonant frequencies of the TE and TM modes are identical. It also means that such a cavity will confine a circularly polarized light propagating along the nanobeam since the relative phase between the fields will be preserved if their oscillation frequencies and intrinsic $Q$s are almost identical.

To make the resonant frequencies of the two orthogonal modes be identical, the cutoff frequencies of the two modes need to be sufficiently close in a photonic band diagram. This will be satisfied for isotropic structures for all directions, however, a structure of a nanobeam cavity is asymmetric in principal. Thus, careful control of both effective index and photonic bandgap effect of two orthogonal modes are required to make the structure effectively symmetric. Figure 6.3 shows a schematic diagram of the field distribution of electric and magnetic fields. The electric field of TE mode mainly localizes at region I and region II as shown in Fig. 6.3(b) (Fig. 6.3(a) indicates each region). On the other hand, that of TM mode is confined in region II (Fig. 6.3(c)). Thus, it is expected that reducing the Region I will read to the decrease of the difference of the cutoff frequencies. In fact, the beam structure will be symmetric for Ey and Ez field with the absence of Region I, and the identical width and thickness of the beam, although the implementation of such structure is impossible since the nanobeam needs to be suspended
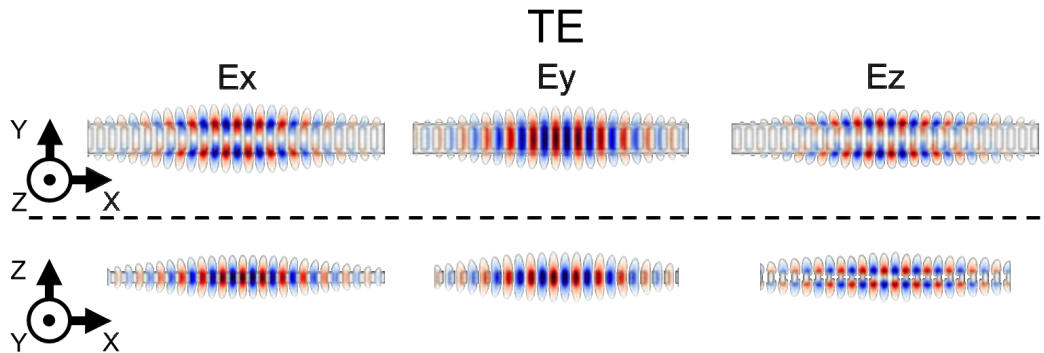
Fig. 6.1. Mode profile of electric field of TE mode in a nanobeam cavity. The top figures are for xy plane and the bottom figures are for yz plane.
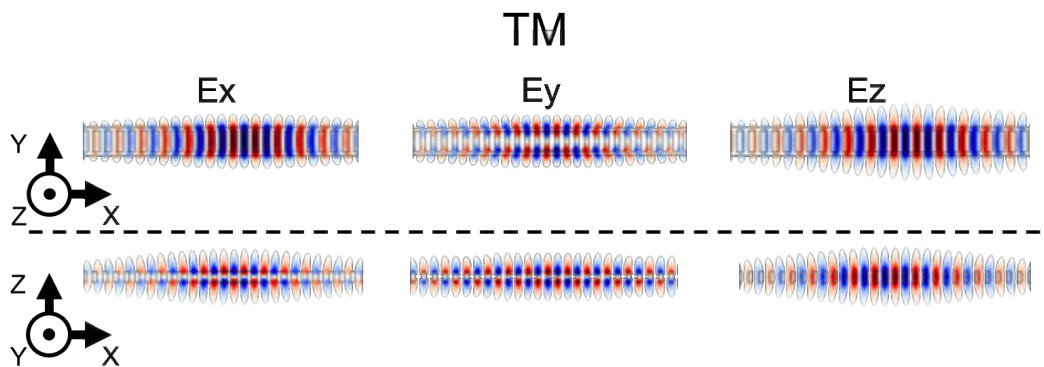


Fig. 6.2. Mode profile of electric field of TM mode in a nanobeam cavity. The top figures are for xy plane and the bottom figures are for yz plane.

in air. On the other hand, reducing Region II will result in the poor confinement of light in dielectric material because dominant electric field components of both modes localize at the region. This may also lead to the reduction of the difference between the cutoff frequencies, however, it is required to take into account the effect of the narrowing of photonic bandgap, which is not an ideal effect for obtaining high $Q$. Investigation of an optimum structure is carried out in the following section.

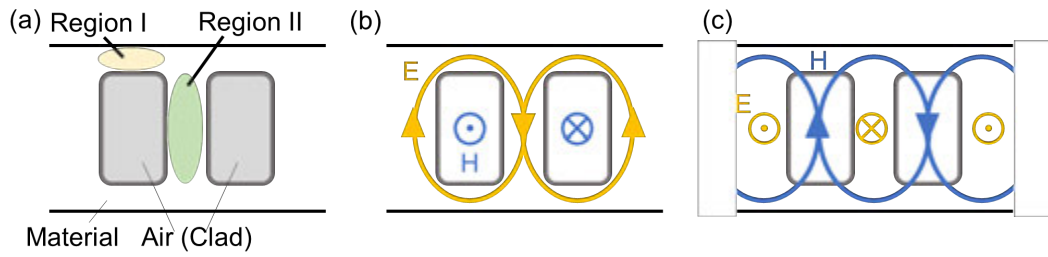Fig. 6.3. (a) Schematic of nanobeam structure. Schematic of electric and magnetic field distribution of (b) TE mode and (c) TM mode.

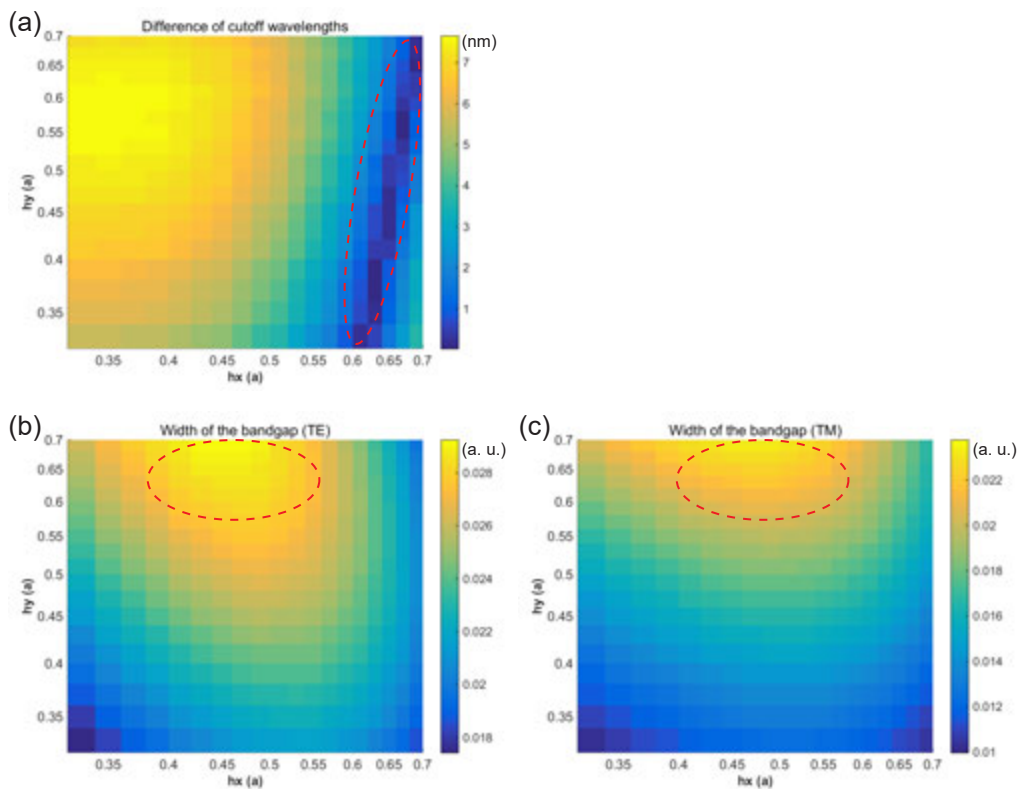# 6.2 Numerical analysis for designing an optimum structure



Fig. 6.4. Mapping of the (a) difference of cutoff wavelengths for different hole sizes, (b) width of the bandgap for TE mode, (c) width of the bandgap for TM mode. Nanobeams with $w = t = 1.0a$ are assumed.
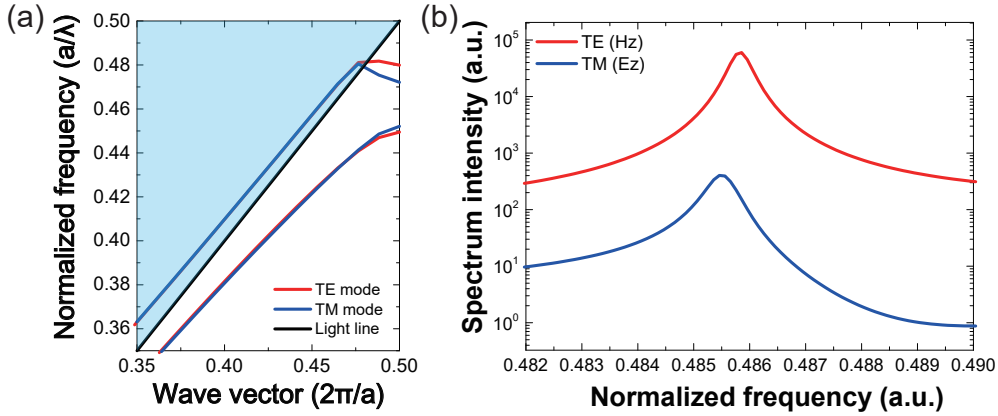
Fig. 6.5. (a) Photonic band diagram of designed structure. Blue shaded region indicates the radiation mode above the light line. (b) Transmission spectrum obtained in FDTD calculation.)

For the quantitative discussion, photonic band diagrams are calculated for nanobeam structure with identical width and thickness, and various hole sizes. Then, difference of the cutoff frequencies between the two orthogonal modes and the width of the photonic bandgap of each mode were calculated. The results are shown in Fig. 6.4. Figure 6.4(a) shows that the difference of the cutoff frequencies decreased with larger hole depth ($h_x$) and width (($h_y$). It is minimized with $h_x$ of about $0.65a$ (indicated by red dashed circle in the figure). However, the widths of the photonic bandgap became small with the design (see Figs. 6.4(b) and (c)), which is not suitable for designing a high $Q$ cavity. The widths of the bandgap are maximized with hole depth of around $h_x = 0.45a$ to $0.50a$ and larger $h_y$ for both modes (indicated by red dashed circles in the figures).

By taking into account these issues, a nanobeam cavity was designed. A photonic band diagram for a unit cell of the cavity and a calculated transmission spectrum are shown in Fig. 6.5. The width and the thickness of the nanobeam were both $w = t = 1.1a$. Hole size of $h_x \times h_y = 0.45a \times 0.55a$ is chosen by considering the trade-off between the frequency difference, $Q$s and the stability of the structure. As shown in Fig. 6.5(a), the dispersion curves of the TE and TM modes are very similar, and which result in the almost identical cutoff frequencies of the two orthogonal modes. In addition, the computed transmission spectra of the two modes were close enough to have sufficient overlap in the spectrum (see Fig. 6.5(b)). To be more specific, the obtained wavelength separation, which corresponds 1.2 nm in the wavelength domain, was smaller than the expected linewidth of the resonance of 1.5 nm ($Q$ of $10^3$ was predicted in FDTD), thus the two orthogonal resonances will be overlapped. Note that the ease of the cavity design can be attributed to the low refractive index silica/air system. This particularly has a strong impact on the TE band structure, leading to moderate band bending. Thus, the frequency difference of two orthogonal modes was initially small. On the other hand, for materials with high refractive indices, it is required to employ special designs, whose fabrication is not easy due to the increase of the slab thickness, to match the two cutoff frequencies [205].

Finally, a circularly polarized light was excited in the nanobeam cavity with Ey and Ez light sources with the phase difference of $\pi/2$ in FDTD simulation. The result is shown in Fig. 6.6. Rotation of electric field was observed for designed structure (Fig. 6.6(b)) whereas only linearly polarized light was observed for the structure designed in previous chapter (Fig. 6.6(a)). This

is due to the fact that Ez component is not confined by the cavity in Fig. 6.6(a). This result proved that the confinement of the circular polarized light propagating along the nanobeam is possible with the designed cavity.
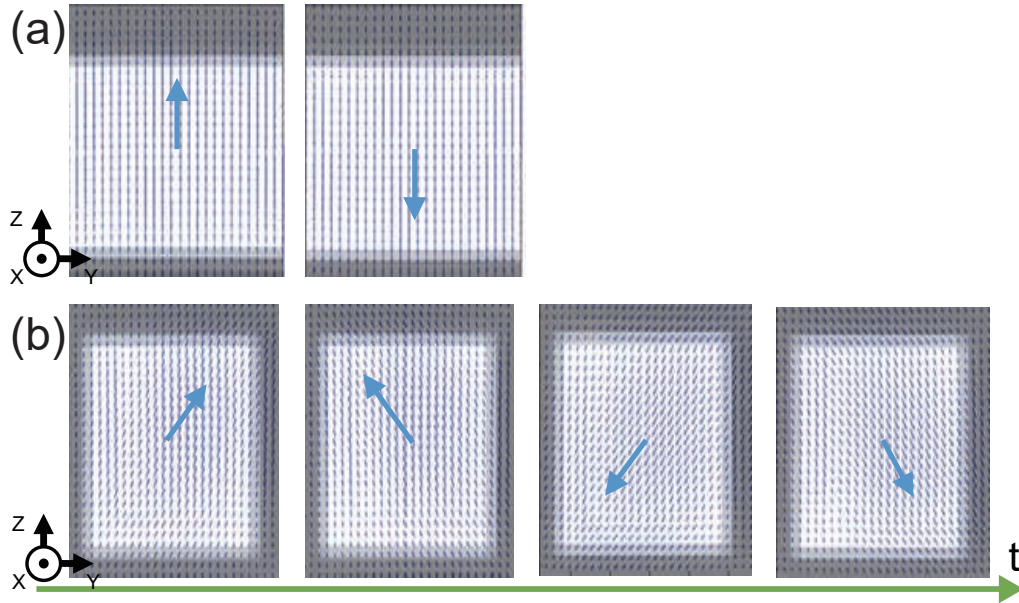


Fig. 6.6. Electric fields in a nanobeam cavity (a) designed in the previous chapter and (b) designed in this chapter.

## 6.3 Experimental characterization
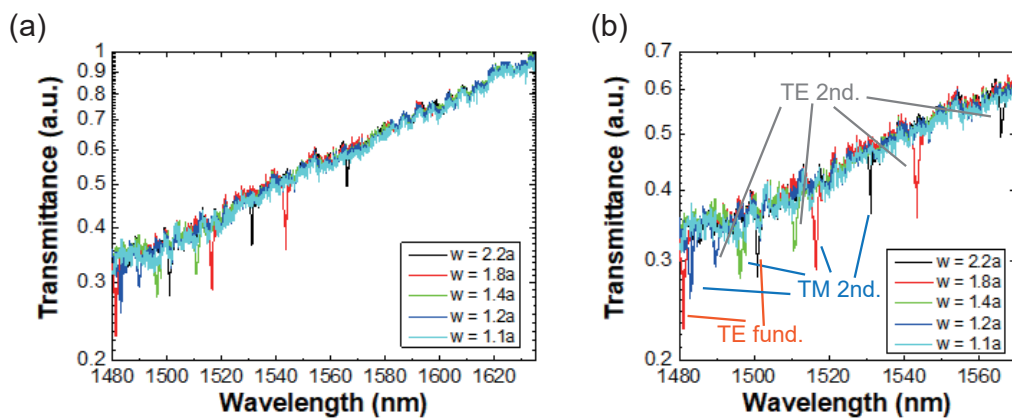


Fig. 6.7. (a) Width vs. transmission spectrum. (b) Enlarged view of (a).

Experimental characterization of nanobeam cavities are presented to show the effectiveness of the design strategy. The fabrication of the cavities was performed in the same way as described in Fig. 5.3. The experimental characterization was also demonstrated with the setup presented in the previous chapter (see Fig. 5.11).

Fig. 6.8. Nanobeam width dependence versus the difference of resonant wavelength of two orthogonal modes.

First, the width dependence versus the resonant wavelength difference was characterized. To address this issue, nanobeam cavities with various widths of $2.2a$, $1.8a$, $1.4a$, $1.2a$, and $1.1a$ are fabricated. The thickness and the hole size were $1.1a$ and $h_x \times h_y = 0.5a \times 0.7w$ respectively. Obtained transmission spectra are shown in Fig. 6.7(a). Polarization of the input light was set so that both TE and TM modes are observ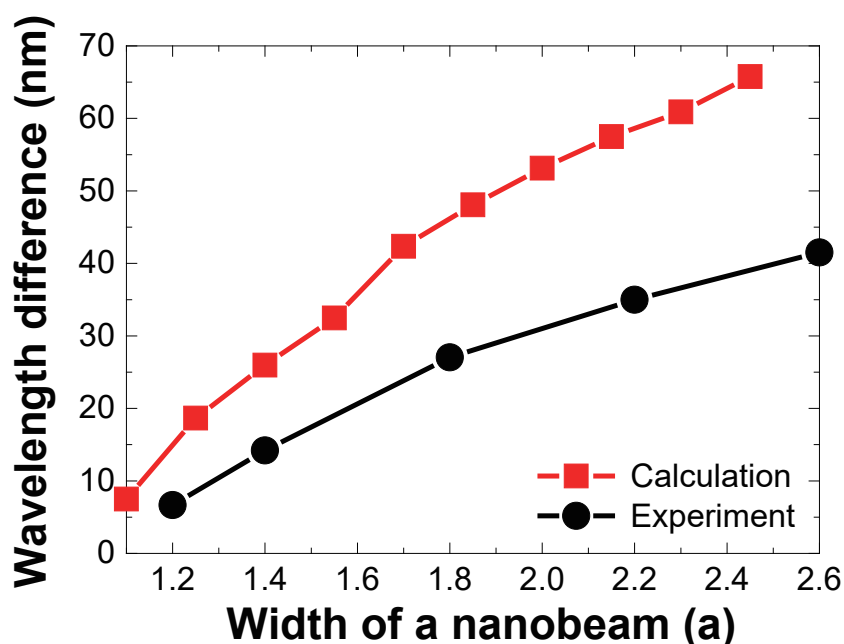ed in the same spectra. Although FDTD calculation predicted that there will be four modes (e.g. the fundamental modes and the second order longitudinal modes of TE and TM modes) in the spectrum (see Fig. 5.2), the fundamental mode of TM mode could not be observed due to the lack of operation wavelength range of the tunable laser diode (1480–1640 nm). Other modes also could not be detected for some cavities. Figure 6.7(b) shows that the resonant wavelengths of each mode shifted toward shorter wavelength as the width became narrower. In addition, the resonant wavelength of the two orthogonal modes got close for a beam with narrower width as shown in Figure 6.8. In other words, the more symmetric structures in the YZ plane showed the small wavelength separation between the orthogonal modes. This result agreed well with the design strategy described in the previous section. Note that the presented calculation result is not for the change in the difference of the resonant wavelengths of the orthogonal mdoes but for the change in the difference of the cutoff wavelengths in photonic band diagrams. This can be the reason for the difference between the experimental results and the calculation result, which implies that FDTD calculation will be required for the precise prediction of an optimum design of the cavity.

Finally, the designed cavity with the spectrally overlapped orthogonal modes was fabricated and measured. Figure 6.9 presents the obtained transmission spectrum. Two orthogonal modes were obtained with the wavelength separation of 3.6 nm. This value was larger than that in the FDTD calculation of 1.2 nm, which will be due to the fabrication imperfection. $Q$ factors of two orthogonal modes are about $1.0 \times 10^3$ which agrees well with calculation. However,
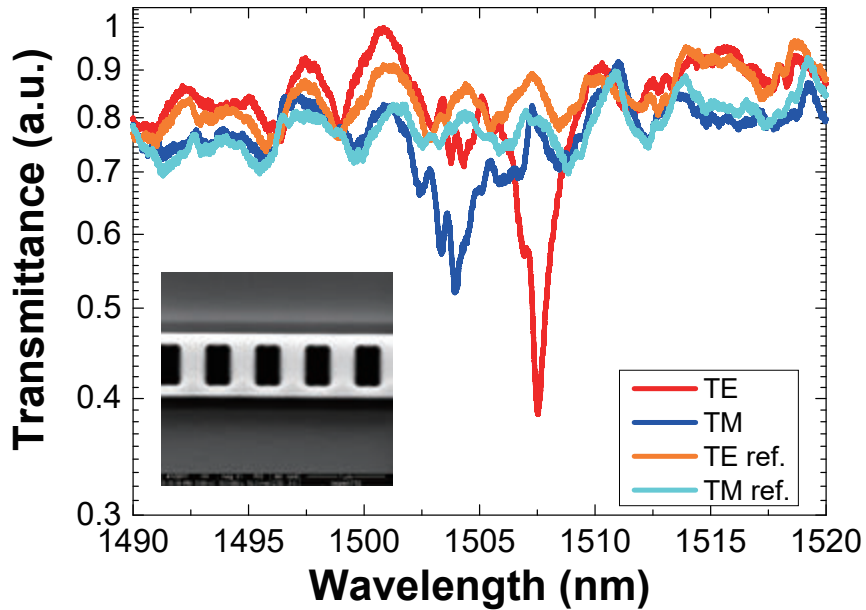
Fig. 6.9. Transmission spectrum of designed cavity. Inset shows a SEM image of the fabricated structure.

this means the lack of the spectral overlap between the two orthogonal modes and the expected functions such as the confinement of the circularly polarized light will not be performed with this cavity.

Although the experimental demonstration of the cavity with spectrally overlapped orthogonal modes was not achieved herein, the obtained results are solid enough to clarify the effectiveness of the described cavity design and its design strategy. The cavity with designed properties will be demonstrated with the improvement of the fabrication technology or the fabrication of cavities with slightly different design parameters to compensate the errors caused by the fabrication.

## 6.4 Summary

Numerical and experimental investigation for obtaining a cavity with spectrally overlapped two orthogonal modes was presented. Design strategy and numerical results were described, which showed the cavity with two orthogonal modes with resonant wavelength separation of 1.2 nm. The localization of the circularly polarized light was also confirmed numerically. In addition, the optimum cavity design was explored experimentally. Nanobeam width dependence versus the wavelength difference between the two orthogonal modes was evaluated. The result showed that the more symmetric design will present the smaller wavelength separation. The fabrication of the designed optimum structure was performed and its transmission spectrum was presented. Two orthogonal modes were obtained with the wavelength separation of 3.6 nm, which was slightly large to obtain sufficient overlap between the orthogonal modes. The optimization of the cavity structure will be made by improving fabrication techniques or fabricating cavities

with different design parameters.

# Chapter 7

# Conclusion

In this chapter, the thesis is concluded. First, the results obtained in each chapter are reviewed to clarify the achievements and the relationship between the chapters. Then, the summary and outlook of the thesis are presented.

## 7.1 Summary of each chapter

### 7.1.1 Fiber-coupled photonic crystal cavity (Chapter 3)

In Chapter 3, the characteristic of a FCPC was presented both numerically and experimentally. The optical properties of the fiber-coupled resonance were studied in detail. First, a sharp dip spectrum was analyzed and a $Q_{load}$ of greater than half million and a high CE of 31% were obtained for the mode, whose strong localization in the PhC waveguide was confirmed by observing an IR image and TO nonlinearity. The fine-tuning of the resonant wavelength was performed with the resolution of 27 pm for 100 nm stage displacement. Next, the conditions for the efficient coupling between the cavity and the nanofiber were investigated. The phase-matching condition was explored experimentally by measuring the PhC waveguides using the nanofibers with various diameters. The obtained coupling wavelength agreed well with the numerical calculation. By employing the nanofiber with an optimum diameter, the highest CE of 99.6% was obtained for a mode with a $Q_{load}$ of $6.1 \times 10^3$, which is the highest value for coupling between a PhC nanocavity and a nanofiber. This result is a crew that $Q_{load}$ can be controlled from an order as low as $10^3$ with our method.

### 7.1.2 Coupled cavity formation on the FCPC platform (Chapter 4)

Chapter 4 investigated the techniques to form a coupling between the two optical modes in the FCPC platform. First, the formation of the coupled resonance was demonstrated by employing the controllability of the resonant wavelength of FCPC resonances. Two modes were tuned so that their resonant wavelengths matched each other. Then, the anti-crossing with coupling strength of 0.94 GHz and 1.8 GHz were obtained clearly in the spectrum. Numerical analysis was performed using coupled mode equations. The result clarified that the dominant path of energy exchange was the direct coupling between the cavities. In the latter half of the chapter,

97

the control of the position of the cavity was presented. A cavity was formed by the effective index modulation of the PhC waveguide, and the reconfigurability of its position was shown. This technique is useful to form a cavity at an arbitrary place in the PhCs and strengthen the coupling between the cavity and other elements. This also means that the modification of the mode profile of a cavity is possible.

### 7.1.3 High-$Q$ silica nanobeam cavity (Chapter 5)

Chapter 5 reported the design, fabrication, and characterization of a silica nanobeam cavity. The TE and TM modes with a high $Q_{\mathrm{load}}$ greater than $10^4$ were demonstrated, which are the record-high values for silica PhC nanocavities. This proves the high quality of the fabrication method using the tri-layer mask. A coupling efficiency greater than 95% was achieved with a nanofiber by controlling the gap distance between the structures. The demonstration showed that a thin nanofiber with a diameter of less than 1 $\mu$m is effective to achieve high CE while avoiding too much degradation of intrinsic $Q$ due to the index modulation caused by the nanofiber. This provides us with the general design strategy for efficient coupling in the side-coupling configuration consisting of a waveguide and a nanocavity with almost the same effective index. In addition, both the tunability of coupling $Q$ and the degradation of intrinsic $Q$ are effective to tune the total loss (loaded $Q$) of the cavity.

### 7.1.4 Silica nanobeam cavity with spectrally overlapped orthogonal modes (Chapter 6)

Chapter 6 described the design of a silica nanobeam cavity with two spectrally overlapped orthogonal modes. FDTD calculation showed that the design of such a cavity with $Q_{\mathrm{int}}$ of the order of $10^3$. It also demonstrated the localization of circularly polarized light in the cavity, which will allow us to control the spin-dependent state in quantum light sources without affecting the degree of freedom of the polarization. Although the fabrication of the designed cavity has not been achieved perfectly, it will be possible with the fine-tuning of fabrication parameters. This study will pave the way to realize a new type of PhC nanocavity with polarization diversity.

## 7.2 Conclusion and outlook of the thesis

In this study, a nanofiber-based tailoring method of optical properties was demonstrated for two types of PhC nanocavities. The technique will meet the requirements for PhC nanocavities in the cavity QED applications. Table. 7.1 summarizes the obtained properties for the two nanocavities. The high CEs of over 95% were achieved for both modes. These are comparable to the typical CE between two optical fibers of about 95%, thus they will meet the requirement for the practical use. The obtained small mode volumes of several qubic wavelengths are small values which are difficult to be achieved in dielectric materials without the presence of PhCs. The demonstrated controllability of $Q_{\mathrm{load}}$ and the resonant wavelength are useful to maximize the spectral overlap between a cavity and an emitter. The $Q_{\mathrm{load}}$ was controlled from the order of $10^5$ to $10^3$ for the FCPC, and from the order of $10^4$ to $10^3$ for the silica nanobeam

cavity, respectively. The resolutions of wavelength tuning of 27 pm and 3 pm were achieved for the FCPC and the silica nanobeam cavity, respectively, which correspond to the emission linewidth of around $\Delta\lambda = \lambda_0/10^6$ =1.5 pm ($\Delta f$ =200 GHz) and $\Delta\lambda = \lambda_0/10^7$ =0.15 pm ($\Delta f$ =20 MHz) ($\lambda_0$ = 1500 nm is assumed). The tunable ranges were about 100 times larger than the resolutions. Therefore, by taking into account the controllability of both $Q_{\text{load}}$ and resonant wavelength, the tailoring method will be effective for the optical resonance tuning into emitters with emission linewidth of $\lambda_0/10^3$ =1.5 nm ($\Delta f$ =200 GHz) to $\lambda_0/10^6$ =1.5 pm ($\Delta f$ =200 MHz) in the FCPC, and $\lambda_0/10^4$ =150 pm ($\Delta f$ =20 GHz) to $\lambda_0/10^7$ =0.15 pm ($\Delta f$ =20 MHz) in the silica nanobeam cavity, respectively. The position control of the cavity was only demonstrated for the FCPCs. The achieved resolution was 1 $\mu$m, which will be reduced to as small as that of the sample stage. Since the cavity length was around 1 $\mu$m, the tuning method will cover all places in a PhC with a precision stage with resolution of the order of less than 1 $\mu$m. Then, this method can be applied to increase the spatial overlap between an optical mode and even a quantum dot, which is the smallest emitter in substrates with a dimension of about tens nanometers. The design of the cavity which support both TE and TM mode at an identical resonant wavelength was presented for a silica nanobeam cavity. Such PhC nanocavities will be required for achieving the polarization diversity. On the other hand, the demonstrated tailoring method will be useful to tune the difference of the resonant wavelengths of two orthogonal modes precisely since the amount of wavelength shift of each mode will be different depending on the approaching direction of a nanofiber as demonstrated for the silica nanobeam cavity.

Table. 7.1: Summary of the obtained properties

| Parameter | Si FCPC | Silica nanobeam |
|---|---|---|
| CE with an optical fiber | Over 99% | Over 95% |
| Small $V$ | $1.9(\lambda/n)^3$ | $1.1(\lambda/n)^3$ |
| Controllability of $Q_{\text{load}}$ | Down to $6.1 \times 10^3$ | Down to $1.0 \times 10^3$ |
| Controllability of resonant wavelength | Resolution of 27 pm [*a] Range of around 2.7 nm | Resolution of 3 pm/nm [*a] Range of around 0.5 nm |
| Position selectivity | Resolution of 1 $\mu$m | Not achieved |
| Polarization diversity | Not achieved | Design is presented |

I believe that the presented tailoring method and the PhC nanocavities are useful for cavity QED applications; however, further research is necessary before the practical implementation of the method. Two issues are addressed as an outlook for describing the remaining challenges in its implementation as followed.

First, the integration of the whole system including a nanofiber is required. Although the PhC nanocavities used in this study were fabricated on chips, a nanofiber was suspended at the zigs outside the chips, and this is problematic for packaging the devices. This problem will be solved by employing the techniques used for the integration of nanofibers and optical microelectromechanical systems (MEMS). Some studies that integrate a nanofiber and nano and microcavities on the same chip have been demonstrated (Fig. 7.1(a)) [206,207]. Following

---

[*a]Resolution is defined by amount of wavelnegth shift for 100 nm–displacement of the sample stage).

the methods presented in the study, the integration of the nanofiber is possible. In addition, the precise control of the position of microstructures is demonstrated in the field of MEMS [208, 209]. For example, the resonant wavelength of a nanobeam cavity was controlled in an optical MEMS system (Fig. 7.1(b)). Combining the two technologies, the complete packaging of a nanofiber and PhC nanocavities in a chip will be achieved with the controllability of the optical properties demonstrated in this study. It is also interesting to control the distance between the cavity and the nanofiber with the radiation force acting between them as demonstrated in Ref. [210].
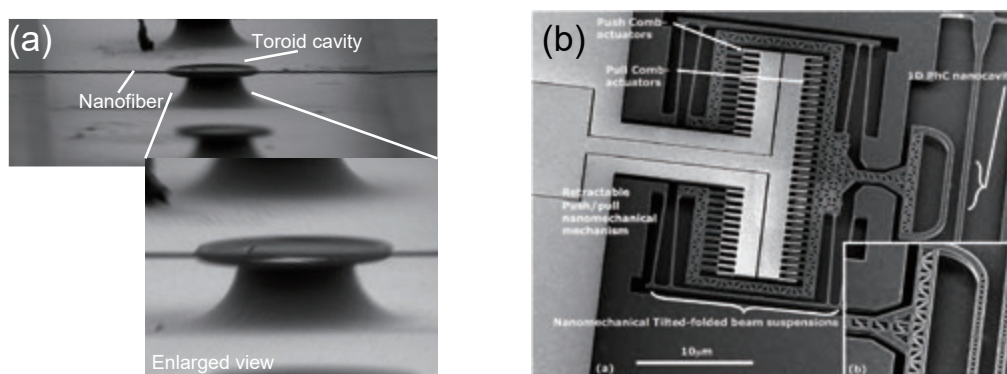


Fig. 7.1. (a) SEM image of a packaged nanofiber [207]. (b) SEM image of a MEMS system to tune the optical resonance [209]. [Reprinted with permission from X. Chew, *et al.*, Opt. Express **18**, 22232–244 (2010).]

The other issue is the implementation of the position selectivity of a cavity in a nanobeam structure. Since the demonstrated formation of a cavity is based on the down-shift of the cutoff frequency of the guided mode of a periodic structure, it is not effective for a nanobeam structure in which a cavity was formed by the up-shift of the cutoff frequency. This is a reason why position selectivity was not achieved for the silica nanobeam cavity. There are two ways to solve this problem. The first method employs a nanofiber with a dimple toward the upper direction. When such a nanofiber is brought close to a nanobeam, the cutoff frequency of the guided mode will be higher than those at the other places. This will result in the formation of a cavity where its position can be controlled by changing the position of the nanofiber. Note that the curvature of the dimple needs to be very small (order of a few micrometers) to obtain the small mode volume for this case. The other option is forming a cavity by the down shift of an air band as demonstrated in the other study [211]. This will be possible with the same way demonstrated in this study; however, it will result in a cavity with poor light confinement in the core layer. For both cases, employing materials with a higher refractive index than silica will be required. The lack of refractive index contrast between the core layer and the nanofiber will degrade the $Q_{int}$ of the cavity. Silicon nitride is a possible alternative material since it possesses a moderate refractive index of 2.0, and hence, the proposed design strategy will be applicable. Further, silicon nitride is transparent in the visible to telecommunication wavelength range.

In addition, the use of the demonstrated cavities for the optical processing is also promising. For example, FCPC can be used as a delay line. The platform is suitable to form a coupled cavity system consisting of a lot of optical cavities as shown in Fig. 3.14. Such system modulates the dispersion relation of light and controls its group velocity as demonstrated in studies on

coupled-resonator optical waveguides [154, 212, 213]. The large group velocity delay and the enhanced strong optical nonlinearity will be achieved with the FCPC formed on a PhC waveguide with multiple cavities.

On the other hand, the silica nanobeam cavity with spectrally overlapped two orthogonal modes will work as a quarter wave plate if the relative phase between the two modes is the half of $\pi$ at a certain wavelength in resonance. As shown in the Chapter 2.2.3, the relative phase of output light from a cavity depends on the wavelength of the light. Thus, the phase difference between the orthogonal modes will be controlled by changing their difference in the resonant wavelength. Note that the resonant wavelength difference can be easily tuned for the PhC nanocavity by changing the design as presented in the Chapter 6. If a linearly polarized light consisting of the two orthogonal modes (polarization of 45 degree) is coupled with a cavity with the relative phase difference between the two modes of half of $\pi$, the output will be circularly polarized light. The compactness of the structure is attractive for integrated optical circuits.

In conclusion, a method for tailoring the optical properties of PhC nanocavities was demonstrated for two types of PhC nanocavities. The obtained properties will be useful for cavity QED applications. I hope that this study will make readers interested in the unique use of the nanofiber and contribute for the development of quantum information technologies.

# Appendix A

# Product values of optical equipments

Table. A.1: Product values of tunable laser diodes

| Parameter | TSL-710 (Santec) | TSL-510 (Santec) |
|---|---|---|
| Wavelength tuning range [nm] | 1480-1640 | 1500-1630 |
| Wavelength setting resolution [pm] | 0.1 | 1 |
| Wavelength absolute accuracy [pm] (25 ± 1 degC) | ±1 | ±2.5 |
| Wavelength repeatability [pm] | ±1 | ±2 |
| Wavelength stability [pm] | ±1 | $\leqq \pm 1$ |
| Wavelength sweep speed [nm/sec.] | 0.5 to 100 | 1 to 100 |
| Max output power [dBm] | 20 | 15 |
| Power stability [dB] | ±0.01 | ±0.01 |
| Spectrum linewidth [KHz] | 100 | 200 |
| Side mode suppression ratio [dB] | $\geqq 45$ | $\geqq 45$ |

Table. A.2: Product values of power meters: Keysight8163b (Keysight)

| Parameter | Keysight81634b | Keysight81636b |
|---|---|---|
| Wavelength range [nm] | 800-1700 | 1250-1640 |
| Power range [dBm] | +10 to -110 | +10 to -80 |
| Uncertainty [%] | ±2.5 | ±2.5 |
| Noise (peak to peak) [pW] | < 0.2 | < 20 |

# APPENDIX A.  PRODUCT VALUES OF OPTICAL EQUIPMENTS

Table.  A.3: Product values of a variable optical attenuator: DA-100-3A (OZ Optic)

| Parameter | Values |
|---|---|
| Typical insertion loss (IL) [dB] | 1.0 |
| Attenuation range [dB] | IL-60 |
| Attenuation resolution [dB] | 0.01 |
| Wavelength dependence of attenuation (1300-1550) [dB] | up to 0.3 |
| Wavelength dependence of attenuation (1520-1570) [dB] | up to 0.1 |
| Typical polarization dependence loss [dB] | up to 0.05 |
| Repeatability of attenuation setting (up to 30 dB) [dB] | ±0.10 |
| Maximum optical power [W] | 2 |

Table.  A.4: Product values of a polarization controller: MLC series (Alnair Lab)

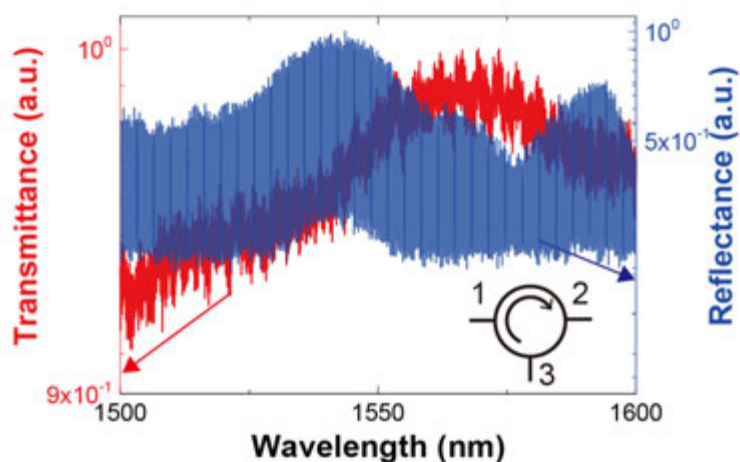| Parameter | Values |
|---|---|
| Operational wavelength range [nm] | 1550 |
| Insertion loss (frame) (max.) [dB] | 0.8 |
| Insertion loss (half and quarter-wave plate) (typical) [dB] | 0.1 |
| Insertion loss (polarizer) (typical) [dB] | 0.1 |
| Loss variation (half and quarter-wave plate) (typical) [dB] | 0.1 |
| Extinction ratio (polarizer) (min.) [dB] | 35 |



Fig.  A.1. Measured transmittance (port1 to port2) and reflectance (port2 to port3) of a circulator. Inset shows a schematic of the circulator. Obtained transmittance and reflectance were normalized by dividing by 76.7 $\mu$W and 0.0127 $\mu$W respectively

Table. A.5: Product values of precision position stages

| Parameter | FS-1020PX (Sigma Tech.) | FS-1010PZ (Sigma Tech.) |
|---|---|---|
| Stroke [mm] | 20 | 10 |
| Resolution [nm] | 10 | 10 |
| Positioning repeatability [nm] | ±20 | ±20 |
| Load-bearing [N](kgf) | 49(5) | 49 (5) |

Table. A.6: Measured product values of a circulator (a schematic is illustrated in Fig. A.1)

| Parameter | FS-1020PX (Sigma Tech.) |
|---|---|
| Transmittance (port 1-2) [dB] | -1.32 |
| Transmittance (port 2-3) [dB] | -0.68 |
| Transmittance (port 3-1) [dB] | -74.0 |
| Transmittance (port 3-2) [dB] | -57.3 |
| Transmittance (port 2-1) [dB] | -61.7 |
| Transmittance (port 1-3) [dB] | -54.3 |

Table. A.7: Product values of an IR camera

| Parameter | SU320KTS-1.7RT (Goodrich Corp.) |
|---|---|
| Spectral response [nm] | 0.9 to 1.7 $\mu$m |
| Quantum efficiency (1.0 to 1.6 $\mu$m) [%] | > 65 |
| Exposure time [ms] | 0.12 to 14.93 in 8 steps *, 16.57 ** |
| Gain (typical) [e$^-$/count] | 180 *, 180 to 16000 in 8 steps ** |
| Full Well (typical) [ke$^-$] | 700 *, 700 to 45000 in 8 steps e$^{-1}$/count in 8 steps ** |
| Mean detectivity [cm$\sqrt{\text{Hz}}$/W] | $5 \times 10^{12}$ |
| Noise (RMS) [e$^-$] | < 300 |
| Noise equivalent irradiance [photons/cm$^2 \cdot$ s] | $< 3.5 \times 10^9$ |
| True dynamic range | > 2500 : 1 |
| Optical fill factor [%] | > 100 |
| Operability [%] | > 99 |

*: in variable integration time modes. **: in variable gain, fixed integration time mode.

# Appendix B

# Derivation of the Purcell enhancement factor

The spontaneous emission rate $W_{\text{cav}}$ for an emitter in a cavity is obtained from the Fermi's Golden Rule [127, 128],

$$W_{\text{cav}}(\omega_0) = \frac{2\pi}{\hbar^2} \int_0^\infty M^2 \rho(\omega) \Lambda(\omega) d\omega \tag{B.1}$$

where $M^2$ is a matrix element for an electric dipole transition, $\rho(\omega)$ and $\Lambda(\omega)$ are the density of states for the cavity and the emitter respectively. Here, $M^2$ is expressed by,

$$M^2 = |<f|H|i>|^2 = \xi^2 \frac{\omega_0 \hbar \mu^2}{2\varepsilon V} \tag{B.2}$$

in which $H$ is the matrix operator for electric dipole radiation, $\xi^2$ is a polarization factor, which is equal to 1/3 when the dipole is randomly oriented, $\mu^2$ is the transition dipole moment, $\varepsilon$ is the permittivity in the medium, $V$ is the mode volume of the cavity. Both values of density of state are usually expressed by Lorentzians. For instance, $\rho(\omega)$ is

$$\rho(\omega) = \frac{2}{\pi} \frac{\Delta\omega_{\text{cav}}}{4(\omega - \omega_{\text{cav}})^2 + \Delta\omega_{\text{cav}}^2} \tag{B.3}$$

where $\omega_{\text{cav}}$ is the FWHM of the cavity resonance. In general, the emitter spectrum is assumed to be much narrower compared to that of cavity. If a delta function centered at the emitter's angular frequency of $\omega_0$ is applied for the emitter density of state of $\Lambda(\omega) = \delta(\omega - \omega_0)$, $W_{\text{cav}}$ becomes,

$$W_{\text{cav}}(\omega_0) = \frac{2\pi}{\hbar^2} \xi^2 \frac{\omega_0 \hbar \mu^2}{2\varepsilon V} \frac{2}{\pi \Delta\omega_{\text{cav}}} \frac{\Delta\omega_{\text{cav}}^2}{4(\omega_0 - \omega_{cav})^2 + \Delta\omega_{\text{cav}}^2} \tag{B.4}$$

The Purcell enhancement factor $F_p$ is the ratio of the spontaneous emission rate in the cavity to that in the free space of $W_{\text{FR}} = \omega_0^3 \mu^2/(3\pi\varepsilon\hbar c^3)$, so it is deformed to be

$$F_p = \frac{2\pi}{\hbar^2} \xi^2 \frac{\omega_0 \hbar \mu^2}{2\varepsilon V} \frac{2}{\pi \Delta\omega_{\text{cav}}} \frac{\Delta\omega_{\text{cav}}^2}{4(\omega_0 - \omega_{cav})^2 + \Delta\omega_{\text{cav}}^2} \frac{3\pi\varepsilon\hbar c^3}{\omega_0^3 \mu^2} \tag{B.5}$$

## APPENDIX B. DERIVATION OF THE PURCELL ENHANCEMENT FACTOR

When the $\omega_{\text{cav}} = \omega_0$ is satisfied, the equation becomes,

$$F_p = \xi^2 \frac{3Q(\lambda/n)^3}{4\pi^2 V} \tag{B.6}$$

where the relations of $\Delta\omega_{\text{cav}} = \omega_{\text{cav}}/Q$, $\omega_0 = 2\pi cn/\lambda$ are used. Equation (B.6) is the simple form where most studies employ. On the other hand, if the relation between the spectrum of the emitter and the cavity is opposite (i.e. cavity linewidth is much narrow than that of emitter), the Eq. (B.1) becomes,

$$W_{\text{cav}}(\omega_{\text{cav}}) = \frac{2\xi^2\mu^2}{\hbar\varepsilon V} \frac{\Delta\omega_0^2}{4(\omega_{\text{cav}} - \omega_0)^2 + \Delta\omega_0^2} \tag{B.7}$$

Note that the equation does not depend on the cavity linewidth $\Delta\omega_{\text{cav}}$ (quality factor) but the cavity volume and the emitter linewidth $\Delta\omega_0$. In other word, high $Q$ of the cavity will not effect the spontaneous emission enhancement. Finally, the general case is described. In this case both cavity and emitter have Lorentzian shape, so the evaluation of the following integral is required.

$$W_{\text{cav}}(\omega_0, \omega_{\text{cav}}) = A \int_0^\infty \frac{1}{\pi^2} \frac{\delta_0}{\delta_0^2 + (\omega - \omega_0)^2} \omega_0 \frac{\delta_{\text{cav}}}{\delta_{\text{cav}}^2 + (\omega - \omega_{\text{cav}})^2} d\omega \tag{B.8}$$

where $A$ represents the constant of $\xi^2\pi\mu^2/(\varepsilon V\hbar)$, $\delta_0$ and $\delta_{\text{cav}}$ are the HWHM of the cavity and the emitter spectra, respectively. Assuming $\delta_{\text{cav}} \ll \omega_{\text{cav}}$ and $\delta_0 \ll \omega_0$, which are satisfied for most cases in applications in the optical domain, the equation is simplified to be as follows [128],

$$W_{\text{cav}}(\omega_0, \omega_{\text{cav}}) = \frac{2\xi^2\mu^2}{\hbar\varepsilon V} \frac{\omega_0\Delta\omega_{\text{cav}} + \omega_{\text{cav}}\Delta\omega_0}{4(\omega_0 - \omega_{\text{cav}})^2 + (\Delta\omega_{\text{cav}} + \Delta\omega_0)^2} \tag{B.9}$$

This express the more general spontaneous enhancement factor. When $\omega_{\text{cav}} = \omega_0$ is satisfied, the equation is deformed to be,

$$\begin{aligned}
W_{\text{cav}}(\omega_0, \omega_{\text{cav}}) &= \frac{2\xi^2\mu^2}{\hbar\varepsilon V} \frac{\omega_0(\Delta\omega_{\text{cav}} + \Delta\omega_0)}{(\Delta\omega_{\text{cav}} + \Delta\omega_0)^2} \\
&= \frac{2\xi^2\mu^2}{\hbar\varepsilon V} \frac{\omega_0}{\Delta\omega_{\text{cav}} + \Delta\omega_0} \\
&= \frac{2\xi^2\mu^2}{\hbar\varepsilon V} \left(\frac{\Delta\omega_{\text{cav}} + \Delta\omega_0}{\omega_0}\right)^{-1} \\
&= \frac{2\xi^2\mu^2}{\hbar\varepsilon V} \left(\frac{\Delta\omega_{\text{cav}}}{\omega_{\text{cav}}} + \frac{\Delta\omega_0}{\omega_0}\right)^{-1} \\
&= \frac{2\xi^2\mu^2}{\hbar\varepsilon V} (Q_{\text{cav}}^{-1} + Q_0^{-1})^{-1}
\end{aligned} \tag{B.10}$$

where $Q_{\text{cav}}$ and $Q_0$ are the quality factor of the cavity and that of the spectrum of the emitter. Therefore, the enhancement factor is limited by the wider spectrum of either the cavity or the emitter.

# Appendix C

# Investigation of the origin of multiple resonances

The origin of multiple resonant peaks is discussed herein. As shown in Fig. 3.14 in Chapter 3, multiple resonant dips were observed. Although these dips exhibit a clear polarization dependence, as shown in the figure, the expected cavity length is much larger compared to the actual contact length of the nanofiber (i.e., the obtained mode spacing is approximately $\Delta\lambda = 0.2$ nm on an average. If the observed modes are assumed to be the longitudinal modes of a single cavity, the cavity length should be approximately 1.5 mm; this length is 10 times larger than the total length of the sample of 100 $\mu$m).

The experiment illustrated in Fig. C.1 was conducted to investigate the origin of the multiple resonant peaks. The samples were measured in both direct and side-coupling configurations. Note that the nanofiber was absent when the direct coupling measurement was demonstrated; during this measurement, light was focused using focusing lenses and coupled to the SSC. The samples for measurement were fabricated via partial etching of the clad using HF, as shown in Fig. C.2(a). Partial etching is necessary because silicon wires and SSCs were flowed away if the wet chemical etched the clad above them. Figure C.2(b) shows an SEM image of the fabricated structure. The window of the air clad was opened only above the PhC structures. Figure C.3 to Fig. C.7 show the experimental results for different PhC waveguides measured using the same nanofiber. These results can be categorized into three groups: Group 1: The results wherein resonances were observed only in the transmission spectrum for side coupling (Fig. C.3 and Fig. C.6); Group 2: The results wherein resonances were observed in both transmission spectra (Fig. C.4 and Fig. C.7); and Group 3: The results wherein no resonance was observed (Fig. C.5(a) and (b)). The results of Group 1 were those initially expected (no resonances are present in the PBG), and the results of Group 3 indicate that the nanofiber diameters were not suitable for side coupling with the samples. However, the results of Group 2 suggest that resonances may have been originally present in the structure. Indeed, 2D FDTD calculation and experimental results in Ref. [214] predict that approximately five resonances exist because of the random localization of light, if the randomness of position and hole size are taken into account. Thus, it is expected that random localization modes existed in all waveguides, however, they were not detected in the measurement for the waveguides of Group 1 and Group 3. Resonances could not be found in the transmission spectrum of the direct coupling configuration possibly because of the number of barrier layers. In other words,

light cannot be coupled to the cavity in a structure with many barrier layers; hence, resonances were not found in the spectrum of Group 1 and Group 3.

Finally, the results measured using a dimpled nanofiber in Fig. 3.14 were compared with those measured using a straight nanofiber (Fig. C.8). As shown, the number of resonances in the spectrum measured using the dimpled nanofiber of 31 is larger than that measured using the straight nanofiber of 15 despite its shorter contact length. Since the dimpled nanofiber modulates the effective index of the PhC waveguide locally, this implies that some resonances are formed by the index modulation caused by the nanofiber as demonstrated in Chapter 4.2.

In summary, several resonant modes formed by the randomness of the PhCs were observed, which means the obtained FCPC modes included two types of modes; one was formed by the randomness of the structure and the other was formed by the effective index modulation. Counting the total number of the random modes is difficult due to two reasons. First, the resonances were sometime not observable in the measurement in direct coupling configuration due to the excessive number of barrier layers. Second, there are too many modes to demonstrate the analysis for identifying random modes as demonstrated in Chapter 4.2.
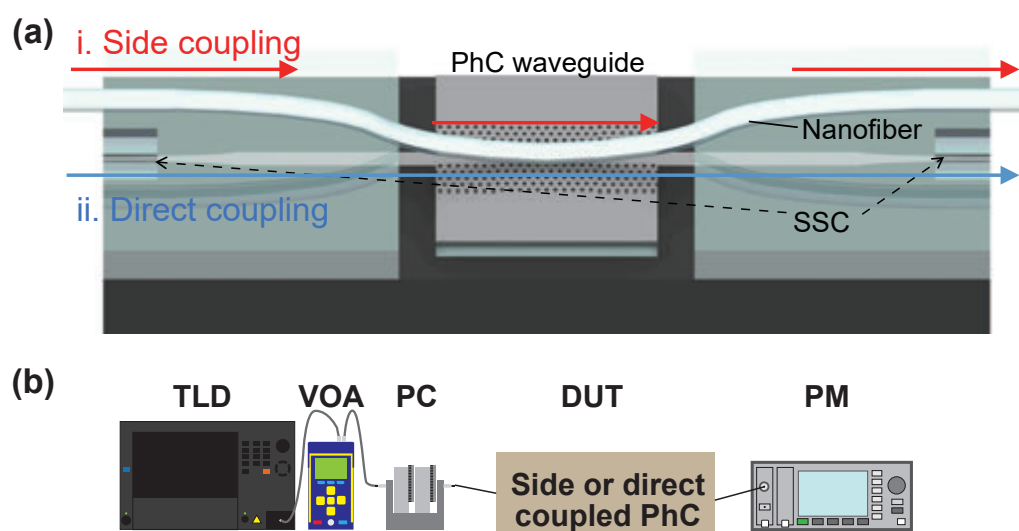


Fig. C.1. (a) Schematic of coupling methods. (b) Experimental setup. TLD: tunable laser diode. VOA: variable optical attenuator. PC: polarization controller. DUT: device under test. PM: power monitor.
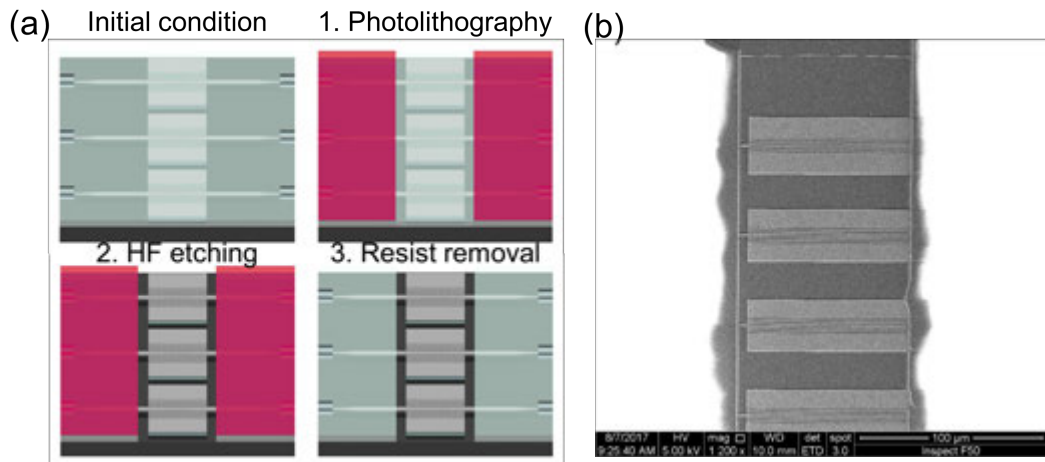
Fig. C.2. (a) Fabrication procedure for partially etched sample. (b) SEM image of fabricated sample.
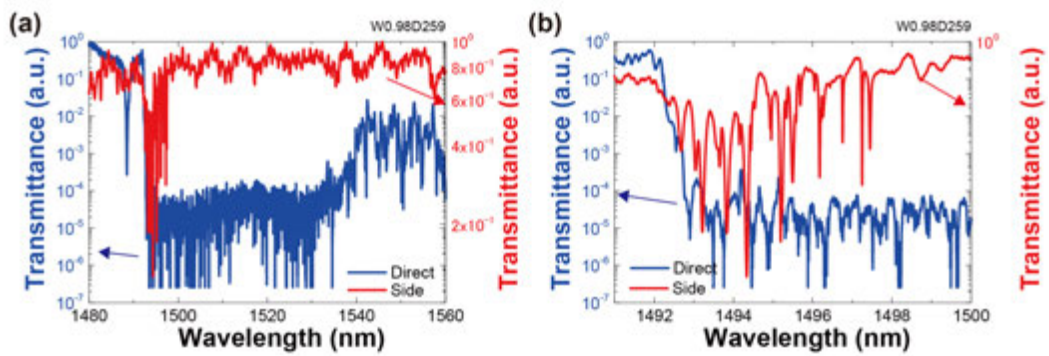


Fig. C.3. (a) Transmission spectrum of PhC waveguide with a width of $0.98 \times \sqrt{3}a$ and a diameter of 259 nm. (b) Enlarged view of (a). Blue and red lines indicate the results measured in direct- and side-coupling configurations, respectively.
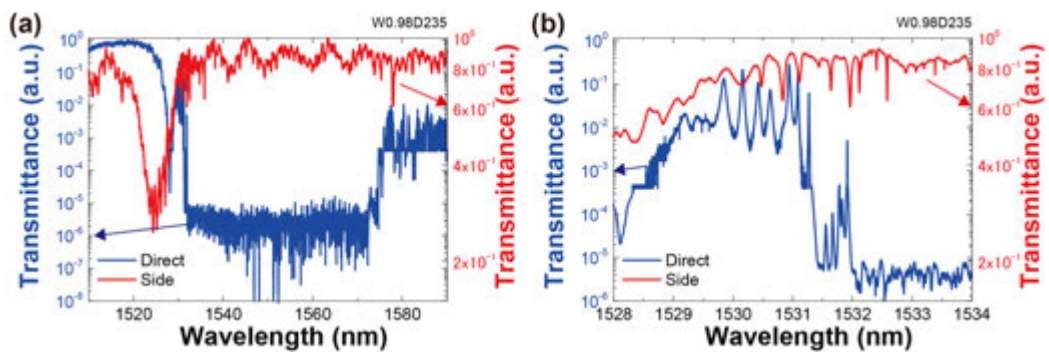


Fig. C.4. (a) Transmission spectrum of PhC waveguide with a width of $0.98 \times \sqrt{3}a$ and a diameter of 235 nm. (b) Enlarged view of (a). Blue and redlines indicate the results measured in direct- and side-coupling configurations, respectively.
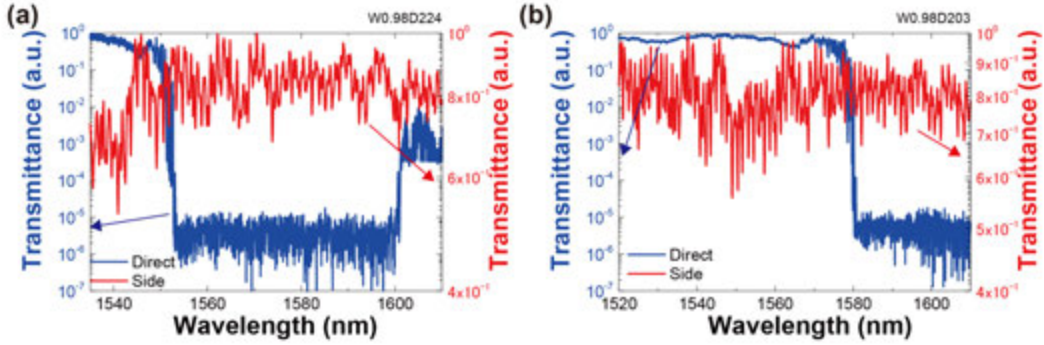
Fig. C.5. (a) Transmission spectrum of PhC waveguide with a width of $0.98 \times \sqrt{3}a$ and a diameter of 224 nm. (b) Transmission spectrum of PhC waveguide with a width of $0.98 \times \sqrt{3}a$ and a diameter of 204 nm. Blue and red lines indicate the results measured in direct- and side-coupling configurations, respectively.
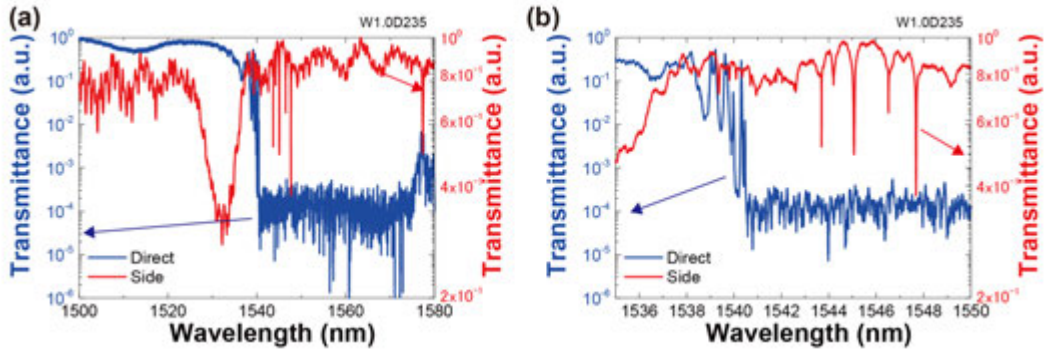


Fig. C.6. (a) Transmission spectrum of PhC waveguide with a width of $1.0 \times \sqrt{3}a$ and a diameter of 235 nm. (b) Enlarged view of (a). Blue and red lines indicate the results measured in direct- and side-coupling configurations, respectively.
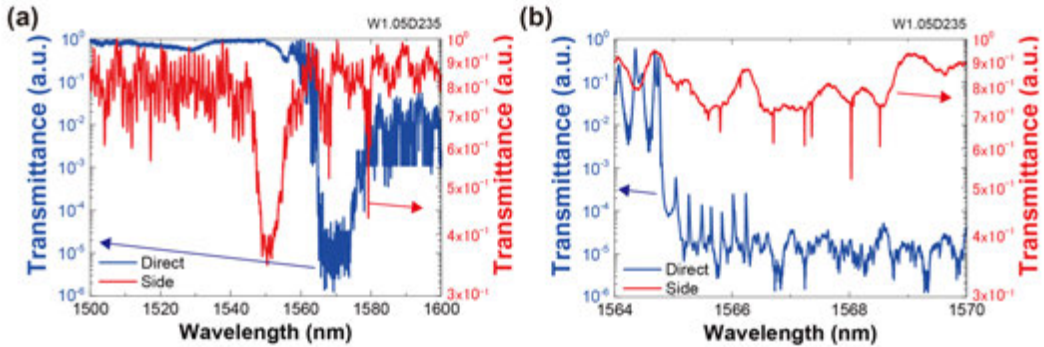


Fig. C.7. (a) Transmission spectrum of PhC waveguide with a width of $1.05 \times \sqrt{3}a$ and a diameter of 235 nm. (b) Enlarged view of (a). Blue and red lines indicate the results measured in direct- and side-coupling configurations, respectively.
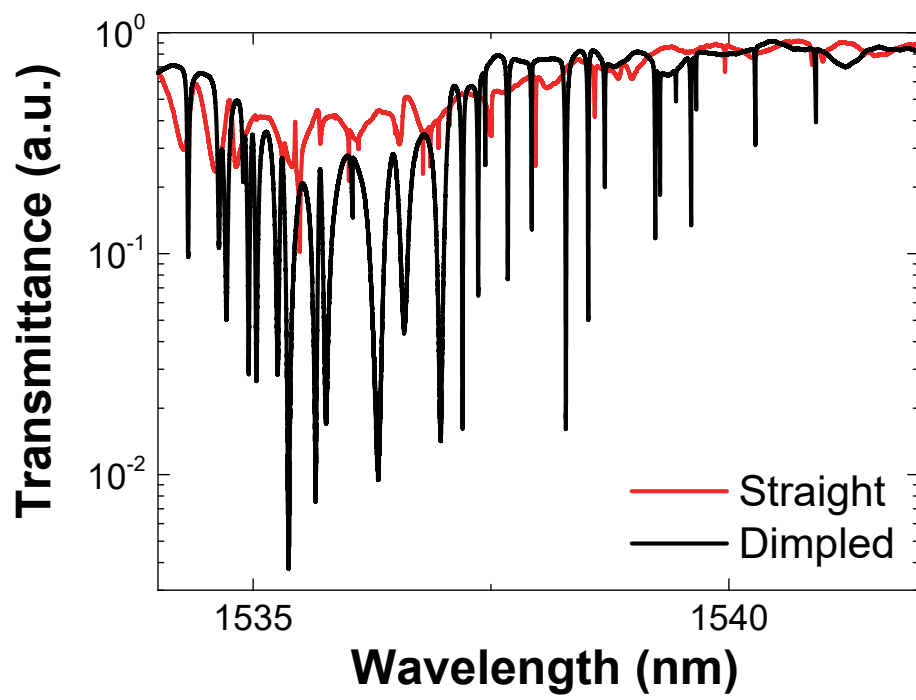
Fig. C.8. Transmission spectrum of the PhC waveguide measured using straight and dimpled nanofibers.

# Appendix D

# Calculation of the coupling efficiency in a FCPC platform

Cavity-mediated coupling between two different platforms is discussed herein for the system presented in Chapter 3. The goal of this chapter is clarifying the relation between transmittance from each port and each quality factor. Calculation models are shown in Fig. D.1. An FP-type cavity, which corresponds to a PhC nanocavity, is formed in a waveguide (indicated by PhC). The cavity is directly coupled to the waveguide and side coupled to another waveguide (nanofiber) with coupling rates of $\gamma_p$ and $\gamma_c$, respectively. The path of input light is different in the three models, as shown in Fig. D.1. The input is launched from (a) the nanofiber and (b) the PhC waveguide, as well as (c) generated inside the cavity with a photon (light) coupling rate of $\gamma_l$. A coupled-mode equation for the model of Fig. D.1(a) is as follows:

$$\frac{\mathrm{d}a}{\mathrm{d}t} = (j\omega_0 - \frac{\gamma_i + 2\gamma_c + 2\gamma_p}{2})a + j\sqrt{\gamma_c}s_{in}, \tag{D.1}$$

where $a$, $s_{in}$, $\omega_0$, $\gamma_i$, j are the amplitude of the mode in the microcavity, the amplitude of the input, the resonant angular frequency of the cavity, the decay rate of the cavity, and an imaginary number which satisfy $j^2 = -1$, respectively. Solving the equation for $a$, we have (similar problems are solved in Chapter 2.2.3),

$$a = \frac{j\sqrt{\gamma_c}s_{in}}{j(\omega - \omega_0) - \frac{\gamma_i + 2\gamma_c + 2\gamma_p}{2}}, \tag{D.2}$$

where $\omega$ is the angular frequency of light in the cavity. The output from each port is presented as follows:

$$s_{out1} = s_{in} + j\sqrt{\gamma_c}a, \tag{D.3}$$
$$s_{out2} = s_{out3} = j\sqrt{\gamma_p}a, \tag{D.4}$$
$$s_{out4} = -j\sqrt{\gamma_c}a, \tag{D.5}$$

The transmittance (reflectance) from each port is calculated from Eq. (D.2), Eq. (D.3), Eq. (D.4) and Eq. (D.5) because the transmittance is $Tr = |s_{out}/s_{in}|^2$. For example, a transmission spectrum of the system for $Q_i = 1.0 \times 10^5$, $Q_c = 1.0 \times 10^4$, and $Q_p = 1.0 \times 10^5$ is shown in

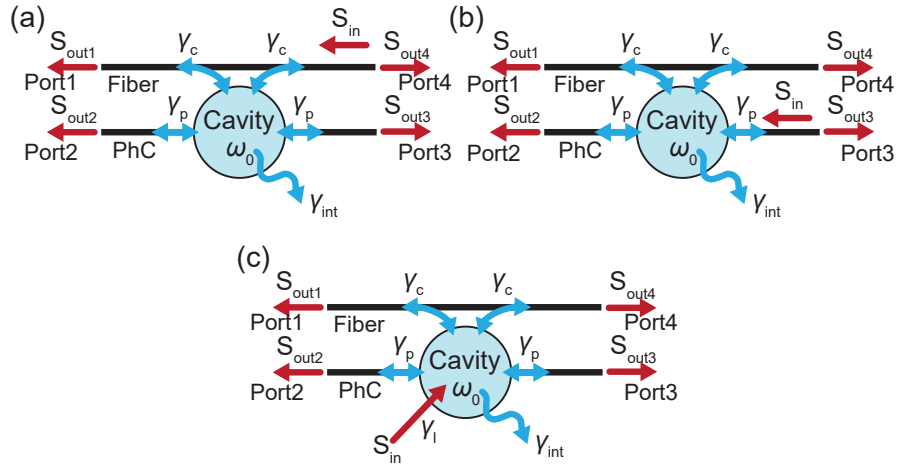# APPENDIX D. CALCULATION OF THE COUPLING EFFICIENCY IN A FCPC PLATFORM



Fig. D.1. Models for a coupled-mode analysis. Input light is launched from (a) a nanofiber, (b) a PhC waveguide, and (c) other sources.

Fig. D.2. The transmittance at the Port 1 approaches nearly zero at resonance. The breakdown of the coupled light is as follows: >70% is transmitted (reflected) to the Port 4, approximately 10% is coupled to the PhC waveguide, and the other component is consumed in the cavity. Both high coupling efficiency (measured at the Port 1) and high reflectance (measured at the Port 4) occurred because of the lower coupling $Q$ (the higher coupling rate) compared with the intrinsic $Q$. In other words, energy was quickly exchanged between the cavity and the nanofiber, within the photon lifetime in the cavity. Note that the reflected light can contribute to the nonlinear effect in the cavity, if the effect responds to the input of light quickly and takes place within the photon lifetime in the cavity (e.g., the Kerr effect). In contrast, the small transmittance at the Ports 2 and 3 is owing to a high coupling $Q$ between the cavity and PhC waveguide.

These transmittance and loss values strongly depend on the ratio of the intrinsic $Q$ and the coupling $Q$s. The values for various coupling quality factors of $Q_p$ and $Q_c$ are summarized in Fig. D.3. Here, an intrinsic $Q$ of $1.0 \times 10^5$ is assumed. As shown in the graph, high coupling between the cavity and the nanofiber (low transmittance at the Port 1, as shown in Fig. D.3(a)) will be obtained using the condition $Q_c \ll Q_i, Q_p$. In contrast, the cavity-mediated coupling between the nanofiber and PhC waveguide becomes high when the condition $Q_p = Q_c$ is satisfied (Fig. D.3(b)). The maximum transmittance values approach 0.25 for the both Ports 2 and 3; thus, 50% of the light was coupled to the PhC waveguide from the nanofiber in total. The energy consumed in the cavity had a maximum value with a critical coupling condition of $2Q_c^{-1} = Q_i^{-1}$ and $Q_c \ll Q_p$ (Fig. D.3(d)).
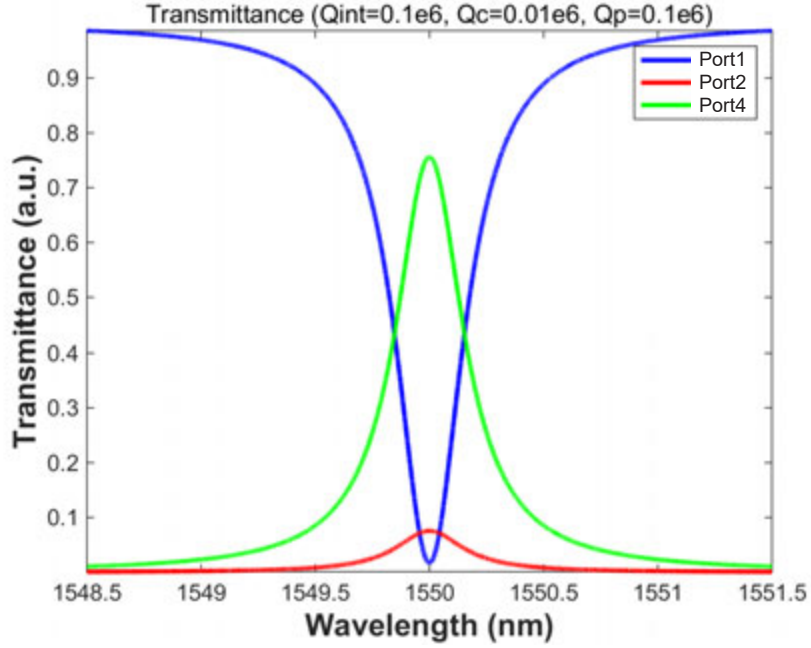
Fig. D.2. Transmission spectrum at each port when $Q_i = 1.0 \times 10^5$, $Q_c = 1.0 \times 10^4$, and $Q_p = 1.0 \times 10^5$.

Next, the solutions of the coupled-mode equation for the model in Fig. D.1(b) are as follows:

$$a = \frac{j\sqrt{\gamma_c}s_{in}}{j(\omega - \omega_0) - \frac{\gamma_i + 2\gamma_c + 2\gamma_p}{2}}, \tag{D.6}$$

$$s_{out1} = s_{out4} = j\sqrt{\gamma_c}a, \tag{D.7}$$

$$s_{out2} = j\sqrt{\gamma_p}a, \tag{D.8}$$

$$s_{cav} = \sqrt{\gamma_i}a, \tag{D.9}$$

where $s_{cav}$ shows the energy consumed in a cavity (loss a the cavity). Here, the transmittance at the Port 3 is $Tr_3 = 1 - Tr_2 - Tr_4 - Tr_{cav}$. Calculated results are shown in Fig. D.4. The transmittance at the Port 2 approaches 1.0 when $Q_p \ll Q_c, Q_i$ is satisfied. This is the opposite case for the Port 3, of which transmittance approaches 0 when $Q_p \ll Q_c, Q_i$. In addition, maximum transmittance (reflectance) takes place in the Port 3, with the condition $Q_c \ll Q_p, Q_i$ (Fig. D.4(c)). The cavity-mediated coupling between the PhC waveguide and nanofiber approaches the highest value of 0.5 (0.25 for the each port) when the condition $Q_p = Q_c < Q_i$ is satisfied (Fig. D.3(a)). The loss in the cavity obtained a maximum value with the critical coupling condition $2Q_p^{-1} = Q_i^{-1}$ and $Q_p \ll Q_c$ (Fig. D.4(d)) in a similar manner as shown in (Fig. D.3(d)).

Finally, the solutions of the coupled-mode analysis for the model in Fig. D.1(c) are as

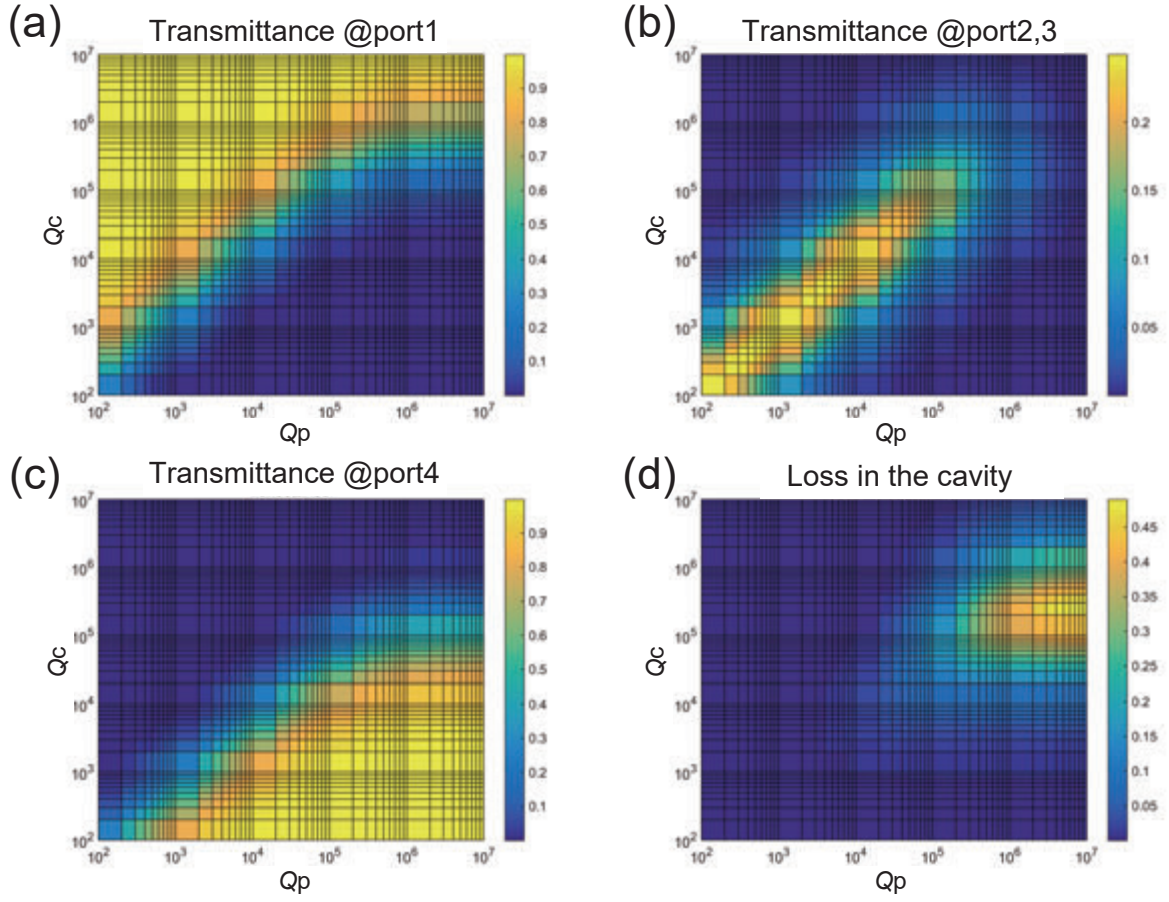# APPENDIX D.  CALCULATION OF THE COUPLING EFFICIENCY IN A FCPC PLATFORM



Fig.  D.3. Mapping of the transmittance at (a) Port 1, (b) Ports 2 and 3, and (c) Port 4. (d) The ratio of the energy consumed in the cavity.

follows:

$$a = \frac{j s_{\text{in}} \gamma_{\text{l}}}{j(\omega - \omega_0) - \frac{\gamma_{\text{i}} + 2\gamma_{\text{c}} + 2\gamma_{\text{p}}}{2}}, \tag{D.10}$$

$$s_{\text{out1}} = s_{\text{out4}} = j\sqrt{\gamma_{\text{c}}}a, \tag{D.11}$$

$$s_{\text{out2}} = s_{\text{out3}} = j\sqrt{\gamma_{\text{p}}}a, \tag{D.12}$$

$$s_{\text{cav}} = \sqrt{\gamma_{\text{i}}}a, \tag{D.13}$$

where $\gamma_{\text{l}}$ is the photon generation rate in the cavity, which is assumed to be 1 for the calculation. The transmittance from each port was obtained, as shown in Fig. D.5. The result is normalized by the total amount of transmittance and loss. As shown, light will couple to either the nanofiber or PhC waveguide with lower coupling $Q$. The maximum value of nearly 100% was obtained for coupling to the nanofiber with the condition $Q_{\text{c}} << Q_{\text{i}}, Q_{\text{p}}$ (Fig. D.5(a)) and for coupling to the PhC waveguide with the condition $Q_{\text{p}} << Q_{\text{i}}, Q_{\text{c}}$ (Fig. D.5(b)). The losses in the cavity increased when both coupling $Q$s were higher than the intrinsic $Q$s of the cavity (Fig. D.5(c)).

In summary, cavity-mediated coupling between the PhC waveguide and nanofiber was demonstrated numerically for the FCPC system. The transmittance approaches 50% for cases
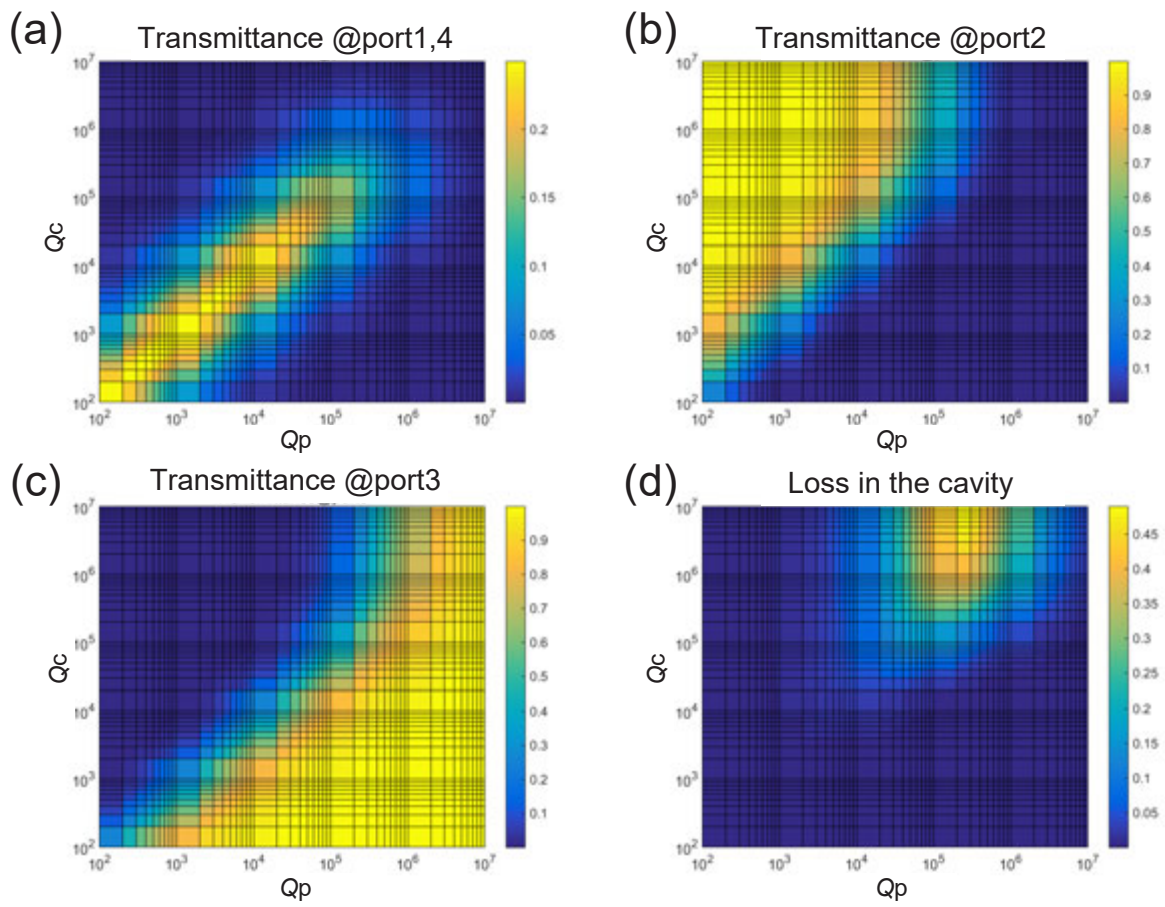
118

Fig. D.4. Mapping of the transmittance at (a) Ports 1 and 4, (b) Port 2, and (c) Port 3. (d) The ratio of the energy consumed in the cavity.

wherein the light is input from either waveguides. In contrast, transmittance reaches approximately 100%, if the light is generated in the cavity; this condition is satisfied in the case wherein cavity QED was demonstrated.

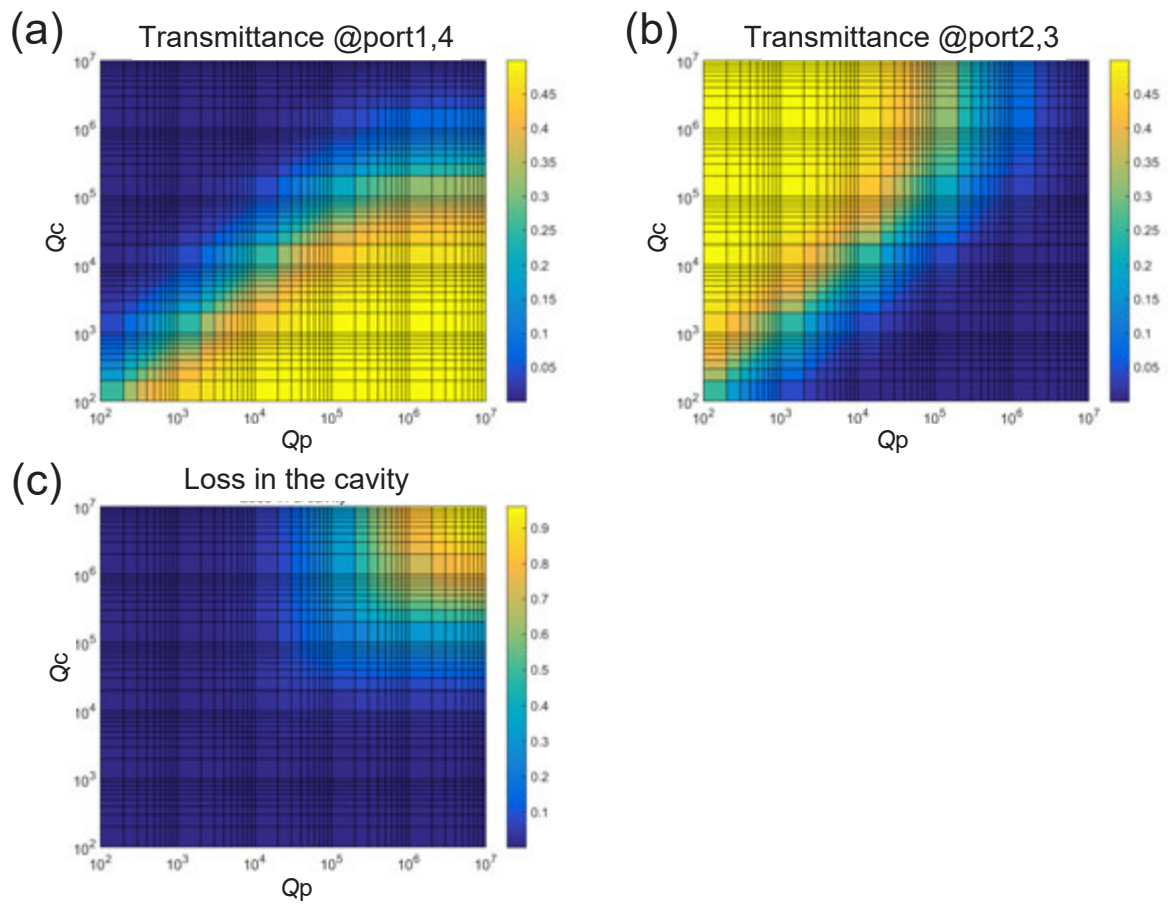# APPENDIX D.  CALCULATION OF THE COUPLING EFFICIENCY IN A FCPC PLATFORM



Fig.  D.5.  Mapping of the transmittance at (a) Ports 1 and 4 and (b) Ports 2 and 3.  (c) The ratio of the energy consumed in the cavity.

# Appendix E

# Reflectance measurement in FCPC platform

As described in Appendix D, usually some amount of reflectance exists when light couples with an FP-type cavity efficiently. This is also applicable for the waveguide because the reflection will occur at the boundary between the PhC and silicon waveguide [114]. Here, the amount of reflectance in an FCPC platform is evaluated experimentally. The experimental setup is shown in Fig. E.1(a) where overall setup is same as that in Chapter 3, however, a circulator is employed to detect reflectance from the PhC waveguide. The reference transmittance and reflectance of the circulator are shown in Fig. E.1(a) (they are also described in Tab. A.6). Note that the transmittance and reflectance are normalized by different values, and the transmittance is 140 times larger than the reflectance. Therefore, the transmittance through Port 1 to 3 and end-surface reflection at the edge of the optical fibers are small enough compared to the reflectance from the PhC waveguide. The measured transmittance and reflectance values are presented in Fig. E.1(c). As shown, the wavelengths of the characteristic peaks and dips match between the two spectra. However, the intensity of the transmittance is approximately 1000 times larger than that of the reflectance. This implies that the reflection at the boundaries between the two types of waveguides is very small and that most coupled light is transmitted to the substrate through the silicon waveguide (the silicon waveguide is attached to the substrate because it collapsed during the HF etching process to remove the clad).
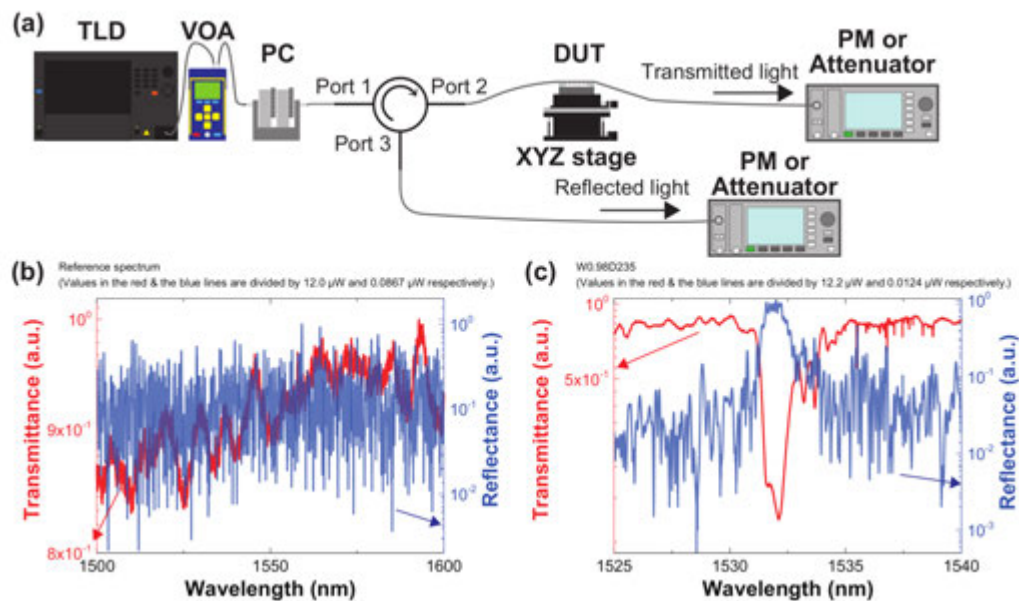
Fig. E.1. (a) Experimental setup for reflectance measurement. (b) Reference transmittance (from Port 1 to 2) and reflectance (from Port 2 to 3). Obtained transmittance and reflectance values were normalized by dividing with 12.0 $\mu$W and 0.0867 $\mu$W, respectively.(c) Transmittance (from Port 1 to 2) and reflectance (from Port 2 to 3) of a PhC waveguide. Obtained transmittance and reflectance values were normalized by dividing with 12.2 $\mu$W and 0.0124 $\mu$W, respectively.

# References

[1] H. J. Kimble, "The quantum internet," Nature **453**, 1023–1030 (2008).

[2] P. Benioff, "The computer as a physical system: A microscopic quantum mechanical hamiltonian model of computers as represented by turing machines," Journal of statistical physics **22**, 563–591 (1980).

[3] D. Deutsch, "Quantum theory, the church-turing principle and the universal quantum computer," "Proceedings of the Royal Society of London A: Mathematical, Physical and Engineering Sciences," (The Royal Society, 1985), vol. 400, pp. 97–117.

[4] D. Deutsch and R. Jozsa, "Rapid solution of problems by quantum computation," "Proceedings of the Royal Society of London A: Mathematical, Physical and Engineering Sciences," (The Royal Society, 1992), vol. 439, pp. 553–558.

[5] P. W. Shor, "Algorithms for quantum computation: Discrete logarithms and factoring," "Foundations of Computer Science, 1994 Proceedings., 35th Annual Symposium on," (Ieee, 1994), pp. 124–134.

[6] Y. Nakamura, Y. A. Pashkin, and J. Tsai, "Coherent control of macroscopic quantum states in a single-cooper-pair box," Nature **398**, 786–788 (1999).

[7] J. T. Muhonen, J. P. Dehollain, A. Laucht, F. E. Hudson, R. Kalra, T. Sekiguchi, K. M. Itoh, D. N. Jamieson, J. C. McCallum, A. S. Dzurak, and A. Morello, "Storing quantum information for 30 seconds in a nanoelectronic device," Nature Nanotechnology **9**, 986–991 (2014).

[8] S. Takeda and A. Furusawa, "Universal quantum computing with measurement-induced continuous-variable gate sequence in a loop-based architecture," Physical Review Letters **119**, 120504 (2017).

[9] A. Kandala, A. Mezzacapo, K. Temme, M. Takita, J. M. Chow, and J. M. Gambetta, "Hardware-efficient quantum optimizer for small molecules and quantum magnets," Nature **549** (2017).

[10] T. Kadowaki and H. Nishimori, "Quantum annealing in the transverse ising model," Physical Review E **58**, 5355 (1998).

[11] M. W. Johnson, M. H. Amin, S. Gildert, T. Lanting, F. Hamze, N. Dickson, R. Harris, A. J. Berkley, J. Johansson, P. Bunyk *et al.*, "Quantum annealing with manufactured spins," Nature **473**, 194–198 (2011).

[12] R. Ursin, F. Tiefenbacher, T. Schmitt-Manderbach, H. Weier, T. Scheidl, M. Lindenthal, B. Blauensteiner, T. Jennewein, J. Perdigues, P. Trojek *et al.*, "Entanglement-based quantum communication over 144 km," Nature Physics **3**, 481–486 (2007).

[13] S. Ritter, C. Nölleke, C. Hahn, A. Reiserer, A. Neuzner, M. Uphoff, M. Mücke, E. Figueroa, J. Bochmann, and G. Rempe, "An elementary quantum network of single atoms in optical cavities," Nature **484**, 195–200 (2012).

[14] A. Furusawa, J. L. Sørensen, S. L. Braunstein, C. A. Fuchs, H. J. Kimble, and E. S. Polzik, "Unconditional quantum teleportation," Science **282**, 706–709 (1998).

[15] S. Takeda, T. Mizuta, M. Fuwa, P. van Loock, and A. Furusawa, "Deterministic quantum teleportation of photonic quantum bits by a hybrid technique," Nature **500**, 315–318 (2013).

[16] A. Osada, R. Hisatomi, A. Noguchi, Y. Tabuchi, R. Yamazaki, K. Usami, M. Sadgrove, R. Yalla, M. Nomura, and Y. Nakamura, "Cavity optomagnonics with spin-orbit coupled photons," Physical Review Letters **116**, 223601 (2016).

[17] K. Fang, M. H. Matheny, X. Luan, and O. Painter, "Optical transduction and routing of microwave phonons in cavity-optomechanical circuits," Nature Photonics **10**, 489–496 (2016).

[18] T. Asano, Y. Ochi, Y. Takahashi, K. Kishimoto, and S. Noda, "Photonic crystal nanocavity with a $Q$ factor exceeding eleven million," Optics Express **25**, 1769–1777 (2017).

[19] D. Vernooy, V. S. Ilchenko, H. Mabuchi, E. Streed, and H. Kimble, "High-$Q$ measurements of fused-silica microspheres in the near infrared," Optics Letters **23**, 247–249 (1998).

[20] P. Seidler, K. Lister, U. Drechsler, J. Hofrichter, and T. Stöferle, "Slotted photonic crystal nanobeam cavity with an ultrahigh quality factor-to-mode volume ratio," Optics Express **21**, 32468–32483 (2013).

[21] S. Manipatruni, K. Preston, L. Chen, and M. Lipson, "Ultra-low voltage, ultra-small mode volume silicon microring modulator," Optics Express **18**, 18235–18242 (2010).

[22] U. P. Dharanipathy, M. Minkov, M. Tonin, V. Savona, and R. Houdré, "High-Q silicon photonic crystal cavity for enhanced optical nonlinearities," Applied Physics Letters **105**, 101101 (2014).

[23] P. B. Deotare, M. W. McCutcheon, I. W. Frank, M. Khan, and M. Lončar, "High quality factor photonic crystal nanobeam cavities," Applied Physics Letters **94**, 121106 (2009).

[24] Y. Lai, S. Pirotta, G. Urbinati, D. Gerace, M. Minkov, V. Savona, A. Badolato, and M. Galli, "Genetically designed L3 photonic crystal nanocavities with measured quality factor exceeding one million," Applied Physics Letters **104**, 241101 (2014).

[25] M. J. Burek, Y. Chu, M. S. Liddy, P. Patel, J. Rochman, S. Meesala, W. Hong, Q. Quan, M. D. Lukin, and M. Loncar, "High quality-factor optical nanocavities in bulk single-crystal diamond," Nature Communications **5** (2014).

[26] T. Kippenberg, S. Spillane, and K. Vahala, "Demonstration of ultra-high-Q small mode volume toroid microcavities on a chip," Applied Physics Letters **85**, 6113–6115 (2004).

[27] X. Ji, F. A. S. Barbosa, S. P. Roberts, A. Dutt, J. Cardenas, Y. Okawachi, A. Bryant, A. L. Gaeta, and M. Lipson, "Ultra-low-loss on-chip resonators with sub-milliwatt parametric oscillation threshold," Optica **4**, 619–624 (2017).

[28] H. Lee, T. Chen, J. Li, K. Y. Yang, S. Jeon, O. Painter, and K. J. Vahala, "Chemically etched ultrahigh-Q wedge-resonator on a silicon chip," Nature Photonics **6**, 369–373 (2012).

[29] A. A. Savchenkov, A. B. Matsko, V. S. Ilchenko, and L. Maleki, "Optical resonators with ten million finesse," Optics Express **15**, 6768–6773 (2007).

[30] V. Lobanov, G. Lihachev, T. Kippenberg, and M. Gorodetsky, "Frequency combs and platicons in optical microresonators with normal GVD," Optics Express **23**, 7713–7721 (2015).

[31] K. Ohtaka, "Energy band of photons and low-energy photon diffraction," Physical Review B **19**, 5057 (1979).

[32] M. Inoue, K. Ohtaka, and S. Yanagawa, "Light scattering from macroscopic spherical bodies. ii. reflectivity of light and electromagnetic localized state in a periodic monolayer of dielectric spheres," Physical Review B **25**, 689 (1982).

[33] K. Inoue and K. Ohtaka, *Photonic crystals: physics, fabrication and applications*, vol. 94 (Springer, 2013).

[34] E. Yablonovitch, "Inhibited spontaneous emission in solid-state physics and electronics," Physical Review Letters **58**, 2059 (1987).

[35] S. John, "Strong localization of photons in certain disordered dielectric superlattices," Physical Review Letters **58**, 2486 (1987).

[36] E. Yablonovitch, T. Gmitter, and K. Leung, "Photonic band structure: The face-centered-cubic case employing nonspherical atoms," Physical Review Letters **67**, 2295 (1991).

[37] S. Iwamoto, S. Takahashi, T. Tajiri, and Y. Arakawa, "Semiconductor Three-Dimensional Photonic Crystals with Novel Layer-by-Layer Structures," "Photonics," (Multidisciplinary Digital Publishing Institute, 2016), vol. 3, p. 34.

REFERENCES

[38] J. E. Wijnhoven and W. L. Vos, "Preparation of photonic crystals made of air spheres in titania," Science **281**, 802–804 (1998).

[39] H. Míguez, F. Meseguer, C. López, Á. Blanco, J. S. Moya, J. Requena, A. Mifsud, and V. Fornés, "Control of the photonic crystal properties of fcc-packed submicrometer SiO$_2$ spheres by sintering," Advanced Materials **10**, 480–483 (1998).

[40] J. Schilling, J. White, A. Scherer, G. Stupian, R. Hillebrand, and U. Gösele, "Three-dimensional macroporous silicon photonic crystal with large photonic band gap," Applied Physics Letters **86**, 011101 (2005).

[41] S. Takahashi, K. Suzuki, M. Okano, M. Imada, T. Nakamori, Y. Ota, K. Ishizaki, and S. Noda, "Direct creation of three-dimensional photonic crystals by a top-down approach," Nature Materials **8**, 721 (2009).

[42] D. Grishina, C. A. Harteveld, L. Woldering, and W. L. Vos, "Method for making a single-step etch mask for 3D monolithic nanostructures," Nanotechnology **26**, 505302 (2015).

[43] M. Deubel, G. Von Freymann, M. Wegener, S. Pereira, K. Busch, and C. M. Soukoulis, "Direct laser writing of three-dimensional photonic-crystal templates for telecommunications," Nature Materials **3**, 444 (2004).

[44] N. Yamamoto, S. Noda, and A. Chutinan, "Development of one period of a three-dimensional photonic crystal in the 5–10 $\mu$m wavelength region by wafer fusion and laser beam diffraction pattern observation techniques," Japanese Journal of Applied Physics **37**, L1052 (1998).

[45] S. Noda, K. Tomoda, N. Yamamoto, and A. Chutinan, "Full three-dimensional photonic bandgap crystals at near-infrared wavelengths," Science **289**, 604–606 (2000).

[46] K. Aoki, H. T. Miyazaki, H. Hirayama, K. Inoshita, T. Baba, K. Sakoda, N. Shinya, and Y. Aoyagi, "Microassembly of semiconductor three-dimensional photonic crystals," Nature Materials **2**, 117–121 (2003).

[47] K. Aoki, D. Guimard, M. Nishioka, M. Nomura, S. Iwamoto, and Y. Arakawa, "Coupling of quantum-dot light emission with a three-dimensional photonic-crystal nanocavity," Nature Photonics **2**, 688–692 (2008).

[48] S. Kawakami, "Fabrication of submicrometre 3D periodic structures composed of Si/SiO$_2$," Electronics Letters **33**, 1260–1261 (1997).

[49] J. Fleming and S.-Y. Lin, "Three-dimensional photonic crystal with a stop band from 1.35 to 1.95 $\mu$m," Optics Letters **24**, 49–51 (1999).

[50] K. Ishizaki, M. Koumura, K. Suzuki, K. Gondaira, and S. Noda, "Realization of three-dimensional guiding of photons in photonic crystals," Nature Photonics **7**, 133–137 (2013).

[51] S. Takahashi, T. Tajiri, Y. Ota, J. Tatebayashi, S. Iwamoto, and Y. Arakawa, "Circular dichroism in a three-dimensional semiconductor chiral photonic crystal," Applied Physics Letters **105**, 051107 (2014).

[52] O. Painter, R. Lee, A. Scherer, A. Yariv, J. O'brien, P. Dapkus, and I. Kim, "Two-dimensional photonic band-gap defect mode laser," Science **284**, 1819–1821 (1999).

[53] T. Yoshie, J. Vučković, A. Scherer, H. Chen, and D. Deppe, "High quality two-dimensional photonic crystal slab cavities," Applied Physics Letters **79**, 4289–4291 (2001).

[54] H.-Y. Ryu, S.-H. Kim, H.-G. Park, J.-K. Hwang, Y.-H. Lee, and J.-S. Kim, "Square-lattice photonic band-gap single-cell laser operating in the lowest-order whispering gallery mode," Applied Physics Letters **80**, 3883–3885 (2002).

[55] K. Srinivasan, P. E. Barclay, O. Painter, J. Chen, A. Y. Cho, and C. Gmachl, "Experimental demonstration of a high quality factor photonic crystal microcavity," Applied Physics Letters **83**, 1915–1917 (2003).

[56] K. Srinivasan and O. Painter, "Momentum space design of high-Q photonic crystal optical cavities," Optics Express **10**, 670–684 (2002).

[57] Y. Akahane, T. Asano, B.-S. Song, and S. Noda, "High-Q photonic nanocavity in a two-dimensional photonic crystal," Nature **425**, 944–947 (2003).

[58] J. Vučković, M. Lončar, H. Mabuchi, and A. Scherer, "Design of photonic crystal microcavities for cavity QED," Physical Review E **65**, 016608 (2001).

[59] Y. Akahane, T. Asano, B.-S. Song, and S. Noda, "Fine-tuned high-Q photonic-crystal nanocavity," Optics Express **13**, 1202–1214 (2005).

[60] B.-S. Song, S. Noda, T. Asano, and Y. Akahane, "Ultra-high-Q photonic double-heterostructure nanocavity," Nature Materials **4**, 207–210 (2005).

[61] E. Kuramochi, M. Notomi, S. Mitsugi, A. Shinya, T. Tanabe, and T. Watanabe, "Ultrahigh-Q photonic crystal nanocavities realized by the local width modulation of a line defect," Applied Physics Letters **88**, 041112 (2006).

[62] T. Asano, B.-S. Song, and S. Noda, "Analysis of the experimental $Q$ factors ($\sim 1$ million) of photonic crystal nanocavities," Optics Express **14**, 1996–2002 (2006).

[63] T. Tanabe, M. Notomi, E. Kuramochi, A. Shinya, and H. Taniyama, "Trapping and delaying photons for one nanosecond in an ultrasmall high-Q photonic-crystal nanocavity," Nature Photonics **1**, 49–52 (2007).

[64] Y. Takahashi, H. Hagino, Y. Tanaka, B.-S. Song, T. Asano, and S. Noda, "High-Q nanocavity with a 2-ns photon lifetime," Optics express **15**, 17206–17213 (2007).

REFERENCES

[65] Y. Taguchi, Y. Takahashi, Y. Sato, T. Asano, and S. Noda, "Statistical studies of photonic heterostructure nanocavities with an average $Q$ factor of three million," Optics Express **19**, 11916–11921 (2011).

[66] Z. Han, X. Checoury, L.-D. Haret, and P. Boucaud, "High quality factor in a two-dimensional photonic crystal cavity on silicon-on-insulator," Optics Letters **36**, 1749–1751 (2011).

[67] S.-W. Jeon, J.-k. Han, B.-S. Song, and S. Noda, "Glass-embedded two-dimensional silicon photonic crystal devices with a broad bandwidth waveguide and a high quality nanocavity," Optics Express **18**, 19361–19366 (2010).

[68] B.-S. Song, S.-W. Jeon, and S. Noda, "Symmetrically glass-clad photonic crystal nanocavities with ultrahigh quality factors," Optics Letters **36**, 91–93 (2011).

[69] H. Sekoguchi, Y. Takahashi, T. Asano, and S. Noda, "Photonic crystal nanocavity with a $Q$-factor of ∼ 9 million," Optics Express **22**, 916–924 (2014).

[70] Y. Tanaka, T. Asano, and S. Noda, "Design of Photonic Crystal Nanocavity With $Q$-Factor of ∼ $10^9$," Journal of Lightwave Technology **26**, 1532–1539 (2008).

[71] Y. Ooka, T. Tetsumoto, A. Fushimi, W. Yoshiki, and T. Tanabe, "CMOS compatible high-Q photonic crystal nanocavity fabricated with photolithography on silicon photonic platform," Scientific Reports **5**, 11312 (2015).

[72] K. Ashida, M. Okano, M. Ohtsuka, M. Seki, N. Yokoyama, K. Koshino, M. Mori, T. Asano, S. Noda, and Y. Takahashi, "Ultrahigh-Q photonic crystal nanocavities fabricated by CMOS process technologies," Optics Express **25**, 18165–18174 (2017).

[73] P. R. Villeneuve, S. Fan, J. Joannopoulos, K.-Y. Lim, G. Petrich, L. Kolodziejski, and R. Reif, "Air-bridge microcavities," Applied Physics Letters **67**, 167–169 (1995).

[74] J. Zhang, D. Chu, S. Wu, W. Bi, R. Tiberio, R. Joseph, A. Taflove, C. Tu, and S. Ho, "Nanofabrication of 1-D photonic bandgap structures along a photonic wire," IEEE Photonics Technology Letters **8**, 491–493 (1996).

[75] J. Foresi, P. R. Villeneuve, J. Ferrera, E. Thoen *et al.*, "Photonic-bandgap microcavities in optical wageguides," Nature **390**, 143–145 (1997).

[76] P. Lalanne and J. P. Hugonin, "Bloch-wave engineering for high-Q, small-V microcavities," IEEE Journal of Quantum Electronics **39**, 1430–1438 (2003).

[77] C. Sauvan, G. Lecamp, P. Lalanne, and J.-P. Hugonin, "Modal-reflectivity enhancement by geometry tuning in Photonic Crystal microcavities," Optics Express **13**, 245–255 (2005).

[78] P. Velha, J.-C. Rodier, P. Lalanne, J.-P. Hugonin, D. Peyrade, E. Picard, T. Charvolin, and E. Hadji, "Ultracompact silicon-on-insulator ridge-waveguide mirrors with high reflectance," Applied Physics Letters **89**, 171121 (2006).

[79] P. Velha, E. Picard, T. Charvolin, E. Hadji, J.-C. Rodier, P. Lalanne, and D. Peyrade, "Ultra-high Q/V fabry-perot microcavity on SOI substrate," Optics Express **15**, 16090–16096 (2007).

[80] A. R. M. Zain, N. P. Johnson, M. Sorel, and M. Richard, "Ultra high quality factor one dimensional photonic crystal/photonic wire micro-cavities in silicon-on-insulator (SOI)," Optics Express **16**, 12084–12089 (2008).

[81] E. Kuramochi, H. Taniyama, T. Tanabe, K. Kawasaki, Y.-G. Roh, and M. Notomi, "Ultrahigh-$Q$ one-dimensional photonic crystal nanocavities with modulated mode-gap barriers on SiO$_2$ claddings and on air claddings," Optics Express **18**, 15859–15869 (2010).

[82] M. W. McCutcheon and M. Lončar, "Design of a silicon nitride photonic crystal nanocavity with a Quality factor of one million for coupling to a diamond nanocrystal," Optics Express **16**, 19136–19145 (2008).

[83] Y. Gong and J. Vučković, "Photonic crystal cavities in silicon dioxide," Applied Physics Letters **96**, 031107 (2010).

[84] Y. Gong, S. Ishikawa, S.-L. Cheng, M. Gunji, Y. Nishi, and J. Vučković, "Photoluminescence from silicon dioxide photonic crystal cavities with embedded silicon nanocrystals," Physical Review B **81**, 235317 (2010).

[85] Q. Quan, I. B. Burgess, S. K. Tang, D. L. Floyd, and M. Loncar, "High-Q, low index-contrast polymeric photonic crystal nanobeam cavities," Optics Express **19**, 22191–22197 (2011).

[86] M. Khan, T. Babinec, M. W. McCutcheon, P. Deotare, and M. Lončar, "Fabrication and characterization of high-quality-factor silicon nitride nanobeam cavities," Optics Letters **36**, 421–423 (2011).

[87] M. Davanco, S. Ates, Y. Liu, and K. Srinivasan, "Si$_3$N$_4$ optomechanical crystals in the resolved-sideband regime," Applied Physics Letters **104**, 041101 (2014).

[88] Q. Quan, P. B. Deotare, and M. Loncar, "Photonic crystal nanobeam cavity strongly coupled to the feeding waveguide," Applied Physics Letters **96**, 203102 (2010).

[89] Q. Quan and M. Loncar, "Deterministic design of wavelength scale, ultra-high Q photonic crystal nanobeam cavities," Optics Express **19**, 18529–18542 (2011).

[90] D. O. Bracher and E. L. Hu, "Fabrication of high-Q nanobeam photonic crystals in epitaxially grown 4H-SiC," Nano Letters **15**, 6202–6207 (2015).

[91] G. Crosnier, D. Sanchez, A. Bazin, P. Monnier, S. Bouchoule, R. Braive, G. Beaudoin, I. Sagnes, R. Raj, and F. Raineri, "High $Q$ factor InP photonic crystal nanobeam cavities on silicon wire waveguides," Optics Letters **41**, 579–582 (2016).

REFERENCES

[92] Y. Zhang, M. Khan, Y. Huang, J. Ryou, P. Deotare, R. Dupuis, and M. Lončar, "Photonic crystal nanobeam lasers," Applied Physics Letters **97**, 051104 (2010).

[93] W. Pernice, C. Xiong, C. Schuck, and H. Tang, "High-Q aluminum nitride photonic crystal nanobeam cavities," Applied Physics Letters **100**, 091105 (2012).

[94] C. Xiong, W. H. Pernice, X. Sun, C. Schuck, K. Y. Fong, and H. X. Tang, "Aluminum nitride as a new material for chip-scale optomechanics and nonlinear optics," New Journal of Physics **14**, 095014 (2012).

[95] K. K. Mehta, J. S. Orcutt, O. Tehar-Zahav, Z. Sternberg, R. Bafrali, R. Meade, and R. J. Ram, "High-Q CMOS-integrated photonic crystal microcavity devices," Scientific Reports **4** (2014).

[96] K. Nayak and K. Hakuta, "Photonic crystal formation on optical nanofibers using femtosecond laser ablation technique," Optics Express **21**, 2480–2490 (2013).

[97] A. W. Schell, H. Takashima, S. Kamioka, Y. Oe, M. Fujiwara, O. Benson, and S. Takeuchi, "Highly efficient coupling of nanolight emitters to a ultra-wide tunable nanofibre cavity," Scientific Reports **5**, 9619 (2015).

[98] J. Keloth, K. Nayak, and K. Hakuta, "Fabrication of a centimeter-long cavity on a nanofiber for cavity quantum electrodynamics," Optics Letters **42**, 1003–1006 (2017).

[99] J. W. S. B. Rayleigh, *The theory of sound*, vol. 2 (Macmillan, 1896).

[100] C. V. Raman, "On whispering galleries," Proc. Indian Ass. Cult. Sci. **7**, 159–172 (1922).

[101] P. Del'Haye, A. Schliesser, O. Arcizet, T. Wilken, R. Holzwarth, and T. Kippenberg, "Optical frequency comb generation from a monolithic microresonator." Nature **450**, 1214–1217 (2007).

[102] T. Kippenberg, H. Rokhsari, T. Carmon, A. Scherer, and K. Vahala, "Analysis of radiation-pressure induced mechanical oscillation of an optical microcavity," Physical Review Letters **95**, 033901 (2005).

[103] H. Rokhsari, T. J. Kippenberg, T. Carmon, and K. J. Vahala, "Radiation-pressure-driven micro-mechanical oscillator," Optics Express **13**, 5293–5301 (2005).

[104] T. Carmon, H. Rokhsari, L. Yang, T. J. Kippenberg, and K. J. Vahala, "Temporal behavior of radiation-pressure-induced vibrations of an optical microcavity phonon mode," Physical Review Letters **94**, 223902 (2005).

[105] S. A. Miller, M. Yu, X. Ji, A. G. Griffith, J. Cardenas, A. L. Gaeta, and M. Lipson, "Low-loss silicon platform for broadband mid-infrared photonics," Optica **4**, 707–712 (2017).

[106] M. H. P. Pfeiffer, A. Kordts, V. Brasch, M. Zervas, M. Geiselmann, J. D. Jost, and T. J. Kippenberg, "Photonic Damascene process for integrated high-Q microresonator based nonlinear photonics," Optica **3**, 20–25 (2016).

[107] J. Pfeifle, V. Brasch, M. Lauermann, Y. Yu, D. Wegner, T. Herr, K. Hartinger, P. Schindler, J. Li, D. Hillerkuss *et al.*, "Coherent terabit communications with microresonator kerr frequency combs," Nature photonics **8**, 375–380 (2014).

[108] P. Marin-Palomo, J. N. Kemal, M. Karpov, A. Kordts, J. Pfeifle, M. H. Pfeiffer, P. Trocha, S. Wolf, V. Brasch, M. H. Anderson *et al.*, "Microresonator-based solitons for massively parallel coherent optical communications," Nature **546**, 274–279 (2017).

[109] S.-H. Kim, S.-K. Kim, and Y.-H. Lee, "Vertical beaming of wavelength-scale photonic crystal resonators," Physical Review B **73**, 235117 (2006).

[110] S. Combrié, A. De Rossi *et al.*, "Directive emission from high-Q photonic crystal cavities through band folding," Physical Review B **79**, 041101 (2009).

[111] H. Takagi, Y. Ota, N. Kumagai, S. Ishida, S. Iwamoto, and Y. Arakawa, "High $Q$ H1 photonic crystal nanocavities with efficient vertical emission," Optics Express **20**, 28292–28300 (2012).

[112] J. C. Knight, G. Cheung, F. Jacques, and T. Birks, "Phase-matched excitation of whispering-gallery-mode resonances by a fiber taper," Optics Letters **22**, 1129–1131 (1997).

[113] S. Spillane, T. Kippenberg, O. Painter, and K. Vahala, "Ideality in a fiber-taper-coupled microresonator system for application to cavity quantum electrodynamics," Physical Review Letters **91**, 043902 (2003).

[114] P. E. Barclay, K. Srinivasan, M. Borselli, and O. Painter, "Efficient input and output fiber coupling to a photonic crystal waveguide," Optics Letters **29**, 697–699 (2004).

[115] K. Srinivasan, P. E. Barclay, M. Borselli, and O. J. Painter, "An optical-fiber-based probe for photonic crystal microcavities," IEEE Journal on Selected Areas in Communications **23**, 1321–1329 (2005).

[116] C. Michael, M. Borselli, T. Johnson, C. Chrystal, and O. Painter, "An optical fiber-taper probe for wafer-scale microphotonic device characterization," Optics Express **15**, 4745–4752 (2007).

[117] P. E. Barclay, K. Srinivasan, and O. Painter, "Design of photonic crystal waveguides for evanescent coupling to optical fiber tapers and integration with high-Q cavities," Journal of the Optical Society of America B **20**, 2274–2284 (2003).

[118] Y. Ding, C. Peucheret, H. Ou, and K. Yvind, "Fully etched apodized grating coupler on the SOI platform with -0.58 dB coupling efficiency," Optics Letters **39**, 5348–5350 (2014).

[119] K. Shiraishi, H. Yoda, A. Ohshima, H. Ikedo, and C. S. Tsai, "A silicon-based spot-size converter between single-mode fibers and Si-wire waveguides using cascaded tapers," Applied Physics Letters **91**, 141120 (2007).

REFERENCES

[120] Y. Terada, K. Miyasaka, K. Kondo, N. Ishikura, T. Tamura, and T. Baba, "Optimized optical coupling to silica-clad photonic crystal waveguides," Optics Letters **42**, 4695–4698 (2017).

[121] R. Miller, T. Northup, K. Birnbaum, A. Boca, A. Boozer, and H. Kimble, "Trapped atoms in cavity QED: coupling quantized light and matter," Journal of Physics B: Atomic, Molecular and Optical Physics **38**, S551 (2005).

[122] C. Law and H. Kimble, "Deterministic generation of a bit-stream of single-photon pulses," Journal of Modern Optics **44**, 2067–2074 (1997).

[123] A. Kuhn, M. Hennrich, T. Bondo, and G. Rempe, "Controlled generation of single photons from a strongly coupled atom-cavity system," Applied Physics B: Lasers and Optics **69**, 373–377 (1999).

[124] M. Hijlkema, B. Weber, H. P. Specht, S. C. Webster, A. Kuhn, and G. Rempe, "A single-photon server with just one atom," Nature Physics **3**, 253–255 (2007).

[125] A. D. Boozer, A. Boca, R. Miller, T. E. Northup, and H. J. Kimble, "Reversible state transfer between light and a single trapped atom," Physical Review Letters **98**, 193601 (2007).

[126] E. M. Purcell, "Spontaneous emission probabilities at radio frequencies," Physical Review **69**, 681 (1946).

[127] A. Yariv, "Quantum electronics," American Journal of Physics (2005).

[128] A. Meldrum, P. Bianucci, and F. Marsiglio, "Modification of ensemble emission rates and luminescence spectra for inhomogeneously broadened distributions of quantum dots coupled to optical microcavities," Optics Express **18**, 10230–10246 (2010).

[129] G. Khitrova, H. Gibbs, M. Kira, S. Koch, and A. Scherer, "Vacuum Rabi splitting in semiconductors," Nature Physics **2**, 81–90 (2006).

[130] P. Lodahl, S. Mahmoodian, and S. Stobbe, "Interfacing single photons and single quantum dots with photonic nanostructures," Reviews of Modern Physics **87**, 347 (2015).

[131] S. Ogawa, M. Imada, S. Yoshimoto, M. Okano, and S. Noda, "Control of light emission by 3D photonic crystals," Science **305**, 227–229 (2004).

[132] P. Lodahl, A. F. Van Driel, I. S. Nikolaev, A. Irman *et al.*, "Controlling the dynamics of spontaneous emission from quantum dots by photonic crystals," Nature **430**, 654 (2004).

[133] M. Fujita, S. Takahashi, Y. Tanaka, T. Asano, and S. Noda, "Simultaneous inhibition and redistribution of spontaneous light emission in photonic crystals," Science **308**, 1296–1298 (2005).

[134] A. Kress, F. Hofbauer, N. Reinelt, M. Kaniber, H. Krenner, R. Meyer, G. Böhm, and J. Finley, "Manipulation of the spontaneous emission dynamics of quantum dots in two-dimensional photonic crystals," Physical Review B **71**, 241304 (2005).

[135] M. Kaniber, A. Laucht, A. Neumann, J. Villas-Bôas, M. Bichler, M.-C. Amann, and J. Finley, "Investigation of the nonresonant dot-cavity coupling in two-dimensional photonic crystal nanocavities," Physical Review B **77**, 161303 (2008).

[136] Y. Ota, M. Shirane, M. Nomura, N. Kumagai, S. Ishida, S. Iwamoto, S. Yorozu, and Y. Arakawa, "Vacuum Rabi splitting with a single quantum dot embedded in a H1 photonic crystal nanocavity," Applied Physics Letters **94**, 033102 (2009).

[137] K. Hennessy, A. Badolato, M. Winger, D. Gerace, M. Atature, S. Gulde, S. Falt, E. L. Hu, and A. Imamoglu, "Quantum nature of a strongly coupled single quantum dot-cavity system," Nature **445**, 896–899 (2007).

[138] R. Ohta, Y. Ota, M. Nomura, N. Kumagai, S. Ishida, S. Iwamoto, and Y. Arakawa, "Strong coupling between a photonic crystal nanobeam cavity and a single quantum dot," Applied Physics Letters **98**, 173104 (2011).

[139] B. J. M. Hausmann, B. J. Shields, Q. Quan, Y. Chu, N. P. de Leon, R. Evans, M. J. Burek, A. S. Zibrov, M. Markham, D. Twitchen *et al.*, "Coupling of NV centers to photonic crystal nanobeams in diamond," Nano Letters **13**, 5791–5796 (2013).

[140] W. Yoshiki and T. Tanabe, "All-optical switching using Kerr effect in a silica toroid microcavity," Optics Express **22**, 24332–24341 (2014).

[141] W. Yoshiki, Y. Honda, M. Kobayashi, T. Tetsumoto, and T. Tanabe, "Kerr-induced controllable adiabatic frequency conversion in an ultrahigh $Q$ silica toroid microcavity," Optics Letters **41**, 5482–5485 (2016).

[142] W. Yoshiki, Y. Honda, T. Tetsumoto, K. Furusawa, N. Sekine, and T. Tanabe, "All-optical tunable buffering with coupled ultra-high Q whispering gallery mode microcavities," Scientific Reports **7**, 10688 (2017).

[143] L. Chang, X. Jiang, S. Hua, C. Yang, J. Wen, L. Jiang, G. Li, G. Wang, and M. Xiao, "Parity-time symmetry and variable optical isolation in active-passive-coupled microresonators," Nature Photonics **8**, 524–529 (2014).

[144] M. Notomi, A. Shinya, S. Mitsugi, G. Kira, E. Kuramochi, and T. Tanabe, "Optical bistable switching action of Si high-Q photonic-crystal nanocavities," Optics Express **13**, 2678–2687 (2005).

[145] T. Tanabe, K. Nishiguchi, E. Kuramochi, and M. Notomi, "Low power and fast electro-optic silicon modulator with lateral pin embedded photonic crystal nanocavity," Optics Express **17**, 22505–22513 (2009).

[146] K. Nozaki, T. Tanabe, A. Shinya, S. Matsuo, T. Sato, H. Taniyama, and M. Notomi, "Sub-femtojoule all-optical switching using a photonic-crystal nanocavity," Nature Photonics **4**, 477–483 (2010).

REFERENCES

[147] T. Tanabe, H. Sumikura, H. Taniyama, A. Shinya, and M. Notomi, "All-silicon sub-Gb/s telecom detector with low dark current and high quantum efficiency on chip," Applied Physics Letters **96**, 101103 (2010).

[148] T. Tanabe, M. Notomi, H. Taniyama, and E. Kuramochi, "Dynamic release of trapped light from an ultrahigh-Q nanocavity via adiabatic frequency tuning," Physical Review Letters **102**, 043907 (2009).

[149] T. Tanabe, E. Kuramochi, H. Taniyama, and M. Notomi, "Electro-optic adiabatic wavelength shifting and $Q$ switching demonstrated using a p-i-n integrated photonic crystal nanocavity," Optics Letters **35**, 3895–3897 (2010).

[150] S. Manipatruni, L. Chen, and M. Lipson, "Ultra high bandwidth WDM using silicon microring modulators," Optics Express **18**, 16858–16867 (2010).

[151] Y. Ooka, T. Tetsumoto, N. A. B. Daud, and T. Tanabe, "Ultrasmall in-plane photonic crystal demultiplexers fabricated with photolithography," Optics Express **25**, 1521–1528 (2017).

[152] K. Nozaki, A. Shinya, S. Matsuo, Y. Suzaki, T. Segawa, T. Sato, Y. Kawaguchi, R. Takahashi, and M. Notomi, "Ultralow-power all-optical RAM based on nanocavities," Nature Photonics **6**, 248–252 (2012).

[153] E. Kuramochi, K. Nozaki, A. Shinya, K. Takeda, T. Sato, S. Matsuo, H. Taniyama, H. Sumikura, and M. Notomi, "Large-scale integration of wavelength-addressable all-optical memories on a photonic crystal chip," Nature Photonics **8**, 474–481 (2014).

[154] M. Notomi, E. Kuramochi, and T. Tanabe, "Large-scale arrays of ultrahigh-Q coupled nanocavities," Nature Photonics **2**, 741–747 (2008).

[155] T. J. Kippenberg and K. J. Vahala, "Cavity opto-mechanics," Optics Express **15**, 17172–17205 (2007).

[156] T. J. Kippenberg and K. J. Vahala, "Cavity optomechanics: back-action at the mesoscale," science **321**, 1172–1176 (2008).

[157] V. B. Braginsky and A. Manukin, *Measurement of weak forces in physics experiments* (University of Chicago Press, 1977).

[158] A. Schliesser, O. Arcizet, R. Rivière, G. Anetsberger, and T. Kippenberg, "Resolved-sideband cooling and position measurement of a micromechanical oscillator close to the heisenberg uncertainty limit," Nature Physics **5**, 509–514 (2009).

[159] J. Chan, T. M. Alegre, A. H. Safavi-Naeini, J. T. Hill, A. Krause, S. Gröblacher, M. Aspelmeyer, and O. Painter, "Laser cooling of a nanomechanical oscillator into its quantum ground state," Nature **478**, 89–92 (2011).

[160] A. H. Safavi-Naeini, T. M. Alegre, J. Chan, M. Eichenfield, M. Winger, Q. Lin, J. T. Hill, D. E. Chang, and O. Painter, "Electromagnetically induced transparency and slow light with optomechanics," Nature **472**, 69–73 (2011).

[161] S. Weis, R. Rivière, S. Deléglise, E. Gavartin, O. Arcizet, A. Schliesser, and T. J. Kippenberg, "Optomechanically induced transparency," Science **330**, 1520–1523 (2010).

[162] A. G. Krause, M. Winger, T. D. Blasius, Q. Lin, and O. Painter, "A high-resolution microchip optomechanical accelerometer," Nature Photonics **6**, 768–772 (2012).

[163] E. Gavartin, P. Verlot, and T. J. Kippenberg, "A hybrid on-chip optomechanical transducer for ultrasensitive force measurements," Nature Nanotechnology **7**, 509–514 (2012).

[164] R. Schilling, H. Schütz, A. Ghadimi, V. Sudhir, D. J. Wilson, and T. J. Kippenberg, "Near-Field integration of a SiN Nanobeam and a SiO$_2$ Microcavity for Heisenberg-Limited Displacement Sensing," Physical Review Applied **5**, 054019 (2016).

[165] G. S. Wiederhecker, L. Chen, A. Gondarenko, and M. Lipson, "Controlling photonic structures using optical forces," Nature **462**, 633–638 (2009).

[166] P. B. Deotare, I. Bulu, I. W. Frank, Q. Quan, Y. Zhang, R. Ilic, and M. Loncar, "All optical reconfiguration of optomechanical filters," Nature Communications **3**, 846 (2012).

[167] T. Tetsumoto and T. Tanabe, "High-Q silica zipper cavity for optical radiation pressure driven MOMS switch," AIP Advances **4**, 077137 (2014).

[168] A. Laucht, F. Hofbauer, N. Hauke, J. Angele, S. Stobbe, M. Kaniber, G. Böhm, P. Lodahl, M. Amann, and J. Finley, "Electrical control of spontaneous emission and strong coupling for a single quantum dot," New Journal of Physics **11**, 023034 (2009).

[169] S. Mosor, J. Hendrickson, B. Richards, J. Sweet, G. Khitrova, H. Gibbs, T. Yoshie, A. Scherer, O. Shchekin, and D. Deppe, "Scanning a photonic crystal slab nanocavity by condensation of xenon," Applied Physics Letters **87**, 141105 (2005).

[170] E. Agrell, M. Karlsson, A. Chraplyvy, D. J. Richardson, P. M. Krummrich, P. Winzer, K. Roberts, J. K. Fischer, S. J. Savory, B. J. Eggleton *et al.*, "Roadmap of optical communications," Journal of Optics **18**, 063002 (2016).

[171] M. Müller, S. Bounouar, K. D. Jöns, M. Glässl, and P. Michler, "On-demand generation of indistinguishable polarization-entangled photon pairs," Nature Photonics **8**, 224–228 (2014).

[172] J. D. Joannopoulos, S. G. Johnson, J. N. Winn, and R. D. Meade, *Photonic crystals: molding the flow of light* (Princeton university press, 2011).

[173] J. ichi Sakai, *Photonic Crystal Fibers (in Japanese)* (Corona, 2011).

[174] K. Sakoda, *Optical properties of photonic crystals*, vol. 80 (Springer Science & Business Media, 2004).

[175] S. G. Johnson and J. D. Joannopoulos, "Block-iterative frequency-domain methods for Maxwell's equations in a planewave basis," Optics Express **8**, 173–190 (2001).

REFERENCES

[176] T. Uno, *Finite difference time domain method for electromagnetic field and antennas* (Corona Publishing CO.,LTD, 1998).

[177] J.-P. Berenger, "A perfectly matched layer for the absorption of electromagnetic waves," Journal of Computational Physics **114**, 185–200 (1994).

[178] A. F. Oskooi, D. Roundy, M. Ibanescu, P. Bermel, J. D. Joannopoulos, and S. G. Johnson, "MEEP: A flexible free-software package for electromagnetic simulations by the FDTD method," Computer Physics Communications **181**, 687–702 (2010).

[179] H. A. Haus, *Waves and fields in optoelectronics* (Prentice-Hall,, 1984).

[180] C. Manolatou, M. Khan, S. Fan, P. R. Villeneuve, H. Haus, and J. Joannopoulos, "Coupling of modes analysis of resonant channel add-drop filters," IEEE Journal of Quantum Electronics **35**, 1322–1331 (1999).

[181] Q. Li, T. Wang, Y. Su, M. Yan, and M. Qiu, "Coupled mode theory analysis of mode-splitting in coupled cavity system," Optics Express **18**, 8367–8382 (2010).

[182] B. E. Little, S. T. Chu, H. A. Haus, J. Foresi, and J.-P. Laine, "Microring resonator channel dropping filters," Journal of Lightwave Technology **15**, 998–1005 (1997).

[183] M. Soljačić, M. Ibanescu, S. G. Johnson, Y. Fink, and J. Joannopoulos, "Optimal bistable switching in nonlinear photonic crystals," Physical Review E **66**, 055601 (2002).

[184] B. E. Saleh, M. C. Teich, and B. E. Saleh, *Fundamentals of photonics*, vol. 22 (Wiley New York, 1991).

[185] M. J. Humphrey, E. Dale, A. Rosenberger, and D. Bandy, "Calculation of optimal fiber radius and whispering-gallery mode spectra for a fiber-coupled microsphere," Optics Communications **271**, 124–131 (2007).

[186] A. Yariv and P. Yeh, *Photonics: optical electronics in modern communications*, vol. 6 (Oxford University Press New York, 2007).

[187] Y. Kokubun, *Lightwave engineering* (CRC Press, 2012).

[188] A. Yariv, *Optical electronics* (Saunders College Publ., 1991).

[189] R. Nagai and T. Aoki, "Ultra-low-loss tapered optical fibers with minimal lengths," Optics Express **22**, 28427–28436 (2014).

[190] A. Di Falco, L. O'faolain, and T. Krauss, "Chemical sensing in slotted photonic crystal heterostructure cavities," Applied Physics Letters **94**, 063503 (2009).

[191] D. Yang, S. Kita, F. Liang, C. Wang, H. Tian, Y. Ji, M. Lončar, and Q. Quan, "High sensitivity and high $Q$-factor nanoslotted parallel quadrabeam photonic crystal cavity for real-time and label-free sensing," Applied Physics Letters **105**, 063118 (2014).

[192] T. Baba, "Biosensing using photonic crystal nanolasers," MRS Communications **5**, 555–564 (2015).

[193] A. Yokoo, T. Tanabe, E. Kuramochi, and M. Notomi, "Ultrahigh-$Q$ nanocavities written with a nanoprobe," Nano Letters **11**, 3634–3642 (2011).

[194] C. L. Smith, U. Bog, S. Tomljenovic-Hanic, M. W. Lee, D. K. Wu, L. O'Faolain, C. Monat, C. Grillet, T. F. Krauss, C. Karnutsch *et al.*, "Reconfigurable microfluidic photonic crystal slab cavities," Optics Express **16**, 15887–15896 (2008).

[195] M.-K. Kim, I.-K. Hwang, M.-K. Seo, and Y.-H. Lee, "Reconfigurable microfiber-coupled photonic crystal resonator," Optics Express **15**, 17241–17247 (2007).

[196] M.-K. Kim, J.-Y. Kim, J.-H. Kang, B.-H. Ahn, and Y.-H. Lee, "On-demand photonic crystal resonators," Laser & Photonics Reviews **5**, 479–495 (2011).

[197] T. Miya, Y. Terunuma, T. Hosaka, and T. Miyashita, "Ultimate low-loss single-mode fibre at 1.55 $\mu$m," Electronics Letters **15**, 106–108 (1979).

[198] T. Carmon and K. J. Vahala, "Visible continuous emission from a silica microphotonic device by third-harmonic generation," Nature Physics **3**, 430–435 (2007).

[199] S. Fujii, T. Kato, R. Suzuki, and T. Tanabe, "Third-harmonic blue light generation from Kerr clustered combs and dispersive waves," Optics Letters **42**, 2010–2013 (2017).

[200] M. LaGasse, D. Liu-Wong, J. G. Fujimoto, and H. A. Haus, "Ultrafast switching with a single-fiber interferometer," Optics Letters **14**, 311–313 (1989).

[201] L. Yang, D. Armani, and K. Vahala, "Fiber-coupled erbium microlasers on a chip," Applied Physics Letters **83**, 825–826 (2003).

[202] T. J. Kippenberg, J. Kalkman, A. Polman, and K. J. Vahala, "Demonstration of an erbium-doped microdisk laser on a silicon chip," Physical Review A **74**, 051802 (2006).

[203] S. Mehrabani and A. M. Armani, "Blue upconversion laser based on thulium-doped silica microcavity," Optics Letters **38**, 4346–4349 (2013).

[204] K. K. Lee, D. R. Lim, H.-C. Luan, A. Agarwal, J. Foresi, and L. C. Kimerling, "Effect of size and roughness on light transmission in a $Si/SiO_2$ waveguide: Experiments and model," Applied Physics Letters **77**, 1617–1619 (2000).

[205] M. W. McCutcheon, P. B. Deotare, Y. Zhang, and M. Lončar, "High-$Q$ transverse-electric/transverse-magnetic photonic crystal nanobeam cavities," Applied Physics Letters **98**, 111117 (2011).

[206] Y.-Z. Yan, S.-B. Yan, Z. Ji, J. Liu, C.-Y. Xue, W.-D. Zhang, and J.-J. Xiong, "Humidity and particulate testing of a high-Q microcavity packaging comprising a UV-curable polymer and tapered fiber coupler," Optics Communications **285**, 2189–2194 (2012).

# REFERENCES

[207] J. Nishimura, M. Kobayashi, R. Saito, and T. Tanabe, "NaCl ion detection using a silica toroid microcavity," Applied Optics **54**, 6391–6396 (2015).

[208] Y. Akihama, Y. Kanamori, and K. Hane, "Ultra-small silicon waveguide coupler switch using gap-variable mechanism," Optics Express **19**, 23658–23663 (2011).

[209] X. Chew, G. Zhou, H. Yu, F. S. Chau, J. Deng, Y. C. Loke, and X. Tang, "An in-plane nano-mechanics approach to achieve reversible resonance control of photonic crystal nanocavities," Optics Express **18**, 22232–22244 (2010).

[210] M. Eichenfield, C. P. Michael, R. Perahia, and O. Painter, "Actuation of micro-optomechanical systems via cavity-enhanced optical dipole forces," Nature Photonics **1**, 416–422 (2007).

[211] H.-J. Lim, C.-M. Lee, B.-H. Ahn, and Y.-H. Lee, "Dual-rail nanobeam microfiber-coupled resonator," Optics Express **21**, 6724–6732 (2013).

[212] A. Yariv, Y. Xu, R. K. Lee, and A. Scherer, "Coupled-resonator optical waveguide: a proposal and analysis," Optics Letters **24**, 711–713 (1999).

[213] F. Xia, L. Sekaric, and Y. Vlasov, "Ultracompact optical buffers on a silicon chip," Nature Photonics **1**, 65 (2007).

[214] Y. Ooka, N. A. B. Daud, T. Tetsumoto, and T. Tanabe, "Compact resonant electro-optic modulator using randomness of a photonic crystal waveguide," Optics Express **24**, 11199–11207 (2016).

# 謝辞 Acknowledgement

Acknowledgement

氏は真面目で優秀な人ばかりで，自分もしっかりとしないといけないなと刺激を受けました．特に，大岡氏とは研究の関連が大きかったですが，同氏はこの代のメンバーの中でも取り分けしっかりした学生で全く手が掛からなかったため，刺激を受けつつも逆にしっかりしない先輩でいられました．

　研究室の第五期生の熊崎基氏，田端智久氏，廣田直弥氏，藤井瞬氏，堀敦裕氏は一見大人しそうに見えて意外と野心がある油断ならない人が多い印象で，抜けがちな気が引き締まりました．熊崎氏とは情報通信研究機構での作製を一年余り共同で行いましたが，一人で行う場合に比べ，格段に作業効率が上がり助かっておりました．

　研究室の第六期生の岡村拓氏，上岡直隆氏，久保田啓寛氏，渕田美夏氏，本多祥大氏は，研究室が成熟してきたこともあり，発展的なテーマへの貢献を求められた人が多い印象でしたが，それでも一生懸命に研究に向き合う姿勢には感心していました．

　研究室の第七期生の石田蘭丸氏，金セイ基氏，田中航平氏，長谷川穂氏は全体的に天然な人が多い印象でしたが，知識を補って余りある一途な頑張りが出来る人が多く，その姿には刺激を受けました．また，同年度に研究室に加入された熊谷傳博士，Tomoki Samuel Lidsanel Prugger Suzuki 氏は二人とも田邉研とは異なるバックグランドを持つ貴重な存在で，熊谷博士の材料に関する深い知識や Suzuki 氏のラテン語を含む 4 か国語を操る教養の深さには尊敬の念を抱かずにはいられませんでした．

　研究室秘書の小嶋直子さん，小野寺かほるさんのお二人には，研究に関わる事務手続きを円滑に進めて頂き，大変助かりました．私自身は研究室秘書がいない時代を経験しているので，お二人の貢献の大きさを特に実感しております．

　最後に，博士進学を許容し，在学期間中惜しみない支援をして下さった両親に感謝を述べたいと思います．幼い頃は，落ち着きがなく，授業中に脱走を繰り返す，我儘に先生を巻き込み授業を遅延させる，など奇行が目立つ子供で，学校に度々呼び出された両親には大変迷惑を掛けました．礼儀や社会規範に関しては厳しい教育をして頂いたおかげで十分に備わったと考えておりますが，その一方で，行動の裏にあった好奇心は決して否定せず，自身の興味を追求することを常に後押しして頂きました．両親が人生の岐路の度に，自分が好きなこと，やりたいことをやりなさい，と言ってくれたことは，私自身の人生の指針を築き，多くの人と異なる道に進むための勇気をくれました．私の博士課程への進学および本研究の完成は両親の理解と献身なくしてはあり得ませんでした．心より感謝しております．残念ながら完成した論文を昨年の 10 月に亡くなった父には直接見せることは叶いませんでしたが，本論文の完成は両親に捧げたいと思います．

# List of publications

## Journal papers (related to this thesis)

[1] <u>T. Tetsumoto</u>, Y. Ooka, and T. Tanabe, "High-$Q$ coupled resonances on a PhC waveguide using a tapered nanofiber with high coupling efficiency," Optics Express, Vol. 23, 16256-16263 (2015).

[2] <u>T. Tetsumoto</u>, H. Kumazaki, K. Furusawa, N. Sekine, and T. Tanabe, "Design, fabrication and characterization of a high Q silica nanobeam cavity with orthogonal resonant modes," IEEE Photonics Journal, Vol. 9, 1-9 (2017).

## Other journal papers

[1] <u>T. Tetsumoto</u> and T. Tanabe, "High-Q silica zipper cavity for optical radiation pressure driven MOMS switch," AIP Advances, Vol. 4, 077137 (2014).

[2] R. Suzuki, T. Kato, <u>T. Tetsumoto</u>, and T. Tanabe, "Octagoonal toroid microcavity for mechanically robust optical coupling," AIP Advances, Vol. 5, 057127 (2015).

[3] Y. Ooka, <u>T. Tetsumoto</u>, A. Fushimi, W. Yoshiki, and T. Tanabe, "CMOS compatible high-Q photonic crystal nanocavity fabricated with photolithography on silicon photonic platform," Scientific Reports, Vol. 5, 11312 (2015).

[4] Y. Ooka, N. A. B. Daud, <u>T. Tetsumoto</u>, and T. Tanabe, "Compact resonant electro-optic modulator using randomness of a photonic crystal waveguide," Optics Express, Vol. 24, 11199-11207 (2016).

[5] W. Yoshiki, Y. Honda, M. Kobayashi, <u>T. Tetsumoto</u>, and T. Tanabe, "Kerr-induced controllable adiabatic frequency conversion in an ultra-high $Q$ silica toroid microcavity," Optics Letters, Vol. 41, 5482-5485 (2016).

[6] Y. Ooka, <u>T. Tetsumoto</u>, N. A. B. Daud, and T. Tanabe, "Ultrasmall in-plane photonic crystal demultiplexers fabricated with photolithography," Optics Express, Vol. 25, 1521-1528 (2017).

[7] N. A. B. Daud, Y. Ooka, T. Tabata, <u>T. Tetsumoto</u>, and T. Tanabe, "Electro-optic modulator based on photolithography fabricated p-i-n integrated photonic crystal nanocavity," IEICE Transactions on Electronics, Vol. E100-C, 670-674 (2017).

[8] W. Yoshiki, Y. Honda, <u>T. Tetsumoto</u>, K. Furusawa, N. Sekine, and T. Tanabe, "All-optical tunable buffering with coupled ultra-high $Q$ whispering gallery mode microcavities," Scientific Reports, Vol. 7, 28758 (2017).

# Conference proceedings

[1] <u>T. Tetsumoto</u>, Y. Ooka, and T. Tanabe, "Fiber-coupled photonic crystal nanocavity for reconfigurable formation of coupled cavity system," Proceedings of SPIE, Vol. 9756, Photonic and Phononic Properties of Engineered Nanostructures VI, Ed. A. Adibi, S.-Y. Lin and A. Scherer, (SPIE Photonics West 2016, San Francisco, USA), 97561J (6 pages), SPIE Publications (2016).

[2] <u>T. Tetsumoto</u>, H. Kumazaki, R. Ishida, and T. Tanabe, "Investigation of the influence of proximity effect and randomness on photolithographically fabricated photonic crystal nanobeam cavity," Proceedings of SPIE, Vol. 10456, SPIE Nanophotonics Australia 2017, Ed. J. W. M. Chon, and B. Jia, (SPIE Nanophotonics Australasia 2017, Melbourne, Australia) 104561Y (7 pages), SPIE Publications (2017).

# International conferences

[1] <u>T. Tetsumoto</u> and T. Tanabe, "Optomechanical waveguide system for switching telecom light," APS March Meeting 2014, H1.00113, Denver, March 3–7 (2014).

[2] <u>T. Tetsumoto</u> and T. Tanabe, "High-Q silica zipper cavity with strong opto-mechanical coupling for optical radiation pressure driven directional switching," IEEE Photonics Conference 2014 (IPC2014), San Diego, October 12–16 (2014)

[3] Y. Ooka, <u>T. Tetsumoto</u>, A. Fushimi, W. Yoshiki, and T. Tanabe, "Carrier-induced fast all-optical switching in a photonic crystal nanocavity fabricated with a CMOS compatible process," The 4th Advanced Lasers and Photon Source (ALPS ' 15), ALPSp14-02, Yokohama, April 22–24 (2015). (best student poster award)

[4] <u>T. Tetsumoto</u>, Y. Ooka, A. Fushimi, and T. Tanabe, "Nanocavity formation with a Q of a half-million using photonic crystal waveguide and nanofiber," Conference on Laser and Electro-Optics/Europe and the European Quantum Electronics Conference (CLEO/Europe EQEC 2015), CK-9.4 TUE, Munich, June 21–25 (2015).

[5] Y. Ooka, <u>T. Tetsumoto</u>, A. Fushimi, W. Yoshiki, and T. Tanabe, "A photolithographic high-Q photonic crystal nanocavity fabricated on a silicon-on-insulator structure," Conference on Laser and Electro-Optics/Europe and the European Quantum Electronics Conference (CLEO/Europe EQEC 2015), CK-9.2 TUE, Munich, June 21–25 (2015).

[6] Y. Ooka, N. A. Daud, <u>T. Tetsumoto</u>, and T. Tanabe, "Efficient electro-optic modulation of a weakly localized resonance in a photonic crystal waveguide," Frontiers in Optics/Laser

Science Conference (FiO/LS), FTu5C.6, San Jose, October 18–22 (2015).

[7] T. Tetsumoto, Y. Ooka, and T. Tanabe, "Fiber-coupled photonic crystal nanocavity for reconfigurable formation of coupled cavity system," SPIE Photonics West, 9756-54, San Francisco, February 13–18 (2016).

[8] W. Yoshiki , A. C.-Jinnai, T. Tetsumoto, S. Fujii, and T. Tanabe, "Time-domain observation of strong coupling between counter-propagating ultra-high Q whispering gallery modes," SPIE Photonics West, 9727-63, San Francisco, February 13–18 (2016).

[9] T. Tetsumoto, Y. Ooka, and T. Tanabe, "Observation of isolated mode and formation of coupled cavity in fiber coupled PhC cavity platform," The 12th International Symposium on Photonic and Electromagnetic Crystal Structures (PECS-XII), A28, University of York, July 17–21 (2016).

[10] T. Tanabe, T. Tetsumoto, H. Itobe, R. Suzuki, and T. Kato, "Optical nonlinear control at a very low power in ultrahigh- Q microcavity systems," 2016 International Conference on Optical MEMS and Nanophotonics (IEEE OMN 2016), We2.3, Singapore, July 31–August 4 (2016).

[11] T. Tanabe, T. Tetsumoto, Y. Ooka, and N. A. B. Daud, "Recent progress on high-Q photonic crystal nanocavities: Photolithographic fabrication and reconfigurable system," Progress In Electromagnetics Research Symposium (PIERS2016), SC3, Shanghai, August 8–11 (2016). (invited)

[12] Y. Ooka, N. A. Daud, T. Tetsumoto, T. Tanabe, "Ultrasmall in-plane photonic crystal demultiplexer fabricated with photolithography," Frontiers in Optics/Laser Science Conference (FiO/LS), FTu2D.3, Rochester, October 17–21 (2016).

[13] Y. Honda, W. Yoshiki, T. Tetsumoto, S. Fujii, K. Furusawa, N. Sekine, and T. Tanabe, "Tuning supermode splitting for stimulated Brillouin scattering," The 6th Advances Lasers and Photon Sources Conference (ALPS'17), ALPS8-4, Yokohama, April 18–21 (2017).

[14] T. Tetsumoto, H. Kumazaki, K. Furusawa, N. Sekine, A. Kasamatsu, and T. Tanabe, "High Q silica nanobeam cavity for simultaneous resonance of TE- and TM-like modes," CLEO:2017, JW2A, San Jose, May 14–19 (2017).

[15] W. Yoshiki, Y. Honda, M. Kobayashi, T. Tetsumoto, and T. Tanabe, "Adiabatic frequency conversion in an ultra-high-Q silica microcavity using the Kerr effect," CLEO:2017, SM2N1, San Jose, May 14–19 (2017).

[16] W. Yoshiki, Y. Honda, T. Tetsumoto, K. Furusawa, N. Sekine, and T. Tanabe, "Demonstration of all-optical tunable buffering using coupled ultra-high-Q silica toroid microcavities," CLEO:2017, SM2N2, San Jose, May 14–19 (2017).

[17] Y. Honda, W. Yoshiki, T. Tetsumoto, S. Fujii, K. Furusawa, N. Sekine, and T. Tanabe, "Brillouin lasing in coupled silica toroid microcavities," Conference on Lasers and Electro-Optics-European Quantum Electronics Conference (CLEO/Europe-EQEC 2017), CD-5.1, Munich, 25–29 June (2017).

List of publications

[18] T. Tetsumoto, H. Kumazaki, Y. Honda, and T. Tanabe, "Demonstration of direct coupling between a toroid microcavity and a photonic crystal waveguide," The Pacific Rim Conference on Lasers and Electro-Optics (CLEO-Pacific Rim 2017), 2-1L-4, Singapore, 31 July–4 August (2017).

[19] N. A. B. Daud, Y. Ooka, T. Tetsumoto, and T. Tanabe, "SiO2 clad active and passive photonic crystal nanocavity devices fabricated with photolithography," The Pacific Rim Conference on Lasers and Electro-Optics (CLEO-Pacific Rim 2017), P3‑119, Singapore, 31 July–4 August (2017).

[20] T. Tetsumoto, H. Kumazaki, Y. Honda, W. Yoshiki, K. Furusawa, N. Sekine, and T. Tanabe, "Experimental investigation of feasability of a hybrid system of a photonic crystal waveguide & a toroidal microcavity," The 24th Congress of the International Commissions for Optics (ICO-24), F1E-06, Tokyo, 21–25 August (2017).

[21] T. Tanabe, Y. Ooka, N. A. B. Daud, and T. Tetsumoto, "Robust CMOS compatible photonic crystal nanocavity and DEMUX filter," Asia Communications and Photonics Conference (ACP 2017), M1F.1, Guangzhou, November 10–13 (2017). (invited)

[22] T. Tetsumoto, H. Kumazaki, K. Furusawa, N. Sekine, and T. Tanabe, "Investigation of an optimal coupling condition with a nanobeam cavity made of low refractive index material," Frontiers in Optics/Laser Science Conference (FiO/LS), FTu2D.3, Washington DC, September 17–21 (2017).

[23] N. Kamioka, T. Tetsumoto, and T. Tanabe, "FDTD with an off-diagonal permittivity tensor component to study the magneto-optical effect in a slow light waveguide," Frontiers in Optics/Laser Science Conference (FiO/LS), JW4A.50, Washington DC, September 17–21 (2017).

# International workshops

[1] T. Tetsumoto and T.Tanabe, "Active formation of high Q nanocavity on photonic crystal waveguide assisted by nanofiber," Workshop on Optical Nanofiber Applications: From Quantum to Bio Technologies (ONNA2015), Okinawa, Japan, May 25–28 (2015).

[2] T. Tetsumoto, Y. Ooka, and T. Tanabe, "Reconfigurable coupled cavity system on a photonic crystal waveguide," The 4th International Workshop on Microcavities and Their Applications, Hokkaido, Japan, December 1–4 (2015)

[3] T. Tetsumoto, Y. Ooka, and T. Tanabe, "Formation of a coupled resonance using a nanofiber-coupled photonic crystal nanocavity," Workshop on Optical Nanofiber Applications: From Quantum to Bio Technologies (ONNA2017), Okinawa, Japan, June 5–8 (2017)

# Domestic conferences

[1]　鐵本 智大，田邉 孝純「シリカ zipper 型共振器を用いた光駆動 MEMS スイッチの検討」第 61 回応用物理学会春季学術講演会，17p-E16-4，青山学院大学相模原キャンパス，平成 26 年 3 月 17 日～20 日．

[2]　大岡 勇太，伏見 亮大，吉岐 航，鐵本 智大，田邉 孝純，「フォトリソグラフィで作製した SiO2 クラッド付き高 $Q$ 値フォトニック結晶共振器」第 75 回応用物理学会秋季学術講演会，17p-C8-3，北海道大学札幌キャンパス，平成 26 年 9 月 17 日～20日．

[3]　大岡 勇太，鐵本 智大，伏見 亮大，吉岐 航，田邉 孝純，「CMOS プロセスで SOI 上に作製した高 $Q$ 値シリコンフォトニック結晶共振器」　レーザー学会学術講演会第 35 回年次大会，11aX-3，東海大学高輪校舎，平成 27 年 1 月 11 日～12 日．

[4]　鐵本 智大，大岡 勇太，伏見 亮大，田邉 孝純，「ナノファイバを用いたフォトニック結晶導波路上での高 $Q$ 値共振器形成」　第 62 回応用物理学会春季学術講演会，13a-A10-5，東海大学湘南キャンパス，平成 27 年 3 月 11 日～14 日．

[5]　鐵本 智大，大岡 勇太，田邉 孝純，「ナノファイバ結合型高 Q 値フォトニック結晶共振器を用いた再構成可能な結合共振器形成」レーザー学会学術講演会第 36 回年次大会，10p-VI5，名城大学天白キャンパス，平成 28 年 1 月 9 日～11 日．

[6]　鐵本 智大，熊崎 基，古澤 健太郎，関根 徳彦，笠松 章史，田邉 孝純，「低屈折率なシリカを用いた高 $Q$ 値 zipper 共振器の作製」第 63 回応用物理学会春季学術講演会，20p-P4-6，東工大大岡山キャンパス，平成 28 年 3 月 19 日～22 日．

[7]　大岡 勇太，ヌル アシキン ダウド，鐵本 智大，田邉 孝純，「フォトニック結晶におけるランダム性の影響とその制御による利用」第 63 回応用物理学会春季学術講演会，22a-S621-6，東工大大岡山キャンパス，平成 28 年 3 月 19 日～22 日．

[8]　鐵本 智大，熊崎 基，本多 祥大，田邉 孝純，「シリカトロイド微小光共振器とフォトニック結晶導波路の結合実験」第 64 回応用物理学会春季学術講演会，16a-F202-4，パシフィコ横浜，平成 29 年 3 月 14 日～17 日．

[9]　本多 祥大，吉岐 航，鐵本 智大，藤井 瞬，田邉 孝純，「シリカトロイド結合共振器によるブリルアン発振」第 64 回応用物理学会春季学術講演会，15p-E205-18，パシフィコ横浜，平成 29 年 3 月 14 日～17 日．

[10]　上岡 直隆，鐵本 智大，田邉 孝純「FDTD 法を用いたフォトニック結晶導波路のスローライト効果による磁気光学効果アイソレータの小型化の数値解析的検討」第 78 回応用物理学会秋季学術講演会，6a-A405-4，福岡国際会議場，平成 29 年 9 月 5 日～8 日．